SYSTEM AND CIRCUIT DESIGN FOR A CAPACITIVE MEMS GYROSCOPE

Doctoral Dissertation

Mikko Saukoski

Helsinki University of Technology
Faculty of Electronics, Communications and Automation
Department of Micro and Nanosciences

SYSTEM AND CIRCUIT DESIGN FOR A CAPACITIVE MEMS GYROSCOPE

Doctoral Dissertation

Mikko Saukoski

Dissertation for the degree of Doctor of Science in Technology to be presented with due permission of the Faculty of Electronics, Communications and Automation for public examination and debate in Auditorium S1 at Helsinki University of Technology (Espoo, Finland) on the 18th of April, 2008, at 12 noon.

Helsinki University of Technology
Faculty of Electronics, Communications and Automation
Department of Micro and Nanosciences

Teknillinen korkeakoulu
Elektroniikan, tietoliikenteen ja automaation tiedekunta
Mikro- ja nanotekniikan laitos

ABSTRACT OF DOCTORAL DISSERTATION	HELSINKI UNIVERSITY OF TECHNOLOGY P. O. BOX 1000, FI-02015 TKK http://www.tkk.fi/

Abstract

In this thesis, issues related to the design and implementation of a micro-electro-mechanical angular velocity sensor are studied. The work focuses on a system based on a vibratory microgyroscope which operates in the low-pass mode with a moderate resonance gain and with an open-loop configuration of the secondary (sense) resonator. Both the primary (drive) and the secondary resonators are assumed to have a high quality factor. Furthermore, the gyroscope employs electrostatic excitation and capacitive detection.

The system design part of the thesis concentrates on selected aspects of the system-level design of a micro-electro-mechanical angular velocity sensor. In this part, a detailed analysis is provided of issues related to different non-idealities in the synchronous demodulation, the dynamics of the primary resonator excitation, the compensation of the mechanical quadrature signal, and the zero-rate output.

The circuit design part concentrates on the design and implementation of the integrated electronics required by the angular velocity sensor. The focus is primarily on the design of the sensor readout circuitry, comprising: a continuous-time front-end performing the capacitance-to-voltage (C/V) conversion, filtering, and signal level normalization; a bandpass $\Sigma\Delta$ analog-to-digital converter, and the required digital signal processing (DSP). The other fundamental circuit blocks are introduced on a more general level. Additionally, alternative ways to perform the C/V conversion are studied.

In the experimental work done for the thesis, a prototype of a micro-electro-mechanical angular velocity sensor is implemented and characterized. The analog parts of the system are implemented with a 0.7-μm high-voltage CMOS (Complimentary Metal-Oxide-Semiconductor) technology. The DSP part is realized with a field-programmable gate array (FPGA) chip. The $\pm 100\,°/\mathrm{s}$ gyroscope achieves $0.042\,°/\mathrm{s}/\sqrt{\mathrm{Hz}}$ spot noise and a signal-to-noise ratio of $51.6\,\mathrm{dB}$ over the $40\,\mathrm{Hz}$ bandwidth, with a $100\,°/\mathrm{s}$ input signal. The system demonstrates the use of $\Sigma\Delta$ modulation in both the primary resonator excitation and the quadrature compensation. Additionally, it demonstrates phase error compensation performed using DSP.

Tekijä   Mikko Saukoski

Väitöskirjan nimi

Kapasitiivisen mikromekaanisen kulmanopeusanturin järjestelmä- ja piiritason suunnittelu

Tiivistelmä

Väitöskirjassa tutkitaan mikromekaanisen kulmanopeusanturin suunnittelua ja toteutusta. Työssä keskitytään järjestelmään, joka pohjautuu värähtelevään kulmanopeusanturielementtiin. Elementti toimii alipäästömuotoisesti ja sen resonanssivahvistus on keskisuuri. Kulmanopeussignaalin havaitsemiseen käytetty toisio- eli sekundääri-resonaattori toimii avoimessa silmukassa. Sekä ensiö- eli primääriresonaattorin että toisioresonaattorin hyvyysluvut oletetaan suuriksi. Ensiöresonaattorin liike herätetään sähköstaattisesti, ja signaalien ilmaisu on kapasitiivinen.

Järjestelmätason suunnittelua käsittelevässä osassa tutkitaan aluksi, kuinka erilaiset epäideaalisuudet vaikuttavat anturielementiltä saatavien signaalien synkroniseen alassekoitukseen. Tämän jälkeen esitetään analyysi ensiö-resonaattorin herätyksen dynaamisesta käyttäytymisestä, mekaanisen kvadratuurisignaalin kompensoinnista sekä kulmanopeusanturin nollapistesignaalista.

Piirisuunnittelua käsittelevässä osassa keskitytään kulmanopeusanturin vaatiman integroidun elektroniikan suunnitteluun ja toteutukseen. Tässä osassa pääpaino on anturin signaalien ilmaisuun käytettävissä piirilohkoissa, jotka esitellään yksityiskohtaisesti. Näistä piirilohkoista ensimmäinen on jatkuva-aikainen etuaste, joka muuntaa kapasitanssimuotoiset signaalit jännitemuotoisiksi, suodattaa ne halutulle kaistanleveydelle, ja normalisoi niiden tasot. Muut ilmaisun vaatimat piirilohkot ovat kaistanpäästö-$\Sigma\Delta$-tyyppinen analogia-digitaalimuunnin sekä sen jälkeen tarvittava digitaalinen signaalinkäsittely. Muut piirilohkot käsitellään yleisemmällä tasolla. Lisäksi tässä osassa tutustutaan erilaisiin tapoihin suorittaa kapasitanssi-jännitemuunnos.

Työn kokeellisessa osassa toteutetun kulmanopeusanturiprototyypin analogiaosat valmistettiin 0,7 μm:n CMOS-puolijohdeprosessilla. Digitaalinen signaalinkäsittelyosa toteutettiin ohjelmoitavalla logiikkapiirillä. Anturiproto-tyyppi suunniteltiin $\pm 100\,°/$s:n kulmanopeusalueelle. Se saavuttaa $0{,}042\,°/$s$/\sqrt{\text{Hz}}$:n kohinatiheyden ja $51{,}6$ dB:n signaali-kohinasuhteen 40 Hz:n kaistanleveydellä, kun tulosignaalin suuruus on $100\,°/$s. Prototyypin avulla on osoitettu, kuinka $\Sigma\Delta$-modulaatiota voidaan käyttää sekä ensiöresonaattorin herätyksessä että mekaanisen kvadratuurisignaalin kompensoinnissa. Lisäksi prototyypillä on toteutettu digitaalinen vaihevirheiden korjaus.

Abstract

In this thesis, issues related to the design and implementation of a micro-electro-mechanical angular velocity sensor are studied. The work focuses on a system based on a vibratory microgyroscope which operates in the low-pass mode with a moderate resonance gain and with an open-loop configuration of the secondary (sense) resonator. Both the primary (drive) and the secondary resonators are assumed to have a high quality factor. Furthermore, the gyroscope employs electrostatic excitation and capacitive detection.

The thesis is divided into three parts. The first part provides the background information necessary for the other two parts. The basic properties of a vibratory microgyroscope, together with the most fundamental non-idealities, are described, a short introduction to various manufacturing technologies is given, and a brief review of published microgyroscopes and of commercial microgyroscopes is provided.

The second part concentrates on selected aspects of the system-level design of a micro-electro-mechanical angular velocity sensor. In this part, a detailed analysis is provided of issues related to different non-idealities in the synchronous demodulation, the dynamics of the primary resonator excitation, the compensation of the mechanical quadrature signal, and the zero-rate output. The use of $\Sigma\Delta$ modulation to improve accuracy in both primary resonator excitation and the compensation of the mechanical quadrature signal is studied.

The third part concentrates on the design and implementation of the integrated electronics required by the angular velocity sensor. The focus is primarily on the design of the sensor readout circuitry, comprising: a continuous-time front-end performing the capacitance-to-voltage (C/V) conversion, filtering, and signal level normalization; a bandpass $\Sigma\Delta$ analog-to-digital converter, and the required digital signal processing (DSP). The other fundamental circuit blocks, which are a phase-locked loop required for clock generation, a high-voltage digital-to-analog converter for the compensation of the mechanical quadrature signal, the necessary charge pumps for the generation of high voltages, an analog phase shifter, and the digital-to-analog converter used to generate the primary resonator excitation signals, together with other DSP blocks, are

introduced on a more general level. Additionally, alternative ways to perform the C/V conversion, such as continuous-time front ends either with or without the upconversion of the capacitive signal, various switched-capacitor front ends, and electromechanical $\Sigma\Delta$ modulation, are studied.

In the experimental work done for the thesis, a prototype of a micro-electro-mechanical angular velocity sensor is implemented and characterized. The analog parts of the system are implemented with a 0.7-μm high-voltage CMOS (Complimentary Metal-Oxide-Semiconductor) technology. The DSP part is realized with a field-programmable gate array (FPGA) chip. The $\pm 100\,^\circ/\mathrm{s}$ gyroscope achieves $0.042\,^\circ/\mathrm{s}/\sqrt{\mathrm{Hz}}$ spot noise and a signal-to-noise ratio of $51.6\,\mathrm{dB}$ over the $40\,\mathrm{Hz}$ bandwidth, with a $100\,^\circ/\mathrm{s}$ input signal.

The implemented system demonstrates the use of $\Sigma\Delta$ modulation in both the primary resonator excitation and the quadrature compensation. Additionally, it demonstrates phase error compensation performed using DSP. With phase error compensation, the effect of several phase delays in the analog circuitry can be eliminated, and the additional noise caused by clock jitter can be considerably reduced.

Tiivistelmä

Tässä väitöskirjassa tutkitaan mikromekaanisen kulmanopeusanturin eli gyroskoopin suunnittelua ja toteutusta. Työssä keskitytään järjestelmään, joka pohjautuu värähtelevään kulmanopeusanturielementtiin. Elementti toimii alipäästömuotoisesti ja sen resonanssivahvistus on keskisuuri. Kulmanopeussignaalin havaitsemiseen käytetty toisio- eli sekundääriresonaattori toimii avoimessa silmukassa. Sekä ensiö- eli primääriresonaattorin että toisioresonaattorin hyvyysluvut oletetaan suuriksi. Ensiöresonaattorin liike herätetään sähköstaattisesti, ja resonaattoreiden signaalien ilmaisu on kapasitiivinen.

Väitöskirja on jaettu kolmeen osaan. Kirjan ensimmäinen osa sisältää kahta muuta osaa varten tarvittavat perustiedot. Tässä osassa esitetään aluksi värähtelevän mikromekaanisen kulmanopeusanturielementin toiminnan perusteet ja tärkeimmät epäideaalisuudet. Tämän jälkeen kuvaillaan lyhyesti erilaisia mikromekaanisten rakenteiden valmistustekniikoita. Lopuksi käydään läpi aiemmin julkaistuja mikromekaanisia gyroskooppeja, ja tutustutaan tällä hetkellä kaupallisesti saatavilla oleviin kulmanopeusantureihin.

Toisessa osassa käsitellään mikromekaanisen kulmanopeusanturin järjestelmätason suunnittelua. Tässä osassa tutkitaan aluksi, kuinka erilaiset epäideaalisuudet vaikuttavat anturielementiltä saatavien signaalien synkroniseen alassekoitukseen. Tämän jälkeen esitetään analyysi ensiöresonaattorin herätyksen dynaamisesta käyttäytymisestä, mekaanisen kvadratuurisignaalin kompensoinnista sekä kulmanopeusanturin nollapistesignaalista. Luvussa tutkitaan myös $\Sigma\Delta$-modulaation käyttöä sekä ensiöresonaattorin herätyksen että kvadratuurisignaalin kompensoinnin tarkkuuden parantamisessa.

Kolmannessa osassa keskitytään kulmanopeusanturin vaatiman integroidun elektroniikan suunnitteluun ja toteutukseen. Tässä osassa pääpaino on anturin signaalien ilmaisuun käytettävissä piirilohkoissa, jotka esitellään yksityiskohtaisesti. Näistä piirilohkoista ensimmäinen on jatkuva-aikainen etuaste, joka muuntaa kapasitanssimuotoiset signaalit jännitemuotoisiksi, suodattaa ne halutulle kaistanleveydelle ja normalisoi niiden tasot. Muut ilmaisun vaatimat piirilohkot ovat kaistanpäästö-$\Sigma\Delta$-tyyppinen analogia-digitaalimuunnin sekä sen jälkeen tarvittava digitaalinen signaalinkäsittely.

Muut tarvittavat piirilohkot - kellosignaalit tuottava vaihelukittu silmukka, mekaanisen kvadratuurisignaalin kompensointiin käytettävä korkeajännitteinen digitaali-analogiamuunnin, korkeiden jännitteiden tuottamiseen tarvittavat varauspumput, analoginen vaihesiirrin sekä ensiöresonaattorin herätyssignaalit tuottava digitaali-analogiamuunnin - käsitellään yleisemmällä tasolla. Samoin muut järjestelmän vaatimat digitaaliosat käsitellään lyhyesti. Näiden piirilohkojen lisäksi tässä osassa tutustutaan erilaisiin tapoihin suorittaa kapasitanssi-jännitemuunnos. Näitä ovat esimerkiksi jatkuva-aikaiset etuasteet, jotka joko suorittavat muunnoksen mekaaniselta toimintataajuudelta tai sekoittavat signaalin korkeammalle taajuudelle, erilaiset kytkin-kondensaattoripiirit, sekä sähkömekaaninen ΣΔ-modulaatio.

Väitöskirjaa varten tehdyssä kokeellisessa työssä toteutettiin ja mitattiin mikromekaanisen kulmanopeusanturin prototyyppi. Anturiprototyypin analogiaosat toteutettiin CMOS-puolijohdeprosessilla, jonka viivanleveys on $0{,}7\,\mu$m:ä ja jolla voidaan valmistaa erilaisia korkeajännitekomponentteja. Digitaalinen signaalinkäsittelyosa toteutettiin ohjelmoitavalla logiikkapiirillä. Anturiprototyyppi suunniteltiin $\pm100\,^\circ$/s:n kulmanopeusalueelle. Se saavuttaa $0{,}042\,^\circ$/s/$\sqrt{\text{Hz}}$:n kohinatiheyden ja $51{,}6$ dB:n signaalikohinasuhteen 40 Hz:n kaistanleveydellä, kun tulosignaalin suuruus on $100\,^\circ$/s.

Toteutetun prototyypin avulla on osoitettu, kuinka ΣΔ-modulaatiota voidaan käyttää sekä ensiöresonaattorin herätyksessä että mekaanisen kvadratuurisignaalin kompensoinnissa. Lisäksi prototyypillä on toteutettu digitaalinen vaihevirheiden korjaus. Tällä korjauksella voidaan poistaa eri analogiaosien aiheuttamien vaihevirheiden vaikutus, sekä vaimentaa merkittävästi kellovärinän tuottamaa lisäkohinaa.

Avainsanat: gyroskoopit, integroidut piirit, kapasitiivisen anturin lukeminen, kapasitiiviset anturit, korkeajännitesuunnittelu, kulmanopeusanturit, mikroelektromekaaniset järjestelmät, mikrojärjestelmät, sähköstaattinen herätys.

Preface

Contents

Symbols and Abbreviations

α	Parameter describing the magnitude of the error signal caused by mechanical quadrature signal
$\vec{\alpha}_{rot}$	Angular acceleration of a rotating frame of reference with respect to an inertial frame of reference
β	Parameter describing the magnitude of the error signal caused by non-proportional damping; parameter describing the shape of the Kaiser window
γ	Parameter describing the magnitude of the error signal caused by electrical cross-coupling in the sensor element
γ_n	Excess noise factor in a MOS transistor
δ	Parameter describing the magnitude of the error signal caused by direct excitation of the secondary resonator
$\Delta\phi$	Half of the difference between ϕ_{USB} and ϕ_{LSB}
$\Delta\omega$	Frequency offset from the operating frequency ω_{0x}
ΔC_D, $\Delta C_D(t)$	Dynamic part of the detection capacitance
$\Delta C_{D,pri}$	Dynamic part of the primary resonator detection capacitance
$\Delta C_{D,sec}$	Dynamic part of the secondary resonator detection capacitance
ΔC_{exc}	Dynamic part of the primary resonator excitation capacitance
$\Delta G_{y/\Omega}$	Half of the difference between $G_{y/\Omega,USB}$ and $G_{y/\Omega,LSB}$

ΔV_{DC}	Amplitude of the signal used to modulate V_{DC} in ZRO measurement
ε_0	Permittivity of vacuum, $8.85418 \cdot 10^{-12}\,\mathrm{F/m}$
ε_r	Relative permittivity
ζ_I, ζ_Q	Parameters describing the magnitude of the error signal caused by variation in the middle electrode biasing voltage
η_I, η_Q	Parameters describing the magnitude of the error signal caused by cross-coupling of clock signals in the electronics
θ	Phase shift of the transfer function from the displacement of the secondary resonator to voltage; overall phase error in the synchronous demodulation resulting from the electronics
θ_1	Difference between phase shifts caused by primary and secondary channels
$\theta_{1,pri}$	Phase shift caused by the primary channel from CSA input to the output of the second HPF
$\theta_{1,sec}$	Phase shift caused by the secondary channel from CSA input to the output of the second HPF
θ_2	Phase shift from the output of the second HPF in the primary channel to the clock input of the ADC in the secondary channel
$\theta_{LPF,pri}$	Phase shift caused by the primary channel LPF
$\theta_{LPF,sec}$	Phase shift caused by the secondary channel LPF
ι_I, ι_Q	Parameters describing the magnitude of the error signal caused by cross-coupling of the primary resonator signal in the electronics
κ	Mode separation, $\kappa = \omega_{0y}/\omega_{0x}$
μ	Carrier mobility in the channel area

ξ_I	Phase shift of the transfer function from the angular velocity input to the in-phase component of the output signal, caused by the secondary resonator transfer function
ξ_Q	Phase shift of the transfer function from the angular velocity input to the quadrature component of the output signal, caused by the secondary resonator transfer function
ρ_{Si}	Density of single-crystal silicon, $2330\,\mathrm{kg/m^3}$
σ	Norm of residuals
υ	Phase of the signal used to modulate V_{DC} in ZRO measurement
ϕ	Phase shift of the secondary resonator transfer function at the operating frequency ω_{0x}
$\overline{\phi}$	Average of ϕ_{USB} and ϕ_{LSB}
ϕ_1, ϕ_2	Two-phase, non-overlapping clock signals
ϕ_{LSB}	Phase shift of the transfer function from the angular velocity input to the secondary resonator displacement in the lower sideband of the Coriolis movement
ϕ_{USB}	Phase shift of the transfer function from the angular velocity input to the secondary resonator displacement in the upper sideband of the Coriolis movement
φ	Phase of a sinusoidally-varying angular velocity
χ	Phase shift in quadrature compensation voltage
ψ	Phase of an interferer causing possibly time-varying ZRO
ω	Angular frequency
$\Omega, \vec{\Omega}$	Angular velocity
ω_Ω	Frequency of a sinusoidally-varying angular velocity
ω_0	Resonance or natural frequency, $\omega_0 = \sqrt{k/m}$
ω_{0x}	Resonance or natural frequency of the x-directional resonator

ω_{0y}	Resonance or natural frequency of the y-directional resonator
ω_c	Cut-off frequency or critical frequency
ω_{cw}	Carrier frequency
ω_e	Frequency of the signal used to modulate V_{DC} in ZRO measurement
ω_{exc}	Excitation frequency in an electrostatic actuator
ω_{UGF}	Unity-gain frequency of an integrator
Ω_z	Dc angular velocity about the z-axis; amplitude of the ac angular velocity
$\Omega_z(t)$	Ac angular velocity about the z-axis
$\Omega_{z,Dyx}$	Output signal inflicted by non-proportional damping, referred to input angular velocity
$\Omega_{z,kyx}$	Output signal inflicted by anisoelasticity, referred to input angular velocity
$\Omega_{z,n}$	Spectral density of the noise in the z-directional angular velocity, in $\mathrm{rad}/\mathrm{s}/\sqrt{\mathrm{Hz}}$ or $°/\mathrm{s}/\sqrt{\mathrm{Hz}}$
$\Omega_{ZRO,noQC}$	Zero-rate output without quadrature compensation applied, referred to input angular velocity
$\Omega_{ZRO,QC}$	Zero-rate output when electrostatic quadrature compensation performed with a dc voltage is applied, referred to input angular velocity
A	Electrode area
$a, \vec{a}$	Acceleration, $a = \dot{v} = \ddot{x}$
$\vec{a}'$	Acceleration of a particle in a rotating frame of reference
a_2, a_3	Gains of nonlinear terms
$\vec{a}_{rot}$	Linear acceleration of a rotating frame of reference with respect to an inertial frame of reference
A_x	Vibration amplitude of the x-directional resonator

C	Capacitance
C_B	Capacitance through which the sensor middle electrode is biased
C_C	Compensation capacitor
C_{CCO}	CCO capacitor
C_{CDS}	Correlated double sampling capacitor
C_D	Static part of the detection capacitance
$C_{D,pri}$	Static part of the primary resonator detection capacitance
$C_{D,sec}$	Static part of the secondary resonator detection capacitance
C_{exc}	Static part of the primary resonator excitation capacitance
C_f	Feedback capacitance
$CGDO$	Gate-drain overlap capacitance per unit width
$CGSO$	Gate-source overlap capacitance per unit width
C_{inW}	Capacitance per unit width seen at the gate of the input transistor
C_L	Load capacitance
C_n	Spectral density of total input-referred noise of the readout circuit, in $F/\sqrt{Hz}$
$C_{n,CSA}$	Spectral density of input-referred noise of the CSA
$C_{n,HPF}$	Spectral density of input-referred noise of the first high-pass filter
$C_{n,opa}$	Spectral density of input-referred noise resulting from the operational amplifier
$C_{n,opa,rms}$	Input-referred r.m.s. noise resulting from the operational amplifier
$C_{n,R}$	Spectral density of input-referred noise resulting from feedback resistors

$C_{n,sw,rms}$	Input-referred r.m.s. noise resulting from switches
C_{OX}	Capacitance of the gate oxide per unit area
C_P	Parasitic capacitance
C_{par}	Parasitic cross-coupling capacitance from the excitation electrode to the input of the detection circuit
d	Displacement
D, $\mathbf{D}$	Damping coefficient; damping matrix
D_{xx}	Damping coefficient in the x-direction
D_{xy}, D_{yx}	Non-proportional damping terms in the 2-D EoM
D_{yy}	Damping coefficient in the y-direction
E	Energy
E_{res}	Relative error in the resonance gain
E_{tot}	Total energy stored in a system
f	Frequency, $f = \omega/(2\pi)$
F, $\vec{F}$, $\mathbf{F}$	Force; force vector
f_Ω	Frequency of a sinusoidally-varying angular velocity, $f_\Omega = \omega_\Omega/(2\pi)$
f_0	Resonance or natural frequency, $f_0 = \omega_0/(2\pi)$
f_{0x}	Resonance or natural frequency of the x-directional resonator, $f_{0x} = \omega_{0x}/(2\pi)$
f_{0y}	Resonance or natural frequency of the y-directional resonator, $f_{0y} = \omega_{0y}/(2\pi)$
f_c	Cut-off frequency or critical frequency, $f_c = \omega_c/(2\pi)$
f_{cw}	Carrier frequency, $f_{cw} = \omega_{cw}/(2\pi)$
f_{cw1}, f_{cw2}	Carrier frequencies
$F_{C,x}$	Coriolis force acting on the x-directional resonator
$F_{C,y}$	Coriolis force acting on the y-directional resonator

F_D	Damping force
F_{es}	Electrostatic force
$F_{feedback}$	Feedback force
F_k	Spring force
F_n	Spectral density of the noise force, in N^2/Hz
f_{NBW}	Noise bandwidth
F_{quc}	Amplitude of the uncompensated quadrature force, $F_{quc} = -k_{yx}A_x$
$F_{quc}(t)$	Uncompensated quadrature force
f_s	Sampling frequency
f_{VCO}	VCO output frequency
F_x	Exciting force in the x-direction
F_y	Exciting force in the y-direction
$F_{y,in}$	All forces acting on the y-directional resonator, except the feedback force
g	Horizontal gap between two comb fingers in a comb-drive actuator
G	Gain
GBW	Gain-bandwidth product
$G_{Fx/V}$	Gain from primary resonator excitation voltage to force
$G_{Fy/V}$	Gain from secondary resonator excitation voltage to force
g_m	Transconductance
$G_{q/V}$	Gain from quadrature compensation voltage to charge
$G_{q/y}$	Gain from secondary resonator displacement to charge, part of $G_{V/y}$
G_{res}	Resonance gain
$G_{res,lim}$	Resonance gain limited by finite quality factor

$G_{V/\Omega}$	Gain from angular velocity input to output voltage
$G_{V/x}$	Gain from primary resonator displacement to voltage
$G_{V/y}$	Gain from secondary resonator displacement to voltage
$G_{y/\Omega}$	Gain from angular velocity input to secondary resonator displacement
$\overline{G_{y/\Omega}}$	Average of $G_{y/\Omega,USB}$ and $G_{y/\Omega,LSB}$
$G_{y/\Omega,I}$	Gain from the angular velocity input to the secondary resonator displacement, which is converted to voltage and demodulated to the in-phase component of the output signal
$G_{y/\Omega,LSB}$	Gain from the angular velocity input to the secondary resonator displacement in the lower sideband of the Coriolis movement
$G_{y/\Omega,Q}$	Gain from the angular velocity input to the secondary resonator displacement, which is converted to voltage and demodulated to the quadrature component of the output signal
$G_{y/\Omega,USB}$	Gain from the angular velocity input to the secondary resonator displacement in the upper sideband of the Coriolis movement
h	Thickness of a comb structure in a comb-drive actuator
$H(s)$	Transfer function
$H_{Fx/V}(s)$	Transfer function from primary resonator excitation voltage to force
$H_{Fx/V}^{*}(s)$	Transfer function from primary resonator excitation voltage to force after frequency transformation to dc
$H_{Fy/V}(s)$	Transfer function from secondary resonator excitation voltage to force
$H_{IF}(z)$	Transfer function of an interpolation filter
$H_{LPF}(s), H_{LPF}(z)$	Low-pass filter transfer function, either continuous-time or discrete-time

$H_{prictrl}(s)$, $H_{prictrl}(z)$	Primary resonator amplitude controller, either continuous-time or discrete-time
$H_{qcctrl}(s)$, $H_{qcctrl}(z)$	Quadrature compensation controller, either continuous-time or discrete-time
$H_{qcomp}(s)$	Transfer function from quadrature compensation voltage to force in electrostatic quadrature compensation performed with a dc voltage
$H_{V/q}(s)$	Transfer function from charge to voltage, part of $H_{V/y}(s)$
$H_{V/x}(s)$	Transfer function from primary resonator displacement to voltage
$H_{V/x}^{*}(s)$	Transfer function from primary resonator displacement to voltage after frequency transformation to dc
$H_{V/y}(s)$	Transfer function from secondary resonator displacement to voltage
$H_{x/F}(s)$	Primary resonator transfer function from force to displacement
$H_{x/F}^{*}(s)$	Primary resonator transfer function from force to displacement after frequency transformation to dc
$F_{y,all}$	All forces acting on the y-directional resonator
$H_{y/F}(s)$	Secondary resonator transfer function from force to displacement
I_{BCOMP1}, I_{BCOMP2}	Biasing currents of the comparator of CCO
I_{BCORE}	CCO static biasing current
I_{BIAS}	Biasing current
I_{CTRL}	CCO control current
I_D	Drain current
$I_{in,pri}$, $I_{in,pri}(t)$	In-phase component of the input of the synchronous demodulator in the primary resonator readout
$I_{in,sec}$	In-phase component of the input of the synchronous demodulator in the secondary resonator readout

$\widehat{I}_{in,sec}$	In-phase component of the input of the synchronous demodulator in the secondary resonator readout, normalized with respect to the primary signal
I_{leak}	Leakage current
$I_{out,pri}$, $I_{out,pri}(t)$	In-phase component of the output of the synchronous demodulator in the primary resonator readout
$I_{out,sec}$, $I_{out,sec}(t)$	In-phase component of the output of the synchronous demodulator in the secondary resonator readout
$I_{out,sec,n}$	Spectral density of the mechanical-thermal noise in the in-phase component of the output after demodulation
$I_{set,pri}$	Target value for the primary resonator vibration amplitude $I_{out,pri}$
j	Imaginary unit, commonly also denoted by i
K	Word length at the output of the interpolation filter, entering the noise-shaping loop
k, $\mathbf{k}$	Spring constant; spring matrix
$K(z)$	Transfer function of a compensator
k_B	Boltzmann constant, $1.38066 \cdot 10^{-23}\,\mathrm{J/K}$
k_{eff}	Effective spring constant after electrostatic spring softening
k_{es}	Electrostatic spring constant
K_F	Flicker (1/f) noise coefficient
k_{xx}	Spring constant in the x-direction
k_{xy}, k_{yx}	Anisoelastic terms in the 2-D EoM
k_{yy}	Spring constant in the y-direction
L	Channel length in a MOS transistor
M	Word length at the input of the DAC
m, $\mathbf{m}$	Mass; mass matrix
m_{IF}	Interpolation factor

m_x	Vibrating mass in the x-direction
m_y	Vibrating mass in the y-direction
n	Arbitrary integer, > 0
N	Word length at the output of the readout circuit
N_{bits}	Number of output bits from an ADC
n_{gap}	Number of horizontal gaps in a comb-drive actuator
n_s	Sample index
N_{stages}	Number of stages in a charge pump
P	Number of bits truncated inside the noise-shaping loop
ppm	Parts per million, 10^{-6}
Q	Quality factor, $Q = \sqrt{km}/D$; charge
$Q_{in,sec}$	Quadrature component of the input of the synchronous demodulator in the secondary resonator readout
$\widehat{Q}_{in,sec}$	Quadrature component of the input of the synchronous demodulator in the secondary resonator readout, normalized with respect to the primary signal
$Q_{out,pri}, Q_{out,pri}(t)$	Quadrature component of the output of the synchronous demodulator in the primary resonator readout
$Q_{out,sec}, Q_{out,sec}(t)$	Quadrature component of the output of the synchronous demodulator in the secondary resonator readout
$Q_{out,sec,n}$	Spectral density of the mechanical-thermal noise in the quadrature component of the output after demodulation
Q_x	Quality factor of the x-directional resonator
Q_y	Quality factor of the y-directional resonator
R	Resistance
$r, \vec{r}$	Radius, position vector
$\vec{r}'$	Position vector in a rotating frame of reference

R_B	Resistance through which the sensor middle electrode is biased
R_{COMP}	Hysteresis-providing resistor in the comparator of CCO
R_{corr}	Correlation coefficient
R_{eff}	Effective resistance
R_f	Feedback resistance
R_{GM}	Ratio between voltage and current in the transconductance amplifier in VCO
s	Laplace variable. For real frequencies, $s = j\omega$
t	Time
T	Absolute temperature
T_d	Delay
T_s	Sampling period, $T_s = 1/f_s$
V	Voltage
$v, \vec{v}$	Velocity, $v = \dot{x}$
$\vec{v'}$	Velocity of a particle in a rotating frame of reference
V_{AC}	Ac voltage
V_B	Detection bias
V_{BIAS}	Biasing voltage
V_{C1}, V_{C2}	Control voltages in an MRC
$V_{c,cm}(t)$	Common-mode component of a balanced carrier
$V_{c,diff}(t)$	Differential-mode component of a balanced carrier
V_{CM}	Target common-mode voltage
V_{CMFB}	Output voltage from the CMFB circuit
V_{CMIN}	Input common-mode level in a CSA
V_{CTRL}	VCO control voltage

V_d	Forward voltage drop of a diode
V_{DC}	Dc voltage
V_{DD}	Supply voltage
V_{DDHV}	High-voltage supply
V_{DDMV}	Medium-voltage supply
$V_{error,I}$	Amplitude of the error signal in phase with the Coriolis signal, reduced to output voltage of the displacement-to-voltage converter
$V_{error,Q}$	Amplitude of the error signal in quadrature with respect to the Coriolis signal, reduced to output voltage of the displacement-to-voltage converter
$V_{error,sec}(t)$	Total error signal in the secondary channel
$V_{exc}(t)$	Excitation voltage
V_{GS}	Gate-source voltage
V_{HV}	High-voltage output of a charge pump
$V_{in}, V_{in}(t)$	Input voltage
V_{inn}	Negative part of a differential input voltage
V_{inp}	Positive part of a differential input voltage
$V_{in,pri}(t)$	Input voltage of the demodulator in the primary resonator readout; output voltage of the respective displacement-to-voltage converter
$V_{in,sec}(t)$	Input voltage of the demodulator in the secondary resonator readout; output voltage of the respective displacement-to-voltage converter
$V_{in,sec,cc}(t)$	Output of the secondary resonator readout circuit (demodulator input) caused by electrical cross-coupling in the sensor element
$V_{in,sec,da}(t)$	Output of the secondary resonator readout circuit (demodulator input) caused by non-proportional damping

$V_{in,sec,de}(t)$	Output of the secondary resonator readout circuit (demodulator input) caused by direct excitation of the secondary resonator
$V_{in,sec,el1}(t)$	Output of the secondary resonator readout circuit (demodulator input) caused by clock signals cross-coupled in the electronics
$V_{in,sec,el2}(t)$	Output of the secondary resonator readout circuit (demodulator input) caused by primary resonator signal cross-coupled in the electronics
$V_{in,sec,mb}(t)$	Output of the secondary resonator readout circuit (demodulator input) caused by variation in the middle electrode biasing voltage
$V_{in,sec,nl}(t)$	Input voltage of the demodulator in the secondary resonator readout after nonlinearities
$V_{in,sec,qu}(t)$	Output of the secondary resonator readout circuit (demodulator input) caused by the mechanical quadrature signal
V_{MID}	Actual middle electrode voltage (dc)
$v_{mid}(t)$	Ac component of the time-varying middle electrode biasing voltage
$V_{mid}(t)$	Time-varying middle electrode biasing voltage
$V_{MIDBIAS}$	Middle electrode biasing voltage (dc)
v_n	Spectral density of noise voltage, in $V/\sqrt{Hz}$
$v_{n,HPF}$	Spectral density of total output noise of the first high-pass filter
$v_{n,opa}$	Spectral density of input-referred noise of the operational amplifier
$v_{n,out}$	Spectral density of noise at the readout circuit output
$V_{out}, V_{out}(t)$	Output voltage
V_{outn}	Negative part of a differential output voltage
V_{outp}	Positive part of a differential output voltage

V_{qcomp}	Dc quadrature compensation voltage; amplitude of the ac quadrature compensation voltage
$V_{qcomp}(t)$	Ac quadrature compensation voltage
V_{REF}	Reference voltage
$V_{sq,pp}$	Peak-to-peak amplitude of the square-wave primary resonator excitation signal
W	Channel width in a MOS transistor
W_{opt}	Transistor width giving the noise optimum
$x, x(t)$	Displacement in the x-direction
x_0	Initial gap with zero biasing voltage
$y, y(t)$	Displacement in the y-direction
$y_{error,I}$	Amplitude of the error signal in phase with the Coriolis signal, reduced to secondary resonator movement
$y_{error,Q}$	Amplitude of the error signal in quadrature with respect to the Coriolis signal, reduced to secondary resonator movement
$y_{quc}(t)$	Uncompensated quadrature movement
z	Frequency variable in a discrete-time system. For real frequencies, $z = e^{j\omega}$
Z_B	Middle electrode biasing impedance
$\Sigma\Delta$	Sigma-Delta
1-D	1-Dimensional
2-D	2-Dimensional
ac	Alternating Current; general symbol for time-varying electrical signal such as current or voltage
A/D	Analog-to-Digital
ADC	Analog-to-Digital Converter
ADI	Analog Devices Inc.

AGC	Automatic Gain Control
ALC	Automatic Level Control
AlN	Aluminum Nitride
AMS	Analog and Mixed-Signal
ASIC	Application-Specific Integrated Circuit
Attn	Attenuator
BiCMOS	CMOS technology which includes bipolar transistors
BITE	Built-In Test Equipment
BP	Band-Pass
BSAC	Berkeley Sensors and Actuators Center
BW	Bandwidth
CCO	Current-Controlled Oscillator
C/D	Capacitance-to-Digital
CDS	Correlated Double Sampling
C/f	Capacitance-to-Frequency
CHS	Chopper Stabilization
CIC	Cascaded Integrator-Comb
CMFB	Common-Mode Feedback
CMOS	Complementary Metal-Oxide-Semiconductor
CoM	Chip-on-MEMS
CQFP	Ceramic Quad Flat Pack
CSA	Charge Sensitive Amplifier, also known as a transcapacitance amplifier
C/V	Capacitance-to-Voltage
D	Differentiator controller, realized by a differentiator
DAC	Digital-to-Analog Converter

D/A	Digital-to-Analog
dc	Direct Current; general symbol for time-constant electrical signal such as current or voltage
DIV	Divider
DNL	Differential Nonlinearity
DoF	Degree(s) of Freedom
DRIE	Deep Reactive Ion Etching
DSP	Digital Signal Processing
EoM	Equation of Motion
ESC	Electronic Stability Control
ESD	Electrostatic Discharge
FDDA	Fully Differential Difference Amplifier
FFT	Fast Fourier Transformation
FIR	Finite Impulse Response
FPGA	Field-Programmable Gate Array
FS	Full-Scale
GPS	Global Positioning System
HARPSS	High Aspect-Ratio Combined Poly- and Single-Crystal Silicon
HP	High-Pass
HPF	High-Pass Filter
HSG-IMIT	Hahn-Schickard-Gesellschaft, Institut für Mikro- und Informationstechnik
HV	High-Voltage
I	Integrator controller, realized by an integrator; in-phase component; current
IC	Integrated Circuit

ICMR	Input Common-Mode Range
INL	Integral Nonlinearity
LP	Low-Pass
LPF	Low-Pass Filter
LSB	Lower Sideband; Least Significant Bit
LV	Low-Voltage
MEMS	Micro-Electro-Mechanical System
MM	Micromachining, micromechanics
MOS	Metal-Oxide-Semiconductor
MOSFET	Metal-Oxide-Semiconductor Field-Effect Transistor
MOSFET-C	MOSFET-Capacitor, circuit topology to implement a continuous-time integrator
MRC	MOS Resistive Circuit
MV	Medium Voltage
NL	Noise-Shaping Loop
NMOS	N-type MOS transistor
OSR	Oversampling Ratio
OTA	Operational Transconductance Amplifier
P	Proportional controller, realized by a gain
PCB	Printed Circuit Board
PFD	Phase-Frequency Detector
PI	Proportional-Integrator controller, a controller formed by a sum of P and I controllers
PID	Proportional-Integrator-Differentiator controller, a controller formed by a sum of P, I, and D controllers
PLL	Phase-Locked Loop
PMOS	P-type MOS transistor

PTAT	Proportional-to-Absolute Temperature
PZT	Lead Zirconate Titanate
Q	Quadrature component
r.m.s.	Root-Mean-Square
RC	Resistor-Capacitor
RIE	Reactive Ion Etching
SBB	Self-Balancing Bridge
SC	Switched-Capacitor
SEM	Scanning Electron Microscope
Si	Silicon
Si_3N_4	Silicon Nitride
SiGe	Silicon-Germanium
SiO_2	Silicon Dioxide
SNR	Signal-to-Noise Ratio
SOI	Silicon-on-Insulator
SPI	Serial Peripheral Interface
SQNR	Signal-to-Quantization Noise Ratio
S.T.	Self-Test
SW	Switch
THD	Total Harmonic Distortion
USB	Upper Sideband
V	Voltage
VCO	Voltage-Controlled Oscillator
VGA	Variable-Gain Amplifier
VHDL	VHSIC Hardware Description Language
VHSIC	Very High-Speed Integrated Circuit

VRG	Vibrating Ring Gyroscope
XOR	Exclusive-Or
ZnO	Zinc Oxide
ZOH	Zero-Order Hold
ZRO	Zero-Rate Output

Chapter 1

Introduction

1.1   Background and Motivation

Beginning from the invention of the transistor in 1947 at the Bell Telephone Laboratories, and the realization of the integrated circuit (IC) in 1959, first at Texas Instruments as a hybrid IC and later in the same year at Fairchild Semiconductor as a fully monolithic IC, the world has witnessed what can be described as a revolution in information processing and communication. Personal computers, laptops, portable music players, digital video disc players, mobile phones, and the internet are but a few examples which have been made possible by the rapid development of microelectronics. In particular, the advances in telecommunications have had a significant impact on everyday life, with examples such as mobile phones, electronic mail, and different web-based services.

The rapid development of microelectronics is partially based on similarly rapid advances in semiconductor manufacturing technologies. These advances have also made possible the miniaturization of various sensors, or, in a broader sense, various mechanical components which can be combined with the electronics to form what is known as a micro-electro-mechanical system (MEMS) or a microsystem. The MEMS technology extends the application range of microchips beyond purely electrical phenomena. A microsystem can sense, for example, acceleration, pressure, light, angular velocity, or angular acceleration, it can act as a controlled microgripper, it can handle fluids and perform various (bio)chemical analyses, or it can control the reflection of light to form a picture on a screen. In short, the MEMS technology provides a possibility of extending the microelectronic revolution even further, to areas where it is necessary to interface with the real world and its various physical phenomena.

The history of MEMS devices already extends back for well over four decades. The resonant gate transistor published by Nathanson et al. for the first time in 1965 [1],

with more details in [2], is generally considered to be the first reported MEMS device. An example of early commercial MEMS technology is the pressure sensors introduced by National Semiconductor in 1973 [3]. In Finland, Vaisala started their technology development as early as 1979, and brought micromechanical silicon capacitive pressure sensors in volume production in the year 1984. In 1991, the technology was transferred from Vaisala to the newly-established company Vaisala Technologies Inc., which later, in the year 2002, became VTI Technologies [4]. The term MEMS itself was introduced, according to [5], in the year 1989 at the Micro Tele-Operated Robotics Workshop held at Salt Lake City, UT, USA. The introduction is credited to Prof. Roger Howe of the University of California, Berkeley.

MEMS devices currently form a very rapidly growing market. According to the NEXUS Association, Neuchâtel, Switzerland [6], the total market of first-level packaged MEMS devices in 2004 was 12 billion USD. The projected annual compound growth rate until the year 2009 is 16%, so that in 2009 the total market will reach a level of 25 billion USD. The top three products, read/write heads, inkjet heads, and MEMS displays, will stay unaltered for the whole period of time, with displays becoming the second-largest product in 2009, ahead of inkjet heads.

A significant change in the MEMS market projected by NEXUS is the growth of the share of consumer devices. In 2000, consumer electronics accounted for 2% of the total MEMS market, in 2004, 6% (a total of 0.7 billion USD), and in 2009, the projected share is 22% (5.5 billion USD). This means that the anticipated average annual growth rate of the consumer market is over 50%. At the same time, the market share of automotive devices will be reduced from 11% (2004) to 8% (2009) (still showing an average annual growth rate of 8.7% in USD), and the share of computer peripherals from 68% to 54%. The three main drivers in the consumer electronics market segment are large screens (MEMS displays), more storage in digital devices such as cameras and music players (read/write heads), and mobile handsets equipped with accelerometers, angular velocity sensors, higher-resolution displays, micro fuel cells, fingerprint sensors etc.

Inertial sensors, which comprise angular velocity sensors and accelerometers, are used to measure either the rotation rate or the acceleration of a body with respect to an inertial frame of reference[1] [7]. According to NEXUS, the market of MEMS inertial sensors in 2004 was approximately 0.8 billion USD, and the projected market in 2009 is approximately 1.4 billion USD. Of this, the consumer market will be approximately 0.3 billion USD, meaning that roughly half of the estimated growth of the inertial sensor market will come from consumer electronics.

---

[1]An inertial frame of reference or an inertial system is at rest or moving with a constant velocity. It is not accelerating, nor does it have any angular velocity or angular acceleration (which are both forms of accelerating motion).

1.2   Angular Velocity Sensors

Angular velocity sensors are devices which are used to measure the rotation rate of a body with respect to an inertial frame of reference. Their application areas include navigation, automotive stability control systems and safety systems, platform stabilization, including picture stabilization in camcorders and cameras, robotics, and various input devices.

Traditionally, angular velocity has been measured with a rotating wheel gyroscope, which is based on the conservation of angular momentum. This has been replaced by fiber optic and ring laser gyroscopes in precision applications[2]. Optical gyroscopes are the most accurate angular velocity sensors available at the moment, and are used, for instance, in inertial navigation systems. However, they are too expensive and too bulky for most of the aforementioned applications. [7]

The automotive applications of angular velocity sensors include chassis stability control systems such as ESC (Electronic Stability Control), and safety systems such as roll-over detection. In particular, the stability control systems have created a rapidly growing market for low- to medium-priced, medium-accuracy angular velocity sensors which can be realized with the MEMS technology [8,9].

As described earlier, a very rapidly growing MEMS angular velocity sensor application area is currently that of consumer applications. These include picture stabilization in cameras and camcorders, GPS (Global Positioning System)-assisted navigation and dead reckoning, and various input devices. An example of the latter application is game controllers, which are equipped with angular velocity sensors. This makes it possible to control a computer game by just turning the game controller in various directions. Another possible example is a mobile handset in which the user interface can be controlled by rotating the device.

The MEMS technology offers the possibility of miniaturizing the angular velocity sensors. At the same time, as a mass fabrication technology, it makes it possible to reduce the price of a single unit, provided that the manufacturing quantities are large enough. Both of these properties can be considered very advantageous, especially when the requirements of consumer electronics are considered.

Almost all the micromechanical angular velocity sensing elements reported in the literature have been vibratory gyroscopes [7]. The reason for this is that, unlike rotating wheel gyroscopes, they do not require bearings, thus providing much simpler design and greater long-term reliability. A vibratory gyroscope is composed of two ideally decoupled resonators. When the gyroscope rotates about its sensitive axis, the Coriolis

---

[2]Strictly speaking, the term *gyroscope* refers to the traditional rotating wheel device, whereas the term *angular velocity sensor* refers to angular rate measurement devices in general. However, they are (mis)used interchangeably in the literature, and the convention will be followed here as well.

effect couples vibration from one resonator to another. By measuring the coupled movement, the angular velocity can be resolved.

The pre-history of MEMS angular velocity sensors starts from 1835, as Coriolis[3] described the imaginary force that causes a moving particle to deviate within a rotating frame of reference. On the basis of this effect, Foucault[4] used his pendulum to detect the Earth's rotation in 1851. In the 1950s, the Sperry Gyroscope Company invented the Gyrotron angular rate tachometer, a device analogous to Foucault's pendulum. This device can be considered to be the first successful artificial vibratory gyroscope. [10]

The first actual MEMS gyroscopes were piezoelectric devices made out of quartz. Systron Donner Inertial was the first firm to commercialize a quartz vibratory gyroscope, in the 1980s. The first batch-fabricated silicon micromachined gyroscope is usually considered to be the device demonstrated by The Charles Stark Draper Laboratory [11] in 1991. [7]

Currently, there are already several companies providing MEMS gyroscopes, both piezoelectric and silicon devices. However, all aspects of microgyroscope design - the mechanical element, the electronics required, and the system-level implementation, as well as the packaging - have been and still are the subjects of active research, both in industry and academia. There are several reasons for this. One is that the challenges and their solutions depend heavily on the implementation details. Another is that most of the research work done in industry is largely unpublished, for commercial reasons.

Perhaps the most important driver in MEMS gyroscope research at the moment is, however, the market pressure to reduce the price of a single device to the 1-USD level. This is a key requirement for both the automotive and the consumer market segments. In order to achieve this, all the three aspects listed above - the mechanical element, the electronics, and the packaging - must be considered. First, the mechanical element must be small and mass-producible, and preferably it should require no post-manufacturing trimming. Second, the electronics must be small and producible using a standard technology. Third, the encapsulation of the devices into a standard plastic package is preferred over special packaging. In particular, hermetic ceramic carriers dramatically increase the price of a single unit and must be avoided if possible. A careful system-level design is necessary to optimize the designs of individual parts and to minimize the manufacturing costs, while assuring that the required performance targets are met. Finally, the production of the devices must be optimized to minimize the costs. In particular, the testing can make a significant contribution to the overall costs in the production of microsystems and must therefore be carefully considered.

---

[3]Gaspard Gustave de Coriolis (May 21, 1792-September 19, 1843), French mathematician, mechanical engineer, and scientist.

[4]Jean Bernard Léon Foucault (September 18, 1819-February 11, 1868), French physicist.

1.3   Research Contribution

The research work reported in this thesis was performed by the author and others at the Electronic Circuit Design Laboratory, Helsinki University of Technology, Espoo, Finland, in the years 2003-2007. The work has two areas of focus. First, it concentrates on the system-level design of a MEMS angular velocity sensor, trying to provide as general-purpose an analysis as possible of selected aspects. Second, it concentrates on the integrated implementation and design of the electronics required by the angular velocity sensor. The research questions that the thesis is intended to answer are what the fundamental system-level non-idealities are that need to be considered during the design of a MEMS angular velocity sensor, and how those non-idealities can be addressed by the means of circuit design, in particular, by applying digital signal processing (DSP) methods whenever possible.

More particularly, the work focuses on a system based on a vibratory microgyroscope, which operates in the low-pass mode with a moderate resonance gain, and with an open-loop configuration of the secondary (sense) resonator (i.e. the secondary resonator is not controlled by a force feedback). Both resonators are assumed to have a high quality factor. Furthermore, the gyroscope employs electrostatic excitation and capacitive detection.

Although some of the effects of high resonance gain and, eventually, mode-matched operation are mentioned on various occasions, they are not of primary interest. The same applies to the use of the force feedback as well. A large amount of the system-level analysis is independent of the actual excitation and detection methods, whereas the circuit design part of the work concentrates purely on electrostatic excitation and capacitive detection. Finally, the mechanical design of the sensor element, together with the sensor packaging, is completely beyond the scope of this work.

Before the system-level design part, the basic properties of a vibratory microgyroscope and the related excitation and detection mechanisms are first introduced. This gives the necessary background information for the rest of the thesis. After this there follows a detailed analysis of issues related to different non-idealities in synchronous demodulation, the dynamics of the primary (drive) resonator excitation, the compensation of the mechanical quadrature signal, and the zero-rate output (ZRO).

The electronics design focuses primarily on the design of the sensor readout circuitry, comprising: continuous-time front-end performing the capacitance-to-voltage (C/V) conversion, filtering, and signal level normalization; a bandpass $\Sigma\Delta$ analog-to-digital (A/D) converter, and the required DSP. The other fundamental circuit blocks, which are a phase-locked loop (PLL) required for clock generation, a high-voltage (HV) digital-to-analog (D/A) converter, the necessary charge pumps for HV generation, an analog phase shifter, and the D/A converter (DAC) used to generate the pri-

mary resonator excitation signals, together with other DSP blocks, are introduced in less detail. Additionally, alternative methods used to perform the C/V conversion are studied on a more general level.

In the experimental work, a MEMS angular velocity sensor was designed and implemented; it was based on a bulk micromachined sensor element designed, fabricated, and characterized by VTI Technologies, Vantaa, Finland [12]. Through extensive measurements, this implementation was used to study various system-level design issues, together with the transistor-level design of the required circuit blocks.

The initial ideas for the system structure were provided by VTI Technologies in several discussions. The author is responsible for the subsequent system-level design and the related analysis presented in this thesis. The readout electronics (both the analog and digital parts) were designed by the author, except the $\Sigma\Delta$ A/D converters (ADCs), which were designed by Dr. Teemu Salo. The PLL, the HV DAC, and the charge pumps were designed by Mr. Lasse Aaltonen. He is also responsible for analyzing the effects of noise in the sine-to-square wave conversion performed by a comparator. Different auxiliary circuit blocks were designed in co-operation between the author and Mr. Lasse Aaltonen. The measurement setup was realized and the measurements performed by the author and by Mr. Lasse Aaltonen.

The material included in this thesis has been published or has been accepted for publication in [13–23]. Additionally, to extend the study of the sensor front-ends to switched-capacitor (SC) circuits, the author participated in the design of a three-axis accelerometer, published in [24, 25]. In this work, the author performed the system-level design, together with the design of the dynamically biased operational amplifiers. The author also instructed the design of the SC C/V converter presented in [26, 27] and applied in the aforementioned system, as well as that presented in [28].

1.4   Organization of the Thesis

This thesis is organized into nine chapters. Chapter 2 presents the basic properties of a vibratory microgyroscope, the most fundamental non-idealities, and the different modes of operation, together with the concept of resonance gain. Additionally, a brief introduction to various manufacturing technologies is provided, and alternative excitation and detection methods are introduced. At the end of the chapter, a brief review of published microgyroscopes and of commercial microgyroscopes is given.

Chapters 3-6 contain the system-level analysis performed in this work. In Chapter 3, the properties of the synchronous demodulation and the effects of various non-idealities on the final output signals are studied.

In Chapter 4, the primary resonator excitation is studied. The basic properties of electrostatic excitation are introduced. After that, the dynamics of the secondary

resonator control loops are studied. The possibility of using $\Sigma\Delta$ modulation to extend the resolution is introduced.

In Chapter 5, issues related to the compensation of the mechanical quadrature signal are studied. First, various compensation methods are introduced. Different ways to implement the control loop for the compensation are presented, concentrating on a case where the compensation voltage is generated with a DAC and the controller is digital. In particular, extending the resolution with $\Sigma\Delta$ techniques is studied.

In Chapter 6, one of the most significant non-idealities of an angular velocity sensor, the ZRO, is studied. Different sources for the ZRO are discussed, and they are given a uniform mathematical representation. Ways to minimize the effect of these sources on the final ZRO are considered. How electrostatic quadrature compensation performed with a dc voltage affects the ZRO is also analyzed.

Chapters 7-8 concentrate on the electronics design and the system that was implemented. In Chapter 7, several possible ways to perform the readout of a capacitive sensor are studied. These include both continuous-time and discrete-time implementations. Additionally, the interaction between the readout circuit and the mechanical element through electrostatic forces is discussed.

In Chapter 8, the implemented MEMS angular velocity sensor is presented. The system design and the design of the sensor readout electronics are introduced in detail. The other analog circuit blocks and the required DSP are discussed on a more general level. The measurement results achieved with the implemented system are presented.

Finally, the thesis is concluded in Chapter 9.

Chapter 2

Micromechanical Gyroscopes

As described in the previous chapter, micromechanical gyroscopes are mainly vibratory gyroscopes that are based on the transfer of energy between two oscillation modes by the Coriolis effect [7]. In this chapter, the basic operation of a vibratory gyroscope will first be described. The description will be kept at a general level, and only the most significant mathematical formulae will be derived.

After this presentation, the mechanical-thermal noise that is present in the sensor element as a result of energy dissipation will be described, as it forms the fundamental noise floor of the gyroscope. Next, different mechanisms that are available to excite and detect movements in the resonators in the gyroscope will be presented. Finally, the fundamental properties of different manufacturing technologies used to realize micro-gyroscopes will be described.

The target of this presentation is to give a basic understanding of vibratory gyroscopes, which is necessary for system and electronics design. For more details, the reader is referred to one of the many textbooks available on basic mechanics [29, 30], vibrating structures [31], or microfabrication [32, 33].

Another part of this introductory chapter consists of a brief literature review of the published micromechanical gyroscopes. In the review, only those implementations that address the necessary readout and control electronics will be described. After that, a survey of commercially available microgyroscopes will be presented.

2.1   Operation of a Vibratory Microgyroscope

To understand the operation of a vibratory microgyroscope, a simple mechanical resonator will be studied first. Then a brief introduction to the Coriolis effect will be given. Finally, the 2-dimensional (2-D) equation of motion (EoM) required to understand both the operation and the most significant non-idealities of a vibratory microgyroscope will

be written. From it, the formulae for the Coriolis signal resulting from angular velocity will be derived. Finally, the dynamic operation will be considered.

All the analysis in this section will be performed for a linear resonator, or a system of linear resonators. However, the formulae can be straightforwardly generalized to torsional resonators as well, by replacing masses with moments of inertia, displacements with angles, and forces with torques. Naturally, this also requires various parameters, such as spring constants and damping coefficients, to assume proper units (for example, Newton-meters per radian instead of Newtons per meter for a spring constant).

2.1.1   1-Degree-of-Freedom Mechanical Resonator

A schematic drawing of a 1-degree-of-freedom (DoF) mechanical resonator is shown in Fig. 2.1. It is formed by a mass m, which is supported in such a way that it can move only in the x-direction, a massless spring k, and a dashpot damper D.
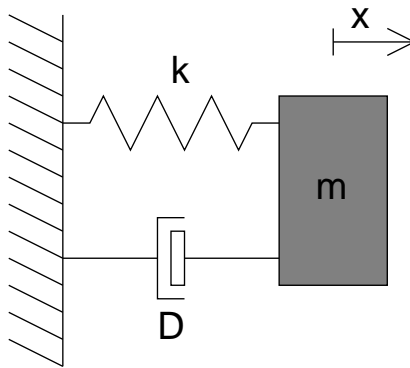
Figure 2.1 A 1-DoF resonator, formed by a mass m, a spring k, and a damper D.

If the mass is displaced from its rest position by a distance x (the positive direction of x is defined in the figure), the spring causes a restoring force

$$F_k = -kx, \tag{2.1}$$

where k is the spring constant. Next, if it is assumed that the damping is purely viscous, then if the mass moves with a velocity $v = \dot{x}$ (the dots denote derivatives with respect to time), the force exerted by the damper is

$$F_D = -Dv = -D\dot{x}, \tag{2.2}$$

where D is the damping coefficient. Newton's second law of motion states that in an inertial frame of reference, the sum of all the forces acting on a mass is the mass times

its acceleration, or

$$\sum \vec{F} = m\vec{a}. \tag{2.3}$$

Now, the 1-dimensional (1-D) EoM for the system can be written as

$$-kx - D\dot{x} + F = m\ddot{x}, \tag{2.4}$$

where the acceleration $a = \dot{v} = \ddot{x}$, and F is any external force that is acting on the mass. By reordering,

$$m\ddot{x} + D\dot{x} + kx = F. \tag{2.5}$$

By taking a Laplace transformation of this and regrouping, the transfer function from the force F to displacement x can be written as

$$H(s) = \frac{x}{F} = \frac{1}{ms^2 + Ds + k} = \frac{1/m}{s^2 + (\omega_0/Q)s + \omega_0^2}, \tag{2.6}$$

where $\omega_0 = \sqrt{k/m}$ is the resonance frequency or the natural frequency and $Q = \sqrt{km}/D$ is the quality factor of the resonator[1].

The magnitude and the phase of the transfer function (2.6) as a function of frequency (at real frequencies) can be resolved by substituting $s = j\omega = j \cdot 2\pi f$. They are

$$|H(j\omega)| = \frac{1/m}{\sqrt{\left(\omega_0^2 - \omega^2\right)^2 + \omega_0^2\omega^2/Q^2}} \tag{2.7a}$$

and

$$\angle H(j\omega) = -\arctan\frac{\omega_0\omega}{\left(\omega_0^2 - \omega^2\right)Q}, \tag{2.7b}$$

respectively.

As an example case, a microresonator with the parameters given in Table 2.1 will be considered. With these values, the resonance frequency $\omega_0 \approx 63\,\text{krad/s}$, or $f_0 = \omega_0/(2\pi) \approx 10\,\text{kHz}$, and $Q \approx 1000$.

Table 2.1 Example parameters for a microresonator.

Parameter	Value
m	$2.5\,\mu\text{g}$
k	$10\,\text{N/m}$
D	$1.6 \cdot 10^{-7}\,\text{kg/s}$

The magnitude and phase of the transfer function (2.6) are plotted in Fig. 2.2. The figure shows the most important qualitative properties of the transfer function, and

---

[1]In this thesis, the symbol Q is also used to denote the amount of charge. If there is a possibility that the two meanings of Q can be confused, the relevant meaning will be clearly stated in the text.

how they relate to ω_0 (f_0) and Q. In the magnitude plot, at low frequencies, the value is equal to $1/(m\omega_0^2)$ or $1/k$. As the resonance frequency is approached, the magnitude of the transfer function starts increasing. At the resonance frequency, when $\omega = \omega_0$, the value is Q times higher, being equal to $Q/(m\omega_0^2) = 1/(D\omega_0)$ or Q/k. At high frequencies, the magnitude rolls off with a slope of $40\,\text{dB}$ per one decade of frequency. In the phase plot, the phase starts at $0°$ and reaches a phase shift of $-90°$ at the resonance frequency, and finally $-180°$ at high frequencies.

By carefully examining the magnitude plot, it can be seen that the actual maximum is reached slightly before the resonance frequency and that the maximum is higher than Q/k. This is illustrated in the inset in Fig. 2.2 (a). By differentiating Eq. (2.7a) with respect to ω, setting the derivative equal to zero, and solving for ω, the frequency where the magnitude plot reaches its maximum is found to be

$$\omega = \omega_0 \cdot \sqrt{1 - \frac{1}{2Q^2}}, \qquad (2.8)$$

assuming that $Q > 1/\sqrt{2}$. The maximum is equal to

$$\left| H\left(j\omega_0 \cdot \sqrt{1 - \frac{1}{2Q^2}} \right) \right| = \frac{Q}{m\omega_0^2} \cdot \frac{2Q}{\sqrt{4Q^2 - 1}}. \qquad (2.9)$$

If $Q \leq 1/\sqrt{2}$, the maximum is always found at $\omega = 0$, and is equal to $1/(m\omega_0^2)$. From Eqs. (2.8) and (2.9), it can be seen that as $Q \to \infty$, then the frequency at which the maximum is reached approaches ω_0 and, at the same time, the maximum approaches $Q/(m\omega_0^2)$. In a practical case, the ratio between the maximum gain and the gain reached at ω_0 is very close to unity and hence the difference can be disregarded. For example, if $Q = 100$, the ratio is approximately 1.0000125, and if $Q = 10$, the ratio is approximately 1.00125.

From Fig. 2.2 and from Eqs. (2.8) and (2.9) it can be seen that if the resonator is excited at its resonance frequency then even with a reasonably low quality factor, the displacement x reached with a certain driving force F is maximized to a very good accuracy. In this case, the displacement of the resonator has a $90°$ phase lag with respect to the force. The velocity of the resonator $v = \dot{x}$ is then in phase with the force. Only with very low quality factors, the difference between the maximum displacement and the displacement reached at the resonance frequency becomes significant.

Figure 2.3 shows another way to represent a mechanical resonator. This kind of model is useful for implementation, for example, in a simulation environment such as Matlab Simulink, or in a system modeling language such as VHDL-AMS [34] (VHDL is an abbreviation for VHSIC Hardware Description Language, where VHSIC stands
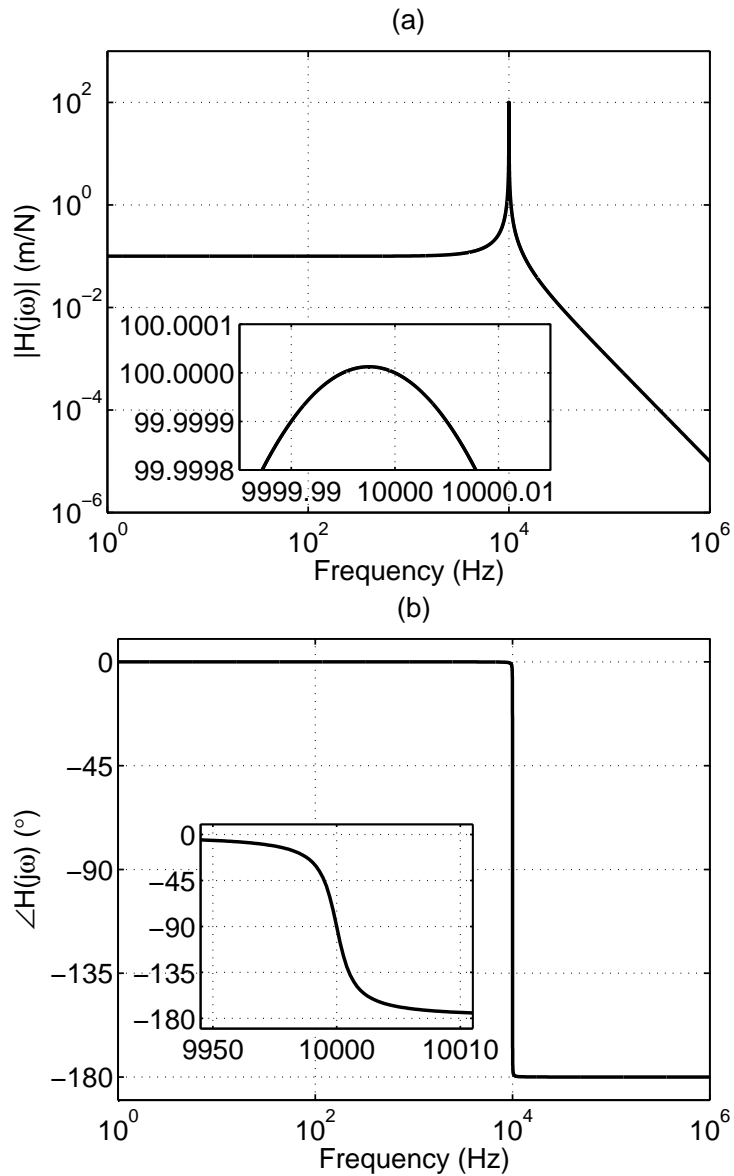
Figure 2.2 Transfer function of an arbitrary resonator, with $f_0 = 10\,\text{kHz}$ and $Q = 1000$. (a) Magnitude transfer plot, with the inset showing a detailed view of the maximum. (b) Phase transfer plot, with the inset showing a detailed view around the resonance frequency f_0.

for Very High-Speed Integrated Circuit. AMS stands for Analog and Mixed-Signal extensions). By writing an equation for *x* based on the block diagram, it can be verified that the model corresponds to Eq. (2.6).
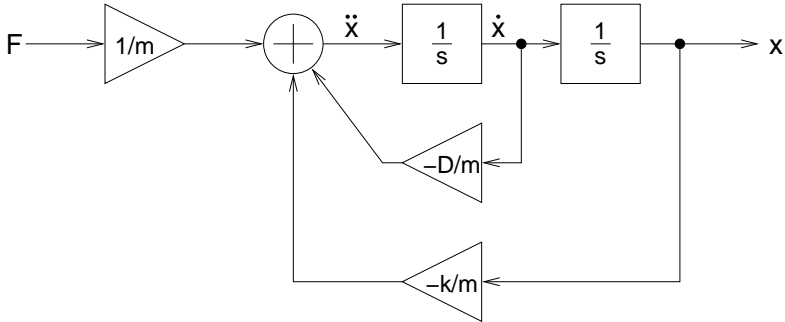
Figure 2.3 A model of a resonator.

2.1.2 Ideal 2-Degree-of-Freedom Mechanical Resonator in Inertial Frame of Reference

The preceding analysis can be easily extended to a 2-DoF resonator in an inertial frame of reference. A schematic drawing of such a system is shown in Fig. 2.4.
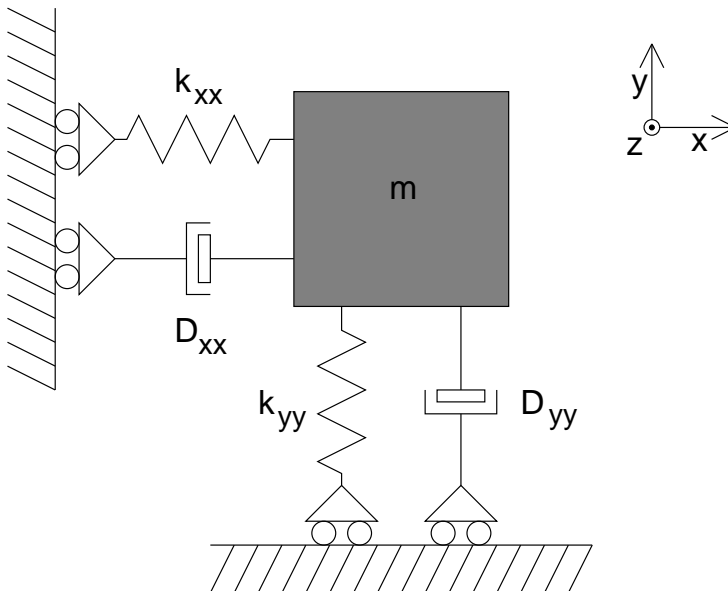
Figure 2.4 A 2-DoF mechanical resonator.

In the figure, the four rollers are used to symbolize the fact that when the mass m is moving in the x-direction, the y-directional spring and damper k_{yy} and D_{yy} have no ef-

fect on its behavior, and vice versa. Thus, the system comprises two 1-DoF resonators, one formed by the spring k_{xx}, the damper D_{xx}, and the mass m, and the second by the spring k_{yy}, the damper D_{yy}, and the mass m. Both springs are assumed to be massless.

In the configuration depicted in Fig. 2.4, the masses of both the x- and y-directional resonators are identical and equal to *m*. However, in order not to limit the generality of the following analysis, the mass of the x-directional resonator will be denoted by m_x and that of the y-directional resonator by m_y.

The 2-D EoM for the system can now be written as

$$\mathbf{m} \begin{bmatrix} \ddot{x} \\ \ddot{y} \end{bmatrix} + \mathbf{D} \begin{bmatrix} \dot{x} \\ \dot{y} \end{bmatrix} + \mathbf{k} \begin{bmatrix} x \\ y \end{bmatrix} = \mathbf{F}, \tag{2.10}$$

where **m**, **D**, and **k** are the mass, damping, and spring matrices, respectively, and **F** is the excitation force vector. The terms *x* and *y* denote the displacements of the x- and y-directional resonators.

By substituting **m**, **D**, **k**, and **F** into (2.10), it can be written as

$$\begin{bmatrix} m_x & 0 \\ 0 & m_y \end{bmatrix} \begin{bmatrix} \ddot{x} \\ \ddot{y} \end{bmatrix} + \begin{bmatrix} D_{xx} & 0 \\ 0 & D_{yy} \end{bmatrix} \begin{bmatrix} \dot{x} \\ \dot{y} \end{bmatrix} + \begin{bmatrix} k_{xx} & 0 \\ 0 & k_{yy} \end{bmatrix} \begin{bmatrix} x \\ y \end{bmatrix} = \begin{bmatrix} F_x \\ F_y \end{bmatrix}. \tag{2.11}$$

Here, F_x and F_y denote the x- and y-directional exciting forces, and the symbols D_{xx}, D_{yy}, k_{xx}, and k_{yy} are defined in Fig. 2.4. The x- and y-directional resonators are fully decoupled, having their own resonance frequencies ω_{0x} and ω_{0y} and quality factors Q_x and Q_y. The transfer functions (2.6) can be written independently for both resonators.

2.1.3 Coriolis Effect

Next, the Coriolis effect, which is the fundamental basis of the operation of a vibratory gyroscope, will be described. As shown in Fig. 2.5, a rotating frame of reference is defined by the axes x', y', and z'. This system rotates counterclockwise within an inertial frame of reference, defined by the axes *x*, *y*, and *z*, with an angular velocity Ω.

An observer situated in the rotating frame of reference is watching a particle moving radially away from the rotation axis z' along the axis y'. To the observer, it appears as if there is a force and hence an acceleration that causes the trajectory of the particle to deflect clockwise, as indicated in the figure. In reality, however, there is neither force nor deflection, but the particle follows a straight trajectory in the inertial frame of reference and only seems to deflect because the observer is rotating with the system, a fact obvious to another observer situated in the inertial frame of reference. This effect is called the *Coriolis effect* and the imaginary force and acceleration the *Coriolis force* and the *Coriolis acceleration*, respectively.
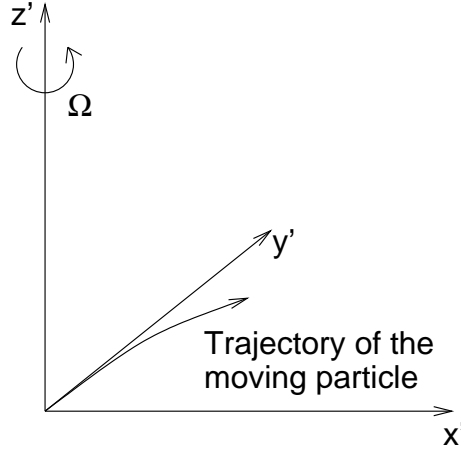
Figure 2.5 Frame of reference formed by the axes x', y', and z', rotating with an angular velocity Ω with respect to an inertial frame of reference.

Next, the magnitude of the Coriolis force will be solved. The velocity $\vec{v}$ of the particle in the inertial frame of reference can be written as

$$\vec{v} = \vec{v'} + \vec{\Omega} \times \vec{r'}, \tag{2.12}$$

where $\vec{v'}$ is the velocity of the particle in the rotating frame of reference, $\vec{\Omega}$ is the angular velocity of the rotating frame of reference with respect to the inertial frame of reference, and $\vec{r'}$ is a position vector from the origin of the rotating frame of reference to the particle. For the sake of generality, all the velocities, both linear and angular, are expressed as vectors and hence can have an arbitrary direction.

Next, by differentiating Eq. (2.12) with respect to time, the acceleration of the particle in the inertial frame of reference can be written as

$$\vec{a} = \vec{a'} + 2\left(\vec{\Omega} \times \vec{v'}\right) + \vec{\Omega} \times \left(\vec{\Omega} \times \vec{r'}\right), \tag{2.13}$$

where $\vec{a'}$ is the acceleration of the particle in the rotating frame of reference. Now, Newton's second law of motion in the inertial frame of reference,

$$\sum \vec{F} = m\vec{a}, \tag{2.14}$$

can be written in the rotating frame of reference, by substituting (2.13) and regrouping, as

$$\sum \vec{F} - 2m\left(\vec{\Omega} \times \vec{v'}\right) - m\vec{\Omega} \times \left(\vec{\Omega} \times \vec{r'}\right) = m\vec{a'} \tag{2.15}$$

Finally, if the rotating frame of reference is additionally accelerating with respect to the inertial frame of reference with a linear acceleration $\vec{a}_{rot}$ and an angular acceleration

$\vec{\alpha}_{rot}$, Eq. (2.15) can be written in its final form as

$$\sum \vec{F} - 2m\left(\vec{\Omega} \times \vec{v'}\right) - m\vec{\Omega} \times \left(\vec{\Omega} \times \vec{r'}\right) - m\vec{a}_{rot} - m\vec{\alpha}_{rot} \times \vec{r'} = m\vec{a'}. \qquad (2.16)$$

In (2.16), there are four imaginary forces acting on the particle in the rotating (and accelerating) frame of reference. The first force, equal to $-2m(\vec{\Omega} \times \vec{v'})$, is the Coriolis force and the second, equal to $-m\vec{\Omega} \times (\vec{\Omega} \times \vec{r'})$, is the *centrifugal force*. The other two forces, $-m\vec{a}_{rot}$ and $-m\vec{\alpha}_{rot} \times \vec{r'}$, are the forces caused by the linear and angular acceleration of the rotating frame of reference, respectively. Whereas the last three terms can be significant sources of error in a vibratory gyroscope[2], something which needs to be taken into account in the design, for the actual operation of the gyroscope, the Coriolis force is the only component of interest.

In principle, an angular velocity sensor could also be based on the centrifugal force. By measuring this force with a linear accelerometer, the angular velocity can be resolved. However, if this kind of measurement setup is used, the sign of the angular velocity cannot be determined. This is because the centrifugal force is proportional to the angular velocity squared. Therefore, such a sensor would more appropriately be called an angular speed sensor. Another problem with this kind of measurement setup is that it is dependent on the radius $\vec{r'}$, representing the distance of the accelerometer from the rotation axis. This measurement method is also sensitive to linear accelerations, which cannot be canceled in a general case.

If the system shown in Fig. 2.4 is now considered in a rotating frame of reference, and it is further assumed that the applied angular velocity $\vec{\Omega}$ is about the z-axis with a magnitude Ω_z (in rad/s), the Coriolis force acting on the y-directional resonator is

$$F_{C,y} = -2m_x \Omega_z v_x = -2m_x \Omega_z \dot{x}, \qquad (2.17a)$$

while the Coriolis force acting on the x-directional resonator is

$$F_{C,x} = 2m_y \Omega_z v_y = 2m_y \Omega_z \dot{y}. \qquad (2.17b)$$

2.1.4 Real 2-Degree-of-Freedom Mechanical Resonator Forming a Vibratory Gyroscope

Now, the 2-D EoM (2.11) can be reformulated taking the Coriolis effect into account. Furthermore, two non-idealities, namely non-proportional damping and anisoelasticity, will be considered [35].

---

[2]The last two terms also form the basis of the operation of a linear and an angular accelerometer, respectively.

Non-proportional damping is an effect whereby the mass is subjected in a certain direction to a force that is proportional to the velocity in another direction. If it is still assumed that all damping in the system is viscous, the non-proportional damping can be modeled by adding the off-diagonal terms D_{xy} and D_{yx} to the damping matrix **D**. Similarly, anisoelasticity means that a spring force proportional to the displacement in one direction is acting on the mass in another direction. The anisoelasticity can be modeled by adding the off-diagonal terms k_{xy} and k_{yx} to the spring matrix **k**.

By adding the off-diagonal terms and the excitation caused by the Coriolis effect, the 2-D EoM for the system can now be written as

$$
\begin{bmatrix} m_x & 0 \\ 0 & m_y \end{bmatrix} \begin{bmatrix} \ddot{x} \\ \ddot{y} \end{bmatrix} + \begin{bmatrix} D_{xx} & D_{xy} \\ D_{yx} & D_{yy} \end{bmatrix} \begin{bmatrix} \dot{x} \\ \dot{y} \end{bmatrix} + \begin{bmatrix} k_{xx} & k_{xy} \\ k_{yx} & k_{yy} \end{bmatrix} \begin{bmatrix} x \\ y \end{bmatrix}
$$
$$
= \begin{bmatrix} 0 & 2\Omega_z m_y \\ -2\Omega_z m_x & 0 \end{bmatrix} \begin{bmatrix} \dot{x} \\ \dot{y} \end{bmatrix} + \begin{bmatrix} F_x \\ F_y \end{bmatrix}.
$$

(2.18)

In the case of a vibratory gyroscope, the coupling between the resonators is weak. Therefore, it can be approximated that both x- and y-directional resonators still act as 1-DoF resonators with a single resonance frequency and a corresponding quality factor.

Now, on the basis of Eq. (2.18), the operation of a vibratory gyroscope can be understood as follows. The x-directional resonator in a vibratory gyroscope is called the *primary resonator* or the *drive resonator*. It is typically excited at its resonance frequency ω_{0x}, called the *operating frequency*, using the external force F_x, and its vibration amplitude is kept constant at A_x by some form of control. Thus, the position of the primary resonator can be written as

$$
x(t) = A_x \sin(\omega_{0x}t), \tag{2.19}
$$

where t is the time.

The y-directional resonator in a vibratory gyroscope is called the *secondary resonator* or the *sense resonator*. By assuming that the external force F_y used to excite it is zero, corresponding to open-loop operation, then, based on Eqs. (2.18) and (2.19), the EoM for the secondary resonator can be written as

$$
m_y \ddot{y} + D_{yy} \dot{y} + k_{yy} y = -\left\{ A_x \omega_{0x} \left[2m_x \Omega_z + D_{yx} \right] \cdot \cos(\omega_{0x}t) + \right.
$$
$$
\left. k_{yx} A_x \cdot \sin(\omega_{0x}t) \right\}.
$$

(2.20)

By disregarding the non-proportional damping and the anisoelasticity for a moment (i.e. setting $D_{yx} = k_{yx} = 0$), this simplifies into

$$
m_y \ddot{y} + D_{yy} \dot{y} + k_{yy} y = -2A_x \omega_{0x} m_x \Omega_z \cdot \cos(\omega_{0x}t). \tag{2.21}
$$

Now, with the help of Eq. (2.7a), the displacement $y(t)$ of the secondary resonator can be written as

$$y(t) = -\frac{2A_x\omega_{0x}m_x\Omega_z}{m_y\sqrt{\left(\omega_{0x}^2 - \omega_{0y}^2\right)^2 + \omega_{0x}^2\omega_{0y}^2/Q_y^2}} \cdot \cos\left(\omega_{0x}t + \phi\right), \qquad (2.22)$$

where ϕ is the phase shift of the secondary resonator transfer function at the operating frequency ω_{0x}. By defining a parameter κ, which describes the separation of the resonance frequencies of the primary and the secondary resonators, as

$$\kappa = \frac{\omega_{0y}}{\omega_{0x}}, \qquad (2.23)$$

Eq. (2.22) can be rewritten as

$$y(t) = -\frac{2A_xm_x\Omega_z}{\omega_{0x}m_y\sqrt{\left(\kappa^2 - 1\right)^2 + \kappa^2/Q_y^2}} \cdot \cos\left(\omega_{0x}t + \phi\right). \qquad (2.24a)$$

The phase shift ϕ can be defined by substituting κ into (2.7b), yielding

$$\phi = \arctan\frac{\kappa}{(1 - \kappa^2) \cdot Q_y}. \qquad (2.24b)$$

Non-proportional damping causes an additional output signal corresponding to the angular velocity

$$\Omega_{z,Dyx} = \frac{D_{yx}}{2m_x} \qquad (2.25a)$$

which is in phase with the actual Coriolis signal, whereas anisoelasticity causes a signal corresponding to the angular velocity

$$\Omega_{z,kyx} = \frac{k_{yx}}{2\omega_{0x}m_x} \qquad (2.25b)$$

which has a 90° phase shift with respect to the Coriolis signal and is hence called the *mechanical quadrature signal*.

2.1.5 Modes of Operation of a Vibratory Gyroscope

The parameter κ is important in describing the gyroscope's operation, as it defines how the resonance frequencies of the primary and secondary resonators are located with respect to each other. Three distinct cases can be identified. The first case is when $\kappa \gg 1$ and the operating frequency is in the flat part of the secondary resonator transfer function (much below 10 kHz in Fig. 2.2). In this case, it is said that the gyroscope operates in the *low-pass mode*. By letting $\kappa \to \infty$ in Eq. (2.24a), the displacement

caused by the angular velocity Ω_z can be written as

$$y(t) = -\frac{2A_x\omega_{0x}m_x\Omega_z}{\omega_{0y}^2 m_y} \cdot \cos(\omega_{0x}t),$$ (2.26)

where it has also been approximated that $\phi = 0$.

As an example, if the masses m_x and m_y are equal and if the operating frequency $f_{0x} = 1\,\text{kHz}$ and the resonance frequency of the secondary resonator $f_{0y} = 10\,\text{kHz}$, then, with an angular velocity of $100°/\text{s}$ ($1.75\,\text{rad/s}$), the amplitude of the Coriolis movement is approximately $5.6\,\text{ppm}$ (parts per million, 10^{-6}) of the amplitude of the primary movement. This example shows how tiny the Coriolis movement is compared to the primary movement.

When the resonance frequencies are brought closer to each other, the Coriolis movement starts getting amplified by the gain of the secondary resonator. In this second case, the displacement caused by the angular velocity Ω_z can be written as

$$y(t) = -\frac{2A_x m_x\Omega_z}{\omega_{0x}m_y(\kappa^2-1)} \cdot \cos(\omega_{0x}t + \phi).$$ (2.27)

The gyroscope is still operating in the low-pass mode, but the so-called *resonance gain* is utilized to amplify the Coriolis movement. The gain depends only on the mode separation κ, as long as the quality factor of the secondary resonator Q_y is sufficient. This is desirable, as it reduces the sensitivity of the gain to environmental variations. By dividing the amplitude of (2.27) by the amplitude of (2.26), the magnitude of the resonance gain can be shown to be

$$G_{res} = \frac{\kappa^2}{\kappa^2-1}.$$ (2.28)

The magnitude of the resonance gain as a function of the mode separation is plotted in Fig. 2.6. Here, it is assumed that Q_y is large enough not to limit the gain.

If Q_y is not large enough, it causes a relative gain error

$$E_{res} = \frac{G_{res} - G_{res,lim}}{G_{res}},$$ (2.29)

where G_{res} is the ideal resonance gain and $G_{res,lim}$ the resonance gain limited by finite Q_y. The value of Q_y necessary to keep the relative gain error below E_{res} is

$$Q_y \geq \frac{\kappa}{\sqrt{E_{res}(E_{res}+2)}(\kappa^2-1)}.$$ (2.30)

For instance, if the mode separation is $\kappa = 1.2$, the resonance gain is $G_{res} \approx 3.3$. Now, $Q_y \geq 61$ is sufficient to keep the relative gain error below 0.1%.
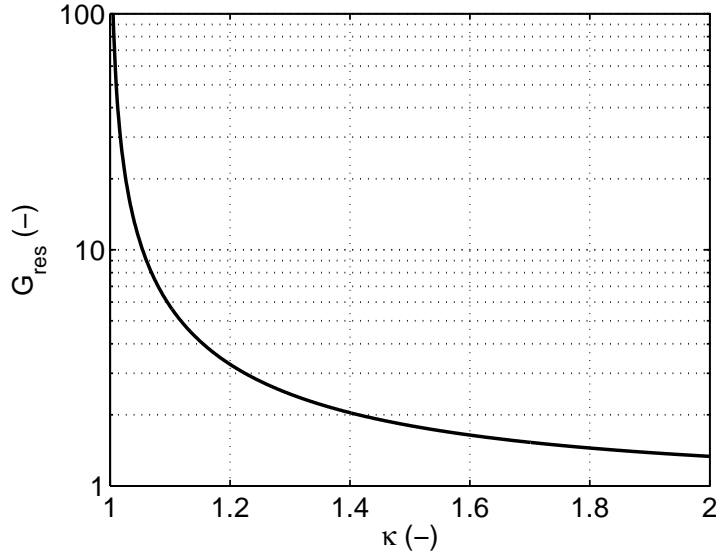
Figure 2.6 Resonance gain as a function of the mode separation κ, assuming that Q_y is large enough not to limit the gain.

Finally, it should be noticed that although the resonance gain G_{res} is independent of Q_y, provided that the quality factor is sufficient, it is still sensitive to the variation of κ. The sensitivity, defined as $(dG_{res}/d\kappa) \cdot (\kappa/G_{res})$, is shown in Fig. 2.7. From the figure, it can be seen that with the previous example $\kappa = 1.2$, the sensitivity is -4.5. This means that if κ increases by 1%, the resonance gain decreases by 4.5%.

When the resonance frequencies are brought close enough to each other, the gain starts saturating to the value determined by Q_y. At the extreme, the modes are equal and $\kappa = 1$. This is the third case, which is called the *mode-matched operation* of the gyroscope. Now, by setting $\kappa = 1$ in Eq. (2.24a), the displacement caused by the angular velocity Ω_z can be written as

$$y(t) = -\frac{2A_x m_x \Omega_z Q_y}{\omega_{0x} m_y} \cdot \cos(\omega_{0x}t - \pi/2) = -\frac{2A_x m_x \Omega_z Q_y}{\omega_{0x} m_y} \cdot \sin(\omega_{0x}t). \qquad (2.31)$$

With $\kappa = 1$, the phase shift $\phi = -90°$ or $-\pi/2$ radians, which is indicated in the equations. The resonance gain is now at its maximum[3] (equal to Q_y), meaning that the Coriolis movement is maximized, but at the same time the sensitivity to the variation of Q_y is maximized as well, and the sensitivity to the variation of κ is high[4].

Apart from the three operating modes described above, the gyroscope could, in

---

[3]Precisely speaking, the gain is not at the exact maximum, as described in Section 2.1.1. However, for any practical purposes, the gain is maximized.

[4]Again, to be precise, when $\kappa = 1$, the sensitivity of G_{res} to the variation of κ as defined above is low (close to zero). However, the sensitivity grows very rapidly as soon as κ deviates from the value of one.
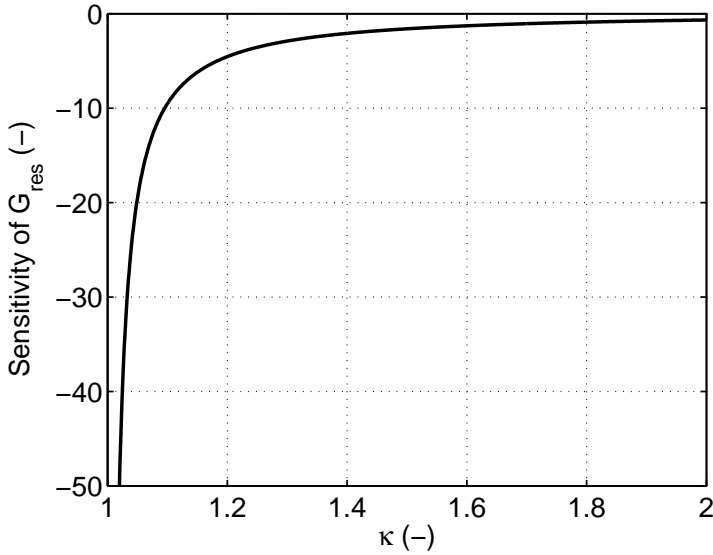
Figure 2.7 Sensitivity of the resonance gain to the variation of the mode separation κ, as a function of κ.

principle, also be operated in a fourth distinct mode, with $\kappa < 1$. However, there are very few examples of this available in the literature [36].

As mentioned at the beginning of this section, the parameter κ is important in describing the operation of the gyroscope, as it defines the mode separation and thus the resonance gain of the device. If only the sensitivity and the resolution of the system are considered, it would be advantageous to use a κ as close to unity as possible. However, in a practical design case, there are several other parameters which are also affected by κ and need to be taken into account. One of these, the sensitivity of the resonance gain to parameter variations, was already described above. Other aspects that need to be considered include the possible phase instability of the Coriolis signal and the mechanical quadrature signal, which can cause instability in both gain and offset, and the shock and vibration sensitivity of the device.

An alternative approach to the use of a 2-DoF resonator with decoupled oscillation modes is to use resonators with multiple DoFs. This has been demonstrated in [37–39]. By using a multiple-DoF primary resonator, the drive mode bandwidth can be increased. With a proper design, the primary resonator can, in principle, always be driven at the secondary resonator resonance frequency, ensuring mode-matched operation despite process and environmental variations. By using a multiple-DoF secondary resonator, the sensitivity of the resonance gain to the varying mode separation can be reduced. Despite these advantages, this approach has not been widely adopted, mostly because of the increased complexity of the design.

2.1.6   Dynamic Operation of a Vibratory Gyroscope

So far, it has been implicitly assumed that the angular velocity Ω_z is constant in time. By replacing it with a time-varying angular velocity $\Omega_z(t)$, the y-directional Coriolis force in the right-hand side of (2.21) turns into

$$F_{C,y} = -2A_x\omega_{0x}m_x\Omega_z(t) \cdot \cos(\omega_{0x}t). \tag{2.32}$$

If the angular velocity is sinusoidal, with amplitude Ω_z, frequency ω_Ω, and phase φ, it can be written as $\Omega_z(t) = \Omega_z \cdot \cos(\omega_\Omega t + \varphi)$. The resulting Coriolis force is then

$$\begin{aligned} F_{C,y} = -&A_x\omega_{0x}m_x\Omega_z \cdot \\ &\left[\cos((\omega_{0x} - \omega_\Omega)t - \varphi) + \cos((\omega_{0x} + \omega_\Omega)t + \varphi)\right]. \end{aligned} \tag{2.33}$$

From the equation, it can be seen that the Coriolis force is again amplitude-modulated, with the operating frequency ω_{0x} as the carrier. Next, this force excites the secondary resonator, causing secondary movement.

If the gyroscope is operated in the low-pass mode, both sidebands of the resulting Coriolis force cause Coriolis movement with equal amplitude and phase shift. However, the closer the resonance frequencies are brought to each other, the more the higher-frequency sideband is amplified relative to the lower-frequency sideband. The phase shifts also start differing. At the extreme, with mode-matched operation, both sidebands go through the same amplification again, if a sufficient quality factor is assumed. In this case, the $-3\,\mathrm{dB}$ bandwidth of the gyroscope is equal to $\omega_{0y}/(2Q_y)$.

This difference in the gain and phase shifts of the two sidebands is revealed when the output signal is synchronously demodulated into in-phase and quadrature components. The effect will be studied in Chapter 3, together with the other effects of synchronous demodulation.

2.2   Mechanical-Thermal Noise

Like all dissipative systems, the mass-spring-damper system of Fig. 2.1, which is a fundamental part of a microgyroscope, also exhibits thermal noise. From the Equipartition Theorem of energy and the Nyqvist Relation [40, 41], the power spectral density of the noise force in N^2/Hz can be written as

$$F_n^2 = 4k_BTD. \tag{2.34}$$

Here, k_B is the Boltzmann constant, equal to $1.38066 \cdot 10^{-23}\,\mathrm{J/K}$, T the absolute temperature, and D the damping coefficient as defined earlier. For the y-directional res-

onator, D should be replaced with D_{yy}.

This noise force is a direct analog of the Johnson noise ($4k_BTR$, where R is the resistance) related to electrical resistances. The expressions are identical, as both forms of noise have the same physical background.

In a gas damped system, the noise force is caused by the Brownian motion of the gas molecules surrounding the resonator. The random movement of the molecules causes random collisions between the molecules and the resonator. This, in turn, creates the noise force, with a power spectral density equal to (2.34). Similarly, in an acoustically damped system, random lattice oscillations cause the noise force, which again has the power spectral density given in Eq. (2.34).

The noise force next excites the respective resonator and creates noise movement, which then traverses through the readout system. The concept of mechanical-thermal noise will be revisited in Chapter 3, after the effects of synchronous demodulation have first been introduced. Only then is it possible to reduce the power spectral density of the noise force (2.34) to input angular velocity.

2.3   Excitation and Detection

In Section 2.1, the structure and operation of a vibratory microgyroscope were described. The gyroscope is composed of two resonators, the primary and the secondary resonators. For proper operation to be possible, the primary resonator needs to be driven into vibration with a certain amplitude, and the amplitude typically needs to be monitored. The Coriolis force couples this vibration to the secondary resonator when the sensor is being subjected to angular velocity. In order to be able to resolve the angular velocity, the secondary resonator vibration also needs to be detected.

To both generate and sense the movements, there is a need for a mechanism to access the resonators from outside. The driving of the primary resonator requires a method to excite or to actuate the resonator, that is, to generate the force F_x in Eq. (2.18). In a microelectromechanical gyroscope, the actuator needs to convert an electrical signal, either a voltage or current, into a force. Similarly, the detection or the readout of both resonators requires a method to convert the position of the resonator (x or y) to a quantity which can be measured with an electronic circuit.

Ideally, the excitation and detection should have no side effects. This means that the excitation should only generate an externally controllable force, without affecting the other parameters of the resonators. Likewise, the detection should only convert the displacement into an electrical signal, without disturbing the system being measured, for example by altering the resonator parameters or the actual displacement being measured. Unfortunately, this is not necessarily always the case. Therefore, the side effects should be carefully considered. Their elimination or compensation usually

requires them to be accounted for in the mechanical design. This implies that the design of the interfaces between the electrical and mechanical domains is a critical area where a sound knowledge of both domains and their interactions is required.

Typical excitation mechanisms that have been utilized in vibratory microgyroscopes are electrostatic (capacitive), piezoelectric, and electromagnetic actuation. The detection methods are capacitive, piezoelectric, and piezoresistive detection. [7] Next, all these methods are described very briefly [42, Ch. 5]. Several examples will be given in Section 2.5.

In this thesis, the focus will be on electrostatic excitation and capacitive detection. A more detailed presentation of electrostatic excitation will be given in Chapter 4. The details of capacitive detection will be considered at the beginning of Chapter 7. In the same chapter, the side effects of capacitive detection (electrostatic spring softening and the nonlinear electrostatic forces) will be analyzed.

In capacitive excitation and detection, there are two electrodes that form a parallel-plate capacitor. One of the electrodes is fixed, while the other electrode moves with the resonator. For excitation, an attractive electrostatic force can be generated between the electrodes by applying a voltage between them. For detection, the structure forms a position-dependent capacitor. By measuring the capacitance of this structure, the position can be resolved.

In piezoelectric excitation, an electric field applied in a piezoelectric material generates the exciting force. Common piezoelectric materials include quartz, zinc oxide (ZnO), lead zirconate titanate (PZT), and aluminum nitride (AlN). Likewise, in piezoelectric detection, a force applied to the material causes a varying voltage. By measuring the voltage, the deformation can be resolved.

In electromagnetic actuation, a magnetic field is used to generate the force. The magnitude of the force can be controlled, for instance, by a current loop.

In piezoresistive detection, the displacement causes mechanical stress, which in turn causes the resistance of the piezoresistor to vary. By measuring the resistance, the stress and hence the displacement can be resolved. In silicon microstructures, a piezoresistor can be formed by a simple n- or p-doped area in the semiconductor, or by a polysilicon (polycrystalline silicon) structure. Single-crystal silicon piezoresistors are highly temperature-dependent, requiring some form of compensation such as the use of the well-known four-resistor Wheatstone bridge. In polysilicon piezoresistors, the temperature dependency is lower, but so is the stress sensitivity.

Of these techniques, capacitive excitation and detection, together with piezoresistive detection, are compatible with a standard silicon technology. Piezoelectric excitation, which has the advantage of being able to generate large excitation forces, requires either the use of a substrate made out of a piezoelectric material, such as quartz or ZnO, or special processing steps to deposit piezoelectric material onto a silicon sub-

strate. Still, large excitation voltages are required. Magnetic excitation, on the other hand, typically requires magnetic materials to generate a permanent magnetic field, which complicates the sensor manufacture and/or packaging.

Apart from these methods, there are some more exotic detection methods. In optical detection, a light-emitting device and a photodetector are used to measure the displacement. Finally, in tunneling-based detection, a tunnel junction is formed over a small gap between the moving structure and the fixed structure. The displacement of the moving structure results in a change in the gap, which alters the tunneling current. As the tunneling current varies exponentially with the gap, this can permit very sensitive detection. Usually a feedback is used to keep the gap and the tunneling current constant. However, a significant disadvantage of tunneling-based detection is that it is very sensitive to temperature variation. [43]

2.4 Manufacturing Technologies

The technologies used to manufacture micromechanical devices can be broadly divided into two groups, bulk and surface micromachining. In bulk micromachining, microstructures are formed by selectively removing parts from bulk material, such as a single-crystal silicon wafer. In surface micromachining, microstructures are formed by growing and etching different kinds of films on top of a supporting structure, such as a silicon wafer. The division between these two groups is not precise, and technologies can be found which either seem to fit into both of these groups or do not fit into either one. However, for the purpose of this brief introduction to the various technologies, this rough division is sufficient.

Another division can be made between single- and two-chip implementations. This classification is more accurate, as in single-chip implementations, both the micromechanical and the microelectronic parts are located on a single die, whereas in two-chip implementations, they are on separate dies which are then combined, using, for example, wire bonding.

In this section, bulk and surface micromachining will first be briefly described. Next, the properties of single- and two-chip implementations will be compared. In Section 2.5, where various published microgyroscopes available in the literature will be discussed, examples of both bulk and surface micromachined devices and of single- and two-chip implementations will be presented.

2.4.1 Bulk Micromachining

In bulk micromachining [33, Ch. 5] [44], which is sometimes also referred to as substrate micromachining, microstructures are formed by selectively removing parts from

bulk material. This material can be, for example, a single-crystal silicon wafer. Additionally, patterned wafers are frequently bonded together to form more complex structures or to hermetically encapsulate microstructures. Wafer bonding can be performed using techniques such as fusion bonding or anodic bonding [32, Ch. 17].

Patterning is performed using various etching techniques [32, Ch. 11] [44]. These techniques can first be divided into wet and dry etching. In wet etching, the wafer is immersed into an etching solution, which then removes bulk material from areas which are not covered by some form of protective mask, such as silicon dioxide (SiO_2) or silicon nitride (Si_3N_4). In dry etching, either vapor or plasma is used to remove material from the unprotected areas. The depth of the etched structures can be controlled by either timed etching or by some form of etch-stop layer which stops the etching in a certain direction. The latter option typically leads to much more precise control.

Second, etching techniques can be divided into isotropic and anisotropic etching. In isotropic etching, the etching proceeds evenly in all directions. In anisotropic etching, some directions are etched more rapidly than others. For example, in the anisotropic wet etching of silicon, the etching speed in the direction of certain crystal planes can be hundreds of times greater than in others. In anisotropic dry etching, such as DRIE (Deep Reactive Ion Etching), the direction perpendicular to the wafer is etched far more rapidly than the direction following the plane of the wafer. In this way, deep and narrow trenches can be formed.

Using bulk micromachining, large devices in both weight and size can be realized. As will be shown later in Section 3.5, a large mass corresponds to low mechanical-thermal noise in microgyroscopes, as well as in micromechanical accelerometers. Additionally, single-crystal silicon is an excellent mechanical material, as it is very linear and strong and its parameters are very stable [32, Ch. 4].

2.4.2 Surface Micromachining

In surface micromachining [33, Ch. 6] [45], microstructures are formed by growing and etching different kinds of films on top of a supporting structure. This supporting structure can be, for example, a silicon wafer. The most commonly used structural material is polysilicon. Other possible materials include various metals and amorphous silicon nitride. The available etching techniques correspond to those described in conjunction with bulk micromachining.

Surface micromachining is based on the use of sacrificial layers to form freely-moving structures [32, Ch. 22]. A very simple illustration of this is shown in Fig. 2.8. First, a sacrificial layer, in this case SiO_2, is deposited onto the substrate and an anchor point is patterned (Fig. 2.8 (a)). Next, the structural polysilicon is deposited and patterned to form the desired structure, in this case a beam (Fig. 2.8 (b)). Finally, the

sacrificial layer is removed, leaving the final freely-moving structure (Fig. 2.8 (c)). With proper planarization, multiple layers of structural material can be patterned and then released, making possible the manufacture of very complex structures.
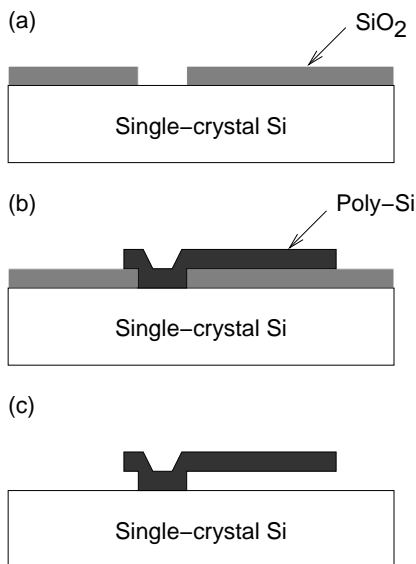
Figure 2.8 Simple illustration of a surface micromachining process and the use of sacrificial layers.

With surface micromachining, much smaller structures can be realized than with bulk micromachining. The achievable masses are also smaller, leading to a higher mechanical-thermal noise level.

In order to achieve larger masses, a so-called epi-poly layer can be used[5]. An epi-poly is a thick structural polysilicon layer, grown on SiO_2 film on a silicon substrate [32, Ch. 6]. By patterning the epi-poly and then releasing by etching the underlying sacrificial SiO_2 film between the structure and the substrate, much thicker structures and hence larger masses can be realized than with thin films.

Another alternative way to realize larger masses is with the use of an SOI (Silicon-on-Insulator) wafer as the starting material. An SOI wafer consists of a thick single-crystal silicon wafer, the so-called handle, on top of which an SiO_2 film is grown. On top of the SiO_2, there is another single-crystal silicon layer, which is much thinner than the handle, with typical thicknesses ranging from micrometers to several dozen micrometers. This layer is called the structural layer. Microstructures are formed in the structural layer and released by etching the sacrificial SiO_2 film between the structural layer and the handle. [46]

---

[5]The term epi-poly is contradictory, as the term epi refers to an epitaxial film which is single-crystal, whereas poly means polycrystalline. The term is used to indicate that the film is grown in an epireactor under epi growth conditions, but the growth is performed on an amorphous substrate, such as SiO_2. [32, Ch. 6]

Epi-poly and, especially, SOI technologies are sometimes considered to be separate categories from actual surface micromachining. In this case, only the actual thin film technologies are considered to be surface micromachining. However, in the interest of keeping this presentation simple, they are included in the group of surface micromachining technologies.

2.4.3 Single- and Two-Chip Implementations

Microelectromechanical devices can be divided into two separate groups, according to whether the micromechanical and electronic parts are on a single chip or on two separate chips. If the structures are on a single chip (also known as monolithic or fully integrated implementation), the mechanical and electronic parts are combined at the die level. If the structures are on separate chips (also known as hybrid implementation), the two dies are typically combined at the packaging level, using, for example, wire bonding.

In a single-chip implementation, the microstructures can be formed either before the electronics, after the electronics, or together with the electronics. In case of a CMOS (Complementary Metal-Oxide-Semiconductor) circuitry, these approaches are called pre-CMOS, post-CMOS, or intra-CMOS micromachining, respectively. While all these alternatives have their own advantages and disadvantages [47], a detailed discussion is beyond the scope of this thesis.

The advantages of a single-chip implementation are reduced size and electronic noise because of smaller parasitics associated with the interconnection between the mechanical and electronic parts. The extra steps required to combine the two dies at the packaging level are also eliminated. On the other hand, two-chip implementation makes possible the separate optimization of the technologies used to realize the mechanical and electronic parts, and allows independent yield control of the processes.

An interesting technology called Chip-on-MEMS (CoM) has recently been described for reducing the parasitics associated with the interconnections in a two-chip implementation [48]. In the CoM technology, the micromechanical part is first manufactured and hermetically encapsulated by employing wafer-bonding techniques. Contact pads are formed on this component. Next, the thinned, unencapsulated ASIC (Application-Specific Integrated Circuit) containing the electronics is soldered directly onto the mechanical component using flip-chip technology. This forms very low-parasitic interconnections between the dies. The combination can then be mounted onto a printed circuit board (PCB), again using flip-chip technology, or it can be encapsulated in a standard package.

In a two-chip implementation, even standard foundry technologies can be used to realize the electronic part, although this can also be possible in a single-chip imple-

mentation if the micromechanical parts are manufactured on top of a fully-processed wafer [49,50]. In a single-chip implementation, there is, however, always an inevitable compromise between the technologies used to realize the mechanical and electronic parts.

It is sometimes claimed that bulk micromachining always leads to a two-chip implementation. However, this is not necessarily the case, as can be seen from examples in [44] and in [32, Ch. 17]. As a final remark, two-chip implementation is still the norm in the industry [32, Ch. 28], although there are manufacturers producing large quantities of components using single-chip implementation as well [51].

2.5   Published Microgyroscopes

In this section, published microgyroscopes available in the literature will be discussed. Only those publications which address both the micromechanical sensor element and the related readout and control electronics will be considered. Beyond this scope there remains a vast amount of publications which address only the mechanical element design and the related fabrication technologies. For a survey of the published sensor elements, a thorough review of micromechanical vibratory gyroscopes up until the year 1998 has been presented in [7]. Another, more recent review from the year 2003 can be found in [47].

The material in this presentation will be divided according to the research institutions. The most important groups are discussed in their own subsections. They are (in no specific order): the Berkeley Sensors and Actuators Center (BSAC); Analog Devices Inc. (ADI); HSG-IMIT (Hahn-Schickard-Gesellschaft, Institut für Mikro- und Informationstechnik); Robert Bosch GmbH; Carnegie Mellon University, and Georgia Institute of Technology. Additionally, other publications will be grouped into the last subsection. After this, a brief summary and discussion will conclude this presentation.

For each published implementation, the following properties will be discussed, provided that they are given in the publication: manufacturing technology; primary and secondary mode configuration; the direction of the sensitive axis; whether the implementation is a single- or two-chip configuration; what kind of excitation and detection mechanisms and circuitry are used, and other properties of the electronics. Additional details from the publication are included if they are considered relevant. While the different readout circuits will be referred to here by their names, a more detailed discussion of these circuits will be given in Chapter 7.

In the subsequent section, commercial microgyroscopes available on the market will be discussed. There will be a slight overlap between the materials in these two sections, as Analog Devices Inc. and Robert Bosch GmbH also have publications about their devices and hence appear in both sections.

2.5.1   Berkeley Sensors and Actuators Center (BSAC)

The Berkeley Sensors and Actuators Center (BSAC) at the University of California, Berkeley (CA, USA) has a long tradition in the research of digitally force-balanced microaccelerometers implemented as electromechanical $\Sigma\Delta$ loops, with the first publications dating back to 1992 [52–56]. The first published system implementations of micromachined gyroscopes are the works of Clark and Juneau from the year 1996 [57,58], with more detailed presentations in [59,60]. These are a surface-micromachined z-axis gyroscope and a surface-micromachined x/y-axis gyroscope, respectively.

The z-axis gyroscope [57, 59] is a single-chip device, fabricated first with Analog Devices' polysilicon surface micromachining technology with a 4-μm BiCMOS (Bipolar Complementary Metal-Oxide-Semiconductor, a CMOS technology which includes bipolar transistors) circuitry, and then with Sandia National Laboratories' process with polysilicon surface micromachining and 2-μm CMOS. Both actuation and detection are performed capacitively. The primary and secondary modes are both lateral, while the sensitive axis is perpendicular to the structure. The primary resonator excitation loop is implemented with a transresistance amplifier combined with an automatic gain control (AGC), which keeps the amplitude constant, and the secondary resonator readout with a charge-sensitive amplifier (CSA). The Coriolis signal is modulated to a higher carrier frequency for detection. Demodulation is performed using clock signals generated by a PLL. The electronics implement an electrostatic quadrature compensation performed with a dc voltage. A block diagram of the implementation is shown in Fig. 2.9.
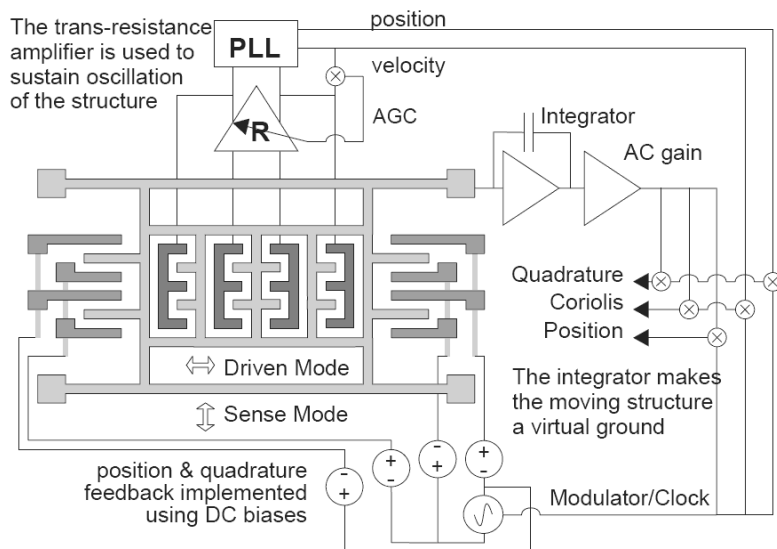
Figure 2.9 Block diagram of the z-axis gyroscope published by BSAC. (From [57], published in 1996.)

The x/y-axis gyroscope [58, 60] is also a single-chip device, with a polysilicon surface-micromachined mechanical structure. The device was fabricated with both Analog Devices' process and Sandia National Laboratories' process, like its z-axis counterpart. The device has a circular design, with rotational primary vibration about the z-axis (perpendicular to the substrate), and rotational secondary movements about the x- and y-axes, one for each sensitive direction. The device employs an electrostatic tuning of the secondary resonator resonance frequency, in order to control the resonance gain. As with its z-axis counterpart, excitation and detection are performed capacitively. The primary resonator excitation loop is implemented with a transresistance amplifier and the secondary resonator readout with a CSA. A single CSA is used, as the x- and y-directional movements are modulated to different carrier frequencies. Demodulation is performed using clock signals generated by a PLL.

The next implementation is the work by Seshia in the year 2002 [61]. This is a z-axis gyroscope, with a single-chip implementation using polysilicon micromachining. The devices were fabricated using the Sandia National Laboratories' technology, with 2.25-μm thick structural polysilicon and 2-μm CMOS. Later, improved devices were fabricated with Analog Devices' process with 6-μm structural polysilicon and 0.8-μm CMOS, but no experimental results are provided for them. The device has lateral primary and secondary modes. Primary resonator excitation is performed electrostatically, using a transresistance amplifier. Coriolis signal detection utilizes the so-called resonant output. Instead of directly measuring the secondary resonator displacement, it affects the resonance frequency of a third resonator through the compressive stress it applies to the structure. By measuring the shift of the resonance frequency, angular velocity is resolved.

The tradition of the digitally force-balanced inertial sensors implemented as electromechanical $\Sigma\Delta$ loops was continued in the gyroscope implementations published by Jiang in 2000/2002 [56, 62, 63] and Petkov in 2004 [64–66]. The work of Jiang is divided into two parts, a z-axis gyroscope with lateral excitation and detection and the sensitive axis perpendicular to the substrate [62], and an x/y-axis gyroscope with vertical primary movement along the z-axis and lateral secondary movements along the x- and y-axes, one for each sensitive direction [63]. Both implementations are single-chip devices, with polysilicon surface-micromachined mechanical structures and capacitive excitation and detection. The z-axis gyroscope was implemented with a technology with 2.25-μm thick structural polysilicon and 2-μm CMOS, while the x/y-axis gyroscope was implemented with a technology with 6-μm thick structural polysilicon and 0.8-μm CMOS. No further details of the technologies are given, but the dimensions correspond to the Sandia National Laboratories' and the Analog Devices' technologies, respectively, which were introduced in Seshia's work. Detailed implementations of the primary resonator excitation circuitry are not given, but at least in the x/y-axis

gyroscope, the primary resonator is driven at the resonance frequency of the secondary resonator instead of driving it at its own resonance frequency. The readout circuit realizing the ΣΔ loop is implemented as an SC circuit.

In Petkov's work, the design of a higher-order ΣΔ interface for a single-axis microgyroscope is studied. The system is implemented as a two-chip solution, with the electronics realized with a 0.5-μm CMOS. The micromechanical sensor element has been published by Robert Bosch GmbH in [67]. The element is implemented by surface micromachining an 11-μm thick polysilicon layer (epi-poly). The device has a circular design, with rotational primary vibration about the z-axis (perpendicular to the substrate) and rotational secondary movement, and with capacitive excitation and detection. The sensitive axis is in the x-direction (parallel to the substrate). Again, the readout circuit is implemented as an SC circuit. The details of the primary resonator excitation are not given.

In the work by Jiang and Petkov, a secondary resonator readout based on a higher-order electromechanical ΣΔ loop is studied in detail. While the concept will be described in more detail in Chapter 7, in brief, it improves the quantization noise shaping and hence the signal-to-noise ratio (SNR) of the interface. The concept of higher-order electromechanical ΣΔ modulation was applied later in microaccelerometer design by other groups, such as in [68].

2.5.2   Analog Devices Inc. (ADI)

Analog Devices Inc. (ADI), Cambridge, MA, USA published parts of the design of the ADXRS150 microgyroscope in [69, 70] in the year 2002. A block diagram of the implementation is shown in Fig. 2.10. The device is a monolithic single-chip implementation, with the sensitive axis perpendicular to the substrate and with lateral excitation and detection. It is fabricated with a 3-μm BiCMOS process with 4-μm thick structural polysilicon.

The device employs capacitive excitation and detection. The primary resonator excitation loop is implemented with a transresistance amplifier and a comparator. No amplitude control is performed. Gain accuracy is improved by open-loop temperature compensation, in which the secondary signal gain is controlled according to the temperature. The temperature is measured using a PTAT (Proportional-to-Absolute Temperature) generator. The secondary resonator detection is performed with a CSA. The detection is performed at the mechanical resonance frequency, without modulating the signal to a higher carrier frequency. The system also includes self-test (S.T.) electrodes to fully exercise the structure and ensure that it is working properly.

Currently, ADI has a wide range of different microgyroscopes available, apart from the ADXRS150, which was the first device introduced. However, no implementation
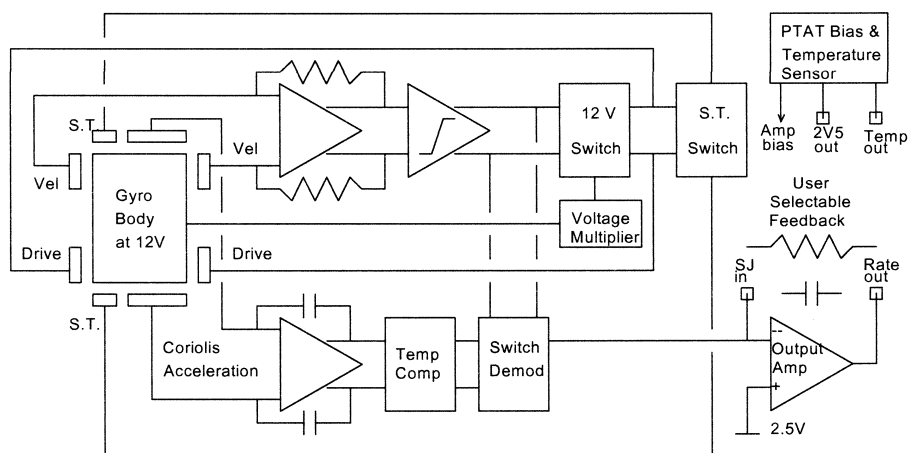
Figure 2.10 Block diagram of the ADXRS150 gyroscope published by Analog Devices Inc. (From [70], published in 2002.)

details of the other devices have been published.

2.5.3   HSG-IMIT

HSG-IMIT (Hahn-Schickard-Gesellschaft, Institut für Mikro- und Informationstechnik), Villingen-Schwenningen, Germany, first reported their gyroscope element design in 1997 [71], with more recent advancements published, for example, in [72] and [73]. They have reported two element designs, one with two rotational modes [71–75] and another with two lateral modes [74]. Both devices employ capacitive excitation and detection. The first implementation is an x-axis gyroscope with a circular design, with rotational primary vibration about the z-axis (perpendicular to the substrate) and rotational secondary movement. The second implementation has both its primary and secondary modes parallel to the substrate and its sensitive axis perpendicular to the substrate (along the z-axis). The elements with two rotational modes were realized with the foundry service provided by Robert Bosch GmbH, by surface micromachining a 10-μm thick structural polysilicon layer (epi-poly). For the elements with two lateral modes, a process flow with SOI substrates and deep silicon etching was developed in-house.

The readout electronics [74, 75], which are based on modulating both the primary and the secondary signals to a higher frequency, were realized using discrete components. A block diagram of the system is shown in Fig. 2.11. The output signal is amplified and high-pass (HP) filtered, after which it is A/D converted using undersampling, in order to gain a lower operating frequency for the following DSP. The DSP then bandpass (BP) filters the signal, demodulates it, and finally performs low-pass (LP) fil-

tering. D/A converters are employed to generate control signals for the element. The required controllers are implemented as PI (Proportional-Integrator) controllers.

In the earlier implementations [73], the primary resonator amplitude control was reportedly performed by employing mechanical stoppers [76]. However, the more recent publications do not mention this, and show an electronic amplitude controller in the block diagram instead. The experimental results for the system employing the element with two rotational modes are presented in [74, 75] and for the element with two lateral modes in [74].

2.5.4   Robert Bosch GmbH

Robert Bosch GmbH, Stuttgart, Germany, has published parts of the implementations of all their three angular velocity sensors, the DRS-MM1, DRS-MM2, and DRS-MM3[6]. All three sensors are two-chip implementations, with the mechanical sensor element and the readout and control electronics on separate chips. The chips are then combined at the packaging level.

The first published sensor, the DRS-MM1 [77] from the year 1997, is realized using combined bulk and surface micromachining of silicon substrates with a 12-μm thick polysilicon layer (epi-poly) on top of a 2.5-μm thermal oxide layer. Both the primary and the secondary modes are lateral, and the sensitive axis is perpendicular to the substrate. The primary resonator excitation is performed using magnetic actuation. For this purpose, a permanent magnet is mounted in the package on the top of the sensor element. The secondary resonator detection is capacitive. The publication does not address the structure of the required electronics in detail, except that the secondary resonator is operated in a closed loop.

The second sensor, the DRS-MM2 [78] from the year 1999, is manufactured by surface micromachining an 11-μm thick structural polysilicon layer (epi-poly). This element has a circular design, with its rotational primary vibration mode about the z-axis (perpendicular to the substrate) and rotational secondary movement. The sensitive axis is parallel to the substrate. Both excitation and detection are performed capacitively. Detection is performed by modulating the position information into a higher carrier frequency. The secondary resonator is operated in an open loop. In the publication, only a block diagram of the readout and control electronics is disclosed.

The third and currently the most recent angular velocity sensor, the DRS-MM3 [9, 79], was published in 2005. Like the DRS-MM2, the element is manufactured by surface micromachining an 11-μm thick structural polysilicon layer (epi-poly). However, in this element, both the primary and secondary modes are again lateral, and

---

[6]Apparently, DRS is an abbreviation for the German word *Drehratensensor*, standing for Rotation Rate Sensor. MM stands for *mikromechanisch*, or micromechanical.
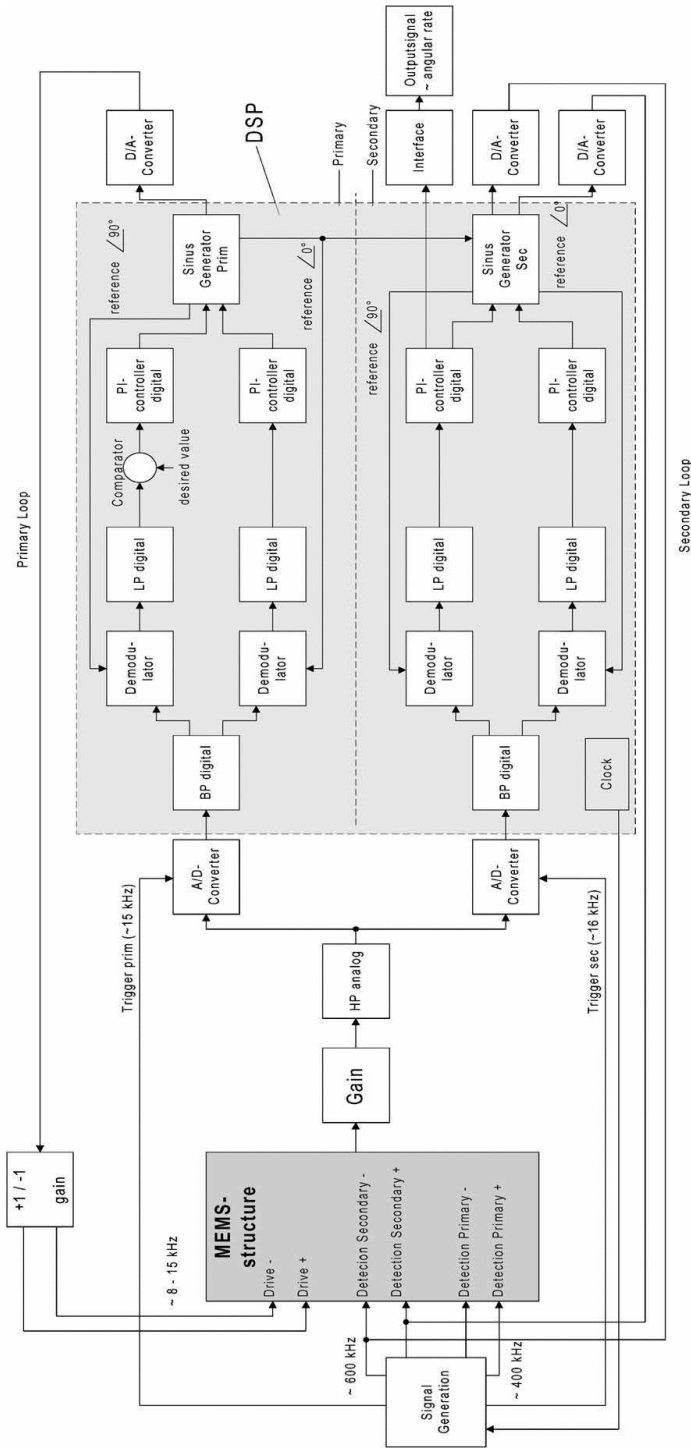
Figure 2.11 Block diagram of the gyroscope published by HSG-IMIT. (From [75], published in 2002.)

the sensitive axis is perpendicular to the substrate. Both excitation and detection are performed capacitively.

A block diagram of the readout and control electronics of the DRS-MM3 is shown in Fig. 2.12. No details of the individual circuit blocks have been published. Primary resonator excitation is performed using a PLL. The vibration amplitude of the primary resonator is controlled by an AGC. The secondary resonator readout is performed using an electromechanical $\Sigma\Delta$ loop. The C/V converter is implemented as an SC circuit. Both the offset and gain stability over temperature are improved by using a temperature sensor and correcting the angular velocity signal digitally on the basis of the temperature information. The output signal is read through an SPI (Serial Peripheral Interface) bus. Finally, there is an internal built-in test equipment (BITE) block for testing the unit.
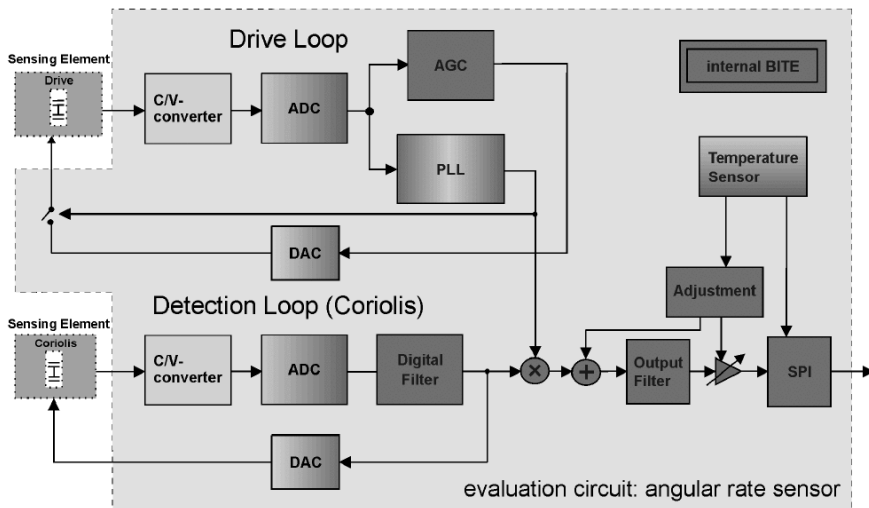
Figure 2.12 Block diagram of the DRS-MM3 gyroscope published by Robert Bosch GmbH. (From [9], published in 2007.)

2.5.5   Carnegie Mellon University

Carnegie Mellon University, Pittsburgh, PA, USA has reported several microgyroscope designs realized by post-processing dies manufactured with standard CMOS processes, with the first publications being from the year 1997 [80]. Figure 2.13 shows an overview of the surface micromachining process that was used. Using the metal layers as etching masks, first, an anisotropic RIE (Reactive Ion Etching) of SiO_2 is performed in order to form the microstructures. Then a silicon isotropic RIE is used to release the structures. The topmost metal layer is used to protect the circuitry from the etchants.

circuits   metal

SiO2 anisotropic RIE

silicon isotropic RIE
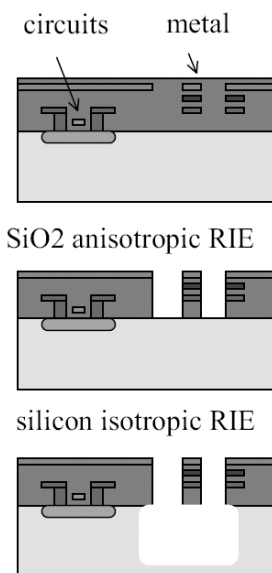
Figure 2.13 Post-CMOS surface micromachining process developed at Carnegie Mellon University. (From [49], published in 2003.)

The first z-axis gyroscope designs were reported in [80], with an improved version in [81]. The devices were manufactured by post-processing dies from a 3-metal, 0.5-μm CMOS process. Both the primary and the secondary modes of the design are lateral, with capacitive excitation and detection. Later, a 6-metal, 0.18-μm copper CMOS process was employed for a similar design in [82].

A lateral-axis gyroscope was reported in [83]. Like the z-axis counterpart, it was also manufactured starting from a 3-metal, 0.5-μm CMOS process. The primary resonator vibration is vertical, whereas the secondary vibration is lateral. The device employs capacitive excitation and detection.

A z-axis gyroscope with details of the readout and control electronics provided was published in [49]. Similar readout circuits were reported in the earlier publications, such as the one in [81]. The original dies were fabricated with a 0.6-μm CMOS process in this case. Primary resonator readout is performed with a unity-gain buffer. Secondary resonator readout is performed with a differential open-loop amplifier. The secondary signal is modulated into a higher frequency for detection and downconverted with an integrated SC demodulator.

2.5.6   Georgia Institute of Technology

A block diagram of the gyroscope published by Sharma et al. from the Georgia Institute of Technology, Atlanta, GA, USA [84–86] is shown in Fig. 2.14. The sensor

element is fabricated by micromachining an SOI substrate with a structural layer either 40 or 50 μm thick. The device is a z-axis gyroscope, with two lateral oscillation modes and capacitive excitation and detection. The electronics, which are realized with a 0.5-μm CMOS technology, are located on a separate chip and combined with the sensor element using wire bonding. Both primary and secondary detection are performed using transresistance amplifiers. Detection is performed at the mechanical resonance frequency, without modulating the signals to a higher carrier frequency. Primary resonator amplitude control is implemented by controlling the transresistance gain with an ALC (Automatic Level Control) circuit. The demodulation of the secondary signal is performed using CMOS Gilbert multipliers followed by low-pass filters (LPFs). All the reference frequencies are generated with an off-chip PLL. An automatic mode-matching algorithm for the system has been reported in [87].
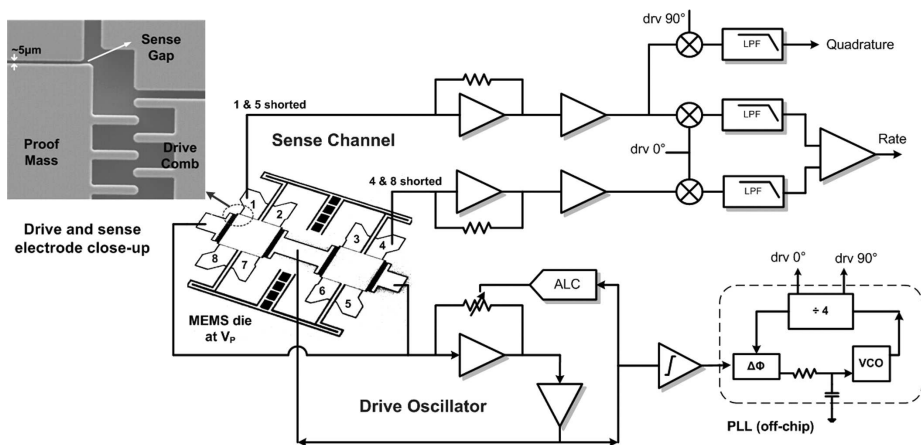
Figure 2.14 Block diagram of the gyroscope published by Georgia Institute of Technology. (From [86], published in 2007.)

2.5.7 Other Publications

In [88, 89], Zarabadi, Chang, et al. from Delphi-Delco Electronics Systems, Troy, MI, USA (formerly Delco Electronics Corporation, Kokomo, IN, USA) have published a z-axis angular rate sensor based on a vibrating ring gyroscope (VRG) manufactured by electroplating on a fully processed CMOS wafer. A VRG has two elliptically-shaped flexural vibration modes that are 45° apart from each other. Hence it differs from the implementations presented so far, as they all have two orthogonal linear or rotational vibration modes. However, the operation of the ring gyroscope is otherwise identical to the other gyroscopes, as the two 45°-separated elliptical vibration modes are ideally decoupled, with the Coriolis effect transferring energy between them when the system is subjected to angular velocity excitation.

The system is a two-chip implementation in that the sensor element, together with the front-end circuit, is located on one chip, whereas the rest of the electronics are located on another chip, which is then combined with the sensor element die to form a complete sensor module. The electronics on both chips are manufactured using a 1.2-μm CMOS technology. The system employs capacitive excitation and detection. Primary resonator excitation is performed using a PLL. The same PLL is used to generate clock signals for the synchronous demodulation of the secondary signal. A force feedback is employed to null the secondary movement.

In [90], Ayazi et al. from the University of Michigan, Ann Arbor (MI, USA), have published a z-axis microgyroscope manufactured using what they call a HARPSS (High Aspect-Ratio Combined Poly and Single-Crystal Silicon) MEMS technology [91]. This technology is a form of bulk micromachining. The sensor element is a VRG 80 μm thick with a diameter of 1.1 mm. Excitation and detection are both performed capacitively.

The integrated C/V front-end, which is implemented as a voltage buffer realized as a source follower, is located on a separate chip. The two chips are then connected using wire bonding. All the other circuitry is implemented with discrete components. Primary resonator excitation is performed using a PLL. An AGC keeps the primary resonator vibration amplitude constant. The same PLL also generates the clock signals for the synchronous demodulation of the secondary signal.

Witvrouw et al. from IMEC, Leuven, Belgium, together with other parties (ASM, Leuven, Belgium; IMSE-CNM, Seville, Spain; Philips, Böblingen, Germany; and Robert Bosch GmbH, Gerlingen-Schillerhöhe, Germany), have published a microgyroscope manufactured by poly-SiGe (Silicon-Germanium) surface micromachining on top of an IC manufactured with a standard CMOS process [50]. The device, which is constructed of a 10-μm thick poly-SiGe layer, is a capacitively excited and detected z-axis gyroscope, with lateral primary and secondary vibration modes. The readout electronics, which are manufactured with a 0.35-μm, 5-metal CMOS technology, are implemented as SC voltage amplifiers.

2.5.8   Summary and Discussion

In this section, several microgyroscopes realized with various technologies have been discussed. The implementations included designs from both academic research institutes and industrial manufacturers. A summary of the publications is presented in Table 2.2. The table indicates the year of publication, the direction of the primary and secondary modes, the direction of the sensitive axis, the excitation and the detection mechanisms, the primary and secondary resonator resonance frequencies, whether the device is bulk or surface micromachined (MM) (here, SOI and epi-poly technologies

are distinguished), whether it is a single- or a two-chip implementation, the noise in $°/s/\sqrt{Hz}$, and the bandwidth (BW) of each device. When a certain parameter is not available, the abbreviation n/a (not available) is used.

As can be seen from the table, the majority of the published devices have capacitive excitation and detection. Only one of the published devices is with magnetic excitation, and one device is with resonant output detection. The direction of primary and secondary modes varies in such a way that the z-axis gyroscopes have two lateral modes, while x- or x/y-directional gyroscopes have either a rotational primary mode about the z-axis and a rotational secondary mode(s) about the x- or x/y-axes, or they have a linear vertical primary mode in the z-direction and lateral secondary mode(s).

The majority of the published implementations are based on surface micromachining. Two devices use SOI technology, four epi-poly technology, and one combined surface and bulk micromachining. Only one device is manufactured using pure bulk micromachining.

Although they are mainly surface micromachined devices, there are both single- and two-chip implementations. Among the commercial gyroscopes, too, both varieties are available, as Analog Devices Inc. sells monolithic devices, while the devices offered by Robert Bosch GmbH are two-chip implementations.

The reported noise levels vary over more than four orders of magnitude. The lowest-noise device (noise floor equal to $0.00075°/s/\sqrt{Hz}$ or $2.7°/h/\sqrt{Hz}$) is that published by Sharma et al. from the Georgia Institute of Technology [86]. The low noise is achieved using a combination of very aggressive resonance gain, large bias voltages, and SOI technology, which makes possible the realization of large detection capacitances and low mechanical-thermal noise.

The devices with the second lowest noise (between 0.001 and $0.01°/s/\sqrt{Hz}$) are the two prototypes from HSG-IMIT with discrete readout electronics [74,75], together with the DRS-MM3 from Robert Bosch GmbH [79] and the prototype from Witvrouw et al. [50]. All these devices were realized using either SOI or epi-poly technology, or a thick poly-SiGe layer.

The worst noise performance (over $1°/s/\sqrt{Hz}$) is reported in [62–64]. The common factor in these devices is the use of electromechanical $\Sigma\Delta$ modulation. In [62,63], the increase in the quantization noise as a result of thermal noise [56] limits the performance. In [64], the low quality factor resulting from atmospheric-pressure operation [66] limits the performance, despite the use of higher-order modulation. Additionally, at least in [63], the small primary resonator vibration amplitude limits the achievable Coriolis signal level. The amplitude is small because the primary resonator is not driven at its resonance frequency but instead at the resonance frequency of the secondary resonator.

Finally, it should be noted that, while the noise and the bandwidth were the only

Table 2.2 Summary of the published MEMS angular velocity sensors.

Ref.	Year	Modes (pri./sec.)	Sens. axis	Exc./ det.	Pri./sec. res.freq. (kHz)	Bulk/ surface MM	1/2-chip	Noise ($°/s/\sqrt{Hz}$)	BW (Hz)	Note
[57]	1996	La/La	z	Ca/Ca	12/12.5	Surface	1	1	n/a	
[58]	1996	Ro/Ro	x/y	Ca/Ca	28.5/28.5	Surface	1	0.033	25	(1,2)
[61]	2002	La/La	z	Ca/Re	3.6/−	Surface	1	0.3	n/a	
[62]	2000	La/La	z	Ca/Ca	n/a	Surface	1	3	n/a	
[63]	2002	Ve/La	x/y	Ca/Ca	13.9/16.2	Surface	1	8.6	n/a	(1)
[64]	2004	Ro/Ro	x	Ca/Ca	n/a	Epi-poly	2	1	n/a	
[69]	2002	La/La	z	Ca/Ca	15/n/a	Surface	1	0.05	20	(3)
[74]	2002	La/La	z	Ca/Ca	n/a	SOI	n/a	0.0035	50	(4,5)
[74, 75]	2002	Ro/Ro	x	Ca/Ca	n/a	Epi-poly	n/a	0.0071	50	(5)
[77]	1997	La/La	z	Ma/Ca	$\approx 2/\approx 2$	Surf./bulk	2	n/a	n/a	
[78]	1999	Ro/Ro	x	Ca/Ca	1.6/2.25	Epi-poly	2	0.37	30	
[79]	2005	La/La	z	Ca/Ca	≈ 15/n/a	Epi-poly	2	0.004	60	
[49]	2003	La/La	z	Ca/Ca	12/n/a	Surface	1	0.5	n/a	
[86]	2007	La/La	z	Ca/Ca	15/15	SOI	2	0.00075	n/a	
[89]	1998	VRG	z	Ca/Ca	n/a	(See notes)	1/2	0.1	50	(6,7)
[90]	2001	VRG	z	Ca/Ca	28/28	Bulk	2	1	> 5	(2)
[50]	2005	La/La	z	Ca/Ca	12/n/a	Surface	1	0.0028	50	

La: Lateral, movement along the substrate
Ve: Vertical, movement perpendicular to the substrate
Ro: Rotational
VRG: Vibratory ring gyroscope
Ca: Capacitive (electrostatic)
Ma: Magnetic
Re: Resonant output
(1) Two-axis, two secondary modes
(2) With electrostatic mode tuning applied
(3) Typical BW 20 Hz, user-selectable to over 1 kHz
(4) Measured in vacuum chamber, not encapsulated
(5) Electronics assembled from discrete components
(6) Mechanical part manufactured by electroplating
(7) Mechanical part and C/V converters on single die, other circuitry on separate chip

performance parameters listed above, several other significant parameters are needed for describing the performance of a microgyroscope. These parameters include the ZRO and its stability, long-term bias stability, gain stability, sensitivity to vibration and to mechanical shocks, variation of different parameters from device to device, packaging etc. However, noise and bandwidth are the parameters which are most commonly reported in publications. In particular, one has to be very careful when comparing commercial devices with devices that have been manufactured for purely research purposes. This is because in a commercial device, several trade-offs have typically been made between the different parameters and also regarding the manufacturing costs, whereas in a research device, a single parameter such as noise could have been optimized and, at the same time, its negative effects on the other parameters disregarded.

2.6 Commercially Available Microgyroscopes

Several companies provide microgyroscopes as standard components. In this section, the basic parameters of the devices provided by the major manufactures will be presented. These manufacturers are (again, in no specific order): Analog Devices Inc. (ADI); Melexis; SensoNor (a part of Infineon Technologies AG); Robert Bosch GmbH (listed under the name Bosch); Systron Donner Inertial (a part of Schneider Electric); Silicon Sensing (a joint venture of BAE Systems and Sumitomo Precision Products, also known as Silicon Sensing Systems Japan in Japan); Epson Toyocom (formed by the quartz device operations division of Seiko Epson and Toyo Communications Equipment Co.); muRata; MEMSense, and InvenSense.

The following parameters will be given for each device: the direction of the sensitive axis; the full scale (FS) range; the noise (typically in $°/s/\sqrt{Hz}$; in some cases the root-mean-square (r.m.s.) noise is given); the bandwidth ($-3\,dB$ bandwidth unless otherwise noted); the ZRO drift; the type of output (analog/digital), and the supply voltage (V) and current (I)[7]. Depending on the manufacturer, the ZRO drift is either over the full-scale temperature range or over the entire lifetime of the device. When a certain parameter is not provided, the abbreviation n/a (not available) is used.

The product information is presented in Tables 2.3-2.6. The information was collected from the data sheets and other information publicly available on the web pages of the companies[8]. An exception is the data for the part number SMG070 from Robert Bosch GmbH, for which the data are taken from [92] as no data sheet was available from the manufacturer.

---

[7]In this thesis, the symbol I is also used to denote either the integrator controller or the in-phase component. If there is a possibility that the different meanings of I can be confused, the relevant meaning will be clearly stated in the text.

[8]The data were collected between July 5th and 6th, 2007. Updates made after this date have not been observed.

The devices from Systron Donner Inertial, Epson Toyocom, and muRata are manufactured using quartz micromachining. All the other devices employ silicon microstructures. As mentioned in the preceding section, the part number ADXRS150 of Analog Devices Inc. corresponds to the device published in [69, 70]. For the devices manufactured by Robert Bosch GmbH, the gyroscope in SGG020 corresponds to the DRS-MM1, the part numbers SMG040, SMG045, SMG060 and SMG061 correspond to the DRS-MM2, and the part number SMG070 corresponds to the DRS-MM3.

Manufacturer	ADI	ADI	ADI	ADI	ADI	ADI
Part code	ADXRS150	ADXRS300	ADXRS401	ADXRS610	ADXRS612	ADXRS614
Sensitive axis	z	z	z	z	z	z
FS range (°/s)	±150	±300	±75	±300	±250	±50
Noise (°/s/$\sqrt{\text{Hz}}$)	0.05	0.10	0.05	0.05	0.06	0.04
Bandwidth (Hz)	dc...2000 [1]	dc...2000 [1]	dc...2000 [1]	dc...2000 [1]	dc...2000 [1]	dc...2000 [1]
ZRO drift (°/s)	±24	±40	n/a	n/a	n/a	n/a
Output type	Analog	Analog	Analog	Analog	Analog	Analog
Supply V/I (V/mA)	5/6.0	5/6.0	5/6.0	5/3.5	5/3.5	5/3.5

Manufacturer	ADI	ADI	ADI	ADI	ADI	ADI
Part code	ADIS16080	ADIS16100	ADIS16120	ADIS16250	ADIS16255	ADIS16251
Sensitive axis	z	z	z	z	z	z
FS range (°/s)	±80	±300	±300	±80/160/320	±80/160/320	±20/40/80
Noise (°/s/$\sqrt{\text{Hz}}$)	0.05	0.05	0.015	0.056 [2]	0.056 [2]	0.056 [2]
Bandwidth (Hz)	dc...40 [1]	dc...40 [1]	dc...320 [1]	dc...50 [1]	dc...50 [1]	dc...49 [1]
ZRO drift (°/s)	±8.3	±10	±20	±1.9	±0.31	±1.9
Output type	Analog/digital	Analog/digital	Analog	Analog/digital	Analog/digital	Analog/digital
Supply V/I (V/mA)	5/7.0	5/7.0	5/95	5/18	5/18	5/18

Manufacturer	ADI	ADI	Melexis	Melexis	Melexis	SensoNor
Part code	ADIS16350 [3],[4]	ADIS16355 [3],[4]	MLX90609-N2	MLX90609-E2	MLX90609-R2	SAR10
Sensitive axis	x/y/z	x/y/z	z	z	z	n/a
FS range (°/s)	±75/150/300	±75/150/300	±75	±150	±300	±250
Noise (°/s/$\sqrt{\text{Hz}}$)	0.07 [2]	0.07	0.03	0.03	0.03	0.21 [5]
Bandwidth (Hz)	350	350	max 75 [1]	max 75 [1]	max 75 [1]	50
ZRO drift (°/s)	±6.25	±0.5	±3.75	±7.5	±15	n/a [6]
Output type	Digital	Digital	Analog/digital	Analog/digital	Analog/Digital	Digital
Supply V/I (V/mA)	5/33	5/33	5/n/a	5/n/a	5/n/a	5/17

1) User-selectable
2) Specified for the maximum FS range version
3) Preliminary datasheet
4) Three-axis gyroscope & accelerometer module
5) R.m.s. noise specified, divided by square root of bandwidth
6) Output is high-pass filtered

Table 2.3 Commercially available microgyroscopes (1/4)

Table 2.4 Commercially available microgyroscopes (2/4)

Manufacturer	Bosch	Bosch	Bosch	Bosch	Bosch
Part code	SGG020 [7]	SMG040	SMG045 [8]	SMG060	SMG061
Sensitive axis	z	x	x	x	x
FS range ($^\circ$/s)	±100	±250	±75	±240	±240
Noise ($^\circ$/s/$\sqrt{\text{Hz}}$)	0.091 [5]	0.38 [5]	0.13 [5]	0.27 [5]	0.27 [5]
Bandwidth (Hz)	30	27	9	30	30
ZRO drift ($^\circ$/s)	±4	n/a	n/a	n/a	n/a
Output type	Analog	Analog	Analog	Digital	Analog
Supply V/I (V/mA)	12/ < 100	4.8/ < 30	n/a/n/a	5/10	5/ < 20

Manufacturer	Bosch	Systron Donner	Systron Donner	Systron Donner	Systron Donner
Part code	SMG070	QRS11 [9]	QRS100 [9]	QRS14-0XXXX-102	QRS14-0XXXX-103
Sensitive axis	z	x	x	x	x
FS range ($^\circ$/s)	±187	±100	±100	$\pm50/100/200/500$	$\pm50/100/200/500$
Noise ($^\circ$/s/$\sqrt{\text{Hz}}$)	0.0065 [5]	0.01	0.0035	0.05 [11]	0.02 [11]
Bandwidth (Hz)	60	60 [10]	60 [10]	50 [10]	50 [10]
ZRO drift ($^\circ$/s)	±1.5	±0.35	±0.35	±3	±3
Output type	Digital	Analog	Analog	Analog	Analog
Supply V/I (V/mA)	n/a/n/a	±5/ < 80	±5/ < 80	$\pm9\dots18$/ < 20	$\pm9\dots18$/25

Manufacturer	Systron Donner	Systron Donner	Systron Donner	Systron Donner	Systron Donner
Part code	HZ1-100-100	HZ1-90-100A	LCG50-00100-100	LCG50-00250-100	LCG50-00500-100
Sensitive axis	x	x	x	x	x
FS range ($^\circ$/s)	±100	±90	±100	±250	±500
Noise ($^\circ$/s/$\sqrt{\text{Hz}}$)	0.025	0.025	0.005	0.006	0.01
Bandwidth (Hz)	60 [10]	18 [10]	50	50	50
ZRO drift ($^\circ$/s)	±4.5	±4.5	±8	±10	±20
Output type	Analog	Analog	Analog	Analog	Analog
Supply V/I (V/mA)	$8\dots15$/ < 20	$8\dots15$/ < 20	5/ < 8	5/ < 8	5/ < 8

[7] Single-axis gyroscope & accelerometer module, data from preliminary target specification (dated 07.05.97)
[8] Partial information, no full datasheet available
[9] Low/high-performance variants available, high-performance version listed in the table
[10] Specified as the point where phase shift equals 90°
[11] $\pm100^\circ$/s version

Manufacturer	Silicon Sensing	Silicon Sensing	Silicon Sensing	Silicon Sensing	Silicon Sensing	Silicon Sensing
Part code	CRS03-01S/02S	CRS03-04S	CRS03-05S	CRS03-11S	CRS05-01	CRS05-02
Sensitive axis	z	z	z	z	z	z
FS range (°/s)	±100	±200	±80	±573	±50	±200
Noise (°/s/$\sqrt{Hz}$)	0.016 [5]	0.032 [5]	0.013 [5]	0.039 [5]	< 2.13°/s r.m.s.	< 0.40°/s r.m.s.
Bandwidth (Hz)	10	10	10	55	80 [10]	30 [10]
ZRO drift (°/s)	±3	±6	±4	±30	±3	±3
Output type	Analog	Analog	Analog	Analog	Analog	Analog
Supply V/I (V/mA)	5/ < 35	5/ < 35	5/ < 35	5/ < 35	5/ < 35	5/ < 35

Manufacturer	Silicon Sensing	Silicon Sensing	Silicon Sensing	Silicon Sensing	Silicon Sensing	Silicon Sensing
Part code	CRS05-75	CRS07-02S	CRS07-11S	CRS07-13S	CRS10 [12]	SiRRS01-01
Sensitive axis	z	z	z	z	z	z
FS range (°/s)	±75	±100	±573	±100	±300	±110 [13]
Noise (°/s/$\sqrt{Hz}$)	< 0.30°/s r.m.s.	0.016 [5]	0.052 [5]	0.016 [5]	0.12 [5]	< 0.35°/s r.m.s.
Bandwidth (Hz)	40 [10]	10	30	10	75	50 [10]
ZRO drift (°/s)	±3	±3	±30	±3	±2	±3
Output type	Analog	Analog	Analog	Analog	Digital	Analog
Supply V/I (V/mA)	5/ < 35	5/ < 35	5/ < 35	5/ < 35	5/ < 60	5/ < 50

Table 2.5 Commercially available microgyroscopes (3/4)

12) Device has both analog and digital outputs, values for digital output
13) Also available with ranges ±50/200/300/1500

Table 2.6 Commercially available microgyroscopes (4/4)

Manufacturer	Epson Toyocom	Epson Toyocom	muRata	muRata	muRata	muRata
Part code	XV-8100CB [8]	XV-3500CB	ENC-03J	ENC-03M	ENC-03R	MEV-50A-R
Sensitive axis	n/a	z	n/a	n/a	n/a	n/a
FS range (°/s)	n/a	±100	±300	±300	±300	±70
Noise (°/s/$\sqrt{Hz}$)	n/a	6.0°/s r.m.s. [14]	n/a	n/a	0.84 [14]	0.08°/s r.m.s. [15]
Bandwidth (Hz)	n/a	200 [10]	50	50	50	n/a
ZRO drift (°/s)	n/a	±75	n/a	n/a	n/a	6
Output type	n/a	Analog	Analog	Analog	Analog	Analog
Supply V/I (V/mA)	n/a/n/a	3/1.7	2.7…5.5/5	2.7…5.25/5	2.7…5.25/1.6	5/8

Manufacturer	MEMSense	MEMSense	MEMSense	InvenSense	InvenSense	InvenSense
Part code	TR0150S050	TR0300S050	TR1200S050	IDG-300 [3]	IDG-1000 [8]	IDG-1004 [3]
Sensitive axis	x/y/z	x/y/z	x/y/z	x/y	x/y	x/y
FS range (°/s)	±150	±300	±1200	±500	±30	±50
Noise (°/s/$\sqrt{Hz}$)	0.05	0.1	0.1	0.014	n/a	0.014
Bandwidth (Hz)	50	50	50	140	n/a	140
ZRO drift (°/s)	n/a	n/a	n/a	±150	n/a	±150
Output type	Analog	Analog	Analog	Analog	Analog	Analog
Supply V/I (V/mA)	5/18	5/18	5/18	3/ < 9.5	3/8.5	3/ < 9.5

Chapter 3

Synchronous Demodulation

In the previous chapter, the fundamental operation of a vibratory gyroscope was described. However, in order to produce the final angular velocity signal, the Coriolis movement needs to be converted into an electrical quantity, typically a voltage, and thereafter demodulated to get the desired output signal $\Omega_z(t)$. In Section 2.3, how the displacement can be converted into various measurable electrical quantities, such as capacitance or resistance, was described. Chapter 7 will describe different circuit implementations to convert a capacitively encoded position information into voltage.

In this chapter, issues related to the subsequent demodulation will be studied. A block diagram of the system formed by the secondary resonator with the transfer function $H_{y/F}(s)$, a displacement-to-voltage converter with the transfer function $H_{V/y}(s)$, and the synchronous demodulation is shown in Fig. 3.1. Additionally, there is a summation of the error signals, which will be discussed shortly in more detail. The error signals are assumed to be located at ω_{0x}, that is, they are sources of offset error in the final angular velocity output. The force $F_{y,all}$ fed into the secondary resonator contains all the exciting forces, including the Coriolis force.

For the purpose of this analysis, the displacement-to-voltage conversion is modeled with the transfer function $H_{V/y}(s)$. When evaluated at the operating frequency ω_{0x}, this leads to a gain $G_{V/y}$ and a phase shift θ. It will be assumed that the gain and the delay of the transfer function $H_{V/y}(s)$ stay constant over the band of interest, i.e. that both sidebands of the sinusoidally varying angular velocity signal experience the same gain and delay in the displacement-to-voltage conversion.

As can be seen from Fig. 3.1, the analysis presented in this chapter assumes that all the error signals are added into the y-directional movement of the secondary resonator. In reality, the error signals are included either in the force $F_{y,all}$, or they are added into the voltage signal after the displacement-to-voltage conversion. Reducing all the error signals into the mechanical movements $y_{error,I}$ and $y_{error,Q}$ is justified for now, as
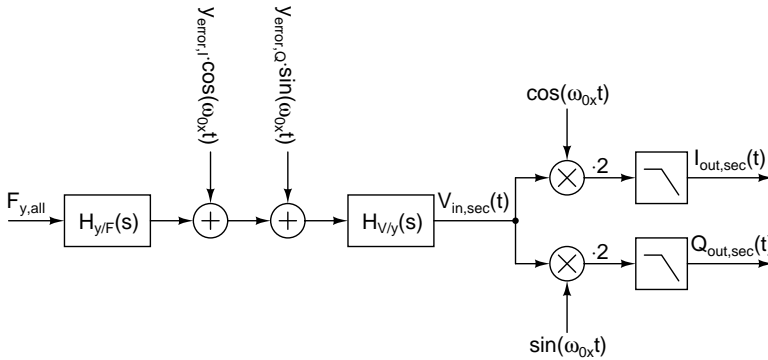
Figure 3.1 A block diagram of the secondary resonator, summation of error signals, displacement-to-voltage conversion, and the synchronous demodulation to in-phase and quadrature components.

it simplifies the following equations significantly without compromising the accuracy of the analysis. If necessary, the possible phase shifts that the signals experience in the secondary resonator, in the displacement-to-voltage conversion, or in both, can be accounted for when the signals are divided into the in-phase and the quadrature components $y_{error,I}$ and $y_{error,Q}$. A more detailed analysis of the error signals will be presented later in Chapter 6.

In this chapter, it is assumed for the sake of simplicity that the multiplying signals used in the demodulation are $\cos(\omega_{0x}t)$ and $\sin(\omega_{0x}t)$. Because these signals are typically derived from the primary resonator movement, their phase shift needs to be taken into account as well. If such is the case, this phase shift can be included into θ. Then θ represents the total phase error in the synchronous demodulation resulting from the electronics.

The target of this chapter is to provide a detailed analysis of how various non-idealities represent themselves after the demodulation. The contribution is the following. First, the demodulation is analyzed in an ideal case, in which the force-to-displacement conversion $H_{y/F}(s)$ can be modeled as a constant gain with zero phase shift, and the phase shift θ of the displacement-to-voltage conversion is equal to zero. Next, the effects of the delay in the displacement-to-voltage conversion will be analyzed. Thereafter, how the possibly nonequal gain and phase shift of the two sidebands of the amplitude-modulated Coriolis signal in the force-to-displacement conversion occurring in the secondary resonator affect the system output will be considered. Next, the effect of nonlinearities in the displacement-to-voltage conversion will be studied. Then the behavior of the mechanical-thermal noise introduced in Section 2.2 will be analyzed, and the power spectral density of the noise force will be reduced to the angular velocity input. Finally, the chapter is concluded by briefly listing the effects of temperature variation on gain stability, a subject that is related to the downconversion.

3.1   Demodulation in Ideal Case

First, the synchronous demodulation will be considered in an ideal case. It is assumed that the Coriolis force (2.33) goes through a force-to-displacement conversion which has an equal gain and zero phase shift for both sidebands. This corresponds to the low-pass mode operation, where resonance gain is not utilized. Based on Eqs. (2.33) and (2.26), the resulting Coriolis movement can be written as

$$y(t) = -\frac{A_x \omega_{0x} m_x \Omega_z}{\omega_{0y}^2 m_y} \cdot \left[\cos\left((\omega_{0x} - \omega_\Omega)t - \varphi\right) + \cos\left((\omega_{0x} + \omega_\Omega)t + \varphi\right) \right]. \quad (3.1)$$

Next, the displacement is converted to voltage. Again, in an ideal case, the phase shift θ is assumed to be equal to zero. The resulting output voltage and the input voltage to the subsequent demodulator is then

$$V_{in,sec}(t) = -\frac{G_{V/y} A_x \omega_{0x} m_x \Omega_z}{\omega_{0y}^2 m_y} \cdot$$
$$\left[\cos\left((\omega_{0x} - \omega_\Omega)t - \varphi\right) + \cos\left((\omega_{0x} + \omega_\Omega)t + \varphi\right) \right]. \quad (3.2)$$

To simplify the equations, the gain from the angular velocity input to the output voltage will be denoted by $G_{V/\Omega}$, so that

$$G_{V/\Omega} = -\frac{2G_{V/y} A_x \omega_{0x} m_x}{\omega_{0y}^2 m_y}. \quad (3.3)$$

Different error signals caused by non-idealities are added to the ideal output voltage of Eq. (3.2), as described before. The total error signal after the displacement-to-voltage conversion can be written as

$$V_{error,sec}(t) = V_{error,I} \cdot \cos(\omega_{0x}t) + V_{error,Q} \cdot \sin(\omega_{0x}t), \quad (3.4)$$

where $V_{error,I} = G_{V/y} \cdot y_{error,I}$ and $V_{error,Q} = G_{V/y} \cdot y_{error,Q}$. The error signal has been divided into two components, one in phase (I)[1] with the Coriolis signal, another in quadrature (Q) with it, as shown in Fig. 3.1. By combining Eqs. (3.2) and (3.4), the resulting voltage is then

$$V_{in,sec}(t) = \frac{G_{V/\Omega} \Omega_z}{2} \cdot \left[\cos\left((\omega_{0x} - \omega_\Omega)t - \varphi\right) + \cos\left((\omega_{0x} + \omega_\Omega)t + \varphi\right) \right] +$$
$$V_{error,I} \cdot \cos(\omega_{0x}t) + V_{error,Q} \cdot \sin(\omega_{0x}t). \quad (3.5)$$

---

[1]In this thesis, the symbol I is also used to denote either the integrator controller or the current. If there is a possibility that the different meanings of I can be confused, the relevant meaning will be clearly stated in the text.

Now, the signal is brought to an ideal synchronous demodulator. It multiplies the signal by $\cos(\omega_{0x}t)$ and $\sin(\omega_{0x}t)$, which yield the in-phase and the quadrature components, respectively. After multiplication, there is a gain of two and an ideal low-pass filter to remove the multiplication results at and around $2\omega_{0x}$. The in-phase and the quadrature components of the demodulator output can be written as

$$I_{out,sec}(t) = G_{V/\Omega}\Omega_z \cdot \cos(\omega_\Omega t + \varphi) + V_{error,I} \tag{3.6a}$$

and

$$Q_{out,sec}(t) = V_{error,Q}, \tag{3.6b}$$

respectively. From the result, it can be seen that the in-phase component now carries the Coriolis signal, that is, the angular velocity information, plus any error signals that are in phase with the Coriolis signal. The quadrature component, on the other hand, carries any error signals that are in quadrature compared to the Coriolis signal.

3.2 Delay in Displacement-to-Voltage Conversion

The first non-ideality affecting the synchronous demodulation which will be introduced is the delay in the displacement-to-voltage conversion. Assuming that the phase shift $\theta(\Delta\omega)$ can be approximated around the operating frequency ω_{0x}, as a function of the frequency offset $\Delta\omega$ from the operating frequency, as

$$\theta(\Delta\omega) = \theta - T_d\Delta\omega, \tag{3.7}$$

representing a constant time delay, then the resulting demodulator input voltage, which was given in Eq. (3.5) for the ideal case, can be rewritten as

$$\begin{aligned} V_{in,sec}(t) = &\frac{G_{V/\Omega}\Omega_z}{2} \cdot \Big[\cos((\omega_{0x} - \omega_\Omega)t - \varphi + \theta + T_d\omega_\Omega) + \\ &\cos((\omega_{0x} + \omega_\Omega)t + \varphi + \theta - T_d\omega_\Omega) \Big] + \\ &V_{error,I} \cdot \cos(\omega_{0x}t + \theta) + V_{error,Q} \cdot \sin(\omega_{0x}t + \theta). \end{aligned} \tag{3.8}$$

Equation (3.8) shows that also the error signals $V_{error,I}$ and $V_{error,Q}$ experience the phase shift θ, as expected.

When the signal is now synchronously demodulated as described in the previous section, the resulting in-phase and quadrature components are

$$\begin{aligned} I_{out,sec}(t) &= \big[G_{V/\Omega}\Omega_z \cdot \cos(\omega_\Omega t + \varphi - T_d\omega_\Omega) + V_{error,I} \big] \cdot \cos\theta + V_{error,Q} \cdot \sin\theta \\ &= \big[G_{V/\Omega}\Omega_z \cdot \cos(\omega_\Omega(t - T_d) + \varphi) + V_{error,I} \big] \cdot \cos\theta + V_{error,Q} \cdot \sin\theta \end{aligned} \tag{3.9a}$$

and

$$
\begin{aligned}
Q_{out,sec}(t) &= V_{error,Q} \cdot \cos\theta - \left[G_{V/\Omega}\Omega_z \cdot \cos\left(\omega_\Omega t + \varphi - T_d\omega_\Omega\right) + V_{error,I} \right] \cdot \sin\theta \\
&= V_{error,Q} \cdot \cos\theta - \left[G_{V/\Omega}\Omega_z \cdot \cos\left(\omega_\Omega\left(t - T_d\right) + \varphi\right) + V_{error,I} \right] \cdot \sin\theta.
\end{aligned}
\tag{3.9b}
$$

The delay has three results. First, the ideal output signals are attenuated by $\cos\theta$. Second, the signal from the quadrature component of the ideal demodulator output leaks to the in-phase component, attenuated by $\sin\theta$. Likewise, the signal from the in-phase component of the ideal output leaks to the quadrature component, with the same attenuation but an opposite sign. Third, the Coriolis signal experiences a delay equal to T_d, which is the slope of the phase shift caused by the displacement-to-voltage conversion with respect to the varying frequency offset $\Delta\omega$, as defined in (3.7).

3.3   Secondary Resonator Transfer Function

So far, it has been assumed that both sidebands of the sinusoidal Coriolis force have an identical transfer function with zero phase shift through the secondary resonator. However, when the resonance gain is utilized to amplify the Coriolis signal, as described in Section 2.1.5, then both the magnitude and the phase shift of the transfer functions of the two sidebands will exhibit frequency dependency [93].

To analyze this effect in more detail, the gain $G_{V/\Omega}$ defined in Eq. (3.3) is divided into two components, $G_{y/\Omega}$ denoting the gain from angular velocity to secondary resonator displacement and $G_{V/y}$ denoting the gain from displacement to voltage as already defined. The term $G_{y/\Omega}$ comprises the gain from angular velocity to the Coriolis force, and from force to displacement. To take the difference of the gain $G_{y/\Omega}$ in the two sidebands into account, the lower sideband (LSB)[2] gain is denoted by $G_{y/\Omega,LSB}$ and the upper sideband (USB) gain by $G_{y/\Omega,USB}$. Taking Eq. (3.3) and replacing the dc force-to-displacement transfer function $1/(\omega_{0y}^2 m_y)$ with the complete amplitude transfer function given in Eq. (2.7a), then

$$
G_{y/\Omega,LSB} = -\frac{2A_x\omega_{0x}m_x}{m_y\sqrt{\left[\omega_{0y}^2 - (\omega_{0x} - \omega_\Omega)^2\right]^2 + \omega_{0y}^2(\omega_{0x} - \omega_\Omega)^2/Q_y^2}}
\tag{3.10a}
$$

and

$$
G_{y/\Omega,USB} = -\frac{2A_x\omega_{0x}m_x}{m_y\sqrt{\left[\omega_{0y}^2 - (\omega_{0x} + \omega_\Omega)^2\right]^2 + \omega_{0y}^2(\omega_{0x} + \omega_\Omega)^2/Q_y^2}}.
\tag{3.10b}
$$

---

[2]In this thesis, the abbreviation LSB is also used to stand for Least-Significant Bit. If there is a possibility that the two meanings of LSB can be confused, the unabbreviated forms are used instead.

Similarly, the phase shift experienced by the lower sideband in the force-to-displacement conversion is denoted by ϕ_{LSB} and that of the upper sideband by ϕ_{USB}. On the basis of Eq. (2.7b), they can be written as

$$\phi_{LSB} = -\arctan\frac{\omega_{0y}\left(\omega_{0x} - \omega_\Omega\right)}{\left[\omega_{0y}^2 - \left(\omega_{0x} - \omega_\Omega\right)^2\right]Q_y} \tag{3.11a}$$

and

$$\phi_{USB} = -\arctan\frac{\omega_{0y}\left(\omega_{0x} + \omega_\Omega\right)}{\left[\omega_{0y}^2 - \left(\omega_{0x} + \omega_\Omega\right)^2\right]Q_y}. \tag{3.11b}$$

In the equations, ω_Ω has been used to denote the frequency of the angular velocity signal, as defined in Section 2.1.6.

To make the following expressions more readable, the sums and differences of the gains and phase shifts will be written as

$$\overline{G_{y/\Omega}} = \frac{G_{y/\Omega,USB} + G_{y/\Omega,LSB}}{2}, \tag{3.12a}$$

$$\Delta G_{y/\Omega} = \frac{G_{y/\Omega,USB} - G_{y/\Omega,LSB}}{2}, \tag{3.12b}$$

$$\overline{\phi} = \frac{\phi_{USB} + \phi_{LSB}}{2}, \tag{3.12c}$$

and

$$\Delta\phi = \frac{\phi_{USB} - \phi_{LSB}}{2}. \tag{3.12d}$$

With these symbols, the demodulator input voltage can now be written as

$$\begin{aligned}
V_{in,sec}\left(t\right) =\ & \frac{G_{V/y}G_{y/\Omega,LSB}\Omega_z}{2}\cdot\cos\left(\left(\omega_{0x} - \omega_\Omega\right)t - \varphi + \phi_{LSB} + \theta + T_d\omega_\Omega\right) + \\
& \frac{G_{V/y}G_{y/\Omega,USB}\Omega_z}{2}\cdot\cos\left(\left(\omega_{0x} + \omega_\Omega\right)t + \varphi + \phi_{USB} + \theta - T_d\omega_\Omega\right) + \\
& V_{error,I}\cdot\cos\left(\omega_{0x}t + \theta\right) + V_{error,Q}\cdot\sin\left(\omega_{0x}t + \theta\right),
\end{aligned} \tag{3.13}$$

where the phase shift of the displacement-to-voltage conversion defined in Eq. (3.7) is also included. Next, the voltage is synchronously demodulated. The in-phase component of the output can be written as

$$\begin{aligned}
I_{out,sec}\left(t\right) =\ & G_{V/y}\overline{G_{y/\Omega}}\Omega_z\cdot\cos\left(\overline{\phi} + \theta\right)\cdot\cos\left(\omega_\Omega t + \varphi + \Delta\phi - T_d\omega_\Omega\right) - \\
& G_{V/y}\Delta G_{y/\Omega}\Omega_z\cdot\sin\left(\overline{\phi} + \theta\right)\cdot\sin\left(\omega_\Omega t + \varphi + \Delta\phi - T_d\omega_\Omega\right) + \\
& V_{error,I}\cdot\cos\left(\theta\right) + V_{error,Q}\cdot\sin\left(\theta\right) \\
=\ & G_{V/y}G_{y/\Omega,I}\Omega_z\cdot\cos\left(\omega_\Omega\left(t - T_d\right) + \varphi + \xi_I\right) + \\
& V_{error,I}\cdot\cos\left(\theta\right) + V_{error,Q}\cdot\sin\left(\theta\right),
\end{aligned} \tag{3.14a}$$

where

$$G_{y/\Omega,I} = \sqrt{\overline{G_{y/\Omega}}^2 \cdot \cos^2\left(\overline{\phi}+\theta\right) + \Delta G_{y/\Omega}^2 \cdot \sin^2\left(\overline{\phi}+\theta\right)} \qquad (3.14b)$$

and

$$\xi_I = \Delta\phi + \arctan\left[\frac{\Delta G_{y/\Omega}}{\overline{G_{y/\Omega}}} \cdot \tan\left(\overline{\phi}+\theta\right)\right]. \qquad (3.14c)$$

Similarly, the quadrature component can be written as

$$Q_{out,sec}\left(t\right) = -G_{V/y}\overline{G_{y/\Omega}}\Omega_z \cdot \sin\left(\overline{\phi}+\theta\right) \cdot \cos\left(\omega_\Omega t + \phi + \Delta\phi - T_d\omega_\Omega\right) -$$
$$G_{V/y}\Delta G_{y/\Omega}\Omega_z \cdot \cos\left(\overline{\phi}+\theta\right) \cdot \sin\left(\omega_\Omega t + \phi + \Delta\phi - T_d\omega_\Omega\right) +$$
$$V_{error,Q} \cdot \cos\left(\theta\right) - V_{error,I} \cdot \sin\left(\theta\right) \qquad (3.15a)$$
$$= G_{V/y}G_{y/\Omega,Q}\Omega_z \cdot \cos\left(\omega_\Omega\left(t - T_d\right) + \phi + \xi_I\right) +$$
$$V_{error,Q} \cdot \cos\left(\theta\right) - V_{error,I} \cdot \sin\left(\theta\right),$$

where

$$G_{y/\Omega,Q} = \sqrt{\overline{G_{y/\Omega}}^2 \cdot \sin^2\left(\overline{\phi}+\theta\right) + \Delta G_{y/\Omega}^2 \cdot \cos^2\left(\overline{\phi}+\theta\right)} \qquad (3.15b)$$

and

$$\xi_Q = \Delta\phi - \arctan\left[\frac{\Delta G_{y/\Omega}}{\overline{G_{y/\Omega}}} \cdot \csc\left(\overline{\phi}+\theta\right)\right]. \qquad (3.15c)$$

From Eqs. (3.14a) and (3.15a) it can be seen that the two error signals $V_{error,I} \cdot \cos(\omega_{0x}t + \theta)$ and $V_{error,Q} \cdot \sin(\omega_{0x}t + \theta)$ behave as earlier. On the other hand, both the gain and the phase shift of the Coriolis signal to the in-phase and the quadrature components of the demodulator output become dependent on the frequency $f_\Omega = \omega_\Omega/(2\pi)$ of the angular velocity input.

The effect is most easily demonstrated graphically. Figures 3.2-3.5 show the behavior of the system in two cases. In both cases, the phase shift θ caused by the secondary resonator readout is assumed to be zero. In the first case, shown in Figs. 3.2 and 3.3, a moderate resonance gain with $\kappa = 1.25$ and $Q_y = 500$ is used. This leads to a gain of 2.8, as defined by Eq. (2.28). Figure 3.2 shows the transfer function (gain and phase) of the Coriolis signal to the in-phase component of the demodulator output. The gain values are normalized with respect to the nominal gain at $f_\Omega = 0$ (that is, they are divided by 2.8). It can be seen that the gain increases slightly over the bandwidth, while the phase delay increases, causing an additional delay from the angular velocity input to the demodulator output. In this case, the delay, which is defined as the derivative of the phase shift with respect to the frequency, is roughly $0.6\,\mu$s.

Figure 3.3 shows the transfer function (gain and phase) of the Coriolis signal to the quadrature component of the demodulator output. The gain values are normalized as above. At $f_\Omega = 0$, the leakage is caused by the phase shift of the secondary resonator
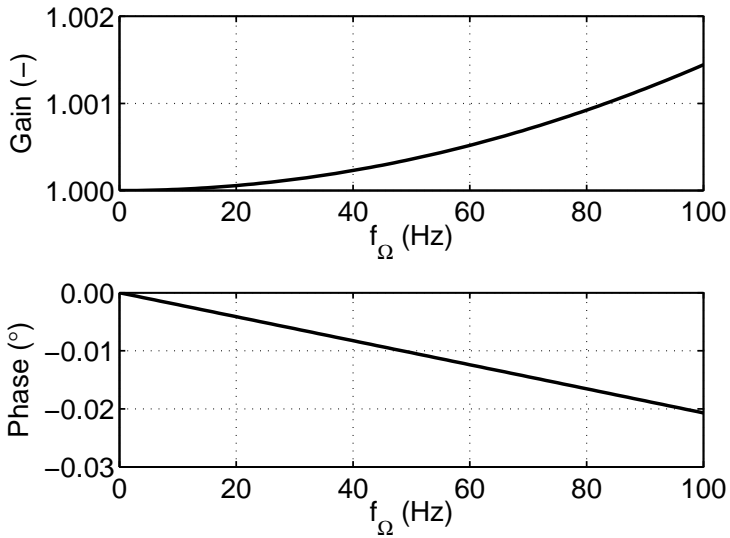
Figure 3.2 Transfer function (gain and phase) of the Coriolis signal to the in-phase component of the demodulator output. ($f_{0x} = 10\,\text{kHz}$, $f_{0y} = 12.5\,\text{kHz}$, $Q_y = 500$)
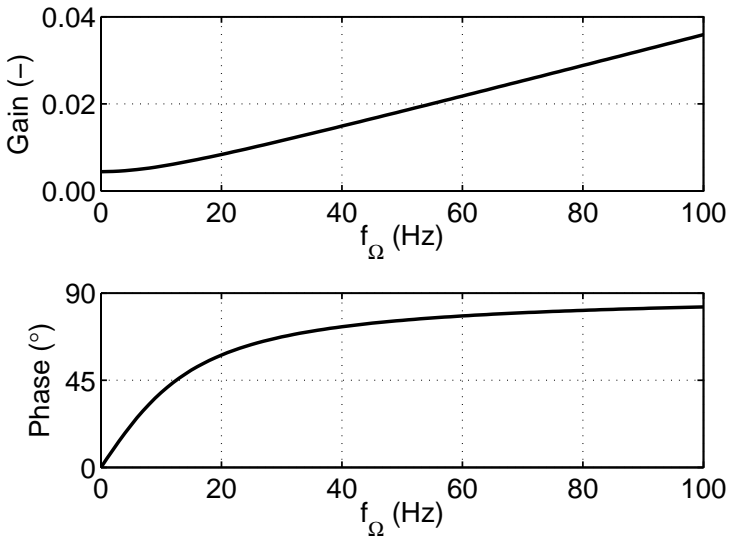
Figure 3.3 Transfer function (gain and phase) of the Coriolis signal to the quadrature component of the demodulator output. ($f_{0x} = 10\,\text{kHz}$, $f_{0y} = 12.5\,\text{kHz}$, $Q_y = 500$)
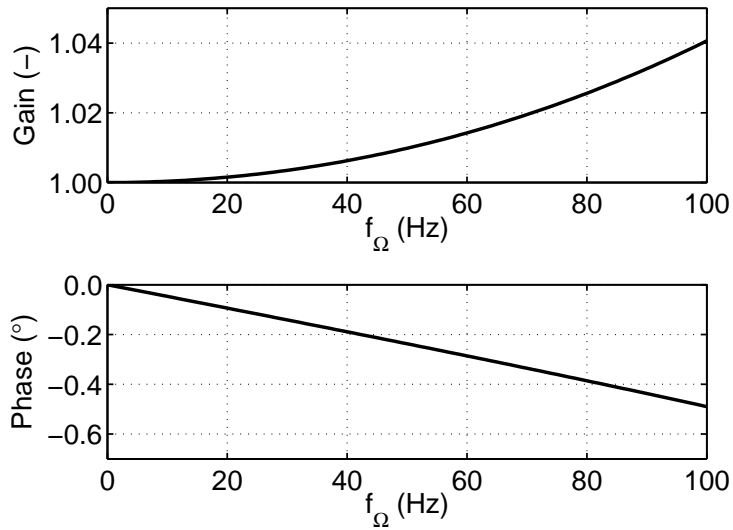
Figure 3.4 Transfer function (gain and phase) of the Coriolis signal to the in-phase component of the demodulator output. ($f_{0x} = 10\,\text{kHz}$, $f_{0y} = 10.5\,\text{kHz}$, $Q_y = 500$)
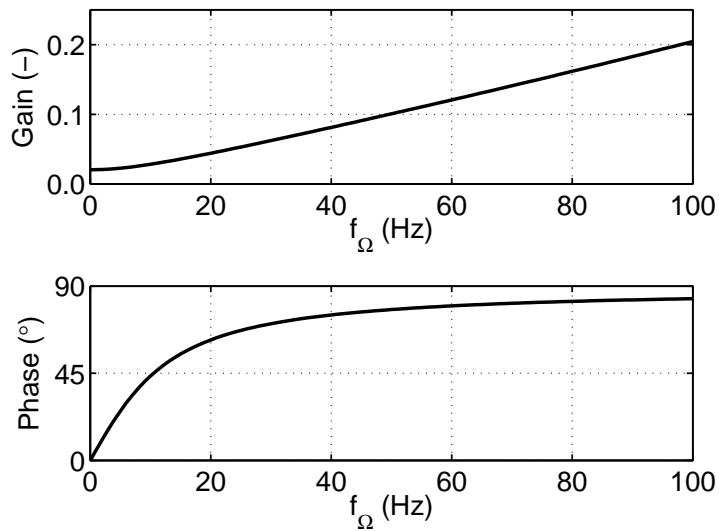
Figure 3.5 Transfer function (gain and phase) of the Coriolis signal to the quadrature component of the demodulator output. ($f_{0x} = 10\,\text{kHz}$, $f_{0y} = 10.5\,\text{kHz}$, $Q_y = 500$)

at the operating frequency (approximately $0.25°$ as evaluated from Eq. (2.7b)). As f_Ω increases, the leakage starts growing. At the same time, the phase shift changes from 0 to $+90°$.

In general, if both sidebands of the Coriolis force stay below the resonance frequency ω_{0y} of the secondary resonator, then the gain of the Coriolis signal to both the in-phase and the quadrature components of the demodulator output increases as a function of f_Ω. With a dc angular velocity input ($f_\Omega = 0$), the outputs are identical to Eqs. (3.9a) and (3.9b), except for the additional phase shift $\overline{\phi} = \phi$ caused by the secondary resonator. This is as expected, as then the two sidebands merge into a single frequency component.

In the second case, shown in Figs. 3.4 and 3.5, a more aggressive resonance gain with $\kappa = 1.05$ and $Q_y = 500$ is used. This leads to a gain of 10.8 at $f_\Omega = 0$. It can be seen that the effects shown in Figs. 3.4 and 3.5 are identical to the previous case, only more pronounced. Now the additional delay caused by the phase shift is roughly $14\,\mu s$.

Figures 3.6 and 3.7 show the phenomenon in the time domain. A step angular velocity input of $100°/s$ is fed to the system at $t = 100\,ms$. The resulting signal is synchronously demodulated to the in-phase and quadrature components, and the outputs are filtered using sixth-order Bessel filters with their cut-off frequencies at $100\,Hz$.
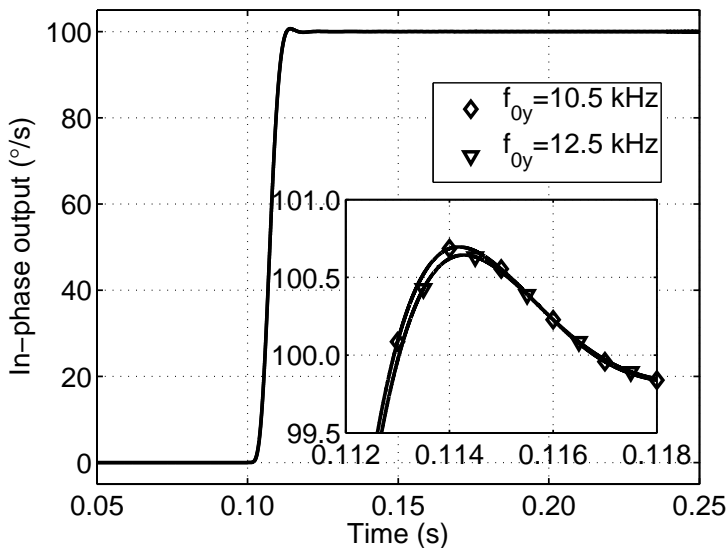
Figure 3.6 In-phase outputs resulting from a step angular velocity input of $100°/s$, with the inset showing a detail of the overshoot. ($f_{0x} = 10\,kHz$, $f_{0y} = 10.5\,kHz$ or $12.5\,kHz$, $Q_y = 500$)

Figure 3.6 shows the resulting in-phase output for the two cases described above. The inset shows a detail of the signal. The overshoot is mostly caused by the Bessel filter, as its simulated overshoot is approximately 0.6%. There is only a slight difference
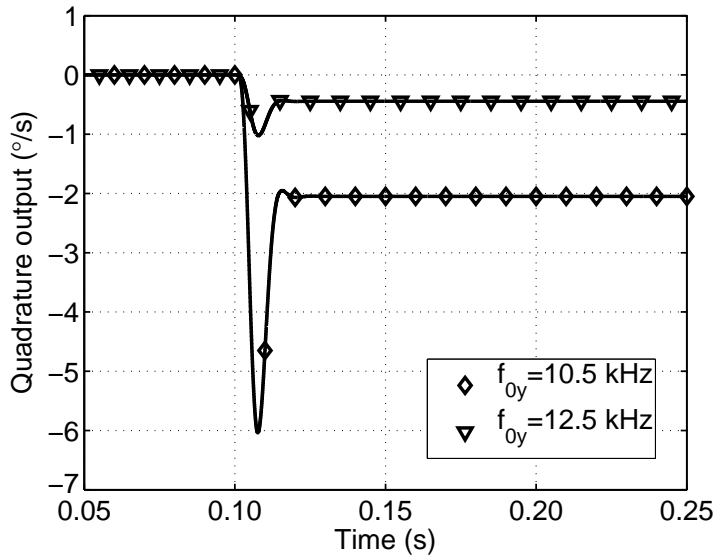
Figure 3.7 Quadrature outputs resulting from a step angular velocity input of $100°/s$. ($f_{0x} = 10\,\text{kHz}$, $f_{0y} = 10.5\,\text{kHz}$ or $12.5\,\text{kHz}$, $Q_y = 500$)

between the two cases. Figure 3.7 shows the corresponding quadrature output. Now the overshoot is caused by the Coriolis signal through the differences in the gains and phase shifts of the two sidebands, as it significantly exceeds the expected overshoot of the filter. The final values where the outputs settle correspond to the dc values in Figs. 3.3 and 3.5.

The fact that the Coriolis signal causes a frequency-dependent output in the quadrature component of the demodulated signal has to be considered if a feedback loop is utilized to compensate for the mechanical quadrature signal. This will be studied in more detail in Section 5.2. The loop has to be designed in such a way that the compensation is not disrupted by this signal. In practice, this involves either limiting the bandwidth of the compensation controller or using a more complex compensation algorithm in order to prevent it from responding to a step angular velocity input and also providing a sufficient dynamic range for the quadrature component of the demodulator output.

As a final remark, it should also be observed that if there is a time-dependent force exciting a mechanical quadrature signal in the secondary resonator, then it appears in the in-phase component of the demodulator output in just the same way that an in-phase force appears in the quadrature component, with an identical frequency dependency (shown in Figs. 3.3 and 3.5). Such a time-dependent mechanical quadrature signal can result, for example, from the quadrature compensation loop or from noise in the compensation voltage.

3.4   Nonlinearities in Displacement-to-Voltage Conversion

Next, the effect of nonlinearities in the displacement-to-voltage conversion will be considered. It is assumed that the signal given in Eq. (3.13) is fed through a nonlinear system, and the resulting in-phase output will be studied after the synchronous demodulation. A nonlinear system with second- and third-order nonlinearities can be modeled as

$$V_{in,sec,nl}(t) = V_{in,sec}(t) + a_2 \cdot [V_{in,sec}(t)]^2 + a_3 \cdot [V_{in,sec}(t)]^3, \qquad (3.16)$$

where $V_{in,sec,nl}(t)$ is the demodulator input signal after the nonlinear effects and $V_{in,sec}(t)$ the input without the nonlinearities. To find the effects of the nonlinearities, the output signal components resulting from each nonlinearity need first to be evaluated from Eq. (3.16). Then the output signal needs to be synchronously demodulated, multiplied by two, and low-pass filtered, as described earlier. The output signal components resulting from the second- and third-order nonlinearities ($[V_{in,sec}(t)]^2$ and $[V_{in,sec}(t)]^3$) are given in Eqs. (A.4) and (A.5) of Appendix A. After evaluating the output of the synchronous demodulation, it can be concluded that a second-order nonlinearity does not cause any distortion to the output signal. This is because no spectral components result at or around the operating frequency ω_{0x} as a result of a second-order nonlinearity.

A third-order nonlinearity, on the other hand, causes distortion to the demodulator output. The in-phase component of the output signal has frequency components at dc, ω_Ω, $2\omega_\Omega$, and $3\omega_\Omega$. The expressions for the components are given in Eqs. (A.6a)-(A.6d) of the appendix[3]. It can be seen that the nonlinearity results in a set of different intermodulation products between the four input components. These products are then demodulated around dc to yield the final output spectrum.

Equations (A.6a)-(A.6d) give the frequency components which result from the third-order nonlinearity, that is, the term $[V_{in,sec}(t)]^3$ in (3.16). In order to compare them to the signal resulting from the fundamental component, which was given in Eq. (3.14a), they still need to be multiplied by a_3 defined in Eq. (3.16), which represents the relative magnitude of the nonlinearity. Only then can their final importance be assessed.

While the expressions (A.6a)-(A.6d) are fairly complicated, two simplified special cases deserve more careful examination. In the first case, only the Coriolis signal is fed into the system, while the error signals $V_{error,I}$ and $V_{error,Q}$ are both zero. By using

---

[3]These results assume that the demodulation is ideal in the sense that no spectral components from harmonic frequencies fold at or around dc. While this is true when the demodulation is performed by multiplying the signal by ideal sine and cosine waves, the result will be different if the demodulation is performed using, for instance, a switching demodulator. These effects will not be considered here.

the substitutions introduced in the appendix[4],

$$A = \frac{G_{V/y}G_{y/\Omega,LSB}\Omega_z}{2} \tag{3.17a}$$

and

$$B = \frac{G_{V/y}G_{y/\Omega,USB}\Omega_z}{2}, \tag{3.17b}$$

the in-phase component of the demodulator output resulting from the nonlinearity is

$$
\begin{aligned}
I_{out,sec}(t) = & \left(\frac{3A^3}{4} + \frac{3AB^2}{2}\right) \cdot \cos(\omega_\Omega(t - T_d) + \varphi - \phi_{LSB} - \theta) + \\
& \left(\frac{3A^2B}{2} + \frac{3B^3}{4}\right) \cdot \cos(\omega_\Omega(t - T_d) + \varphi + \phi_{USB} + \theta) + \\
& \frac{3A^2B}{4} \cdot \cos(3\omega_\Omega(t - T_d) + 3\varphi - 2\phi_{LSB} + \phi_{USB} - \theta) + \\
& \frac{3AB^2}{4} \cdot \cos(3\omega_\Omega(t - T_d) + 3\varphi - \phi_{LSB} + 2\phi_{USB} + \theta).
\end{aligned}
\tag{3.18}
$$

From the result, it can be seen that the third-order nonlinearity affects the amplitude of the spectral component at the frequency of the angular velocity excitation (ω_Ω), and it causes a third harmonic component to the output spectrum.

In another special case, it is assumed that the input angular velocity is at dc. The Coriolis signal can then be merged with the in-phase component of the error signal. By now using the substitutions

$$C = G_{V/y}G_{y/\Omega}\Omega_z + V_{error,I} \tag{3.19a}$$

and

$$D = V_{error,Q}, \tag{3.19b}$$

the in-phase component of the demodulator output resulting from the nonlinearity is

$$
\begin{aligned}
I_{out,sec}(t) = & \left(\frac{3C^3}{4} + \frac{3CD^2}{4}\right) \cdot \cos\theta + \left(\frac{3C^2D}{4} + \frac{3D^3}{4}\right) \cdot \sin\theta \\
= & \frac{3C^3}{4} \cdot \cos\theta + \frac{3C^2D}{4} \cdot \sin\theta + \frac{3CD^2}{4} \cdot \cos\theta + \frac{3D^3}{4} \cdot \sin\theta.
\end{aligned}
\tag{3.20}
$$

The nonlinearity causes four error terms to the in-phase output. First, there is a third-order error (C^3). Second, if the quadrature component $V_{error,Q}$ is nonzero, there is also a second-order error (C^2), but the error is attenuated by $\sin\theta$. Third, the nonlinearity causes signal-dependent leakage of the quadrature component of the demodulator input

---

[4]The symbol A, together with the symbols C and D used later in this section, is used with other meanings elsewhere in this thesis. The use of the definitions given here is limited to this section and to Appendix A.

signal to the in-phase output. If the quadrature component $V_{error,Q}$ is constant, the error appears as a gain error, because it is linearly proportional to the Coriolis signal. Finally, it causes an offset which is dependent on the quadrature component $V_{error,Q}$. Again, this error is attenuated by $\sin\theta$.

In a practical case, the Coriolis signal has such a small amplitude that it is unlikely that the nonlinearities would be a significant source of error in the displacement-to-voltage conversion. On the other hand, the mechanical quadrature signal can be considerably larger than the full-scale Coriolis signal [57]. Therefore, depending on the system implementation, the mechanical quadrature signal can form the limiting factor for the overall accuracy of the system.

3.5   Mechanical-Thermal Noise

Finally, how the mechanical-thermal noise introduced in Section 2.2 behaves in synchronous demodulation is studied. The power spectral density of the noise force was given in Eq. (2.34). Rewritten here for the y-directional resonator,

$$F_n^2 = 4k_BTD_{yy}. \qquad (3.21)$$

After traversing through the force-to-displacement and displacement-to-voltage conversions, the synchronous demodulation, and the subsequent gain of two and the low-pass filtering, the power spectral density of the noise voltage, which appears in both the in-phase and the quadrature components of the demodulator output, as a function of the frequency ω_Ω, is

$$I_{out,sec,n}^2 = Q_{out,sec,n}^2 = \frac{4G_{V/y}^2 \cdot 2k_BTD_{yy} \cdot \left(\overline{G_{y/\Omega}}^2 + \Delta G_{y/\Omega}^2\right)}{\left(2A_x\omega_{0x}m_x\right)^2}. \qquad (3.22)$$

The detailed derivation of the result is given in Appendix B.

The amplitude transfer function of the angular velocity input to the in-phase output signal was given in Eq. (3.14a) as $G_{V/y}G_{y/\Omega,I}$, with $G_{y/\Omega,I}$ defined in Eq. (3.14b). By reducing the spectral density of the noise voltage in the in-phase output by this gain, the mechanical-thermal noise spectral density, referred to angular velocity input, can be written as

$$\Omega_{z,n} = \frac{\sqrt{2k_BTD_{yy}}}{A_x\omega_{0x}m_x} \cdot \sqrt{\frac{\overline{G_{y/\Omega}}^2 + \Delta G_{y/\Omega}^2}{\overline{G_{y/\Omega}}^2 \cdot \cos^2\left(\overline{\phi}+\theta\right) + \Delta G_{y/\Omega}^2 \cdot \sin^2\left(\overline{\phi}+\theta\right)}}, \qquad (3.23)$$

with the units of $\mathrm{rad/s/\sqrt{Hz}}$.

Figure 3.8 shows the input-referred noise spectral density evaluated from Eq. (3.23) and normalized by the spectral density at $f_\Omega = 0$ for the two cases described previously in Section 3.3. With the low resonance gain, the noise stays relatively stable over the signal band. When the resonance gain is increased, the noise increase towards higher frequencies becomes more pronounced.
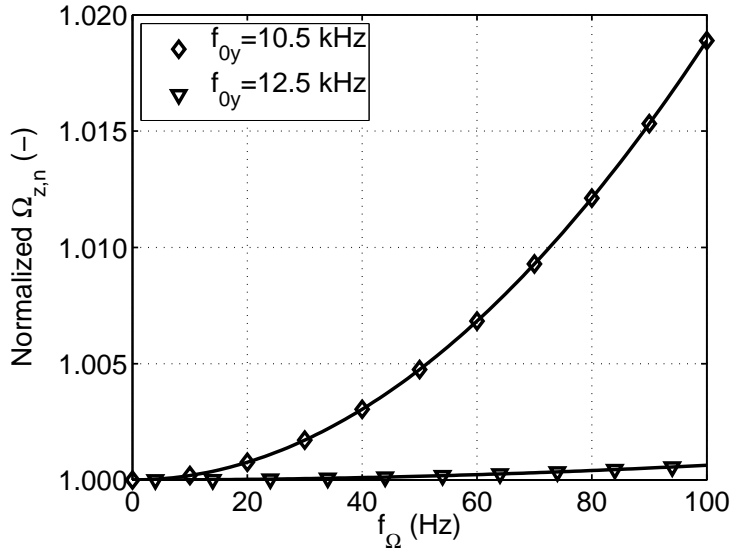
Figure 3.8 Mechanical-thermal noise, referred to angular velocity input and normalized by the noise at $f_\Omega = 0$. ($f_{0x} = 10\,\text{kHz}$, $f_{0y} = 10.5\,\text{kHz}$ or $12.5\,\text{kHz}$, $Q_y = 500$)

From Eq. (3.23) and Fig. 3.8, it can be observed that while the signal transfer function given in Eq. (3.14a) increases as a function of f_Ω, the noise transfer function increases even more rapidly. This results in the frequency-dependent *input-referred* mechanical-thermal noise shown in Fig. 3.8. The phenomenon is caused by the cosine squared and sine squared terms in Eq. (3.14b), which do not appear in Eq. (3.22). This, in turn, is caused by the fact that while the two sidebands of the Coriolis force are phase coherent, the phase of the signal caused by the mechanical-thermal noise is purely random.

It has to be kept in mind that during the previous analysis only the mechanical-thermal noise was considered. If the noise contributed by the displacement-to-voltage conversion is assumed to be white, then its input-referred power spectral density decreases as a function of frequency. This is because the signal transfer function (3.14a) increases as a function of f_Ω, as already described.

Equation (3.23) can be simplified by assuming that the gain and the phase shift of the force-to-displacement conversion stay constant over the band of interest. This is a reasonable assumption in the event that a moderate resonance gain and/or small

bandwidth is employed. Then $\overline{G_{y/\Omega}} = G_{y/\Omega}$, $\Delta G_{y/\Omega} = 0$, and $\overline{\phi} = \phi$, and the noise spectral density simplifies to

$$\Omega_{z,n} = \frac{\sqrt{2k_B T D_{yy}}}{A_x \omega_{0x} m_x} \cdot \frac{1}{\cos{(\phi + \theta)}}. \tag{3.24}$$

This is the form in which the noise spectral density is typically presented in the literature. Often the effects of the phase shift $\phi + \theta$ are disregarded as well, and the equation is written in mode-matched operation.

3.6   Effects of Temperature on Gain Stability

On the basis of the results derived in this and the previous chapter, the effects of temperature variation on the stability of the gain from the angular velocity input to the output signal can be listed. The gain was written in Eq. (3.14a), taking various non-idealities into account. In the sensor element, the gain stability is determined by the stability of the resonance gain G_{res}, of the vibration amplitude A_x, and of the primary resonator resonance frequency ω_{0x}. As defined in Eq. (2.28), the resonance gain depends on the separation of the resonance frequencies of the primary and the secondary resonators, denoted by κ. Thus, if the resonance frequencies track each other over temperature with a constant κ, the gain variation is minimized. Additionally, in mode-matched operation, the quality factor Q_y of the secondary resonator affects the resonance gain. The vibration amplitude A_x is typically controlled in a feedback loop, as will be shown in Chapter 4 and hence, its effect on the gain stability is minimized, depending on the controlling accuracy. Finally, the effect of the variation of ω_{0x} is typically small. If necessary, it could be compensated for in the electronics.

Second, the phase shift $\overline{\phi}$ in the sensor element and θ in the displacement-to-voltage conversion affect the gain stability. The phase shift $\overline{\phi}$ depends on the mode separation κ and the quality factor Q_y. On the other hand, θ and its stability are determined purely by the circuit design.

Finally, the gain $G_{V/y}$ of the displacement-to-voltage conversion affects the overall gain, as should be expected. Like the respective phase shift θ, the gain stability is determined purely by the circuit design.

3.7   Discussion

In this chapter, issues related to the synchronous demodulation of the secondary signal from a vibratory microgyroscope were studied. First, the ideal operation was considered. After that, the effects of various non-idealities were analyzed. These

non-idealities were: delay in the displacement-to-voltage conversion; differences in the transfer functions of the two sidebands in the force-to-displacement conversion in the secondary resonator; nonlinearities in the displacement-to-voltage conversion, and mechanical-thermal noise.

The effects of delay in the displacement-to-voltage conversion were found to be that first, the ideal output signals are attenuated by $\cos\theta$, second, the signals leak between the in-phase and quadrature components, attenuated by $\sin\theta$, and third, the Coriolis signal experiences a delay.

The effects of the differences in the transfer functions of the two sidebands through the secondary resonator were found to be that first, the gain and phase shift of the Coriolis signal to the in-phase component of the demodulator output change as a function of frequency, and second, the Coriolis signal leaks to the quadrature component of the output with a high-pass transfer function. The same also applies to the mechanical quadrature signal.

The effects of nonlinearities on the displacement-to-voltage conversion were found to be that a second-order nonlinearity does not have any effect on the output, whereas a third-order nonlinearity causes various error terms, including signal-dependent leakage of the quadrature component of the demodulator input signal to the in-phase output.

Next, an expression for mechanical-thermal noise reduced to angular velocity input was written. It was found that the input-referred mechanical-thermal noise also exhibits frequency dependency, in such a way that the noise increases slightly towards higher frequencies. Finally, the effects of temperature variations on gain stability were briefly listed.

Chapter 4

Primary Resonator Excitation

The operation of a vibratory microgyroscope requires the primary resonator to be excited to vibration. Typically, the excitation is performed at its resonance frequency ω_{0x}, in order to achieve a maximum displacement with a given excitation force. There are several possible mechanisms to generate the excitation force, as described in Section 2.3, such as electrostatic (capacitive), piezoelectric, and electromagnetic excitation.

In this chapter, issues related to the primary resonator excitation are studied. Because the focus of this thesis is on microgyroscopes with capacitive excitation and detection, it will be assumed that the excitation is performed electrostatically. However, excluding Section 4.1, the analysis is largely also applicable to gyroscopes with other types of actuators.

The contribution of the chapter is the following. First, the basics of the operation of various electrostatic actuators are described. Then the dynamics of a basic primary resonator excitation loop are analyzed. Finally, because of their importance to the experimental work presented in Chapter 8, different digital techniques related to the primary resonator excitation will be studied. The use of $\Sigma\Delta$ modulation in generating the excitation voltages, including the effect of the quantization noise resulting from the modulation, will be analyzed in detail.

4.1 Electrostatic (Capacitive) Actuator

An electrostatic actuator is based on the attractive electrostatic force generated between two electrodes when an electric field is applied between them. As a system always tends to an equilibrium point at which its total energy is minimized, the force in a 1-DoF system can be expressed as a partial derivative of the energy with respect to the

displacement, or

$$F = -\frac{\partial E_{tot}}{\partial d}, \tag{4.1}$$

where E_{tot} and d are the total energy and the displacement, respectively[1]. If the actuator is now considered to be a simple parallel-plate actuator [94, Ch. 6] as shown in Fig. 4.1, comprising two electrodes with an area A, one of which is fixed while the other one can move in the x-direction, then the capacitance between the plates is

$$C = \frac{A\varepsilon_0\varepsilon_r}{x_0 + x}, \tag{4.2}$$

where ε_0 is the permittivity of vacuum, equal to $8.85418 \cdot 10^{-12}\,\text{F/m}$, ε_r the relative permittivity of the insulator between the plates (for vacuum or air, $\varepsilon_r = 1$), x_0 is the initial gap between the plates with no voltage applied, and x is the displacement. When the capacitor is biased with a constant voltage V, the energy stored in it is

$$E = \frac{1}{2}CV^2 = \frac{A\varepsilon_0\varepsilon_r V^2}{2(x_0 + x)}. \tag{4.3}$$

Now, the electrostatic force can be written as

$$F_{es} = -\frac{A\varepsilon_0\varepsilon_r V^2}{2(x_0 + x)^2}. \tag{4.4}$$

The direction of the force is along the negative x-axis, that is, the force is attractive[2].
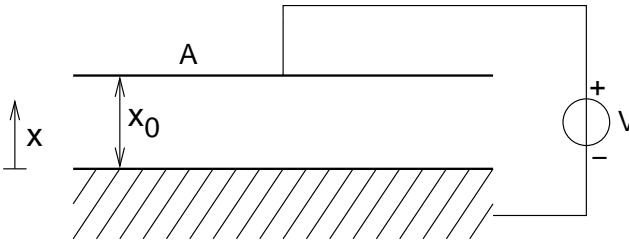
Figure 4.1 A simple voltage-controlled parallel-plate actuator, with an initial gap x_0 between the plates when $V = 0$, and plate area A. (Side view.)

Equation (4.4) shows that the electrostatic force is a nonlinear function of both the voltage V and the displacement x. If the displacement x is assumed to be small

---

[1] For a more general analysis, F and d in Eq. (4.1) need to be replaced with vector quantities, leading to a slightly more complex expression. For this analysis, however, scalar quantities are sufficient.

[2] When comparing Eq. (4.4) with Eqs. (4.3) and (4.1), it appears as if there were a sign inconsistency between the two. The equations are consistent, however, as Eq. (4.1) considers the total energy of the system, whereas Eq. (4.3) expresses only the energy stored in the capacitance C. The constant-voltage biasing causes the energy stored in C to change as x changes, requiring an other energy storage element in the system. A detailed analysis can be found in Appendix C

compared to the initial gap x_0, then the force can be linearized by taking the first two terms of the Taylor series of (4.4). In that case, the force can be written as

$$F_{es} \approx -\frac{A\varepsilon_0\varepsilon_r V^2}{2x_0^2} + \frac{A\varepsilon_0\varepsilon_r V^2}{x_0^3} \cdot x. \tag{4.5}$$

The first term of the series can be interpreted as a displacement-independent attractive electrostatic force, which is used to excite the resonator, while the second term is a repulsive force with a linear dependency from the displacement. By adding F_{es} to the right-hand side of the 1-D EoM given in Eq. (2.5) and reordering, the EoM can be written as

$$m\ddot{x} + D\dot{x} + \left(k - \frac{A\varepsilon_0\varepsilon_r V^2}{x_0^3}\right) x = -\frac{A\varepsilon_0\varepsilon_r V^2}{2x_0^2} + F. \tag{4.6}$$

Now, it can be seen that in an electrostatically excited mass-spring-damper system, the repulsive force acts as a *negative electrostatic spring* k_{es}, which reduces the effective spring constant k_{eff}. This phenomenon is known as *electrostatic spring softening*, and it is one of the most significant side effects of both capacitive excitation and detection. The electrostatic spring constant can be written as

$$k_{es} = -\frac{A\varepsilon_0\varepsilon_r V^2}{x_0^3}, \tag{4.7}$$

and the resulting effective spring constant as

$$k_{eff} = k + k_{es} = k - \frac{A\varepsilon_0\varepsilon_r V^2}{x_0^3}. \tag{4.8}$$

As a result of the electrostatic spring softening, the resonance frequency is reduced to

$$\omega_0 = \sqrt{\frac{k_{eff}}{m}}. \tag{4.9}$$

Because of the inherent nonlinearity of the parallel-plate actuator, its applicability may be limited when large relative displacements (x/x_0) need to be generated. If a wider linear actuation range is required, the parallel-plate actuator can be run with a charge control. In that case, the structure is biased with a constant charge Q[3]. Now, the energy stored in the capacitance, and, at the same time, the total energy of the system is

$$E = \frac{Q^2}{2C} = \frac{(x_0 + x)Q^2}{2A\varepsilon_0\varepsilon_r}. \tag{4.10}$$

---

[3]In this thesis, the symbol Q is also used to denote the quality factor. If there is a possibility that the two meanings of Q can be confused, the meaning is clearly stated in the text.

The electrostatic force is then

$$F_{es} = -\frac{Q^2}{2A\varepsilon_0\varepsilon_r}, \tag{4.11}$$

which is now independent of the displacement x.

Another way to extend the linear actuation range is to use a comb-drive actuator with voltage control [95, 96]. The comb-drive actuator is formed by two comb structures sliding between each other, as shown in Fig. 4.2. If the comb fingers are narrow and the horizontal gap between the fingers small, the parallel-plate capacitor formed by the tip of each finger with the opposite electrode can be ignored, and the total capacitance between the fixed electrode and the moving electrode can be assumed to be a linear function of the displacement[4]. If the thickness of the structure of Fig. 4.2 extending into the page is denoted by h, the width of each horizontal gap by g, and the number of the horizontal gaps by n_{gap}, and if the only capacitance is assumed to be formed by the horizontal parallel-plate capacitors between the fingers, then the total capacitance between the electrodes is

$$C = \frac{\varepsilon_0\varepsilon_r \cdot n_{gap}(x_0 - x)h}{g}. \tag{4.12}$$

Then the energy stored in the capacitance is

$$E = \frac{1}{2}CV^2 = \frac{\varepsilon_0\varepsilon_r \cdot n_{gap}(x_0 - x)hV^2}{2g}, \tag{4.13}$$

and the electrostatic force

$$F_{es} = -\frac{\varepsilon_0\varepsilon_r \cdot n_{gap}hV^2}{2g}. \tag{4.14}$$

Again, the force can be seen to be attractive, but now it is independent of the displacement x.

In reality, the fringing electric field can make a significant contribution to the total capacitance C in the comb-drive actuator. This, however, can be taken into account by adding a correction factor (> 1) into Eq. (4.12).

Some further remarks regarding the comb-drive actuator need to be made. First, the n_{gap} parallel-plate capacitors also generate electrostatic forces acting in the horizontal direction. If all the gaps have an equal width g, the horizontal forces cancel each other, but still cause spring softening and thus increase the compliance of the structure in the horizontal direction. If the gaps have different widths, the electrostatic forces are not

---

[4]Sometimes the term *comb structure* is also used to refer to a structure which is identical to that shown in Fig. 4.2 but where the moving structure can move in the horizontal direction, instead of the vertical direction as in the figure. In such a structure, the left-hand-side edges of each finger of the fixed structure are connected to form the negative electrode and the right-hand-side edges to form the positive electrode. Hence, a three-terminal structure with a moving middle electrode between two fixed electrodes is formed. In this thesis, however, comb structure always refers to the structure described here.
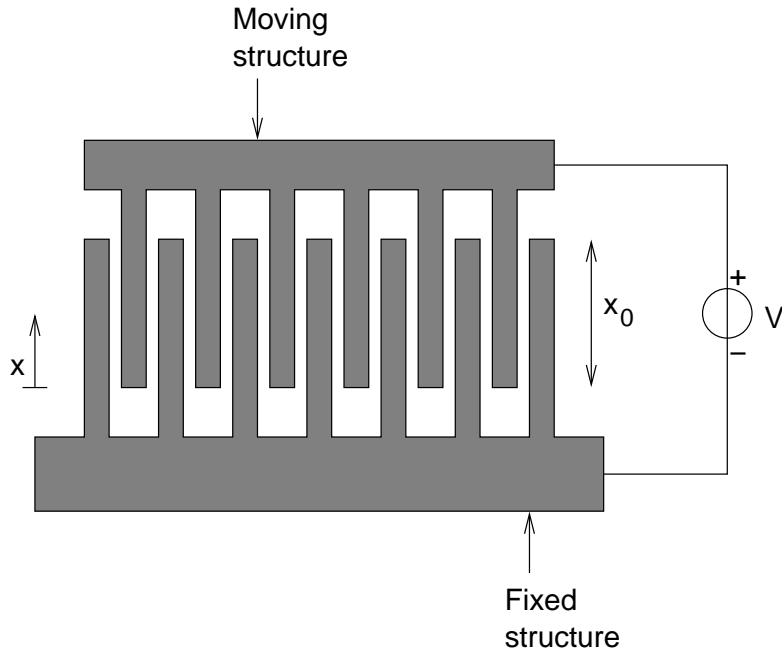
Figure 4.2 A voltage-controlled comb-drive actuator, with initial displacement of x_0 when $V = 0$. (Top view.)

canceled, but an additional net force remains acting in the horizontal direction.

Second, if there is a voltage difference between the moving structure and the underlying substrate, a vertical electrostatic force is generated. This force pulls the moving structure towards the substrate, collapsing them together in an extreme case. Since the moving structure forms a parallel-plate actuator with the substrate, electrostatic spring softening is observed in this direction as well. These effects can be prevented by either removing the substrate under the moving structure or by adding a ground plane under it, and biasing the ground plane and the moving structure to the same potential. [97]

Third, the fringing electric field can also generate an electrostatic force pulling the moving structure away from the substrate. This phenomenon is known as the electrostatic levitation effect. It can be prevented by proper biasing of the fingers and of the underlying ground plane. This, however, reduces the electrostatic force in the lateral direction as well because the fringing fields are reduced. [97]

Regardless of whether the actuator is a parallel-plate or a comb-drive actuator, the generated electrostatic force is proportional to the square of the control voltage. If it is assumed that the excitation voltage is of the form

$$V_{exc}(t) = V_{DC} + V_{AC} \cdot \sin\left(\omega_{exc}t\right), \tag{4.15}$$

where V_{DC} and V_{AC} are the dc and ac components of the excitation voltage, respectively,

and ω_{exc} is the frequency at which the excitation is performed, then the resulting force is proportional to

$$
\begin{aligned}
F_{es} &\sim [V_{DC} + V_{AC} \cdot \sin(\omega_{exc}t)]^2 \\
&= V_{DC}^2 + 2V_{DC}V_{AC} \cdot \sin(\omega_{exc}t) + V_{AC}^2 \cdot \sin^2(\omega_{exc}t) \\
&= V_{DC}^2 + \frac{V_{AC}^2}{2} + 2V_{DC}V_{AC} \cdot \sin(\omega_{exc}t) - \frac{V_{AC}^2}{2} \cdot \cos(2\omega_{exc}t).
\end{aligned}
\tag{4.16}
$$

From Eq. (4.16), it can be seen that there are forces generated at three distinct frequencies, at dc, at ω_{exc}, and at $2\omega_{exc}$. In single-ended excitation, the force generated at dc causes a static displacement of the resonator. The latter two of these forces can be used to excite the primary resonator. If the excitation frequency is chosen to be such that $\omega_{exc} = \omega_{0x}$, then the resulting force component exciting the primary resonator at its resonance frequency is

$$
F_{es} \sim 2V_{DC}V_{AC} \cdot \sin(\omega_{0x}t). \tag{4.17}
$$

If, on the other hand, the excitation frequency is chosen to be such that $\omega_{exc} = \omega_{0x}/2$, then the resulting force component exciting the primary resonator is

$$
F_{es} \sim -\frac{V_{AC}^2}{2} \cdot \cos(\omega_{0x}t). \tag{4.18}
$$

This result implies that the excitation of the resonator can be performed either at the resonance frequency, in which case the force is proportional to the product of the dc and ac components of the excitation voltage, or at half the resonance frequency, in which case the force is proportional to the ac component squared.

If the resonator is excited differentially with voltages $\pm V_{exc}(t)/2$, the forces at dc and at $2\omega_{exc}$ are canceled. In that case, only the exciting force at ω_{exc} can be used to drive the resonator. However, it should be kept in mind that although the static displacement is canceled, the forces at dc still cause electrostatic spring softening in the parallel-plate actuator, as described earlier in the text.

Finally, it needs to be emphasized that the preceding analysis is based on the assumption that the electrostatic force used to excite the resonator is independent of the displacement x. While this is true for the comb-drive actuator and the parallel-plate actuator with charge control, an assumption that the relative displacement x/x_0 is small (less than approximately $1/10$) needs to be made when considering a parallel-plate actuator with voltage control. Additionally, it has been implicitly assumed that the only effect of the nonlinearity of the parallel-plate actuator is the electrostatic spring softening.

In a practical case, when a parallel-plate electrostatic actuator is used to excite the primary resonator in a vibratory microgyroscope, the vibration amplitude is often not

limited to the linear area of operation. This is because the primary resonator vibration amplitude needs to be maximized in order to maximize the Coriolis movement in the secondary resonator. Because of the strong nonlinearity of the full expression of F_{es} in Eq. (4.4) with respect to the displacement x, a more detailed analysis with sinusoidal excitation voltage and sinusoidally varying displacement x needs to be performed to ensure that the actuator works as desired. The analysis is most conveniently performed using appropriate computer software to solve the expressions numerically. Theoretical analysis of the large-signal phenomena can be found, for example, in [98, 99].

As a numerical example, the microresonator introduced in Chapter 2 will be reconsidered. The parameters were given in Table 2.1. If it is assumed that the mass is made out of single-crystal silicon, the density of which is $\rho_{Si} = 2330\,\mathrm{kg/m^3}$, the example resonator can be approximately $25\,\mu$m thick, with an area of $200\,\mu$m times $200\,\mu$m. If the electrode area A is now assumed to be $100\,\mu$m times $100\,\mu$m, then with this and the other parameters given in Table 4.1, the amplitude of the resulting force at ω_{exc} in the case of a voltage-controlled parallel-plate actuator is $F_{es} \approx 8.9\,\mathrm{nN}$. If the resonator is excited at $1\,\mathrm{kHz}$, the amplitude of the resulting displacement x is merely $0.89\,\mathrm{nm}$. If the resonator is excited at its resonance frequency $10\,\mathrm{kHz}$, the displacement is $0.89\,\mu$m. It can be seen that the ratio x/x_0 is small enough for the linear approximation to hold. In this example, the electrostatic spring softening can be disregarded, as it is insignificantly small.

Table 4.1 Example parameters for electrostatic excitation of a microresonator.

Parameter	Value
A	$100\,\mu$m $\cdot$ $100\,\mu$m
ε_r	1
x_0	$10\,\mu$m
V_{DC}	$10\,\mathrm{V}$
V_{AC}	$1\,\mathrm{V}$

The small magnitude of the resulting force and displacement in the previous example is characteristic of the electrostatic actuator. For this reason, the primary resonator of a microgyroscope is practically always driven at the resonance frequency. The force can be increased either by increasing the excitation voltage or by increasing the electrode area A and by reducing the gap x_0. However, the large voltages require special high-voltage semiconductor technologies in order to be able to realize the driving circuitry. On the other hand, increasing the electrode area and reducing the gap increases the squeeze film damping caused by the residual gas remaining in the gap, reducing the quality factor of the resonator. Both methods also increase the effect of electrostatic spring softening. In a comb-drive actuator, the actuating force can also be increased by increasing the number of comb fingers.

4.2   Dynamics of Excitation

The excitation of the primary resonator is typically performed in a closed-loop config-
uration. With a properly phased positive feedback around the resonator, an electrome-
chanical oscillator is created at the resonance frequency ω_{0x}. As shown in Section
2.1.1, the transfer function $H_{x/F}(s)$ of the primary resonator has a phase lag of $90°$ at
the resonance frequency. This means that in order to achieve a positive feedback in
the loop, a phase lead of $90°$ is required to cancel the phase lag of the resonator. The
phase lead can be obtained with an explicit phase shifter such as a differentiator or an
integrator combined with phase inversion, with a transresistance amplifier performing
the displacement-to-voltage conversion [57, 58, 70, 86], or with a PLL that outputs a
properly-phased excitation signal [9, 79, 88, 90].

Generally, there is another feedback loop which monitors the vibration amplitude
A_x and keeps it constant at a desired value. The amplitude control is performed by con-
trolling the exciting force by varying either the dc or the ac component of the excitation
voltage. The relationship between these was shown in Eq. (4.16). If the amplitude is
not controlled, either the angular velocity output needs to be normalized with respect
to the amplitude or gain instability will result in an open-loop system. As an example
of another possibility for amplitude control, a mechanically controlled oscillator has
been reported in [76] and applied in [73].

Figure 4.3 shows a conceptual block diagram of the excitation loop. Here, it is
assumed that the excitation frequency $\omega_{exc} = \omega_{0x}$ and the amplitude of the resulting
electrostatic force is thus proportional to $2V_{DC}V_{AC}$. The position signal from the res-
onator is first converted into voltage, demodulated, and filtered with an LPF, resulting
in the primary resonator amplitude information $I_{out,pri}(t)$. In the feedback path, the
desired amplitude $I_{set,pri}$ is first subtracted from this, resulting in the error signal. This
signal is brought to a controller and modulated back to the operating frequency ω_{0x}.
The modulating signal is taken from the output of the displacement-to-voltage con-
verter, with the necessary phase lead of $90°$.

The controller $H_{prictrl}(s)$ can set either the dc or the ac component of the excitation
voltage. If it sets the dc component, then the modulation is performed using the signal
$V_{AC} \cdot \cos(\omega_{0x}t)$, which has a normalized constant amplitude. If the controller sets the ac
amplitude instead, then its output is first multiplied by $\cos(\omega_{0x}t)$ to yield the ac signal,
and further by the constant dc component V_{DC}. In Fig. 4.3, these two operations are
combined to yield a modulation using the signal $V_{DC} \cdot \cos(\omega_{0x}t)$. After the modulation,
the voltage is converted to force, which in turn is used to excite the primary resonator,
with the transfer function $H_{x/F}(s)$.

To make possible the linear analysis of the amplitude control loop, the frequency
conversions (multipliers) need to be eliminated. This is done using a frequency trans-
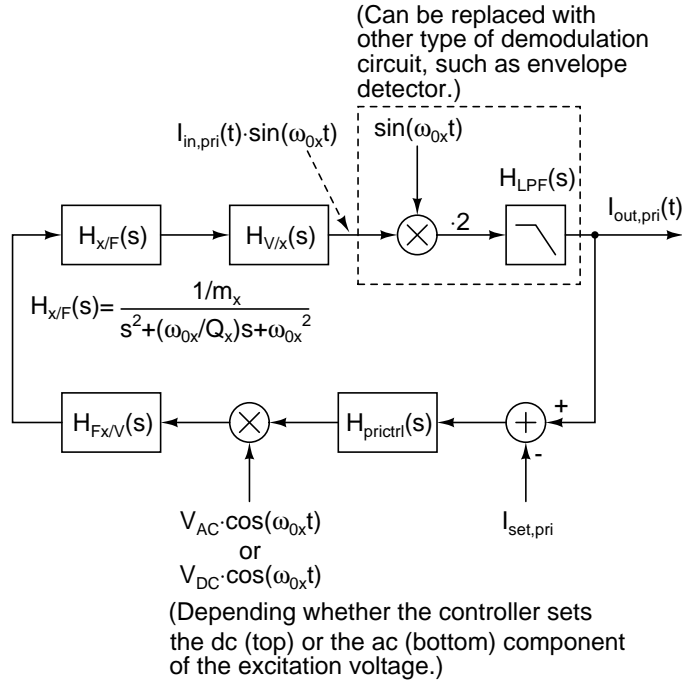
Figure 4.3 Complete block diagram of the primary resonator excitation loop.

formation to convert the blocks operating at ω_{0x} (voltage-to-force converter, resonator, and displacement-to-voltage converter) to dc. Assuming that the quality factor of the primary resonator is high, the loop can now be drawn in the simplified form shown in Fig. 4.4. It has also been assumed that the low-pass filter transfer function $H_{LPF}(s)$ does not affect the loop dynamics. Now, only the amplitude control loop remains for the linear analysis.

If it is further assumed that the displacement-to-voltage conversion $H_{V/x}(s)$ and the voltage-to-force conversion $H_{Fx/V}(s)$ act as constant gains equal to $G_{V/x}$ and $G_{Fx/V}$, respectively, in the band of interest, the transfer function from the desired amplitude $I_{set,pri}$ to the actual amplitude $I_{out,pri}$ can be written as

$$\frac{I_{out,pri}}{I_{set,pri}} = -\frac{H_{prictrl}(s) \cdot G \cdot G_{Fx/V} \cdot H_{x/F}^*(s) \cdot G_{V/x}}{1 - H_{prictrl}(s) \cdot G \cdot G_{Fx/V} \cdot H_{x/F}^*(s) \cdot G_{V/x}}. \tag{4.19}$$

From the equation, it can be seen that in order to have the actual amplitude as accurately equal to the desired amplitude as possible, the loop gain $H_{prictrl}(s) \cdot G \cdot G_{Fx/V} \cdot H_{x/F}^*(s) \cdot G_{V/x}$ of the amplitude control loop needs to be as high as possible. In the simplest case, the controller $H_{prictrl}(s)$ can be a proportional (P) controller, implemented as a gain. In this case, the loop remains a single-pole loop. If the amplitudes need to match exactly,
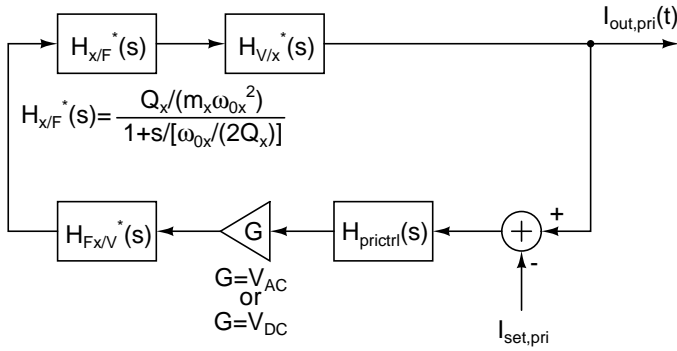
Figure 4.4 Simplified block diagram of the primary resonator excitation loop, with the frequency conversions removed.

an integrator (I)[5] controller can be used. However, this introduces another pole to the loop and limits the control bandwidth. If the bandwidth needs to be increased, a more complex controller with zeroes can be used.

In the block diagram in Fig. 4.3, the modulating signal (either $V_{AC} \cdot \cos(\omega_{0x}t)$ or $V_{DC} \cdot \cos(\omega_{0x}t)$) has an amplitude that is independent of $I_{out,pri}(t)$. This requires amplitude normalization, which can be performed, for example, by a comparator. If the modulating signal is taken directly from the output of the displacement-to-voltage converter, as, for example, in [57,58,86], then the loop cannot be linearized as it was here. In this case, numerical methods are perhaps the only way to ensure loop stability and verify the settling properties.

If the voltage-to-force converter is formed by a parallel-plate actuator operated in the nonlinear region, the amplitude-dependent gain needs to be taken into account in the design of the control loop. In such a case, the electrostatic force generated with a given voltage increases as the amplitude increases, also causing the gain $G_{Fx/V}$ of the voltage-to-force converter to increase. Like all nonlinear phenomena, this is most conveniently analyzed using appropriate numerical analysis software.

Another nonlinear phenomenon that needs to be considered is the nonlinearity of the displacement-to-voltage conversion. The effects of the nonlinearity after the synchronous demodulation were considered in detail in Section 3.4. This analysis is directly applicable to the primary resonator readout as well. Because the primary resonator movement is much larger than the Coriolis movement, the nonlinearities might be even more significant here than in the secondary resonator readout.

Finally, the behavior of the primary resonator excitation loop needs to be considered in the case when the phase shift in the electronics is not exactly $+90°$. In such a

---

[5]In this thesis, the symbol I is also used to denote either the in-phase component or the current. If there is a possibility that the different meanings of I can be confused, the relevant meaning will be clearly stated in the text.

case, after the loop has reached a steady-state operation, the primary resonator vibrates with a frequency that yields a total phase shift of $0°$ around the feedback loop. This frequency can be solved from Eq. (2.7b), and it is slightly deviated from the resonance frequency ω_{0x}. With a sufficient quality factor, the effective electrostatic force exciting the resonator is, at the same time, reduced by the cosine of the phase error (i.e. the difference of the actual phase shift from the ideal value of $+90°$).

4.3 Digital Techniques in Primary Resonator Excitation

The primary resonator amplitude control loop presented in Fig. 4.3 is an example of an analog, or a continuous-time, continuous-amplitude control loop. However, the primary signal can also be converted to the digital domain, and the controller can then be implemented with DSP. Then the control loop takes the form shown in Fig. 4.5. In the figure, the signal is A/D converted before demodulation, and downconverted and filtered in the digital domain. The ADC could also be located after the low-pass filter, in which case the demodulation is performed in the analog domain. The demodulation can also be performed using subsampling techniques.

$$H_{x/F}(s) = \frac{1/m_x}{s^2 + (\omega_{0x}/Q_x)s + \omega_{0x}^2}$$
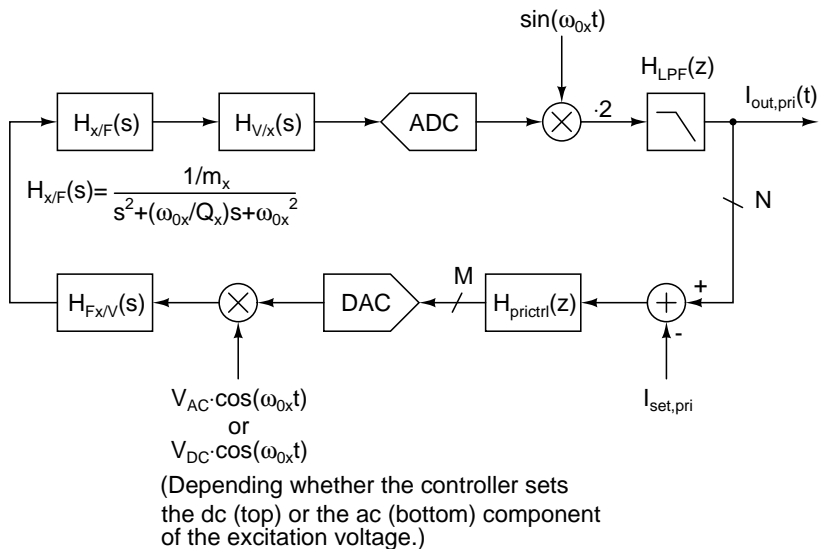
Figure 4.5 Block diagram of the primary resonator excitation loop with digital control.

As the block diagram shown in Fig. 4.5 implies, the use of digital control leads to a discrete number of possible levels of the excitation signal. In this case, the D/A converter is M bit, and hence there are 2^M possible values available. This means that it might not be possible to obtain the desired primary resonator vibration amplitude. The

discrete number of excitation levels can also lead to an oscillation of the primary resonator vibration amplitude between two values, even though the actual linear control loop is perfectly stable. This can happen if the controller $H_{prictrl}(z)$ contains an integrator and if the signal at the controller input changes by more than one least-significant bit (LSB)[6] when the DAC output changes by one LSB. Now it might happen that the controller input cannot be brought to zero with any DAC output level. The integrator in the controller integrates the residual signal until the DAC output changes by one LSB. Then the integrator output starts moving in the opposite direction until it returns to the original value, after which the oscillation cycle starts over again.

The oscillation amplitude can be reduced or the oscillation completely eliminated by increasing the resolution M of the DAC. One way to perform this is to increase the number of actual output levels of the DAC which generates the analog voltage used to set either the dc or the ac component of the excitation signal. Because the primary resonator typically has a high quality factor and thus a narrow bandwidth, another possibility is to use oversampling and $\Sigma\Delta$ modulation, with a small number of actual output levels from the DAC. The primary resonator transfer function then filters the quantization noise out, leaving an excitation signal at ω_{0x} with an amplitude which can now be set to the desired accuracy by the DSP.

A block diagram of the configuration is shown in Fig. 4.6. In the figure, the actual DAC is preceded by an interpolator, interpolation filter $H_{IF}(z)$, and a noise-shaping loop (NL). These building blocks form a second-order $\Sigma\Delta$ DAC [100, Ch. 7]. The figure also shows the word lengths and the sampling rates at different parts. The limiter inside the NL prevents an overflow at the summer output in the event of the input signal growing too high. Because the excitation voltage is no longer a single-frequency sinusoidal signal, the quadratic nature of the voltage-to-force conversion must now be taken into account. This is indicated in the block diagram.

As the controller output signal can be considered to be a dc signal, the interpolation filter can usually be removed and the interpolation performed with a simple zero-order hold (ZOH). The design of the $\Sigma\Delta$ DAC involves choosing the word lengths K and $M+P$, the interpolation factor m_{IF}, and the number of final quantization levels M. The parameters m_{IF} and M are used to set the quantization noise in the excitation signal to a desired level. The parameter K is used to achieve a sufficient resolution, as described above. Finally, $M+P$ is chosen to be such that the NL functions properly without clipping the summer output.

The DAC output can set either the dc or the ac component of the excitation voltage. While both methods lead to the same electrostatic force at the frequency ω_{0x}, both the spectrum of the exciting voltage and the generated electrostatic force around the

---

[6]In other parts of this thesis, the abbreviation LSB is also used to stand for Lower Sideband. If there is a possibility that the two meanings of LSB can be confused, the unabbreviated forms are used instead.
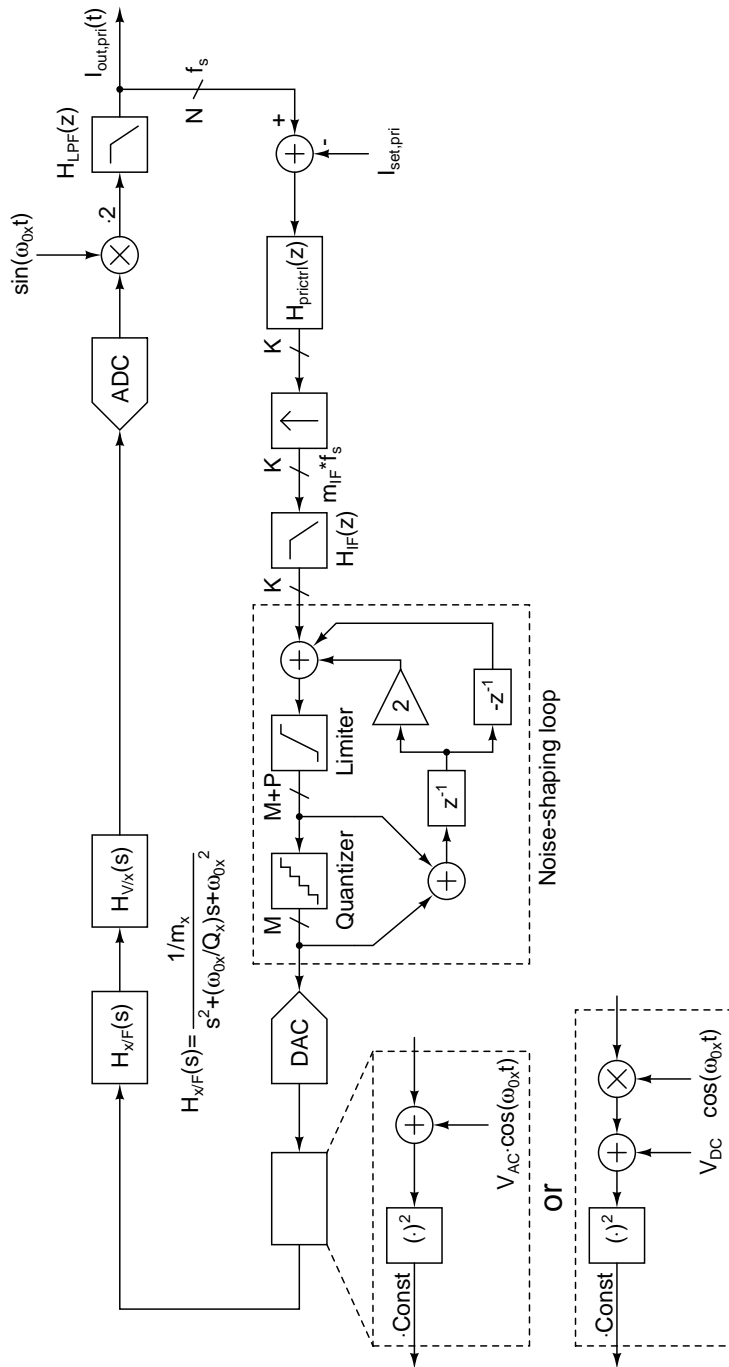
Figure 4.6 Block diagram of the primary resonator excitation loop with digital control and a $\Sigma\Delta$ DAC. The DAC output sets either the dc or the ac component of the excitation voltage. Values V_{AC} and V_{DC} are considered constant.

resonance frequency ω_{0x} resulting from the shaped quantization noise differ. If the exciting voltage cross-couples to the secondary resonator detection circuit, the two methods lead to different cross-coupled spectra at the output of the detection circuit.

An important consideration is to prevent the quantization noise at the DAC output from causing the final SNR to deteriorate. This noise can traverse to the angular velocity output through two paths. The first is the electrical cross-coupling to the secondary resonator detection circuit. If the DAC sets the dc component of the excitation voltage, then this noise source can be eliminated by selecting $f_s \cdot n \cdot m_{IF} = \omega_{0x}/(2\pi)$, where n is an integer greater than zero. Now, because of the ZOH at the DAC output, the continuous-time output spectrum has a zero at ω_{0x}, and the noise coupling is thus minimized. If the DAC sets the ac component, the $\Sigma\Delta$ modulated spectrum is upconverted to ω_{0x}, and hence the quantization noise shaping takes care of generating a zero to the final spectrum at ω_{0x} and thus minimizes the noise coupling.

The second noise coupling path is the possible direct excitation of the secondary resonator by the primary resonator excitation signal. To make this noise source low enough, the parameters m_{IF} and M are used to lower the quantization noise. Both of these coupling mechanisms will be discussed in more detail in Chapter 6, in conjunction with the ZRO.

As an example case, a system with parameters $\omega_{0x} = 2\pi \cdot 10\,\text{kHz}$, $f_s = 125\,\text{Hz}$, $K = 18$, $m_{IF} = 80$, $M = 5$ and $P = 13$ is simulated using Matlab Simulink. The parameters are taken from the implemented system prototype, and will be described in more detail in Section 8.5.2. Two cases are simulated, one where the dc and another where the ac component of the excitation voltage is set by the DAC. In both cases, the mean dc level is $-7\,\text{V}$ and the mean ac amplitude of the square wave signal is $0.5\,\text{V}$.

Figure 4.7 shows the simulated time-domain output of the DAC for both cases. From the simulated time-domain data, a spectrum is calculated with Matlab using FFT (Fast Fourier Transformation). In order to prevent spectral leakage, the time-domain data are windowed using the Kaiser window function [101], where the parameter β describes the shape of the window (sidelobe attenuation and the width of the main lobe)[7,8]. In Fig. 4.8, an overview of the resulting spectra is shown for both cases. When the dc component is controlled (Fig. 4.8 (a)), the ZOH response of the DAC results in a zero in the quantization noise spectrum at ω_{0x}, as described earlier. When the ac component is controlled (Fig. 4.8 (b)), the noise spectrum is simply modulated around ω_{0x}. This results in a higher quantization noise floor around the operating frequency.

---

[7]In his original paper [101], Kaiser actually used α as the shape parameter. However, Matlab uses the symbol β instead, while α is reserved to denote the sidelobe attenuation.

[8]In this thesis, the symbol β is also used to describe the properties of the ZRO. If there is a possibility that the two meanings of β can be confused, the meaning is clearly stated in the text.
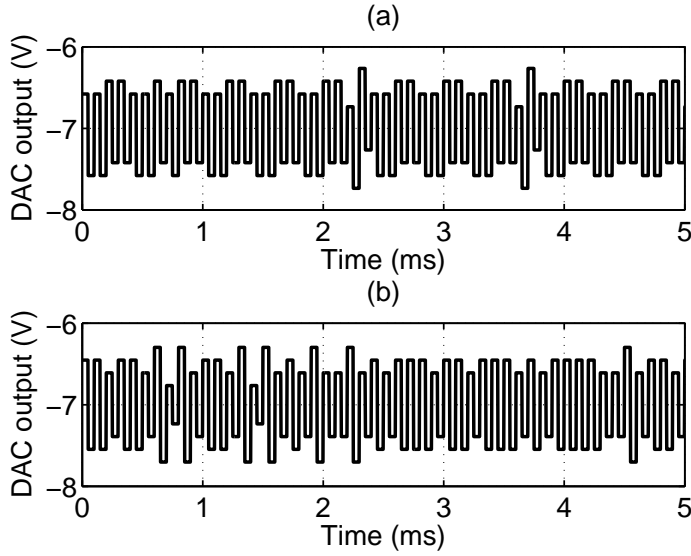
Figure 4.7 Simulated time-domain output from the ΣΔ DAC used for primary resonator excitation. (a) DAC sets the dc component of the excitation signal. (b) DAC sets the ac component of the excitation signal.

Figure 4.9 (a) shows a close-up of the resulting DAC output voltage spectrum for both cases. These spectra show clearly that the quantization noise level is approximately 40 dB higher when the ac component is controlled, compared to the case when the dc component is controlled. Finally, Fig. 4.9 (b) shows the spectra of the resulting electrostatic force for both cases. Because the DAC output voltage is squared, the difference in the force around the operating frequency between the two cases is significantly reduced.

4.4   Discussion

In this chapter, issues related to the primary resonator excitation were studied. First, the basics of the operation of various electrostatic actuators were described. Then the dynamics of the primary resonator excitation loop were analyzed. A simplified model was derived, which can be used to design the controller required in the loop.

After that, different digital techniques related to the primary resonator excitation were studied. Because of the limited number of possible excitation signal levels, the desired amplitude cannot always be reached, and oscillations may be observed in an otherwise stable loop.

To overcome this, the use of ΣΔ modulation in generating the excitation voltages was analyzed. It was found out that there are two possibilities, as either the dc or the
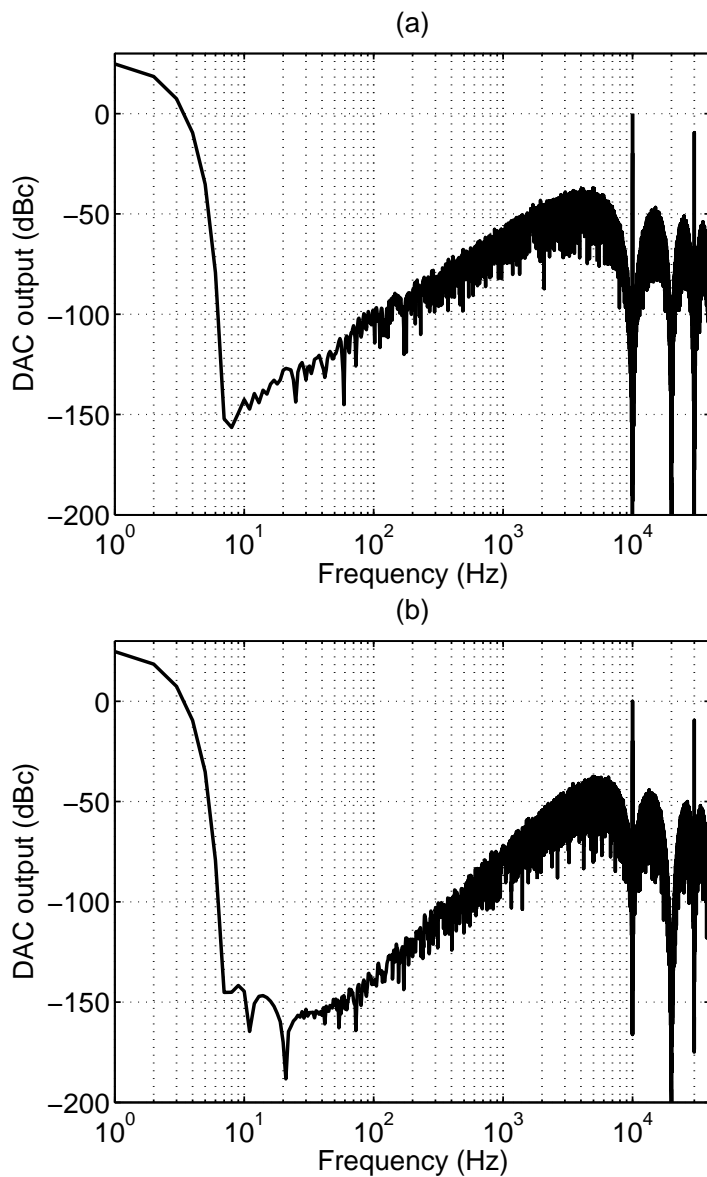
Figure 4.8 Overview of the simulated output spectra from the ΣΔ DAC used for primary res-
onator excitation. (a) The DAC sets the dc component of the excitation signal. (b) The DAC
sets the ac component of the excitation signal. (400 000-point FFT, Kaiser window with β = 20,
sampling frequency 400 kHz, reference level signal at 10 kHz)

Figure 4.9 Close-up of the resulting excitation voltage and force spectra at 10 kHz, when the ΣΔ DAC sets either the dc or ac component of the excitation signal. (a) Voltage. (b) Resulting electrostatic force. (400 000-point FFT, Kaiser window with $\beta = 20$, sampling frequency 400 kHz, reference level signal at 10 kHz)

ac component of the excitation voltage can be modulated. There are two paths for the resulting quantization noise to couple to the secondary signal, either through electrical cross-coupling or through the possible direct excitation of the secondary resonator by the primary resonator excitation signal. The modulation of the dc component of the excitation voltage was found to lead to a smaller noise caused by electrical cross-coupling, whereas the noise caused by possible direct excitation is nearly identical in both cases.

Chapter 5

Compensation of Mechanical Quadrature Signal

As shown in Chapter 2, the off-diagonal terms in the spring matrix **k** of the 2-D EoM (2.18) cause a mechanical quadrature signal to the secondary resonator. This signal can be considerably larger than the Coriolis signal produced by the full-scale angular velocity [57]. However, the mechanical quadrature signal has a $90°$ phase shift compared to the Coriolis signal, and therefore it can be distinguished using synchronous demodulation, as demonstrated in Chapter 3. Then the maximum tolerable mechanical quadrature signal depends on the dynamic range of the secondary resonator readout electronics, together with the achievable phase accuracy θ of the demodulation.

The magnitude of the mechanical quadrature signal can be controlled by element design [102, 103], by process control, and by post-manufacturing trimming and screening. There are also various ways to compensate the remaining mechanical quadrature signal using the electronics, if required. This can be performed by using electrostatic forces [57, 102, 104], or the compensation can be fully electronic [102]. The choice of different methods is dependent on the required performance and cost.

In this chapter, various methods for electrostatic or purely electronic quadrature signal compensation will first be presented. After that, ways to implement the control loop for electrostatic quadrature compensation performed with a dc voltage [57, 104] will be discussed. In particular, the case where the compensation voltage is generated with a DAC and the control is digital will be considered in detail.

The contribution of the chapter is to provide, first, a basic understanding of alternative compensation methods, and second, an analysis of the dynamics of different feedback loops used to control the compensation. Because of their importance to the experimental work presented in Chapter 8, different digital techniques related to the

quadrature signal compensation are studied. As in the previous chapter, the use of $\Sigma\Delta$ modulation in generating the compensation voltage will be analyzed in detail, including the excess noise inflicted by the modulation.

5.1   Compensation Methods

When considering the different methods to compensate for the remaining mechanical quadrature signal, the point at which the signal is removed is an important factor. The first possibility is to remove the signal at the sensor element, before the quadrature movement is generated. This implies that a force opposite to the force caused by the anisoelasticity needs to be created, possibly complicating the design of the sensor element. The second possibility is to let the quadrature movement be generated but to remove the signal before it is converted to voltage. In this case, it needs to be made sure that the quadrature movement does not limit the linearity of the mechanical element. The third possibility is to let the quadrature movement be converted to voltage, and remove it only thereafter. Now, the quadrature signal needs to be taken into account while designing the dynamic range of the electronics, up to the point where it is removed.

In this thesis, only the first two alternatives are considered to be quadrature signal compensation, as they truly remove the need for extending the dynamic range of the electronics because of the quadrature signal. Three different compensation methods can be identified, two falling into the first and one into the second category.

First, the mechanical quadrature signal can be compensated electronically by injecting a signal with the same amplitude but opposite phase to the input of the secondary resonator detection circuit, canceling the mechanical quadrature signal [102]. This method falls into the second category described above. A block diagram of the implementation is shown in Fig. 5.1. In the figure, the uncompensated quadrature force $F_{quc}(t) = -k_{yx}A_x \cdot \sin(\omega_{0x}t)$ is inflicted by the primary resonator movement, as described in Chapter 2. The force excites the secondary resonator with the transfer function $H_{y/F}(s)$, causing uncompensated quadrature movement with displacement $y_{quc}(t)$. The displacement is then converted to charge, which in turn is converted to voltage. The compensating voltage is also converted to charge, and added to the charge caused by the displacement at the input of the charge-to-voltage converter.

To effectively compensate the quadrature signal with this method, both the amplitude and the phase of the feedback signal need to be carefully controlled. Although the amplitude can be controlled in a feedback loop, correct phasing needs to rely on tight phase control in the electronics. A phase shift χ in the compensating signal causes a part of the signal to leak to the in-phase component in the synchronous demodulation, causing offset to the angular velocity output.
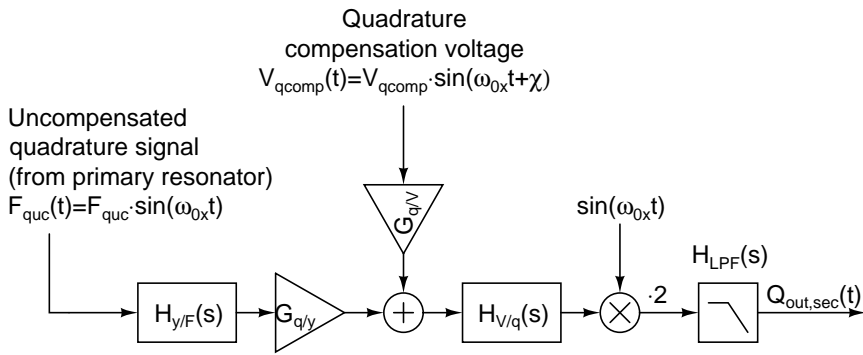
Figure 5.1 Quadrature compensation by canceling the signal at the input of the readout electronics.

Second, the same effect as with electronic compensation can be achieved by exciting the secondary resonator electrostatically with a force that has the same frequency and an opposite phase compared to the mechanical quadrature signal, through the term F_y in the 2-D EoM (2.18) [102]. A block diagram of the implementation is shown in Fig. 5.2. The same limitations apply to this method as to electronic compensation, except that now the phase shift ϕ caused by the secondary resonator has no effect on the compensation. In this case, the quadrature movement is not generated at all, meaning that the method falls into the first category.
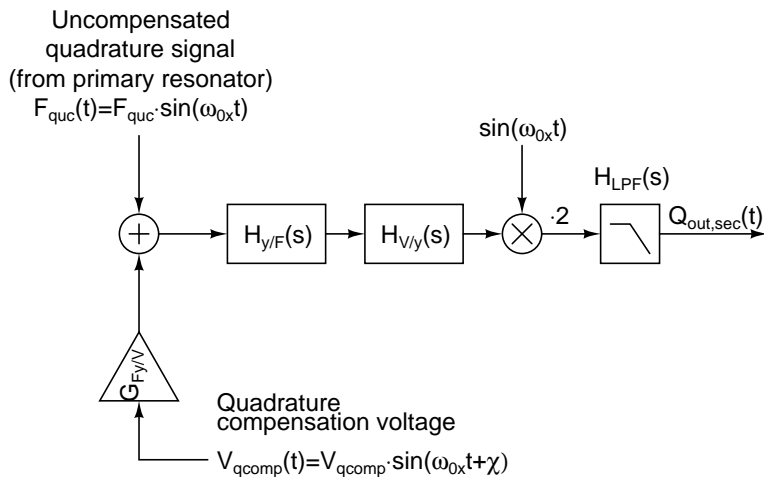
Figure 5.2 Quadrature compensation by canceling the signal by electrostatic excitation of the secondary resonator.

In these two methods, the compensation signal is typically taken from the primary resonator readout circuit. As described in Chapter 4, in order to generate a force at ω_{0x} in Fig. 5.2, a dc voltage needs to be summed to the ac voltage in the second method.

Another possibility would be to perform the excitation at $\omega_{0x}/2$, but this would need a frequency divider to achieve the final electrostatic force at a proper frequency.

A third option is to compensate the mechanical quadrature signal electrostatically by bringing a dc voltage to properly placed compensation electrodes [57, 104], as shown in Fig. 5.3. This generates a compensating force with a frequency ω_{0x}, in proper phase to cancel the force caused by anisoelasticity. This method also removes the quadrature movement, thus falling into the first category.
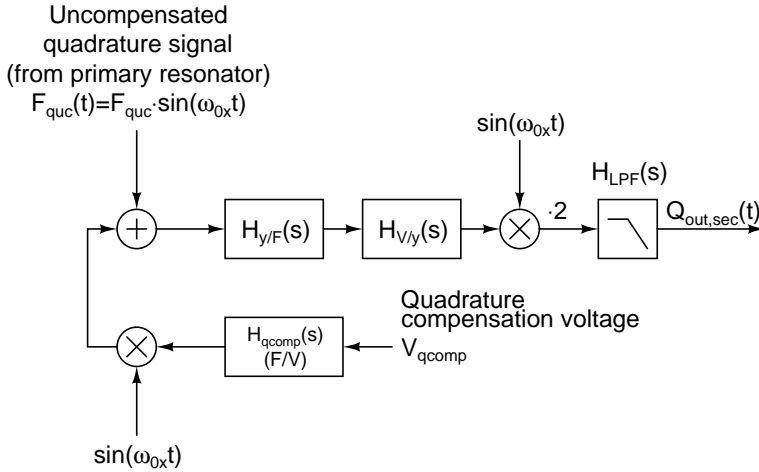
Figure 5.3 Quadrature compensation by dc voltage creating a compensating electrostatic force.

The transfer function $H_{qcomp}(s)$ in Fig. 5.3 includes the dynamics from the compensation voltage to the resulting force. In the real device, the conversion from voltage to force and the further upconversion to ω_{0x} occur simultaneously. Depending on the actuator topology, the relationship between the quadrature compensation voltage and the amplitude of the force generated can be linear, or it can have a higher-order dependence, such as a quadratic one.

5.2 Control Loops for Quadrature Signal Compensation

As can be seen from Figs. 5.1-5.3, the quadrature compensation voltage V_{qcomp} needs to be generated, regardless of the compensation method applied. In the simplest possible implementation, the voltage can be set to a constant value, so that the remaining quadrature signal is brought low enough to allow sufficient performance. The advantage of this is that there is no need to implement any kind of control loop, saving in design complexity, circuit area, and power consumption. However, the remaining me-

chanical quadrature signal can vary with changes in the operating conditions and the lifetime of the angular velocity sensor, and this needs to be carefully considered.

A more sophisticated implementation could include, for example, a temperature sensor, which controls the compensation voltage V_{qcomp} to take the temperature dependence of various parts of the implementation into account. The highest level of flexibility in terms of compensation accuracy and speed is provided by a feedback loop, in which V_{qcomp} is controlled on the basis of $Q_{out,sec}(t)$. However, it also brings along with it the typical complications related to the design of a closed-loop control system, most importantly stability issues.

In this section, different control loop structures for electrostatic quadrature signal compensation performed with a dc voltage (the third method described above) will be studied. All the structures are also applicable to the two other methods, provided that the necessary changes to the block diagrams are made. Because of its importance to the experimental work presented in Chapter 8, the case where the compensation voltage is generated with a DAC and the control is digital will be considered in particular detail.

5.2.1 Continuous-Time Compensation

A simple continuous-time quadrature compensation loop is presented in Fig. 5.4. If the feedback part is ignored for a while, the uncompensated quadrature force $F_{quc}(t)$ excites the secondary resonator as described earlier, resulting in the uncompensated quadrature movement $y_{quc}(t)$. This signal goes through the displacement-to-voltage conversion $H_{V/y}(s)$ and is synchronously downconverted to dc. Then it is amplified by two and filtered to the desired bandwidth with a low-pass filter, yielding the output signal $Q_{out,sec}(t)$.
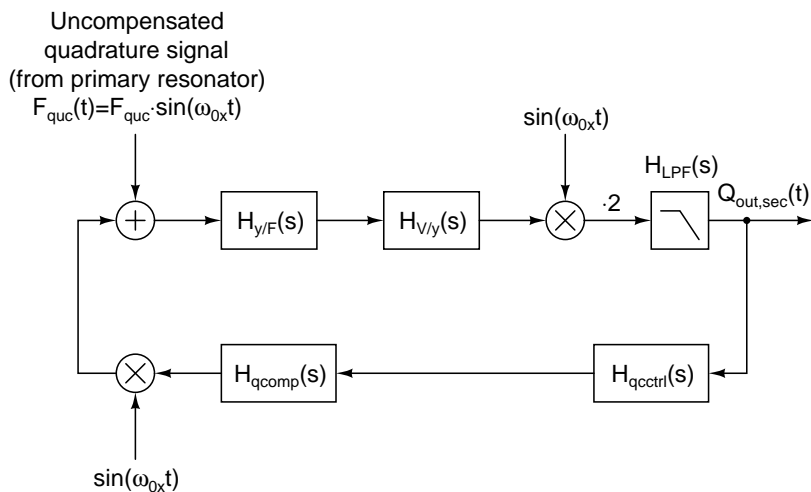
Figure 5.4 A continuous-time feedback loop for quadrature signal compensation.

In the feedback part, the signal is first brought to a controller $H_{qcctrl}(s)$, which outputs the voltage for the quadrature compensation electrodes. In the micromechanical element, the compensation voltage is converted to an electrostatic force and modulated to the operating frequency ω_{0x} in a proper phase. Finally, the result is summed to the uncompensated force $F_{quc}(t)$.

Typically, the quadrature signal needs to be zeroed at dc, requiring the controller to have a pole in the origin. The simplest solution would be a single integrator, with $H_{qcctrl}(s) = \omega_{UGF}/s$. Because of the low-pass mode operation, the compensation bandwidth is most probably limited by the low-pass filter after the demodulation. If the bandwidth needs to be increased beyond this limitation, a more complex controller with zeroes that provide phase lead at higher frequencies might be required. In this case, a complete PID (Proportional-Integrator-Differentiator) controller can be used, for instance.

5.2.2 Compensation Using DAC with Digital Controller

When the quadrature signal is converted to the digital domain and the controller is implemented with DSP, the loop takes the form shown in Fig. 5.5. In the figure, the signal is A/D converted before demodulation, and downconverted and filtered in the digital domain. The ADC could also be located after the low-pass filter, in which case the demodulation is performed in the analog domain. The demodulation can also be performed using subsampling techniques.
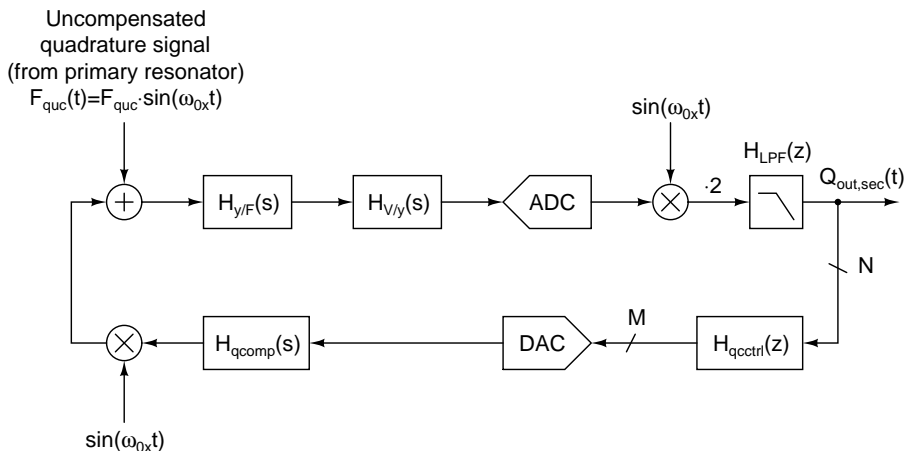
Figure 5.5 A feedback loop with A/D and D/A conversion for quadrature signal compensation.

As described in Section 4.3 in conjunction with the primary resonator excitation, the output signal $Q_{out,sec}(t)$ can also exhibit oscillations between two values because of the limited resolution of the feedback DAC. Again, this requires the controller

$H_{qcctrl}(z)$ to contain an integrator and the signal at the controller input to change by more than one LSB when the DAC output changes by one LSB. A detailed explanation of the mechanism was provided in Section 4.3. Because of the phase shifts ϕ and θ, and also because of the differences of the transfer functions of the two sidebands of the force through the secondary resonator, the oscillation couples to the Coriolis output and causes a spurious angular velocity signal whose spectral content depends on the uncompensated quadrature movement $y_{quc}(t)$ and the exact loop gain.

If the ADC is a $\Sigma\Delta$-type converter [100], then, with a dc input signal, the input voltage can be revealed with unlimited resolution by integrating it for a long enough time[1]. The same applies to an input signal at ω_{0x} if the converter is a bandpass $\Sigma\Delta$ ADC [100, Ch. 5]. This means that the DAC output will always oscillate between two values.

If the DAC resolution is sufficient, so that a change of one LSB at the DAC output causes a change of less than one LSB at the controller input, then in the case of a non-$\Sigma\Delta$ ADC, the signal $Q_{out,sec}(t)$ integrated in $H_{qcctrl}(z)$ can be kept at zero, and the output stays stable. With simulations, it can be shown that an identical resolution requirement applies for a $\Sigma\Delta$ ADC, as changes below one LSB at the ADC output are dithered to noise because of the $\Sigma\Delta$ modulation. Because the gain from the DAC output to the controller input is typically high, this leads to a very strict resolution requirement in the DAC.

5.2.3 $\Sigma\Delta$ Techniques in Quadrature Compensation

A solution for the stringent resolution requirement is to increase the DAC resolution with $\Sigma\Delta$ modulation. Now, the resolution of the DAC output at dc is not limited by the converter itself, but rather by the word length at the modulator input (controller output). By setting the word length to be sufficiently long, the spurious components can be brought as low as desired, or completely removed.

A block diagram of the configuration is shown in Fig. 5.6. As in the case of the $\Sigma\Delta$ modulation of the amplitude control signal already described in Section 4.3, an interpolator, interpolation filter, and a noise-shaping loop form a second-order $\Sigma\Delta$ DAC [100, Ch. 7]. The parameters in the figure are identical to those in Fig. 4.6.

As with the $\Sigma\Delta$ modulation of the amplitude control signal, an important consideration is to prevent the quantization noise at the DAC output from causing the final SNR to deteriorate. Again, this noise can traverse to the angular velocity output through two paths. The first is the noise in the actual compensation voltage, which couples to the Coriolis output like the oscillating quadrature signal, as described earlier. To make this noise source low enough, the parameters m_{IF} and M are used. The second path

---

[1]Ignoring other noise sources apart from the quantization noise.

Figure 5.6 A feedback loop with ΣΔ DAC for quadrature signal compensation.

is cross-coupling through parasitic capacitances. This noise source can be eliminated by selecting $f_s \cdot n \cdot m_{IF} = \omega_{0x}/(2\pi)$. As in the modulation of the dc voltage in the primary resonator excitation, because of the ZOH at the DAC output, the continuous-time output spectrum now has a zero at ω_{0x}, and the noise coupling is thus minimized.

As an example case, a system with parameters $\omega_{0x} = 2\pi \cdot 10\,\text{kHz}$, $f_s = 125\,\text{Hz}$, $K = 15$, $m_{IF} = 4$, $M = 7$ and $P = 8$ is simulated using Matlab Simulink. The parameters are taken from the implemented system prototype and will be described in more detail in Section 8.5.2. Figure 5.7 shows the simulated DAC output in the time domain. It should be recognized that this is the time-varying part of the compensation voltage, into which a constant dc level will still be summed. The corresponding spectrum is shown in Fig. 5.8.
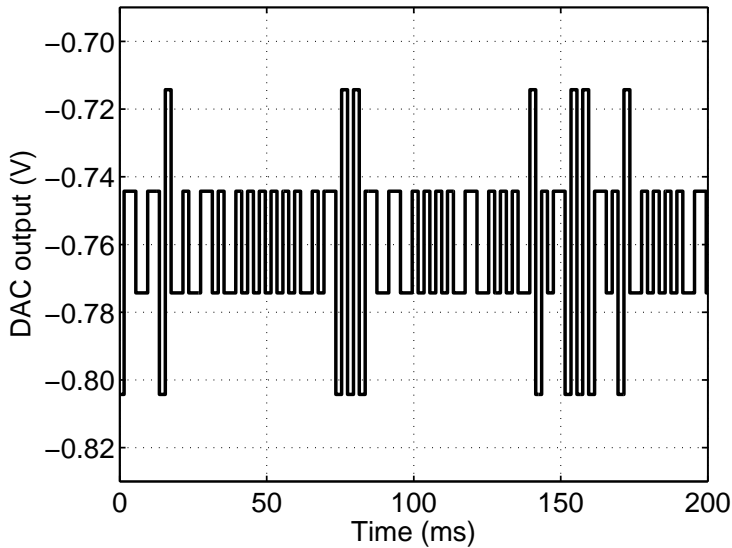
Figure 5.7 Simulated time domain output from the $\Sigma\Delta$ DAC used for quadrature compensation.

The voltage spectrum shown in Fig. 5.8 is next converted to electrostatic force and modulated to ω_{0x} to compensate the quadrature movement, as indicated in the block diagram of Fig. 5.6. Figure 5.8 (b) demonstrates that the ZOH at the DAC output does indeed create a zero to the output spectrum at ω_{0x}, thus minimizing the cross-coupling noise. More effects of the $\Sigma\Delta$ modulation of the compensation voltage will be studied experimentally in Section 8.6.

(a)

(b)
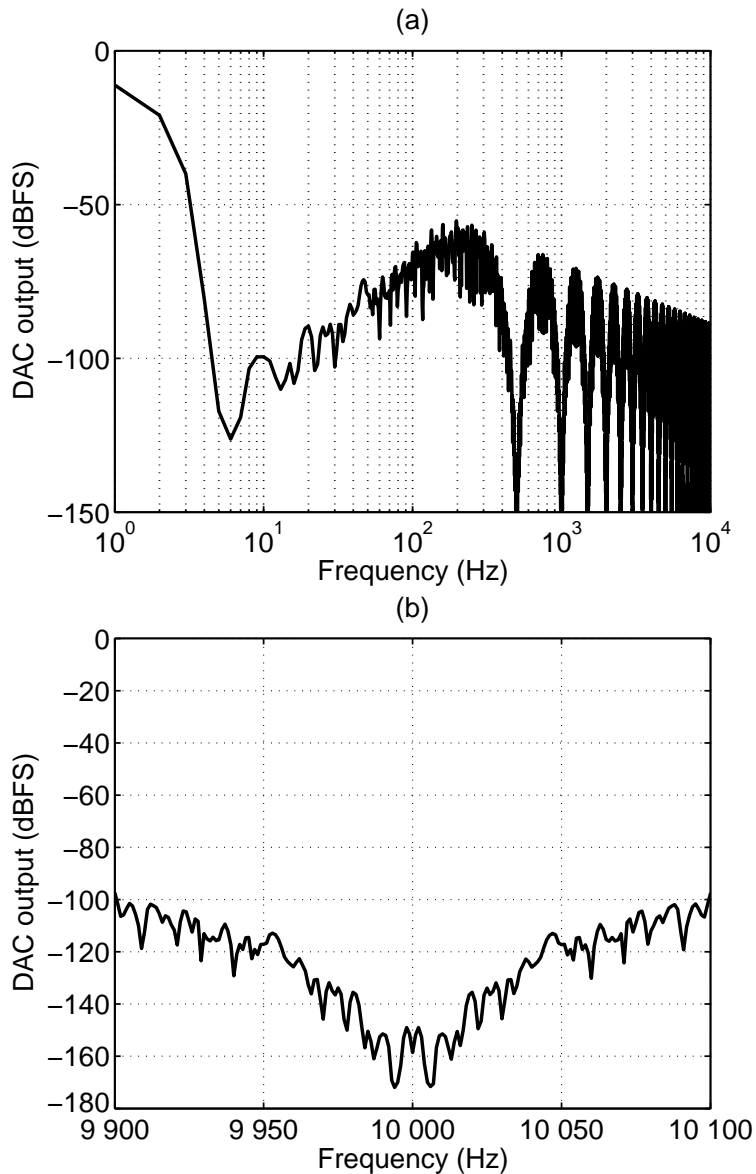
Figure 5.8 Simulated output spectrum from the $\Sigma\Delta$ DAC used for quadrature compensation. (a) Overview of the spectrum. (b) Spectrum around ω_{0x}. (400 000-point FFT, Kaiser window with $\beta = 13$, sampling frequency $400\,\text{kHz}$, FS $= 1.92\,\text{V}$)

5.3   Discussion

In this chapter, issues related to the compensation of the mechanical quadrature signal were studied. First, various methods for electrostatic or purely electronic quadrature signal compensation were presented, in order to provide a basic understanding of the alternative compensation methods. After that, ways to implement the control loop for electrostatic quadrature compensation performed with a dc voltage were discussed, and various loops were analyzed. In particular, the case where the compensation voltage is generated with a DAC and the control is digital was considered in detail, because of its importance to the experimental work in Chapter 8. The use of $\Sigma\Delta$ modulation in generating the compensation voltage was analyzed, including the excess noise inflicted by the modulation.

Chapter 6

Zero-Rate Output

The zero-rate output is the signal that an angular velocity sensor outputs when no angular velocity is applied [7]. It resembles the offset in electronic circuits, and can also be referred to as the offset signal or the zero-rate offset. If the target application area of the sensor requires that the measurement bandwidth should extend down to dc, that is, to constant angular velocities, then the ZRO or, more precisely, its possible instability, is a very significant parameter describing the performance of the device. Examples of such applications are inertial navigation and automotive stability control systems.

If the ZRO of a gyroscope were stable over time and environmental variations, such as variations in temperature, then as long as it does not limit the dynamic range of the system, it would be possible to remove it from the final output signal with calibration, either analog or digital. In practice, the ZRO rises from various parasitic effects which are typically not well controlled. Hence, it is important to carefully analyze various sources and to minimize their absolute values in order to improve ZRO stability.

In this chapter, the fundamental sources of the ZRO signal in a micromechanical vibratory gyroscope with capacitive excitation and detection will be discussed. After that, a description will be provided of how synchronous demodulation and electrostatic quadrature compensation performed with a dc voltage (described in Section 5.1) affect the final ZRO.

The discussion will be kept at a general level, with applicability to any vibratory gyroscope fulfilling the necessary assumptions. The final significance of each source is dependent on the actual system, and can be determined only after the design is known. To gain more insight into the theory presented, the ZRO properties of the implemented angular velocity sensor will be experimentally analyzed in Section 8.6.4. In the same section, methods for performing the ZRO measurements in such a way that various terms can be distinguished from each other will be discussed.

The contribution of the chapter is the following. First, different ZRO sources are identified on the basis of the literature. Each source will be given a uniform mathematical representation. Possible methods for minimizing the effect of different sources will be described. Attention will be paid to the stability of each source. Next, how the signals caused by various sources express themselves after synchronous demodulation will be analyzed. Then the effect of the electrostatic quadrature compensation performed with a dc voltage on the ZRO will be analyzed. Finally, the temperature stability of the ZRO is briefly described.

6.1 Sources of Zero-Rate Output

To identify the sources of ZRO, the nature of the signals that can cause ZRO needs to be analyzed first. As the output signal of a micromechanical gyroscope is amplitude modulated around the operating frequency $f_{0x} = \omega_{0x}/(2\pi)$, an error signal needs to reside in the vicinity of this frequency[1] in order to be able to cause ZRO. Therefore, the sources of ZRO are typically synchronized to the primary resonator output. Such a signal can be either a mechanical signal, such as the mechanical quadrature signal or the signal resulting from the non-proportional damping, which were introduced in Section 2.1.4, or it can be an electrical signal, such as a clock which is synchronized to the primary resonator.

An external interferer with a frequency close to f_{0x} can also couple to the secondary resonator detection circuit. The coupling can be either electrical, if the interferer is an electrical signal, or it can be mechanical if the interferer is a mechanical vibration. If it is assumed that such an interferer is at the frequency $\omega_{0x} + \Delta\omega$, it can be written as $\sin\left((\omega_{0x} + \Delta\omega)t + \psi\right)$. The result of synchronous demodulation is then

$$I_{out,sec}(t) = \sin\left(\Delta\omega \cdot t + \psi\right) \tag{6.1a}$$

for the in-phase component, and

$$I_{out,sec}(t) = \cos\left(\Delta\omega \cdot t + \psi\right) \tag{6.1b}$$

for the quadrature component. The result means that the interferer can also cause a time-dependent ZRO if it appears within the signal band.

The following analysis will concentrate on the ZRO sources which rise from those signals that are internal to the system. All these signals have a frequency of f_{0x} or its integer multiples. This implies that the resulting ZRO is a dc signal. The sources of the

---

[1]Depending on the structure of the demodulator, signals from harmonic frequencies can also cause ZRO. Here it is assumed that the demodulation is performed by multiplying the signal by ideal sine and cosine waves, and hence the only source of ZRO is signals at f_{0x}.

ZRO fulfilling this condition can be identified as residing in either the sensor element, the interface electronics, or an unintended interaction between the two resulting from packaging anomalies. In this analysis, sensor packaging will not be addressed. The sources residing in the sensor element can be further divided into two groups, those resulting from the off-diagonal terms in the 2-D EoM (2.18) and those resulting from other non-idealities.

As described in Section 2.1.4, the sources resulting from the off-diagonal terms in the 2-D EoM are 1) the mechanical quadrature signal [35, 47, 57, 105] and 2) the signal resulting from the non-proportional damping [35]. The sources related to other non-idealities of the sensor element are 3) the direct electrical cross-coupling of the primary resonator excitation signal to the secondary resonator detection [105] and 4) the direct excitation of the secondary resonator by the primary resonator excitation signal [47, 106]. In the electronics, the possible sources of ZRO are 5) the non-zero middle electrode biasing impedance and 6) the cross-coupling of the primary signal and different clock signals to the secondary resonator detection.

Throughout the following analysis, it will be assumed that the voltage signal used to excite the primary resonator is

$$V_{exc}(t) = V_{DC} + V_{AC} \cdot \cos(\omega_{0x} t), \qquad (6.2)$$

and that the resulting primary resonator motion is

$$x(t) = A_x \cdot \sin(\omega_{0x} t). \qquad (6.3)$$

Further, the gain and phase shift of the secondary resonator detection circuit (displacement-to-voltage converter) at the operating frequency ω_{0x} are assumed to be $G_{V/y}$ and θ, respectively.

6.1.1 Mechanical Quadrature Signal

The mechanical quadrature signal [35, 47, 57, 105] is generated when the primary resonator movement couples directly to the secondary resonator as a result of the non-diagonal terms in the spring matrix **k** of the 2-D EoM. The magnitude of the force generated is directly proportional to the primary resonator displacement. Hence, the mechanical quadrature signal at the output of the detection circuit can be written as

$$V_{in,sec,qu}(t) = \alpha A_x G_{y/F} G_{V/y} \cdot \sin(\omega_{0x} t + \phi + \theta), \qquad (6.4)$$

where α is a parameter that determines the magnitude of the coupling. With the parameters defined in Section 2.1.4, α is equal to $-k_{yx}$.

Various ways to bring the mechanical quadrature signal to a desired level or to remove it completely were discussed in detail in Chapter 5. The magnitude of the mechanical quadrature signal can be controlled by element design, by process control, and by post-manufacturing trimming and screening. The remaining signal can be compensated either by using electrostatic forces or by canceling the signal fully electronically. The compensation can be performed in either open or closed loop. The choice of different methods is dependent on the targeted performance and cost.

When the mechanical quadrature signal is compensated in closed loop, either electrostatically or fully electronically, the compensation affects the ZRO caused by the other sources through the phase shifts $\overline{\phi}$ and θ in the synchronous demodulation. The interactions resulting from electrostatic compensation performed with a dc voltage (the third method described in Section 5.1) will be analyzed in detail in Section 6.2.

6.1.2   Non-Proportional Damping

If there are off-diagonal terms in the damping matrix **D** in the 2-D EoM, a force proportional to the velocity $A_x \omega_{0x} \cdot \cos(\omega_{0x}t)$ of the primary resonator will be acting on the secondary resonator [35]. At the output of the detection circuit, this signal can be expressed as

$$V_{in,sec,da}(t) = \beta A_x \omega_{0x} G_{y/F} G_{V/y} \cdot \cos(\omega_{0x}t + \phi + \theta), \qquad (6.5)$$

where β is a parameter that determines the magnitude of the non-proportional damping[2]. Again, with the parameters defined in Section 2.1.4, β is equal to $-D_{yx}$.

The only way to minimize this source is to minimize the parameter β by mechanical design. To keep the source stable, β, together with the gain $A_x \omega_{0x} G_{y/F} G_{V/y}$, needs to be kept stable.

6.1.3   Electrical Cross-Coupling in Sensor Element

In electrical cross-coupling [105], the primary resonator excitation signal couples to the secondary resonator detection circuit through stray capacitances. Because only the time-varying component $V_{AC} \cdot \cos(\omega_{0x}t)$ can couple through capacitances, the cross-coupled signal at the output of the detection circuit can be written as

$$V_{in,sec,cc}(t) = \gamma V_{AC} \cdot \cos(\omega_{0x}t + \theta), \qquad (6.6)$$

where γ is a parameter that determines the magnitude of the cross-coupling. Fig. 6.1 shows the electrical cross-coupling path through the capacitor C_{par} to the input of a de-

---

[2]In this thesis, the symbol β is also used to describe the shape of the Kaiser window. If there is a possibility that the two meanings of β can be confused, the meaning is clearly stated in the text.

tection circuit implemented as a charge integrator. Disregarding the other components for now, $\gamma = -C_{par}/C_f$.
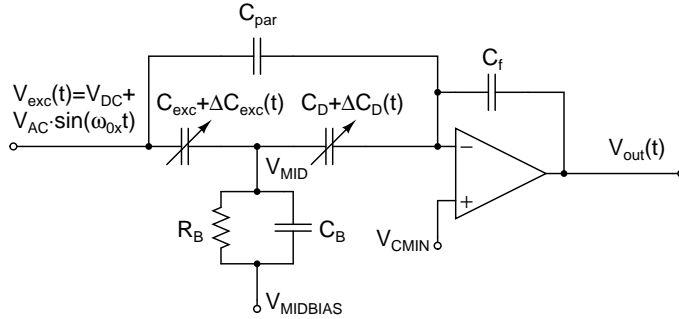
Figure 6.1 Possible sources of electrical cross-coupling in the sensor element.

There are several ways to avoid electrical cross-coupling. First, and most obviously, the stray capacitances should be kept as small as possible. Next, in the case of differential detection, the cross-coupling to both inputs should be as symmetrical as possible, in order to have the coupled signal as a common-mode component in the input and hence rejected by the detection circuit. Additionally, if the excitation is differential, both signals should cross-couple symmetrically to the detection circuit so that they cancel each other.

Third, the primary resonator excitation and secondary resonator detection can be separated in the frequency domain. This can be done either by exciting the primary resonator at $\omega_{0x}/2$, which is made possible by the quadratic relationship between the excitation voltage and force, or by modulating the secondary signal to a higher frequency for detection [107].

Fourth, the primary resonator excitation and secondary resonator detection can be separated in the time domain as well. This means that the excitation and detection are performed in separate phases, leading to a discrete time implementation. Finally, the source of cross-coupling could be eliminated by using some other form of excitation than electrostatic, such as magnetic [77].

To keep the output signal caused by cross-coupling constant, the product γV_{AC} should be kept constant. In other words, both the strength and the source of cross-coupling should be as stable as possible throughout the full range of operating conditions.

As an additional remark, if the $\Sigma\Delta$ modulation described in Section 4.3 is used in the primary resonator excitation, the quantization noise of the excitation signal can also cross-couple to the secondary resonator readout circuit. This will appear as additional noise in the angular velocity output. The properties of the cross-coupling signal, together with possible methods to minimize it, were studied at the end of Section 4.3.

6.1.4   Direct Excitation of Secondary Resonator

The direct excitation of the secondary resonator by the primary resonator excitation signal [47,106] (called "direct motion coupling" in [106]) means that as a result of non-idealities in the sensor element, the voltage signal $V_{exc}(t)$ used to excite the primary resonator also excites a motion in the secondary resonator through the term F_y in the 2-D EoM (2.18). As in the primary resonator, the magnitude of the force created and hence also the amplitude of the cross-coupled signal is relative to the product $V_{DC}V_{AC}$. Therefore, the magnitude of this signal at the output of the detection circuit can be written as

$$V_{in,sec,de}(t) = \delta V_{DC} V_{AC} G_{y/F} G_{V/y} \cdot \cos(\omega_{0x} t + \phi + \theta), \qquad (6.7)$$

where δ is a parameter that determines the magnitude of direct excitation.

The only ways to eliminate the effect of direct excitation are either to ensure the orthogonality of the primary resonator excitation force and the secondary resonator motion by element design, by process control, or by post-process trimming and screening, or by exciting the primary resonator in such a way that the secondary resonator cannot respond to it directly. It should be observed that if the secondary resonator movement rises from the primary resonator movement through anisoelasticity, the resulting signal will be in quadrature, whereas the signal resulting from direct excitation is in phase with the Coriolis signal.

To keep the direct excitation force and hence the output signal constant, the term δ should be constant, together with the product $V_{DC}V_{AC}$. If the primary resonator vibration amplitude is controlled, then the latter term varies. In this case, the term δ needs to be minimized until the required level of ZRO stability is achieved. The gain $G_{y/F} G_{V/y}$ also needs to be kept constant in order to keep the output signal caused by direct excitation stable.

As described in the previous section, if the $\Sigma\Delta$ modulation described in Section 4.3 is used in the primary resonator excitation, the quantization noise of the excitation signal can cross-couple to the secondary resonator readout circuit. Likewise, it can also excite the secondary resonator through direct excitation. While the primary resonator filters the noise with its high quality factor, the secondary resonator can respond to it directly in low-pass mode operation. Thus, care must again be taken to prevent the cross-coupled quantization noise from degrading the final SNR.

Direct excitation plagues not only vibratory gyroscopes with electrostatic excitation, but also those with piezoelectric excitation. In [108], the sources of the parasitic secondary signal in a tuning fork gyroscope with piezoelectric excitation and piezoresistive detection are analyzed. In the reference, the direct excitation of secondary movement is referred to as "actuation unbalance".

6.1.5   Variation of Middle Electrode Biasing Voltage

Figure 6.1 also illustrates another issue which is related to electrical cross-coupling and needs to be considered. Here, the excitation capacitance C_{exc} and the detection capacitance C_D have a common middle electrode, biased to voltage $V_{MIDBIAS}$ through a parallel combination of R_B and C_B. Now, depending on the biasing impedance $Z_B = R_B/(1 + j\omega_{0x}R_BC_B)$, the actual middle electrode voltage V_{MID} can vary with the frequency ω_{0x}, as a result of the primary resonator excitation signal or time-dependent capacitances. The phase of the voltage variation is dependent on Z_B and the source of the error. This signal traverses directly to the output of the detection circuit through the capacitor C_D, and it also appears in the output because of the variation of the detection bias. The contribution of this source, referred to the output of the secondary resonator detection circuit, can be written as

$$V_{in,sec,mb}(t) = \zeta_I \cdot \cos(\omega_{0x}t + \theta) + \zeta_Q \cdot \sin(\omega_{0x}t + \theta), \qquad (6.8)$$

where ζ_I and ζ_Q describe the magnitudes of the resulting error signals. The parameter ζ_I refers to a signal that is in phase with the Coriolis signal and ζ_Q to a signal that is in quadrature with the Coriolis signal.

Although not explicitly stated in Eq. (6.8) for the sake of simplicity, both ζ_I and ζ_Q can vary proportionally to V_{AC} and A_x. The sensitivity to variation in V_{AC} is because of cross-coupling through the capacitor C_{exc} in Fig. 6.1, whereas the sensitivity to variation in A_x is caused by the time-dependent parts of C_{exc} and C_D. This issue will be addressed again in Section 8.6.4, when methods used to distinguish between the various ZRO sources in measurements will be discussed.

The error signal caused by this effect can be reduced by making the biasing impedance and the ac component of the excitation voltage small enough. Additionally, the methods used to reduce the effect of electrical cross-coupling in the sensor element, including differential excitation and detection, and time and frequency domain multiplexing, are also applicable.

6.1.6   Cross-Coupling in Electronics

Because of parasitic stray capacitances or inductances in the electronics, various signals can couple to the secondary resonator detection circuit and inflict ZRO. The source of coupling can be either the signal from the primary resonator or a clock signal that is synchronized to the primary resonator. The contribution of the clock signals, referred to the output of the secondary resonator detection circuit, can be written as

$$V_{in,sec,el1}(t) = \eta_I \cdot \cos(\omega_{0x}t + \theta) + \eta_Q \cdot \sin(\omega_{0x}t + \theta), \qquad (6.9)$$

where η_I and η_Q describe the magnitudes of the cross-coupled signals. The parameter η_I refers to a signal that is in phase with the Coriolis signal and η_Q to a signal that is in quadrature with the Coriolis signal.

The cross-coupling primary resonator output signal, again referred to the output of the secondary resonator detection circuit, can be written as

$$V_{in,sec,el2}(t) = \iota_I A_x \cdot \cos(\omega_{0x}t + \theta) + \iota_Q A_x \cdot \sin(\omega_{0x}t + \theta), \qquad (6.10)$$

where ι_I and ι_Q describe the magnitudes of cross-coupling. Again, ι_I refers to a cross-coupled signal that is in phase with the Coriolis signal and ι_Q to a signal that is in quadrature with the Coriolis signal. If identical detection circuits are used for both the primary and secondary resonators, the primary signal is $90°$ phase shifted relative to the Coriolis signal, and $\iota_I \ll \iota_Q$. This source of coupling can be significant if the primary and secondary resonator detection circuits are located close to each other, which needs to be the case if good matching of the components in the circuits is required.

6.2 Effects of Synchronous Demodulation

In the previous section, the different sources of ZRO were expressed at the output of the secondary resonator detection circuit in Eqs. (6.4)-(6.10). However, because of the synchronous demodulation, these equations do not directly represent the magnitude of the final resulting ZRO.

After the signals of (6.4)-(6.10) are summed at the output of the detection circuit, they enter the demodulator. The signal at the input of the demodulator is then

$$\begin{aligned}
V_{in,sec}(t) = {} & \alpha A_x G_{y/F} G_{V/y} \cdot \sin(\omega_{0x}t + \phi + \theta) + \\
& \beta A_x \omega_{0x} G_{y/F} G_{V/y} \cdot \cos(\omega_{0x}t + \phi + \theta) + \\
& \gamma V_{AC} \cdot \cos(\omega_{0x}t + \theta) + \\
& \delta V_{DC} V_{AC} G_{y/F} G_{V/y} \cdot \cos(\omega_{0x}t + \phi + \theta) + \\
& \zeta_I \cdot \cos(\omega_{0x}t + \theta) + \zeta_Q \cdot \sin(\omega_{0x}t + \theta) + \\
& \eta_I \cdot \cos(\omega_{0x}t + \theta) + \eta_Q \cdot \sin(\omega_{0x}t + \theta) + \\
& \iota_I A_x \cdot \cos(\omega_{0x}t + \theta) + \iota_Q A_x \cdot \sin(\omega_{0x}t + \theta).
\end{aligned} \qquad (6.11)$$

Next, the signal is downconverted into two components, the in-phase component, which also carries the Coriolis information, and the quadrature component. The downconversion is performed by multiplying by $\cos(\omega_{0x}t)$ for the in-phase component and by $\sin(\omega_{0x}t)$ for the quadrature component[3], and by filtering the signal with a low-pass

---

[3]If the phase shift of the multiplying signals used in the demodulation needs to be taken into account, it

filter. Assuming that there is a further gain of two after the filtering, the resulting output signals from the demodulator are

$$
\begin{aligned}
I_{out,sec} =& \alpha A_x G_{y/F} G_{V/y} \cdot \sin(\phi + \theta) + \\
& \beta A_x \omega_{0x} G_{y/F} G_{V/y} \cdot \cos(\phi + \theta) + \\
& \gamma V_{AC} \cdot \cos(\theta) + \\
& \delta V_{DC} V_{AC} G_{y/F} G_{V/y} \cdot \cos(\phi + \theta) + \\
& \zeta_I \cdot \cos(\theta) + \zeta_Q \cdot \sin(\theta) + \\
& \eta_I \cdot \cos(\theta) + \eta_Q \cdot \sin(\theta) + \\
& \iota_I A_x \cdot \cos(\theta) + \iota_Q A_x \cdot \sin(\theta)
\end{aligned}
\tag{6.12a}
$$

and

$$
\begin{aligned}
Q_{out,sec} =& \alpha A_x G_{y/F} G_{V/y} \cdot \cos(\phi + \theta) - \\
& \beta A_x \omega_{0x} G_{y/F} G_{V/y} \cdot \sin(\phi + \theta) - \\
& \gamma V_{AC} \cdot \sin(\theta) - \\
& \delta V_{DC} V_{AC} G_{y/F} G_{V/y} \cdot \sin(\phi + \theta) - \\
& \zeta_I \cdot \sin(\theta) + \zeta_Q \cdot \cos(\theta) - \\
& \eta_I \cdot \sin(\theta) + \eta_Q \cdot \cos(\theta) - \\
& \iota_I A_x \cdot \sin(\theta) + \iota_Q A_x \cdot \cos(\theta)
\end{aligned}
\tag{6.12b}
$$

for the in-phase and quadrature components, respectively. Now, Eq. (6.12a) gives the ZRO when the mechanical quadrature signal is not compensated, under the assumptions made earlier.

To gain more insight into the result of Eq. (6.12a), it needs to be reduced to input angular velocity. This can be done by dividing by the gain from the input angular velocity to the output of the detection circuit, which is equal to $2 A_x \omega_{0x} G_{y/F} G_{V/y} m_x \cdot \cos(\theta)$, leading to

$$
\begin{aligned}
\Omega_{ZRO,noQC} \approx \frac{1}{2m_x} \Bigg\{ & \beta + \frac{\gamma V_{AC}}{A_x \omega_{0x} G_{y/F} G_{V/y}} + \frac{\delta V_{DC} V_{AC}}{A_x \omega_{0x}} + \frac{\zeta_I}{A_x \omega_{0x} G_{y/F} G_{V/y}} + \\
& \frac{\eta_I}{A_x \omega_{0x} G_{y/F} G_{V/y}} + \frac{\iota_I}{\omega_{0x} G_{y/F} G_{V/y}} + \left[\frac{\alpha}{\omega_{0x}} + \frac{\zeta_Q}{A_x \omega_{0x} G_{y/F} G_{V/y}} + \right. \\
& \left. \frac{\eta_Q}{A_x \omega_{0x} G_{y/F} G_{V/y}} + \frac{\iota_Q}{\omega_{0x} G_{y/F} G_{V/y}} \right] \cdot \tan(\theta) \Bigg\},
\end{aligned}
\tag{6.13}
$$

---

can be included into θ. Then θ represents the total phase error in the synchronous demodulation resulting from the electronics.

where it has also been assumed for the sake of simplicity that $\phi \ll \theta$. From (6.13), it can be seen which parameters affect the input-referred ZRO and how it can be minimized.

When considering the various terms in Eq. (6.13), one should be careful to realize the effect of the variation in the gains $G_{y/F}$ and $G_{V/y}$. Although they have been reduced from the terms α, β, and δ in the equation, their variation still affects the ZRO stability. This is because in open-loop operation, the gain is typically measured when the device is calibrated, after which it is assumed to be stable. If the gain now varies, it inflicts scale factor instability, together with ZRO variation, depending on the magnitudes of α, β, and δ. Naturally, if some form of temperature compensation for the gain is used, it also helps the ZRO stability in this sense.

In a practical implementation, the mechanical quadrature signal $\alpha A_x G_{y/F} G_{V/y}$ can be so high [57] that the degree to which the phase shift θ (or $\phi + \theta$) needs to be controlled to yield good ZRO stability is impractically strict. If the mechanical quadrature signal is, for example, 10 times the full-scale Coriolis signal, then a phase shift of $0.06°$ causes the ZRO inflicted by the mechanical quadrature signal to rise to one percent of the full-scale Coriolis signal. This also means that a tiny variation in the phase shift, or a variation in the gain $G_{y/F} G_{V/y}$, causes significant variations in the ZRO. Additionally, a mechanical quadrature signal 10 times higher than the full-scale Coriolis signal could limit the dynamic range of the secondary resonator detection circuit.

6.3   Effects of Quadrature Compensation

Next, the effect of electrostatic quadrature compensation performed with a dc voltage is analyzed. The compensation is performed in a closed-loop configuration, as described in Section 5.2. The detailed implementation of the feedback loop can be ignored for the purpose of this analysis. A steady-state operation will be assumed, i.e. it will be assumed that there are no transients. This is justified, as it was stated at the beginning that only the dc ZRO will be considered. It will also be assumed that the quadrature compensation at dc is perfect, i.e. there is an ideal integrator in the feedback loop. As the dynamic operation will not be analyzed, the detailed controller parameters are not important as such, as long as they ensure the stable operation of the feedback loop.

When applied, the quadrature compensation drives the signal given in Eq. (6.12b) to zero. When there are no other components apart from the actual mechanical quadrature signal $\alpha A_x G_{y/F} G_{V/y} \cdot \cos(\phi + \theta)$ present, it is nulled, irrespective of the phase shift $\phi + \theta$. However, if the other terms given in (6.12b) are present, they cause a fraction of the mechanical quadrature signal to be left after the compensation, so that the sum is

equal to zero. The remaining mechanical quadrature signal is then

$$
\begin{aligned}
\alpha A_x G_{y/F} G_{V/y} = {} & \frac{\beta A_x \omega_{0x} G_{y/F} G_{V/y} \cdot \sin(\phi+\theta)}{\cos(\phi+\theta)} + \frac{\gamma V_{AC} \cdot \sin(\theta)}{\cos(\phi+\theta)} + \\
& \frac{\delta V_{DC} V_{AC} G_{y/F} G_{V/y} \cdot \sin(\phi+\theta)}{\cos(\phi+\theta)} + \\
& \frac{\zeta_I \cdot \sin(\theta)}{\cos(\phi+\theta)} - \frac{\zeta_Q \cdot \cos(\theta)}{\cos(\phi+\theta)} + \\
& \frac{\eta_I \cdot \sin(\theta)}{\cos(\phi+\theta)} - \frac{\eta_Q \cdot \cos(\theta)}{\cos(\phi+\theta)} + \\
& \frac{\iota_I A_x \cdot \sin(\theta)}{\cos(\phi+\theta)} - \frac{\iota_Q A_x \cdot \cos(\theta)}{\cos(\phi+\theta)}.
\end{aligned}
\tag{6.14}
$$

By substituting this into (6.12a), the ZRO signal in the presence of the quadrature compensation can be written as

$$
\begin{aligned}
I_{out,sec} = {} & \beta A_x \omega_{0x} G_{y/F} G_{V/y} \cdot [\cos(\phi+\theta) + \sin(\phi+\theta)\tan(\phi+\theta)] + \\
& \gamma V_{AC} \cdot [\cos(\theta) + \sin(\theta)\tan(\phi+\theta)] + \\
& \delta V_{DC} V_{AC} G_{y/F} G_{V/y} \cdot [\cos(\phi+\theta) + \sin(\phi+\theta)\tan(\phi+\theta)] + \\
& \zeta_I \cdot [\cos(\theta) + \sin(\theta)\tan(\phi+\theta)] + \\
& \zeta_Q \cdot [\sin(\theta) - \cos(\theta)\tan(\phi+\theta)] + \\
& \eta_I \cdot [\cos(\theta) + \sin(\theta)\tan(\phi+\theta)] + \\
& \eta_Q \cdot [\sin(\theta) - \cos(\theta)\tan(\phi+\theta)] + \\
& \iota_I A_x \cdot [\cos(\theta) + \sin(\theta)\tan(\phi+\theta)] + \\
& \iota_Q A_x \cdot [\sin(\theta) - \cos(\theta)\tan(\phi+\theta)].
\end{aligned}
\tag{6.15}
$$

From Eq. (6.15), it can be seen that while the term $\alpha A_x G_{y/F} G_{V/y}$ has been removed, the effect of the quadrature compensation is present through the sine times tangent and cosine times tangent terms that have appeared in the equation compared to (6.12a). The error terms are not proportional to the magnitude of the uncompensated mechanical quadrature signal $\alpha A_x G_{y/F} G_{V/y}$; they depend only on the phase shift terms ϕ and θ.

If it is assumed again that the element is operated in low-pass mode with $\phi \ll \theta$, then with reasonable values of the phase shift θ, the terms involving the sine times the tangent in (6.15) are rendered negligible compared to the terms involving the cosine. Furthermore, the terms ζ_Q, η_Q, and ι_Q are completely cancelled. The ZRO can then be written as

$$
\begin{aligned}
I_{out,sec} \approx {} & (\beta A_x \omega_{0x} G_{y/F} G_{V/y} + \gamma V_{AC} + \delta V_{DC} V_{AC} G_{y/F} G_{V/y} + \zeta_I + \\
& \eta_I + \iota_I A_x) \cdot \cos(\theta).
\end{aligned}
\tag{6.16}
$$

The equation shows the components that affect the final ZRO after the quadrature compensation. They are the signal caused by non-proportional damping, the signal electrically cross-coupled at the sensor element, and the direct excitation. Additionally, the in-phase error signal caused by the variation of the middle electrode biasing voltage and any cross-coupled clock signals or a component of the signal from the primary resonator that are in phase with the Coriolis signal cause ZRO. Further, the phase shift θ determines the magnitude of the ZRO. If θ is small, then, as a result of the cosine function, the ZRO is not very sensitive to variations in θ. If, for example, θ varies between $1°$ and $2°$, the variation in the ZRO is less than $500\,\text{ppm}$. The ZRO stability is also dependent on the stability of the gain $G_{y/F}G_{V/y}$.

After reducing (6.16) to input angular velocity, it can be written as

$$\Omega_{ZRO,QC} \approx \frac{1}{2m_x}\left[\beta + \frac{\gamma V_{AC}}{A_x\omega_{0x}G_{y/F}G_{V/y}} + \frac{\delta V_{DC}V_{AC}}{A_x\omega_{0x}} + \frac{\zeta_I}{A_x\omega_{0x}G_{y/F}G_{V/y}} + \right.$$
$$\left. \frac{\eta_I}{A_x\omega_{0x}G_{y/F}G_{V/y}} + \frac{\iota_I}{\omega_{0x}G_{y/F}G_{V/y}}\right]. \tag{6.17}$$

Compared to (6.13), the terms involving α, ζ_Q η_Q and ι_Q have been removed. Otherwise, identical methods can be applied to minimize the input-referred ZRO.

6.4   Effects of Temperature

As was stated at the beginning of this chapter, the most important parameter regarding ZRO is often not its absolute value but its stability over time and in the presence of environmental variations. Typically, temperature is one of the most significant environmental parameters that affects ZRO. Because the various ZRO sources depend heavily on the actual implementation, a general theoretical analysis of ZRO stability over temperature is not possible. However, by examining Eqs. (6.12a) and (6.15), some general remarks on its stability can be made.

The first remark is that the same terms which affect the gain stability (Section 3.6), that is, the resonance gain, the vibration amplitude A_x, the resonance frequency of the primary resonator ω_{0x}, and the phase shifts ϕ and θ, affect the ZRO. Hence, by optimizing the gain stability, the ZRO stability is also improved. Especially when quadrature compensation is not applied, variation in the phase shifts can cause significant ZRO variation, as already mentioned.

Second, the dc and ac components of the excitation voltage V_{DC} and V_{AC} can be seen in two of the ZRO terms, in the electrical cross-coupling in the sensor element and in the direct excitation of the secondary resonator. While the product of the terms must vary in order to control the primary resonator vibration amplitude, the cross-coupling

source in the electrical cross-coupling can be stabilized by using a constant V_{AC} and by controlling V_{DC}.

Third, the stability of the various parameters (α, β, γ, δ, $\zeta_{I/Q}$, $\eta_{I/Q}$, and $\iota_{I/Q}$) needs to be considered. This is where it is the most difficult to draw any general conclusions. The effect of the parameter α (mechanical quadrature signal) can be eliminated by applying quadrature compensation. The parameter β (non-proportional damping) is likely to be temperature-dependent, especially if gas damping dominates the total damping in the sensor element. All the other terms with their temperature stabilities depend very greatly on the implementation of the mechanical element and of the electronics, on the packaging, or on all of these factors.

6.5   Discussion

In this chapter, the ZRO of a micromechanical vibratory gyroscope with capacitive excitation and detection was analyzed. Different ZRO sources were identified on the basis of the literature, and they were given a uniform mathematical representation. These sources were: the mechanical quadrature signal; non-proportional damping; electrical cross-coupling in the sensor element; direct excitation of the secondary resonator; variation in the middle electrode biasing voltage, and the cross-coupling of either various clock signals or the primary resonator output signal in the electronics.

After this, how the signals caused by various sources express themselves after synchronous demodulation was analyzed, together with the effect of electrostatic quadrature compensation performed with a dc. It was found out that the two cases resemble each other, with the difference being that when electrostatic quadrature compensation is applied, the sources in quadrature with the Coriolis signal are eliminated under the assumptions made. Most importantly, the ZRO caused by the mechanical quadrature signal is removed, which is an expected result. Finally, the temperature stability of the ZRO was briefly considered.

Chapter 7

Capacitive Sensor Readout

The readout of a micromechanical gyroscope involves converting the position information of the primary and the secondary resonators into a form suitable for further processing[1]. The position information can be encoded in different forms, such as capacitance, resistance, or voltage, depending on the readout mechanism. Various readout mechanisms were introduced briefly in Section 2.3.

In case of a sensor element with capacitive detection, the position is encoded as capacitance between two or more separate electrodes in the sensor element. These capacitances can be configured in different ways, as shown in Fig. 7.1. The simplest way is to have a single position-dependent capacitor, as in Fig. 7.1 (a). By adding another capacitor with an opposite positional dependency, the capacitive half-bridge shown in Fig. 7.1 (b) is achieved. Two of these half-bridges can be combined to form a pseudo-full bridge as shown in Fig. 7.1 (c). Finally, the capacitive full bridge is formed by four independent electrodes and four position-dependent capacitors between them (Fig. 7.1 (d)).
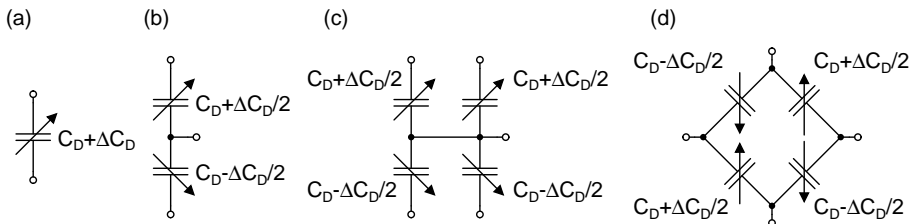
Figure 7.1 Different configurations of the detection capacitances. (a) Single capacitance. (b) Capacitive half-bridge. (c) Capacitive pseudo-full bridge. (d) Capacitive full bridge.

---

[1]This process is also commonly referred to as "detection". Both terms are used interchangeably in this thesis.

Typically, the capacitive position signal is first converted to voltage[2] [109]. There-after, it can be further processed with standard signal processing blocks, such as filters, amplifiers, and data converters. Another way is to convert the capacitance directly to a digital word with a suitable capacitance-to-digital (C/D) converter. This chapter mostly concentrates on C/V converters. The electromechanical $\Sigma\Delta$ loop described in Section 7.3.3 inherently provides a digital output. Additionally, some further remarks on C/D implementations are made in Section 7.3.4.

There are two fundamental ways to perform C/V conversion. One way is to use a continuous-time front-end that converts the capacitance to a continuously varying volt-age. Another alternative is to use an SC front-end, in which the detection capacitance is embedded into the SC structure. This is possible, as the capacitances of micromechan-ical sensor elements are typically in the picofarad range, comparable to the capacitors in a typical IC technology.

An alternative technique for C/V conversion is provided by capacitance-to-frequen-cy (C/f) conversion. In C/f conversion, the capacitive position information modulates the frequency of an output signal. A C/f converter can be implemented as an oscillator whose output frequency depends on the detection capacitance. As no implementa-tions related to the readout of a micromechanical gyroscope have been reported in the literature, C/f conversion will not be discussed in any more detail.

C/f conversion should be distinguished from the detection method used in the reso-nant output gyroscope presented in [61]. Whereas a C/f converter converts the capaci-tance of a capacitor to a frequency, the resonant output gyroscope contains a resonator, whose resonance frequency ω_0 is proportional to the input angular rate. This means that the resonant output gyroscope does not contain the angular rate-to-capacitance conversion which is required by a readout performed using C/f conversion.

This chapter first describes the electrostatic effects related to capacitive readout. These result from the electrostatic forces that act between the plates of a detection capacitance as a result of biasing. Next, the chapter describes continuous-time front-ends, which are divided into those operating at the resonance frequency of the mi-cromechanical element and those that modulate the signal to a higher frequency. Dif-ferent implementations that are described include the transimpedance amplifier and different voltage buffers. Then a brief introduction to discrete-time signal processing will be provided. After that, different SC discrete-time front-ends, including voltage amplifiers, electromechanical $\Sigma\Delta$ loops, and various other implementations will be pre-sented. The chapter concludes with a discussion and a brief comparison between the front-end types that have been introduced.

---

[2]To be precise, capacitance is always first converted to charge, and the charge subsequently to voltage.

7.1 Effects of Electrostatic Forces

As described in Section 2.3, there are various undesired side effects related to different excitation and detection methods. In capacitive detection, the side effects result from the electrostatic forces. To measure the capacitance between two electrodes, the structure needs to be biased, either with a known voltage or charge. This biasing then results in attractive electrostatic forces between the electrodes, as described in Section 4.1 when an electrostatic actuator was studied. These forces can affect the resonator parameters or even distort the capacitance being measured.

If the detection capacitance is formed by the comb structures shown in Fig. 4.2, the resulting electrostatic force is constant, regardless of the displacement, as shown in Eq. (4.14). This means that the applied detection bias results in an offset in the capacitance being measured. The offset can be canceled to a certain degree with the differential structures shown in Figs. 7.1 (b)-(d), depending on the matching of the parameters of the individual capacitances.

On the other hand, if the detection capacitance is formed by the parallel-plate structure shown in Fig. 4.1 and if the structure is biased using a constant voltage, then the electrostatic forces are nonlinearly dependent on the displacement, as shown in Eq. (4.4). As already discussed in Section 4.1, this leads to electrostatic spring softening, an effect which alters the resonance frequency of the resonator. Additionally, if the displacement is large compared to the initial gap, the nonlinearity of the electrostatic forces causes distortion to the displacement being measured.

These effects can be avoided by using constant-charge biasing, which again leads to constant electrostatic forces, as in the comb structure. However, because of the difficulty of maintaining the constant charge bias, a constant-voltage bias is often employed in capacitive detection. In the following two subsections, the effects of spring softening and nonlinear electrostatic forces will be analyzed. Additionally, some methods for improving the linearity degraded by the nonlinear electrostatic forces will be discussed.

Another possible source of nonlinearity in capacitive detection that needs to be considered is the relationship between the displacement x and the detection capacitance C_D. Again, in the comb structure, the relationship is linear to the first order, whereas it is strongly nonlinear in the parallel-plate structure. This source of distortion has to be distinguished from the distortion caused by the electrostatic forces, as it is a property of the displacement-to-capacitance conversion and affects the detection even if the electrostatic forces are not present[3].

---

[3]These two sources of distortion are still related, as the electrostatic force is proportional to the derivative of the detection capacitance with respect to the displacement. Therefore, if the displacement-to-capacitance conversion is linear, the electrostatic force is signal-independent. Only with a nonlinear displacement-to-capacitance conversion does the electrostatic force become signal-dependent (and possibly also nonlinear).

7.1.1   Spring Softening

The electrostatic force resulting from a constant-voltage biasing of a parallel-plate structure was given in Eq. (4.4). Rewritten here,

$$F_{es} = -\frac{A\varepsilon_0\varepsilon_r V^2}{2(x_0 + x)^2}. \tag{7.1}$$

The equation and the following analysis are written for the x-directional displacement. However, they are applicable to other directions as well, by simply replacing the parameters x_0 and x with the respective parameters for the direction of interest.

With small displacements, the force can be approximated to be linearly dependent on x using the first two terms of the Taylor series[4]. This results in electrostatic spring softening, which was described in detail in Section 4.1. The effective spring constant is then

$$k_{eff} = k + k_{es} = k - \frac{A\varepsilon_0\varepsilon_r V^2}{x_0^3}, \tag{7.2}$$

and the resonance frequency

$$\omega_0 = \sqrt{\frac{k_{eff}}{m}}. \tag{7.3}$$

In addition to the spring softening, the constant part of the electrostatic force causes offset. As discussed earlier, this offset can be canceled to a certain extent by utilizing differential structures. However, at the same time, the absolute value of the electrostatic spring constant increases, as the force terms with linear dependency on x are summed.

Electrostatic spring softening thus reduces the resonance frequency. Because of the small amplitude of the Coriolis signal, the electrode area needs to be made large and the gap small in the secondary resonator detection in a typical microgyroscope, in order to maximize the gain in the displacement-to-capacitance conversion. This leads to a more pronounced spring softening in the secondary resonator detection than in the primary resonator excitation or detection, which in turn reduces the mode separation κ and increases the resonance gain. Therefore, in order to achieve a certain mode separation and resonance gain, the secondary resonator resonance frequency ω_{0y} without the bias voltage applied may need to be designed to be significantly higher than the desired resonance frequency in operation. Then, after the bias voltage is applied, the modes are set to their final positions and the desired κ is achieved.

---

[4]The linearization can also be performed around the rest position of the mass after the biasing voltage V is applied. In this case, x_0 needs to be replaced with the resulting gap.

7.1.2 Nonlinear Electrostatic Forces

If the relative displacement x/x_0 is not small, the Taylor series approximation is not sufficient to describe the behavior of the system. Then the complete expression of Eq. (7.1) needs to be used in the 1-D EoM of Eq. (2.5) instead of the Taylor approximation, leading to

$$m\ddot{x} + D\dot{x} + kx = -\frac{A\varepsilon_0\varepsilon_r V^2}{2(x_0 + x)^2} + F. \tag{7.4}$$

The result is a nonlinear differential equation which cannot be solved into a closed form. Hence, numerical methods are needed to verify that the distortion caused by the nonlinear electrostatic forces is not degrading the performance too much. Typically, the Coriolis movement is such a small signal that this source of distortion remains insignificant.

Although it is beyond the scope of this work, it is worth mentioning that in a capacitive microaccelerometer, these nonlinear electrostatic forces can cause significant distortion to the output. The effect has been studied in detail for the differential structure shown in Fig. 7.1 (b) in [26].

If the distortion inflicted by the nonlinear electrostatic forces cannot be disregarded, their effect can be reduced in various ways. The most obvious way is to design the parameters of Eq. (7.4) in such a way that the distortion stays below the permitted level. If this is not possible, for example because it would reduce the sensitivity of the device too much, the nonlinearity can be canceled by keeping the displacement x constant by employing force feedback. Now, the electrostatic force stays constant as well, causing only an offset to the output. A third option is to control the biasing voltages of the capacitances in a differential structure in such a way that the charges and hence the electrostatic forces on both sides are equal. One way to achieve this is the so-called self-balancing bridge (SBB), first presented in [110], with more recent implementations in [24–27].

7.1.3 Pull-In

In the extreme case, the electrostatic forces can lead to a phenomenon known as *pull-in* [111]. In pull-in, the mass-spring-damper system is brought to an area of instability, where the electrostatic force displacing the mass increases more rapidly than the restoring spring force as a function of the increasing displacement. This causes the displacement to grow until the mass collapses either to the detection electrode or to some displacement-limiting mechanism such as a mechanical stopper.

When the detection of a vibratory gyroscope is considered, the pull-in needs to be analyzed as a dynamic phenomenon, with a sinusoidally varying displacement. The achieved results differ from the typical analysis, which assumes the system to be quasi-

static. While a detailed analysis is beyond the scope of this thesis, it can be found, for example, in [98, 99]. Although written for an electrostatic actuator, the concepts are also applicable to capacitive detection. It should also be recognized that long before pull-in, the nonlinearity starts causing significant distortion to the output signal.

7.2 Continuous-Time Front-Ends

Continuous-time front-ends convert the capacitively encoded position information into a continuously varying voltage. They can be divided into two subgroups, those that work at the resonance frequency of the micromechanical element and those that modulate the signal to a higher frequency.

7.2.1 Resonance Frequency Operation

The most straightforward continuous-time implementation is to perform the C/V conversion directly at the resonance frequency of the micromechanical element. If a well-controlled gain is required, the C/V converter can be implemented as a transimpedance amplifier, the schematic of which is shown in Fig. 7.2. In the figure, the amplifier is connected to a capacitive half-bridge. If the detection capacitance were a single capacitor, then a single-ended transimpedance amplifier would be sufficient. The figure also depicts the parasitic capacitances C_P, connected from the amplifier inputs to the ground. If the operating frequency $\omega_{0x} < 1/(R_f C_f)$, the resistance R_f dominates the feedback impedance and the amplifier is called a transresistance amplifier [69, 85]. If, on the other hand, $\omega_{0x} > 1/(R_f C_f)$, the capacitance C_f dominates the impedance. In this case, the amplifier that forms a lossy charge integrator is called a transcapacitance amplifier, or a charge-sensitive amplifier, or, in short, a CSA [69].
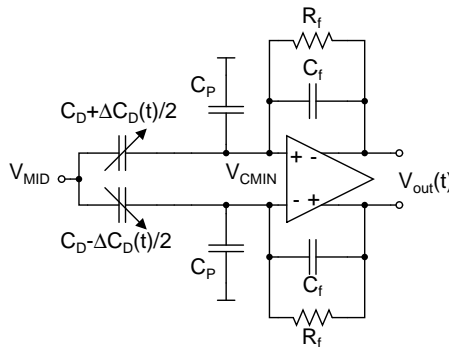
Figure 7.2 Schematic of a transimpedance amplifier, with V_{CMIN} the common-mode voltage at the input.

With an ideal operational amplifier, the transfer function of the transimpedance amplifier from the change in capacitance ΔC_D to the differential output voltage V_{out} is

$$H(s) = \frac{V_{out}(s)}{\Delta C_D(s)} = -\frac{s \cdot V_B/C_f}{s + 1/(R_f C_f)}, \tag{7.5}$$

where $V_B = V_{CMIN} - V_{MID}$ is called the *detection bias*, and C_f, R_f, V_{MID}, and V_{CMIN} are defined in Fig. 7.2. The transfer function is a single-pole high-pass function, with zero at the origin and pole at $1/(R_f C_f)$. An important property of the transfer function is that it is independent of both C_D and C_P.

From the transfer function of Eq. (7.5) it can be seen that the detection bias V_B over the sensor element directly determines the gain. This means that to keep the gain stable, this biasing voltage has to be held constant. If it is assumed that the middle electrode bias voltage V_{MID} is constant, the input common-mode level V_{CMIN} also has to be held constant. Possible reasons why the input common-mode level differs from the output common-mode level include leakage currents drawn by the sensor element, external interference capacitively coupling to the high-impedance input, and variation in the common-mode part C_D of the detection capacitance.

The noise inflicted by the transimpedance amplifier originates from two primary sources, the feedback resistors and the operational amplifier. The power spectral density of noise resulting from the resistors referred to a change in the input capacitance ΔC_D (in F^2/Hz) can be written as

$$C_{n,R}^2 = \frac{8 k_B T}{V_B^2 R_f \omega_{0x}^2}. \tag{7.6}$$

Assuming that the noise of the operational amplifier is dominated by the differential input pair and that the input pair is realized using MOS (Metal-Oxide-Semiconductor) transistors that operate in strong inversion, the power spectral density of the noise resulting from the amplifier can be written as [112, 113]

$$C_{n,opa}^2 = \left[\frac{1 + \omega_{0x} R_f (C_f + C_D + C_P + C_{inW} W)}{V_B R_f \omega_{0x}} \right]^2 \cdot$$
$$\left[\frac{16}{3} k_B T \gamma_n \left(2\mu C_{OX} \frac{W}{L} I_D \right)^{-1/2} + \frac{2 K_F}{C_{OX}^2 W L f_{0x}} \right], \tag{7.7a}$$

where W and L are the dimensions of the input transistor, γ_n the excess noise factor which describes how much the thermal noise differs from the traditional long-channel, strong inversion noise equation, μ the carrier mobility in the channel area, C_{OX} the capacitance of the gate oxide per unit area, I_D the drain current, and K_F the flicker noise coefficient. In Eq. (2) of [17], there is erroneously a factor $8/3$ instead of the

correct value, which is 16/3. C_{inW} is the capacitance per unit width seen at the gate of the input transistor, defined as

$$C_{inW} = CGDO + CGSO + 0.67 \cdot C_{OX} \cdot L, \tag{7.7b}$$

where $CGDO$ and $CGSO$ are the gate-drain and gate-source overlap capacitances per unit width, respectively. It should be observed that while the transfer function of Eq. (7.5) was independent of C_D and C_P, they do affect the noise inflicted by the operational amplifier.

In the case of a CSA, $\omega_{0x} \gg 1/(R_f C_f)$. Now the transfer function can be approximated as $H(s) = V_B/C_f$ and Eq. (7.7a) can be written in simplified form as

$$\begin{aligned} C_{n,opa}^2 &\approx \left(\frac{C_f + C_D + C_P + C_{inW} W}{V_B} \right)^2 \cdot \\ &\quad \left[\frac{16}{3} k_B T \gamma_n \left(2\mu C_{OX} \frac{W}{L} I_D \right)^{-1/2} + \frac{2 K_F}{C_{OX}^2 W L f_{0x}} \right]. \end{aligned} \tag{7.8}$$

From (7.8), an optimal W can be derived for a given C_D and C_f [112]. An optimum exists as an increasing W on one hand increases the input capacitance $C_{inW} W$, leading to an increased noise level but, on the other hand, reduces the thermal noise through increased transconductance and the flicker noise through an increased gate area. If only the thermal noise is considered, the optimum is given by

$$W_{opt} = \frac{C_f + C_D + C_P}{3 \cdot C_{inW}}. \tag{7.9a}$$

Similarly, if only the flicker noise is considered, the optimum is given by

$$W_{opt} = \frac{C_f + C_D + C_P}{C_{inW}}. \tag{7.9b}$$

The final optimal W depends on the contributions of thermal and flicker noise to the total input-referred noise.

As W is increased while the drain current I_D is kept constant, the input pair starts entering first the moderate and ultimately the weak inversion region, as the current density I_D/W decreases. The limits of the different regions are technology-dependent, and they also vary as a function of L. In weak inversion, the transconductance and hence also the thermal noise do not change any more as a function of increasing W. For this reason, in weak inversion, a minimum W always leads to a minimum thermal noise. This can shift W_{opt} to a smaller value than that achieved from Eq. (7.9a), when thermal noise is considered. On the other hand, the optimization of the flicker noise is valid regardless of the region of operation.

The optimization can also be performed with a constant gate-source voltage V_{GS} of the input transistor. Now, I_D/W is constant, leading to slightly different results [56]. As the current density does not change, the input pair stays in the same operating region.

Theoretically, the feedback resistors R_f are not necessary for the operation of a CSA. In practice, however, they are required to set the dc voltage V_{CMIN} at the operational amplifier input. To reduce their noise contribution to one that is as small as possible, they should be dimensioned as large as possible, taking the implementation constraints, including leakage currents and silicon area, into account.

If $\omega_{0x} \ll 1/(R_f C_f)$ and the amplifier is operated as a transresistance amplifier, the effect of C_f can be ignored. In principle, it could be removed from the circuit completely, but practical implementation may require it either for stability reasons or to prevent high-frequency noise from limiting the dynamic range. Assuming that the capacitance C_f is equal to zero, the transfer function of the transresistance amplifier can be written as

$$H(s) = \frac{V_{out}(s)}{\Delta C_D(s)} = s \cdot V_B R_f. \tag{7.10}$$

In this case, the transfer function is that of a differentiator, with a single zero at origin and no poles. The transresistance amplifier causes a $90°$ phase lead to the signal, meaning that if it is used in the primary resonator readout, the excitation loop can be closed directly from the amplifier output.

The input-referred noise of the transresistance amplifier is identical to that of the CSA, and Eqs. (7.8)-(7.9b) are directly applicable if $\omega_{0x} \gg 1/[R_f(C_f + C_D + C_P + C_{inW}W)]$. If not, the approximation made in (7.8) is not valid, and Eqs. (7.9a) and (7.9b) have to be rewritten as

$$W_{opt} = \frac{2 \cdot \sqrt{(C_f + C_D + C_P)^2 + \frac{3}{4\omega_{0x}^2 R_f^2}} - (C_f + C_D + C_P)}{3C_{inW}} \tag{7.11a}$$

for thermal noise, and

$$W_{opt} = \frac{\sqrt{(C_f + C_D + C_P)^2 + \frac{1}{\omega_{0x}^2 R_f^2}}}{C_{inW}} \tag{7.11b}$$

for flicker noise.

The largest issue in the design of a transimpedance amplifier for the readout of a micromechanical gyroscope and for resonance frequency operation is often the need for large time constants in order to avoid attenuating and excessively phase shifting the mechanical signal, which typically has a low frequency. As the resistor quite often also determines the noise level of the amplifier, it needs to be relatively large. As an

example, a gyroscope operating with a resonance frequency of 10 kHz is considered. To implement a CSA with a 10 pF feedback capacitor and a pole frequency which is one tenth of the signal frequency, the resistor size would be approximately 16 MΩ. With $V_B = 5$ V, the input-referred noise of the resistor would be $1.4 \cdot 10^{-19}$ F/$\sqrt{\text{Hz}}$. Depending on the sensitivity of the mechanical element, this can easily be too high for Coriolis signal detection. This means that the resistor size becomes even greater, typically in the range of hundreds of megaohms. Different possibilities to realize the large resistors with their advantages and disadvantages will be considered in more detail in the next chapter, where the implemented CSA is described.

In principle, by using a transresistance amplifier, a smaller resistor can be used to yield an identical gain when compared with a CSA. As the gain of a CSA at the operating frequency is equal to V_B/C_f and that of a transresistance amplifier $\omega_{0x}V_B R_f$, then a feedback resistance

$$R_f = \frac{1}{\omega_{0x}C_f} \tag{7.12}$$

is sufficient to make the gains equal. With the values taken from the previous example, a resistor size of approximately 1.6 MΩ is achieved. This is only one tenth of that required for a CSA. However, it has to be kept in mind that at the same time, the input-referred noise increases according to Eq. (7.6). Other drawbacks of a transresistance amplifier that need to be considered are the amplification of high-frequency noise and possible problems with stability.

If the front-end does not require a well-controlled gain, a voltage buffer can also be used in the readout at resonance frequency. This is the case, for example, in closed-loop detection of the secondary signal where the mechanical movement is canceled by employing force feedback. This readout scheme has been implemented in the primary signal detection of [49], as well as in the detection circuits of [89, 90, 114]. A simplified schematic of the readout electronics is shown in Fig. 7.3 (a). The circuits in [49, 114] use a differential amplifier configured as a voltage follower as in the figure, whereas [89, 90] use a simple source follower instead.

If the input biasing voltage is assumed to be V_{CMIN} when $\Delta C_D = 0$, then the output voltage resulting from ΔC_D is

$$V_{out}(t) = \frac{V_{CMIN} \cdot (C_D + C_P) + V_{MID} \cdot \Delta C_D(t)}{C_D + C_P + \Delta C_D(t)}, \tag{7.13}$$

with C_D, $\Delta C_D(t)$, C_P, and V_{MID} defined in Fig. 7.3 (a). If the detection bias V_B is again defined as $V_B = V_{CMIN} - V_{MID}$, then, by substituting $V_{CMIN} = V_{MID} + V_B$ into Eq. (7.13), the output voltage can be written as

$$V_{out}(t) = V_{MID} + \frac{(C_D + C_P) \cdot V_B}{C_D + C_P + \Delta C_D(t)}. \tag{7.14}$$
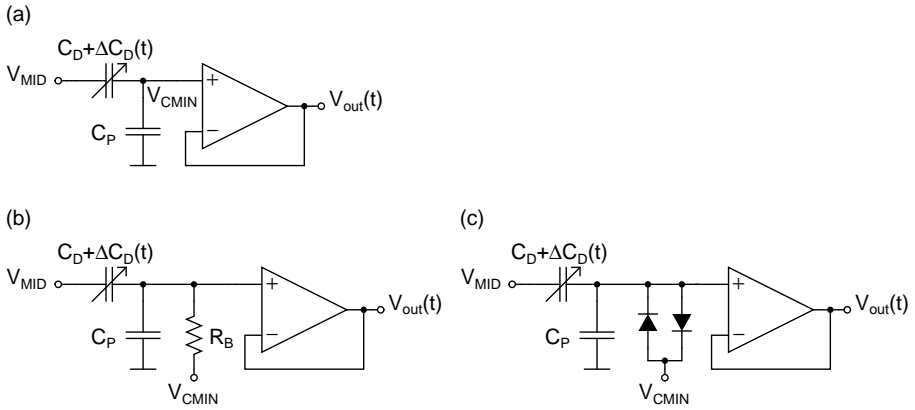
Figure 7.3 Voltage buffer used for capacitive sensor readout. (a) Simplified schematic. (b) Input biasing with a resistor. (c) Input biasing with back-to-back diodes.

Now, if it is assumed that $\Delta C_D(t) \ll C_D + C_P$, then by using the Taylor series approximation, the linear transfer function from the change in capacitance ΔC_D to output voltage V_{out} is

$$H(s) = \frac{V_{out}(s)}{\Delta C_D(s)} = -\frac{V_B}{C_D + C_P}. \tag{7.15}$$

It can be seen that the transfer function is dependent on the size of the detection capacitance, together with any parasitics connected to the input. Both of these can be considered as poorly controlled values. It should also be noticed that the circuit shown in Fig. 7.3 (a) is suitable only for the readout of a single capacitance. If the capacitive element forms a half-bridge, then differential detection is required and the amplifier should be replaced with a fully differential difference amplifier (FDDA) [115].

As with the CSA, the amplifier input also needs to be biased in the case of a voltage buffer. This can be done either with a large resistor, or with two diodes or diode-connected MOS transistors. These cases are shown in Fig. 7.3 (b) and (c), respectively. It should be noticed that after the biasing devices are added, the transfer function of Eq. (7.15) turns into a high-pass transfer function, with a pole at the frequency determined by the RC (Resistor-Capacitor) time constant in the input. All the biasing circuits cause additional noise current to the amplifier input, which needs to be taken into account in the design.

7.2.2 Modulation to a Higher Frequency

As noted in the previous section, performing the continuous-time readout at the resonance frequency of the sensor element leads to certain design complications, together with performance limitations. The most notable of these are the need for large time constants to avoid attenuating the signal and causing excess phase shift, the need for

large biasing resistors to avoid excess noise, and the flicker (1/f) noise inflicted by all the active components. The effects of all of these factors can be reduced if the output signal is modulated to a frequency higher than the mechanical resonance frequency. Typical frequencies used in the modulation range from hundreds of kilohertz to megahertz. This reduces the required time constants by approximately one or two orders of magnitude, and reduces the flicker noise power by the same amount. Additionally, it reduces the magnitude of noise inflicted by the feedback resistors, if their size is kept constant. The drawbacks of the modulation include a possibly higher current consumption, the need for another demodulation (although the two demodulation operations can be combined, as demonstrated in [60]), and the need for the circuitry to generate the carrier signal with sufficient quality.

In principle, the circuit topologies used for the detection of the modulated signal are the same as described in the case of the detection at the resonance frequency. By replacing the dc bias voltage V_{MID} with an ac voltage $V_{mid}(t) = V_{MID} + v_{mid}(t)$, the signal is modulated to the frequency of the carrier signal $v_{mid}(t)$. This frequency will be referred to as $f_{cw} = \omega_{cw}/(2\pi)$.

In case of a capacitive half-bridge, there are two ways to perform the modulation. Either a single-ended carrier can be used to excite the middle electrode and the detection is performed differentially from the outer electrodes, or a differential carrier is used to excite the outer electrodes and detection is performed single-endedly from the middle electrode. These cases are illustrated in Fig. 7.4 for a transimpedance amplifier. The single-ended excitation shown in Fig. 7.4 (a) is easy to perform, but the common-mode charge flowing into and out of the sensor element has to be carefully taken into account in the design. On the other hand, in the case of differential excitation shown in Fig. 7.4 (b), the required precisely balanced carrier $V_{c,cm} \pm V_{c,diff}$ can be difficult to generate, giving rise to offset signals at the carrier frequency. Additionally, in this case, the common-mode noise in the differential carrier is converted to output noise when the differential detection capacitances are not equal.

If only the output common-mode voltage of the operational amplifier in Fig. 7.4 (a) is controlled, the carrier signal $V_{mid}(t)$ is capacitively divided between the detection capacitance C_D and the feedback capacitor C_f. This causes variation in the amplifier input common-mode level, requiring a sufficient input common-mode range (ICMR). The carrier signal over the detection capacitances is also attenuated, affecting the differential signal transfer function $V_{out}(s)/\Delta C_D(s)$.

When the signal is modulated to a higher frequency, it also needs to be demodulated in order to reveal the original angular velocity information. As described in Chapter 2, in vibratory gyroscopes, the angular velocity input is amplitude-modulated to the operating frequency ω_{0x}. A modulating front-end further converts this double sideband amplitude-modulated signal to the carrier frequency f_{cw}. The spectrum of the final
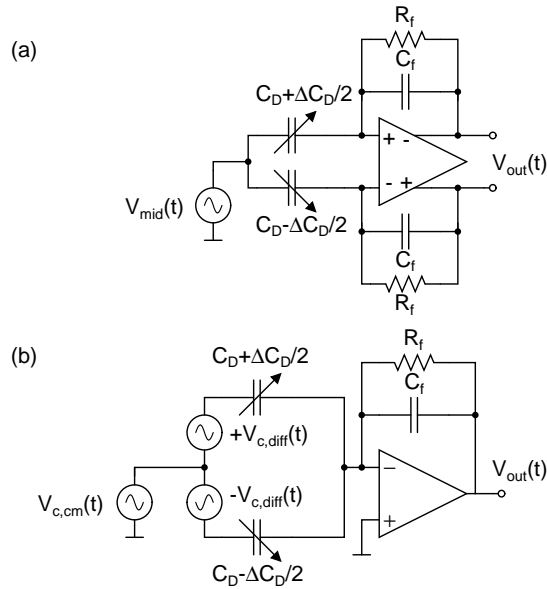
Figure 7.4 Alternative ways to perform modulation with a capacitive half-bridge. (a) Exciting the middle electrode. (b) Exciting the outer electrodes.

output signal is illustrated in Fig. 7.5. This implies that to achieve the original angular velocity, the signal needs to be doubly demodulated, first to ω_{0x} and further to the baseband.

In [107], an example implementation of a modulating front-end for a microgyroscope is presented. The circuit description also includes the switching demodulator used to downconvert the signal to ω_{0x}. Thereafter, it is A/D converted and digitally demodulated to the baseband. Another example is presented in [75]. In that implementation, the signal is modulated to the carrier frequency using a square wave carrier, and the first demodulation is performed by using undersampling before the A/D conversion.

The implementation of [60] gives an interesting example of how a two-axis gyroscope can be read with a single front-end circuit by modulating the two signals to separate carrier frequencies f_{cw1} and f_{cw2}. Two switching demodulators are used to convert the signals directly to baseband, one for each axis. This is made possible by first multiplying the clock signals f_{cw1} and f_{cw2} with f_{0x} using an exclusive-or (XOR) gate, and then using the products to drive the demodulators.

In [57], the use of a CSA and a voltage buffer in a modulating front-end are compared. A similar comparison is performed in [109]. Finally, in the secondary signal detection of [49], a capacitive full bridge is excited with a differential carrier signal and an open-loop amplifier is used to buffer and amplify the resulting voltage.
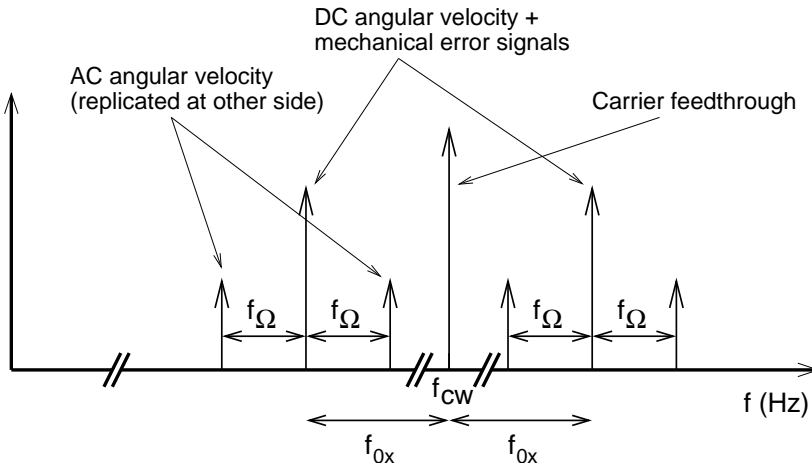
**Figure 7.5** Output spectrum from a modulating front-end.

7.3   Switched-Capacitor Discrete-Time Front-Ends

All the front-ends described so far can be classified as continuous-time circuits. This means that the signal is not time-discretized, or sampled, at any stage during the C/V conversion, but it is defined for any value of the time t. On the other hand, a discrete-time signal is defined only at specific sampling instances. As an example of time discretization, Fig. 7.6 depicts an example of a continuous-time signal and its time-discretized counterpart.

An interface circuit for a capacitive sensor can also be implemented as a discrete-time circuit. This typically leads to an SC implementation. An SC interface circuit takes samples of the capacitive signal and converts them to voltage or directly to a digital word. These samples are then output from the front-end circuit.

A fundamental property of a discrete-time system such as an SC circuit is its sampling frequency f_s. It is the frequency at which samples are taken from the original continuous-time signal. It is typically also the frequency at which the converter outputs the samples, although a discrete-time block can also perform decimation or interpolation, the former referring to a decrease and the latter to an increase in the sampling frequency. Figure 7.6 shows a graphical definition of the sampling frequency, which is the inverse of the period T_s, or $T_s = 1/f_s$.

When designing a discrete-time signal processing system such as an SC C/V converter, the Nyqvist sampling theorem must be taken into account. It states that in a discrete-time signal with a sampling frequency f_s, only signals at frequencies less than $f_s/2$ can be represented. This is also referred to as the Nyqvist frequency. If the continuous-time signal contains components at higher frequencies, they all fold to the band $[0 \ldots f_s/2[$ when sampled. An immediate effect of this is the folding of all
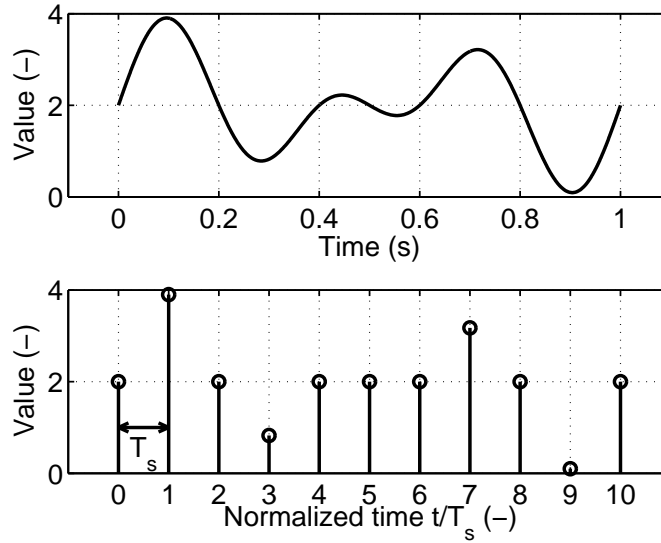
Figure 7.6 (a) Arbitrary continuous-time signal. (b) The same signal discretized in time, with sampling frequency $f_s = 1/T_s$.

wide-band noise in the sampling process. If a white noise source with a power spectral density of v_n^2 and a bandwidth of f_{NBW} is sampled with a frequency f_s, the resulting noise density in the discrete-time signal is $(2f_{NBW}/f_s) \cdot v_n^2$.

7.3.1 Voltage Amplifiers

A straightforward way to implement an SC C/V converter is to start from the basic voltage amplifier shown in Fig. 7.7 (a). The signals ϕ_1 and ϕ_2 are two non-overlapping clock signals, as depicted in the figure. The notion used for the switches means that, for instance, the switch SW1 conducts (is "on" or "closed") when ϕ_1 is high and does not conduct (is "off" or "open") when the clock is low. Similarly, SW2 conducts when ϕ_2 is high and does not conduct when ϕ_2 is low.

During the clock phase ϕ_1, the input signal $V_{in}(t)$ (which can be either continuous or discrete-time) is sampled into the capacitor C_1. Meanwhile, the capacitor C_2 is reset. During the clock phase ϕ_2, the sampled charge is transferred from C_1 to C_2, and the output signal $V_{out}(t)$ after the transfer has finished is equal to $(C_1/C_2) \cdot V_{in}((n_s - 1/2) \cdot T_s)$, with $(n_s - 1/2) \cdot T_s$ the sampling instance (the instance when ϕ_1 goes low) and n_s the sample index. This voltage is now sampled into the load capacitance C_L, and can be transferred to the subsequent signal processing block.

The charge stored in C_1 at the end of the sampling phase is $Q((n_s - 1/2) \cdot T_s) = C_1 \cdot V_{in}((n_s - 1/2) \cdot T_s)$. This implies that the voltage amplifier can be used as a C/V
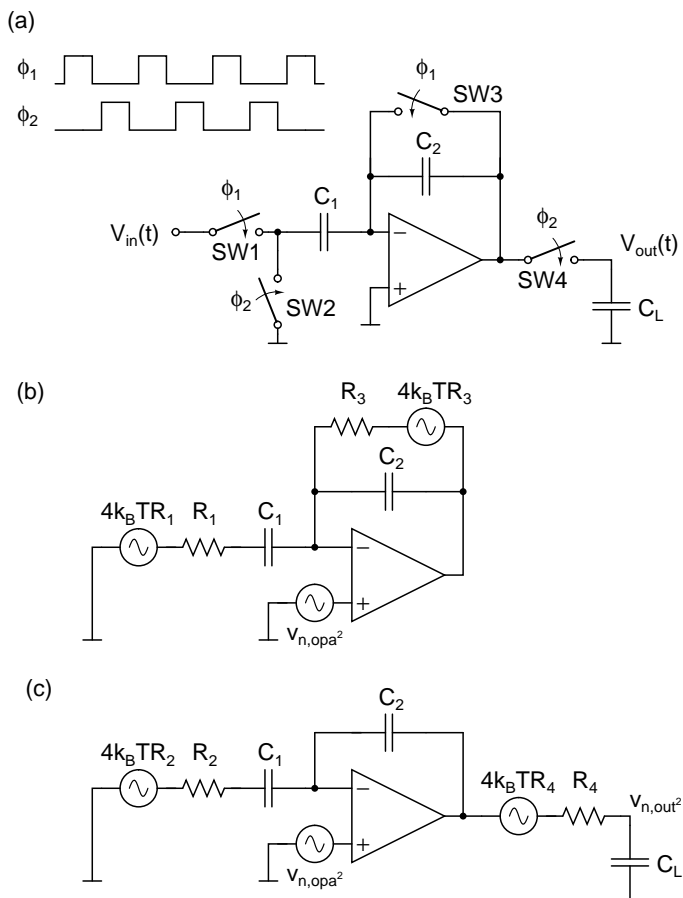
Figure 7.7 (a) Schematic of a basic SC voltage amplifier. (b) Noise sources of the SC voltage amplifier in clock phase ϕ_1. (c) Noise sources in clock phase ϕ_2.

converter, if C_1 is the time-dependent detection capacitance and $V_{in}(t) = V_{REF}$, or a constant dc reference voltage. Now $Q((n_s - 1/2) \cdot T_s) = C_1((n_s - 1/2) \cdot T_s) \cdot V_{REF}$, and the output voltage after charge transfer is $(V_{REF}/C_2) \cdot C_1((n_s - 1/2) \cdot T_s)$. This forms the basis of the operation of all SC front-end circuits for capacitive sensors.

The clock signals for the switches SW1 and SW2 can be interchanged, i.e. SW1 can also be clocked with ϕ_2, and SW2 with ϕ_1. This delays the sampling instance of the voltage amplifier by half a clock period and inverts the gain of the circuit, but otherwise has no effect on the functionality.

A disadvantage with the single-ended readout circuit in Fig. 7.7 (a) is that the static part of the detection capacitance causes an offset to the output of the readout circuit. In a typical microgyroscope, the dynamic part of the secondary resonator detection capacitance can be orders of magnitude smaller than the static part. This means that the dynamic range of the detection circuit is severely limited by the static capacitance.

The problem can be solved by adding another capacitance in parallel with C_1 and charging it to a negative reference voltage $-V_{REF}$. With a properly sized capacitor, the charge from the static part of C_1 can be canceled and hence the dynamic range improved. Another option is to use one of the differential configurations of the detection capacitances (Figs. 7.1 (b)-(c)) with a proper differential front-end circuit. These configurations will be presented later in this section.

The noise of the SC voltage amplifier shown in Fig. 7.7 (a) comes from two sources: from the switches and from the amplifier [116]. Figures 7.7 (b) and (c) show the noise sources in both clock phases. The resistors R_1, R_2, R_3, and R_4 represent the series resistances of the switches SW1, SW2, SW3, and SW4 in Fig. 7.7 (a), respectively, and C_L represents the sampling capacitor of the subsequent stage. If it is assumed that the operational amplifier is a single-stage OTA[5] (Operational Transconductance Amplifier), the *GBW* (gain-bandwidth product) of which is determined by its transconductance g_m and the output load and that $1/g_m \gg R_{1...4}$, and if $C_1 > C_2$[6], then the total mean-square noise power induced by the switches and referred back to the change in the input capacitance can be written as

$$C_{n,sw,rms}^2 \approx \frac{k_B T \cdot g_m R_1 C_1}{V_{REF}^2} + \frac{k_B T \cdot C_2}{V_{REF}^2} + \frac{k_B T \cdot g_m R_2}{\left(\frac{1}{C_1} + \frac{C_L}{C_1 C_2} + \frac{C_L}{C_1^2} \right) \cdot V_{REF}^2} +$$

$$\frac{k_B T}{\left(\frac{C_L^2}{C_1 C_2^2} + \frac{C_L^2}{C_2^3} + \frac{C_L}{C_2^2} \right) \cdot V_{REF}^2}. \tag{7.16a}$$

---

[5]In this thesis, the term *operational transconductance amplifier (OTA)* is used to denote a specific class of operational amplifiers that comprise a single stage and have high output impedance.

[6]With the single-ended implementation shown in Fig. 7.7, this assumption might not be realistic, as it limits the reference voltage V_{REF} to small values. However, if the charge from the static part of the detection capacitance is compensated or a differential configuration is used, then the assumption can be made. It should be noticed that the additional capacitor then doubles the mean-square noise power resulting from C_1, the effect of which is not included in the equations.

In this equation, the first two terms are caused by the noise of SW1 and SW3 sampled into C_1 and C_2, respectively, at the end of clock phase ϕ_1, and the last two terms are caused by the noise of SW2 and SW4 sampled into C_L at the end of clock phase ϕ_2. If $C_2 > C_1$, then the last two terms are not correct, and the noise contribution of SW2 in clock phase ϕ_2 needs to be calculated by integrating the transfer function from the noise source to the output.

By examining the equation, it can be seen that while the first and the third terms contain the factor $g_m R$, which was assumed to be much less than one, and which results from the operational amplifier limiting the noise bandwidth, the second and the fourth terms do not contain this factor. This means that the terms without the bandwdith limitation will dominate the noise contribution of the switches.

The input-referred mean-square noise power caused by the operational amplifier is given by

$$C^2_{n,opa,rms} = \frac{4\gamma_n k_B T}{3} \cdot \left[\frac{C_1}{V^2_{REF}} + \frac{(C_1+C_2)^2}{\left(C_1+C_L+\frac{C_1 C_L}{C_2}\right) \cdot V^2_{REF}} \right]. \tag{7.16b}$$

Here, it has been assumed that the input-referred noise of the operational amplifier consists only of thermal noise, with power spectral density equal to

$$v^2_{n,opa} = \frac{16\gamma_n k_B T}{3 g_m}. \tag{7.17}$$

The first term in Eq. (7.16b) is caused by the noise of the amplifier sampled into C_1 at the end of clock phase ϕ_1 and the second term by the noise sampled into C_L at the end of clock phase ϕ_2.

If the operational amplifier is a multi-stage frequency compensated amplifier with $GBW = g_m/C_C$ instead of a single-stage OTA, the mean-square noise power induced by the switches is

$$C^2_{n,sw,rms} \approx \frac{k_B T \cdot g_m R_1 C_1^2}{C_C \cdot V^2_{REF}} + \frac{k_B T \cdot C_2}{V^2_{REF}} + \frac{k_B T \cdot g_m R_2 C_1^2}{C_C \cdot V^2_{REF}} + \frac{k_B T}{\left(\frac{C_L^2}{C_1 C_2^2} + \frac{C_L^2}{C_2^3} + \frac{C_L}{C_2^2}\right) \cdot V^2_{REF}}, \tag{7.18a}$$

and the mean-square noise power of the operational amplifier is

$$C^2_{n,opa,rms} = \frac{4\gamma_n k_B T}{3} \cdot \left[\frac{C_1^2}{C_C \cdot V^2_{REF}} + \frac{(C_1+C_2)^2}{C_C \cdot V^2_{REF}} \right]. \tag{7.18b}$$

The sources of the various noise terms correspond to those of Eqs. (7.16a) and (7.16b).

The difference is caused solely by the *GBW* difference between the two configurations. It should be observed that the assumption that the amplifier noise is purely thermal might not be reasonable with a simple voltage amplifier, as the flicker noise easily dominates the input-referred noise at low frequencies.

Next, the noise formulae (7.16a) and (7.16b) will be evaluated with representative values, in order to gain some insight into the magnitude of the resulting noise. It is assumed that $C_1 = 4\,\text{pF}$, $C_2 = 1\,\text{pF}$, and $C_L = 1\,\text{pF}$. Further, $f_s = 50\,\text{kHz}$ and $V_{REF} = 2.5\,\text{V}$. The *GBW* of the operational amplifier should be approximately $700\,\text{kHz}$, in order to achieve sufficient single-pole settling for 10-bit accuracy. To achieve this in both clock phases, $g_m = 40\,\mu\text{A/V}$ for a single-stage OTA. Finally, switch on-state resistance is assumed to be $1\,\text{k}\Omega$, and the excess noise factor $\gamma_n = 1$.

By substituting these values and evaluating, the resulting input-referred r.m.s. noise levels are $C_{n,sw,rms} = 33.3\,\text{aF}$ and $C_{n,opa,rms} = 77.4\,\text{aF}$. This yields a total r.m.s. noise of $C_{n,rms} = 84.2\,\text{aF}$ and thus a noise spectral density of $0.53\,\text{aF}/\sqrt{\text{Hz}}$.

If the single-stage OTA is replaced with a multi-stage amplifier, its noise can be reduced to a negligible level by increasing the size of the compensation capacitor C_C. Then only the switch noise $C_{n,sw,rms}$, the value of which does not change significantly from the figures shown above ($C_{n,sw,rms} = 32.4\,\text{aF}$ with a multi-stage amplifier, when $C_C \to \infty$ such that $g_m/C_C = 2\pi \cdot 700\,\text{kHz}$), sets the noise limit[7]. To reduce the noise further, the effect of the wide-band switch noise, in particular that of SW3 folding into C_2, needs to be eliminated.

Analysis of the circuit shown in Fig. 7.7 (a) quickly reveals that it suffers from the offset voltage and the flicker (1/f) noise of the operational amplifier. Because the signal frequency of the micromechanical element is rather low, the flicker noise can easily dominate the whole output noise of the circuit. There are two basic approaches to avoiding this problem, chopper stabilization (CHS) and correlated double sampling (CDS) [117]. CHS means that the polarity of V_{REF} is typically inverted every sampling period. This modulates the capacitive signal around the Nyqvist frequency $f_s/2$, whereas the offset and the flicker noise of the amplifier stay around dc. After demodulation and filtering (in any order), the undistorted capacitive signal can be recovered.

CDS, on the other hand, means that the offset and flicker noise of the operational amplifier are sampled during the reset phase ϕ_1, and subtracted from the output signal during the charge transfer phase ϕ_2. Three alternative circuit configurations that perform such an operation are shown in Fig. 7.8. The circuits in Figs. 7.8 (a) and (b) cancel the offset and flicker noise at the operational amplifier input, whereas the circuit in Fig. 7.8 (c) [118, 119] performs the cancellation at the operational amplifier output. In the third configuration, the falling edge of the clock signal ϕ_1' needs to be

---

[7]The same effect can be achieved by connecting an additional load capacitor to the output of the single-stage OTA and making its capacitance large enough.

sufficiently advanced that the operational amplifier output has time to settle before the clock ϕ_1 goes low. To prevent error in the output voltage, the circuit shown in Fig. 7.8 (c) has to drive either a high-impedance point, such as a voltage buffer, or, alternatively, a virtual ground of the subsequent stage.
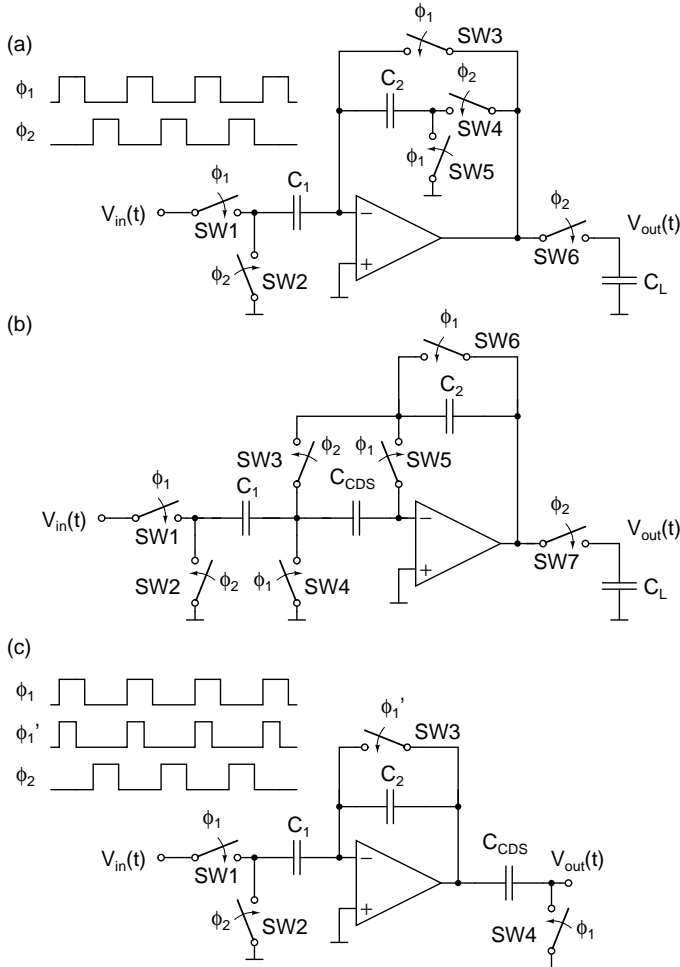
Figure 7.8 Three alternative SC voltage amplifier configurations with CDS. (a, b) Configurations which perform the cancellation at the operational amplifier input. (c) Configuration which performs the cancellation at the operational amplifier output.

CDS creates a high-pass transfer function for the amplifier input-referred low-frequency noise and offset, whereas the signal goes through the same transfer function as in the circuit in Fig. 7.7. Additionally, the CDS configuration in Fig. 7.8 (c) cancels the wide-band thermal noise resulting from the switch SW3 that is sampled into the capacitor C_2.

For the CDS configurations in Fig. 7.8, noise equations similar to those in (7.16a)-

(7.18b) can be written by first identifying the noise sources in both clock phases and then evaluating the noise contribution of each source to the output. Finally, the total output noise is referred back to the input by dividing it by the gain of the circuit. The equations are given in Appendix D.

From the results given in the appendix, it can be seen that the noise properties of the circuit in Fig. 7.8 (b) are inferior compared to the other configurations. This is because the noise of SW1 and SW4 folds into C_1 and the noise of SW6 folds into C_2, both without bandwidth limitation. The noise folding into C_1 is especially detrimental from the noise performance point of view, as $C_1 > C_2$. In the circuits in Figs. 7.8 (a) and (c), the only wide-band switch noise source is the noise of SW2, SW4, and SW6 folding into C_L at the end of clock phase ϕ_2 (Fig. 7.8 (a)), or the noise of SW1 and SW4 folding into C_{CDS} at the end of clock phase $\phi_1 \& \overline{\phi_1'}$ (Fig. 7.8 (c)).

An SC voltage amplifier with CDS is used for both primary and secondary signal detection in [50]. The implementation presented in the paper uses two single-ended circuits identical to the one in Fig. 7.8 (a) to perform the detection of a capacitive half-bridge. The circuit also allows the use of CHS, but its use is not indicated in the publication.

If one terminal of the sensor element needs to be constantly grounded or connected to a fixed voltage, for example because of a large parasitic capacitance towards ground, the configurations shown in Figs. 7.7 and 7.8 can be modified for this purpose. The modified circuits drawn with the time-dependent detection capacitance $C_1 = C_D$ and a fixed reference voltage V_{REF} are shown in Fig. 7.9. The switching configuration shown in Fig. 7.9 (a) can be applied directly to the circuit in Fig. 7.7 and to those in Figs. 7.8 (a) and (c). The configuration in Fig. 7.9 (b) is derived from the circuit shown in Fig. 7.8 (b).

The drawback with the constant grounding of one of the terminals is that while sampling the reference voltage V_{REF} into C_1, the wide-band thermal noise of the reference switch SW1 folds into the capacitor without bandwidth limitation. This leads to a minimum input-referred mean-square noise power equal to $k_B T \cdot C_1 / V_{REF}^2$. With the example values given above ($C_1 = 4\,\text{pF}$, $V_{REF} = 2.5\,\text{V}$, and $f_s = 50\,\text{kHz}$), the minimum r.m.s. noise is $51.5\,\text{aF}$ and the noise spectral density is $0.33\,\text{aF}/\sqrt{\text{Hz}}$.

The effect of this noise source can be reduced by limiting the bandwidth of the buffer driving the reference voltage V_{REF} into the detection capacitance C_1. Because now the buffer limits the noise bandwidth instead of the on-state resistance of SW1, this prevents the full wide-band noise of SW1 from folding into C_1, making possible a significant SNR improvement by reducing the on-state resistance and hence the thermal noise of SW1. Obviously, the bandwidth has to be kept high enough to ensure a sufficient settling accuracy of the reference voltage. Additionally, care must be taken that the noise of the buffer circuit, especially the flicker (1/f) noise, does not degrade
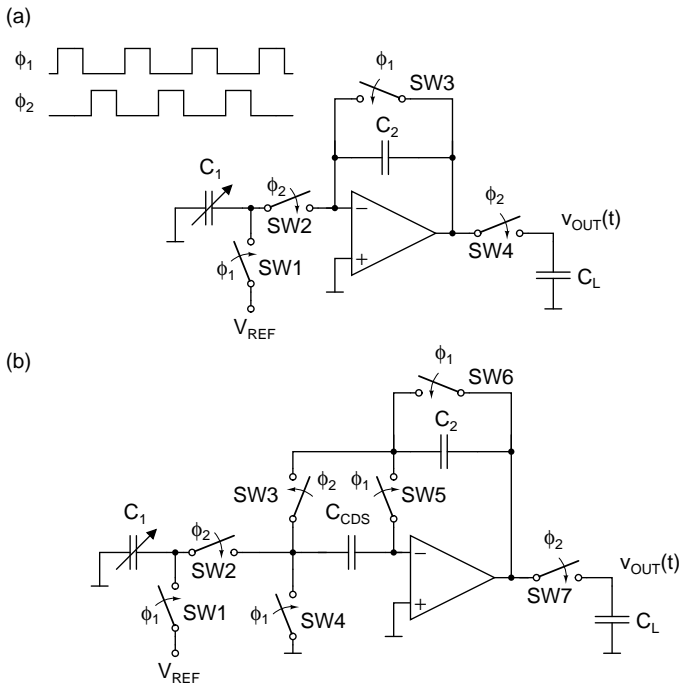
Figure 7.9 (a) SC voltage amplifier with one node of the sensor element constantly grounded. (b) Similar amplifier configuration, with CDS.

the SNR.

The final remark about SC front-ends based on voltage amplifiers is that while all the circuits presented have been drawn for the single capacitance shown in Fig. 7.1 (a), with modifications they can also be applied for the other configurations shown in Fig. 7.1. The pseudo-full bridge (c) and the full bridge (d) can be read directly with a differential version of the front-end circuit, the former with either of those shown in Fig. 7.9 [68] and the latter with those shown in Figs. 7.7 and 7.8. The configurations for the simple voltage amplifier are shown in Figs. 7.10 (a) and (b).

For the half-bridge shown in Fig. 7.1 (b), there are three options. The first is that of [50], where two single-ended circuits are used, one for each side. Next is the configuration shown in Fig. 7.10 (c), where a single-ended front-end is used for the detection of the differential capacitance.

If the common electrode cannot be connected to the virtual ground, the circuits shown in Fig. 7.9 are also applicable, with obvious modifications to the configuration presented in Fig. 7.10 (c)[8]. This configuration can also be used to read the pseudo-full bridge as two parallel half-bridges[9], but there is no advantage to doing this.

---

[8]This leads to a result identical to taking the lower half of the configuration shown in Fig. 7.10 (a)

[9]Which it effectively is.

A final way to read the half-bridge is shown in Fig. 7.10 (d). It should be noticed that while in all the other configurations the common-mode charge is canceled at the input of the operational amplifier, in this configuration, special measures such as the input common-mode feedback circuit of [62] need to be taken to cancel the common-mode charge. On the other hand, the last circuit requires only a single-ended reference, whereas all the others require differential reference voltages. The requirement to handle the common-mode charge resembles that of a modulating front-end presented in Section 7.2.2, where the common-mode charge also needs to be taken into account.
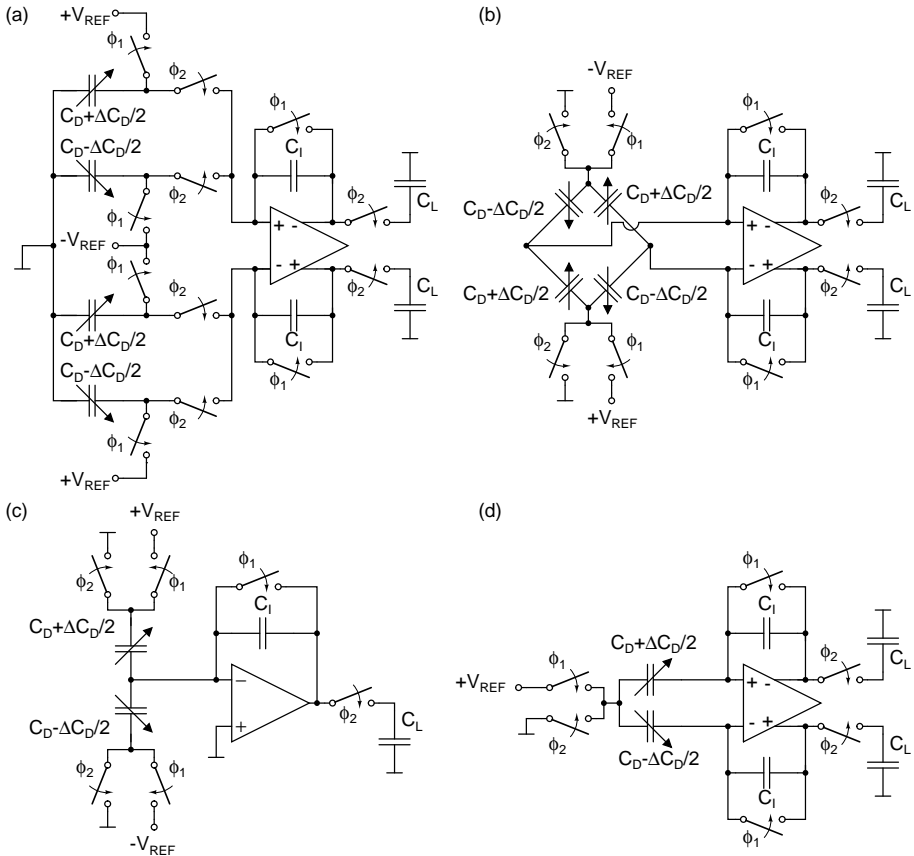
Figure 7.10 (a) Differential circuit to read a capacitive pseudo-full bridge. (b) Differential circuit to read a capacitive full bridge. (c), (d) Circuits to read a capacitive half-bridge.

7.3.2   Noise Bandwidth-Limited Discrete-Time Circuits

The largest issue with all of the SC front-end circuits presented in the previous section is the folding wide-band noise originating from either the switches or from the operational amplifier. Although the noise from the operational amplifier can be made

negligible by using a multi-stage frequency compensated amplifier with a sufficiently large compensation capacitor[10], this increases the current consumption unnecessarily. Even then, the switch noise forms a fundamental noise floor in all the circuits.

A more attractive alternative would be to use some mechanism to limit the bandwidth of the folding noise in an SC front-end circuit. The circuit shown in Fig. 7.8 (c) is used as a starting point, as it always requires a buffering stage to avoid the attenuation of the output signal. Next, the circuit needs to be modified in such a way that first, the noise of the operational amplifier and of the switches SW1 and SW4 sampled into C_{CDS} at the end of clock phase $\phi_1 \& \overline{\phi_1'}$ is either eliminated or compensated in the following stage, and second, the noise of the operational amplifier and the switch SW2 in clock phase ϕ_2 are bandwidth-limited. In this way, the thermal noise of the operational amplifier can be reduced by increasing the transconductance g_m of the input stage, even if a single-stage OTA is used without an additional load.

The resulting circuit is shown in Fig. 7.11 [56, 62, 65, 118]. The first operational amplifier (which now, like all the amplifiers in the circuit, must be an OTA in order to limit the short-circuit current flowing from the outputs through the switches SW4, SW6, and SW8 into ground during the reset phase), together with the capacitor C_I, forms the actual C/V converter stage, followed by two gain stages with gains of C_1/C_2 and C_3/C_4. The gain stages can also act as bandwidth limiters for the noise of the first and the second OTAs, and for that of the switch SW1 in clock phase ϕ_S. With the unusual configuration of the reset switches SW3-SW8, the noise of the first OTA sampled into C_1 at the end of clock phase ϕ_{R2} is eliminated. The reset switches are clocked in such a way that their wideband thermal noise folding into C_I and C_2, together with amplifier flicker noise and offset voltage, is canceled at the output or input of each stage. Only the noise of the last stage is not canceled. This, however, is reduced by the gain of the preceding stages. Additionally, the effect of flicker noise and offset voltage of the last amplifier can be eliminated by using CHS or some other form of CDS in the last stage.

Figure 7.12 shows two possible differential versions of the circuit. The circuit shown in Fig. 7.12 (a) is drawn for the capacitive half-bridge. As in the circuit shown in Fig. 7.10 (d), special measures such as the input common-mode feedback circuit of [62] need to be taken to cancel the common-mode charge at the operational amplifier input. The detection of the capacitive half-bridge could also be performed with the single-ended configuration, as shown in Fig. 7.10 (c). In Fig. 7.12 (b), the configuration is drawn for the capacitive full bridge.

An alternative implementation of the circuit shown in Fig. 7.12 (b) has been presented in [120]. In this realization, the charge integrator has been replaced with a voltage amplifier with gain G, as shown in Fig. 7.13. Now, the wide-band noise of the

---

[10]Or by connecting a sufficiently large additional load capacitor to the output of the single-stage OTA.
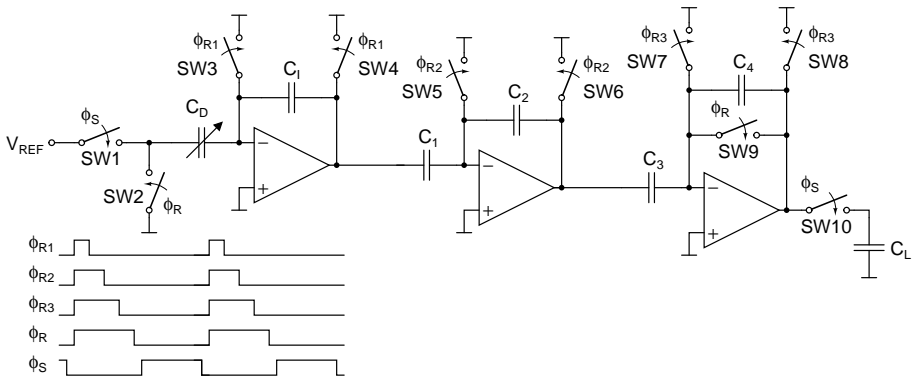
**Figure 7.11** SC readout circuit with CDS that cancels flicker (1/f) noise, offsets, and noise from the reset switches.
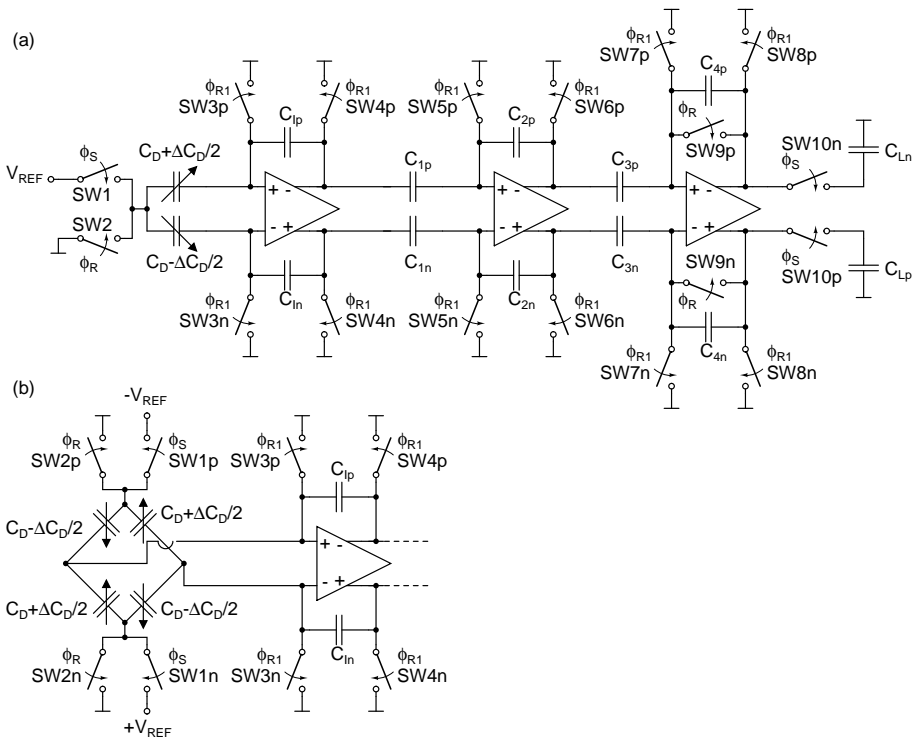
Figure 7.12 Differential version of the SC readout circuit with CDS that cancels flicker (1/f) noise, offsets, and noise from the reset switches. (a) Configuration with capacitive half-bridge. (b) Configuration with capacitive full bridge.

reset switches clocked with ϕ_R folds into the detection capacitances without bandwidth limitation. This could be canceled with a CDS at the output of the voltage amplifier, as in the implementations presented before. In [120], however, CDS is not applied, but the effect of folding noise is reduced by performing the reset only every 16th clock cycle. The implementation presented there also employs CHS to cancel the offset and flicker noise of the operational amplifier. In this configuration, the signal gain becomes sensitive to the possible parasitic capacitances at the input of the voltage amplifier.
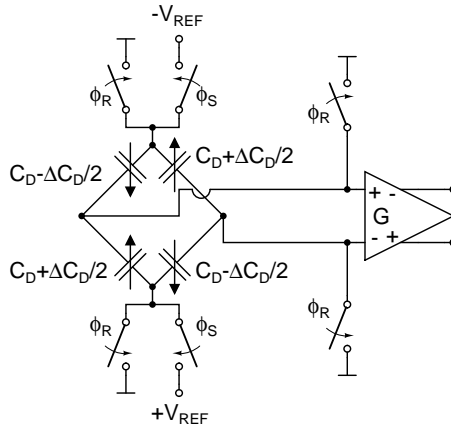
Figure 7.13 Discrete-time readout of a capacitive full bridge, using a voltage amplifier.

Using the configurations presented in this section, an extremely low-noise SC front-end can be implemented. The drawback with the circuit is that it requires one terminal of the sensor element to be switched, while the other is connected to the virtual ground of the operational amplifier. In principle, one terminal of the sensor element could also be grounded or connected to a fixed voltage using the switching configuration used in Fig. 7.9 (a). Then, however, the folding wide-band noise from the reference switch or switches again becomes a limiting factor for the minimum achievable noise level unless a bandwidth-limiting buffer is applied, as described earlier.

7.3.3   Electromechanical ΣΔ Loops

Another widely used discrete-time front-end circuit is called an electromechanical ΣΔ loop. An electromechanical ΣΔ loop is based on an electronic ΣΔ A/D converter or, as it is sometimes referred to, a ΣΔ modulator [100]. Electromechanical ΣΔ loops have been widely used in the readout of micromechanical accelerometers and gyroscopes [52–55, 62–64, 68, 79, 121–123].

It can be argued that the electromechanical ΣΔ loop should be classified as an overall system architecture, with an arbitrary C/V conversion method together with time discretization, signal quantization, and force feedback. The C/V converter could utilize

any of the methods described so far, including the continuous-time implementations. However, in this thesis it is classified as a front-end type of its own because the parts of the loop form an intimate system that would not behave as expected if any of them were missing. In a general feedback system that first performs the C/V conversion at the final desired accuracy and then uses this signal for the force feedback, the system would still give the desired output with the feedback removed, although this can have adverse effects on other parameters, such as linearity. On the other hand, the output signal from an electromechanical $\Sigma\Delta$ loop carries very little useful information until the feedback loop is closed. The electromechanical $\Sigma\Delta$ loop also performs an inherent C/D conversion, unlike a general feedback system, where a separate ADC would be required. Some further remarks on this classification will be given at the end of this section.

A block diagram of a second-order electromechanical $\Sigma\Delta$ loop is shown in Fig. 7.14 [55, 121]. This is the simplest possible loop, with only the micromechanical sensor element acting as a loop filter. The loop filter filters the input force signal $F_{y,all} = F_{y,in} + F_{feedback}$. Here, $F_{y,in}$ contains all the force components acting on the y-directional resonator, excluding the feedback force. These force components include the Coriolis force and the forces inflicted by anisoelasticity and non-proportional damping.

The output of the loop filter is position information, which is converted to voltage, amplified, fed through a compensation filter, and quantized, typically to a single-bit digital output. The output is then converted to the feedback force $F_{feedback}$ and brought to the sensor element, thus closing the loop. After downconverting, decimating, and filtering the single-bit signal, a digital output signal with the final desired resolution is achieved.
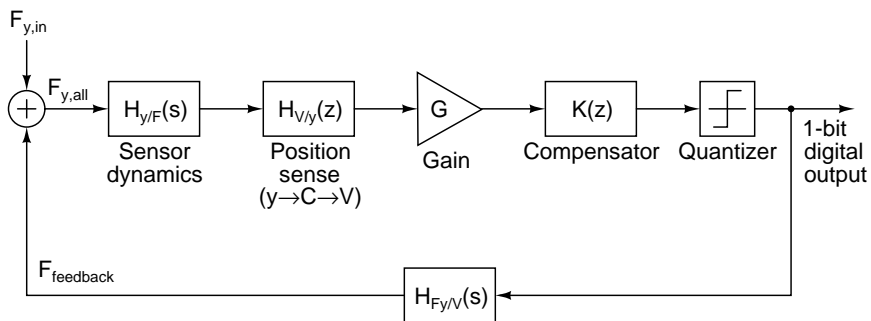
Figure 7.14 Second-order electromechanical $\Sigma\Delta$ loop.

Unlike the case of a $\Sigma\Delta$ A/D converter, the electronic noise added after the loop filter at the input of the position sense circuit has a significant effect on the output noise of the electromechanical $\Sigma\Delta$ loop [56, 63]. This is because the loop filter does not provide enough gain at the signal band to suppress the electronic noise. The gain is

increased with a wide-band gain block. Therefore, the high frequency electronic noise forms a significant part of the quantizer input signal, reducing the quantizer gain and increasing the level of quantization noise at the quantizer output significantly. It has been shown [56] that the quantization noise always dominates the in-band noise of a second-order electromechanical ΣΔ loop, regardless of the oversampling ratio.

In [64, 65], the quantization noise is reduced by replacing the gain block with an electronic resonator, thus creating a fourth-order (two-resonator) bandpass ΣΔ interface circuit. To keep the overall ΣΔ loop stable, feedbacks have to be added from the output into the second resonator as well. Now, the combination of the micromechanical element and the electronic resonator provides high gain only at the signal band, thus reducing the electronic noise at the quantizer input so that the quantization noise dominates the input signal power. This same technique has also been applied to improve the SNR of a micromechanical accelerometer in an electromechanical ΣΔ loop [68, 122, 123]. In this case, the resonator is replaced with either one [122] or two [68, 123] integrators, yielding a high loop gain at dc.

In the case of a third- or fourth-order ΣΔ loop, the signal from the front-end circuit remains usable even if the electrostatic feedback loop is cut, provided that the loop remains stable. In this case, the circuit reduces to a first- or a second-order fully electronic ΣΔ ADC, with a C/V converter driving its input and with no electrostatic feedback. This means that the third- and fourth-order ΣΔ interfaces can be considered to be closer to a traditional feedback system than the second-order loop. However, in this case too, the in-band noise level increases as the order of the ΣΔ loop drops. In [68], an SNR reduction of over 20 dB has been reported for a microaccelerometer when the feedback is cut.

7.3.4   Other Switched-Capacitor Front-Ends

In Section 7.3.1, how an SC voltage amplifier can be utilized as a sensor front-end was described. This was done by replacing the varying input voltage with a constant, known reference voltage and the constant sampling capacitor with the varying detection capacitance. Thus, a charge which is dependent on the detection capacitance is sampled and can be transferred for further processing. The same method can be applied in principle to all switched capacitor circuits, for example other amplifier circuits, filters, and data converters.

For this purpose, SC ADCs form an interesting group of circuits. If the sampling capacitors are replaced with detection capacitors, they can be used to perform a direct C/D conversion. An interface circuit for a micromechanical capacitive pressure sensor has been implemented as a second-order ΣΔ ADC in [124].

As described at the beginning of this chapter, the electrostatic forces imposed by the reference voltages applied between the electrodes of the micromechanical sensor element can distort the displacement being measured. One way to improve the linearity is to use the differential detection capacitance shown in Fig. 7.1 (b), together with the SBB [110], which keeps the charges and hence the electrostatic forces on both sides equal. A complete micropower interface ASIC for a micromechanical capacitive three-axis accelerometer that employs an SBB as the C/V converter has been presented in [24, 25], with a more detailed description of the front-end given in [26, 27].

A front-end circuit that provides a direct C/D conversion and a ΣΔ-modulated output has been presented in [125, 126] and more recently in [28]. As the circuit maintains the average charge integrated from both capacitances of a capacitive half-bridge equal, it also attenuates the nonlinear electrostatic forces, like the SBB. It should be noticed that the circuit does not perform electrostatic force feedback like the electromechanical ΣΔ loop presented in Section 7.3.3, it just tries to null the average electrostatic force acting on the sensor element.

7.4   Discussion

In this chapter, various circuits for the readout of a micromechanical gyroscope with capacitive detection were presented. The circuits were divided into two categories, continuous-time and discrete-time. The continuous-time circuits were further divided into those that perform the readout at the mechanical resonance frequency and those that modulate the position information into a higher carrier frequency.

A continuous-time readout circuit operating at the mechanical resonance frequency can be realized as a transimpedance amplifier (either CSA or transresistance amplifier), or as a voltage buffer, depending on whether a stable gain is required or not. However, the typically low resonance frequency requires the realization of a large time constant, in order not to attenuate and/or excessively phase-shift the signal. The input-referred noise of the resistor used for dc biasing is also higher at low frequencies, typically calling for even greater resistance than that required for the realization of the time constant. The low signal frequency also requires the flicker (1/f) noise contribution of the operational amplifier to be carefully analyzed.

Another option is to modulate the signal to a higher carrier frequency for detection. In this way, both the need for a large resistor and the contribution of the flicker noise are reduced. The drawbacks include a possibly higher current consumption, the need for another demodulation, and the need for the circuitry to generate the carrier signal with sufficient quality.

An alternative approach is to implement the C/V conversion using a discrete-time SC circuit. Now the need for a large resistor bringing the dc bias for the sensor element

is completely eliminated, as the switching takes care of the proper biasing. Additionally, the flicker (1/f) noise of the amplifier can be rejected by employing either chopper stabilization or CDS. The largest drawback with an SC implementation is the noise folding (together with the folding of other interfering signals), which causes the SNR of the front-end circuit to be inferior to that of its continuous-time counterparts. To improve the SNR, either high sampling frequencies need to be employed or the front-end circuit needs to be configured in such a way that the bandwidth from which the noise folding occurs is limited. One possibility for this is the implementation shown in Fig. 7.11. A significant advantage of a discrete-time front-end is the smaller silicon area requirement, as large resistors do not need to be implemented. This makes it a very attractive solution, despite the difficulties involved in reaching a high SNR.

The SC implementation also makes it possible to perform a direct C/D conversion. However, this would again lead to the noise-folding issue. If a sufficient SNR cannot be reached, then the readout needs to be divided into two parts, one performing the C/V conversion and ensuring a sufficient SNR, and the other performing the A/D conversion.

Chapter 8

Implementation

A prototype of a MEMS gyroscope was designed and implemented in order to be able to experimentally study the presented theory and issues related to microgyroscopes, in particular to the design of the interface electronics. The design is based on a bulk-micromachined sensor element designed and fabricated by VTI Technologies, Vantaa, Finland.

This chapter will present the implemented system in detail. First, in Section 8.1, the sensor element and the electrical model used in the design are introduced. Then, in Section 8.2, the structure of the implemented system is described. Next, in Sections 8.3 and 8.4, the various analog circuit blocks used to realize the system are described. In Section 8.5, the digital signal processing part will be introduced. Finally, in Section 8.6, the experimental results are given.

8.1 Sensor Element

The sensor element used in the implemented system is a silicon bulk-micromachined structure, comprising two torsional resonators. An early development version of this element was published in [127]. Detailed characterization data for the current version of the element used in this work are documented in [128].

Figures 8.1 and 8.2 represent the structure of the sensor element. In Fig. 8.1, a schematic drawing illustrates the structural (middle) wafer and the two encapsulating wafers around it. The figure also shows the coordinate system used in this description. In Fig. 8.2, a scanning electron microscope (SEM) image of the structural wafer is shown. The innermost part of the structure is the x-directional primary resonator. It is attached to the surrounding frame by two torsional springs, one at each end of the mass. The frame forms the y-directional secondary resonator. Again, two torsional springs connect it to the supporting part of the wafer. The two sets of springs are located in

such a way that the resonators are ideally orthogonal, with no mechanical coupling between them. Thus, they form two 1-DoF resonators, being in accordance with the theory presented in Chapter 2. The z-directional sensitive axis is perpendicular to the plane of the structural wafer.
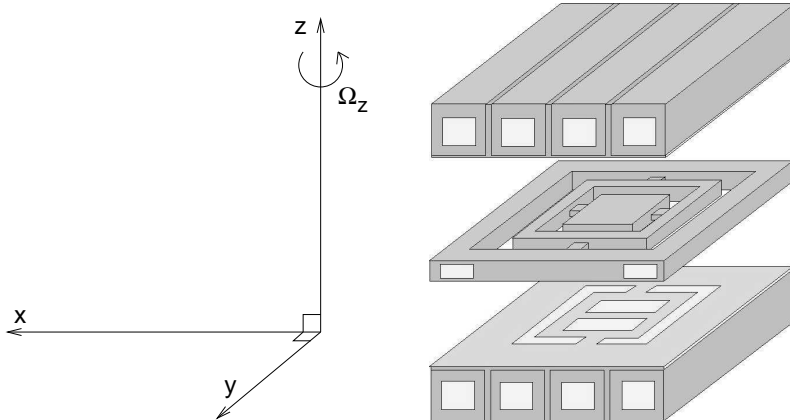
Figure 8.1 Schematic drawing of the structure of the sensor element, with the coordinate system used in the text. (Courtesy of VTI Technologies, Vantaa, Finland)
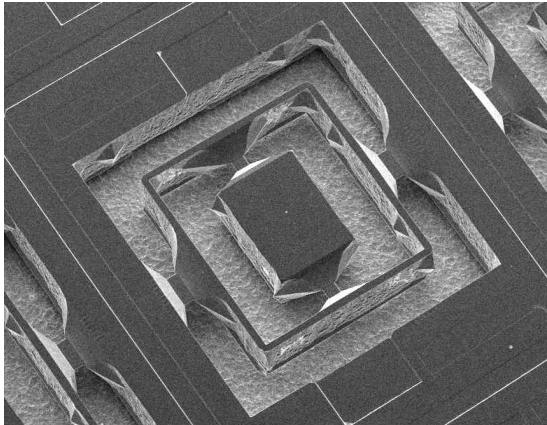
Figure 8.2 SEM image of the structural (middle) wafer. (Courtesy of VTI Technologies, Vantaa, Finland)

The resonance frequency of the primary resonator is $f_{0x} \approx 10\,\text{kHz}$ and that of the secondary resonator $f_{0y} \approx 12\,\text{kHz}$. This yields a mode separation factor $\kappa \approx 1.2$ and thus a moderate resonance gain of 3.27 or about 10 dB.

The excitation and detection are both performed capacitively through the electrodes patterned on the encapsulating wafers. The middle wafer has a low resistivity and is biased at a constant potential, whereas all the other electrodes are independently accessible through external contacts. The excitation of the primary resonator and the

detection of both primary and secondary resonators are all differential. Figure 8.3 shows a simple electrical model of the sensor element. In addition to the excitation and detection electrodes shown in the figure, there is a pair of quadrature compensation electrodes which are used to control the mechanical quadrature signal with a dc voltage, as described in Section 5.1. The most important parameters of the element are summarized in Table 8.1.
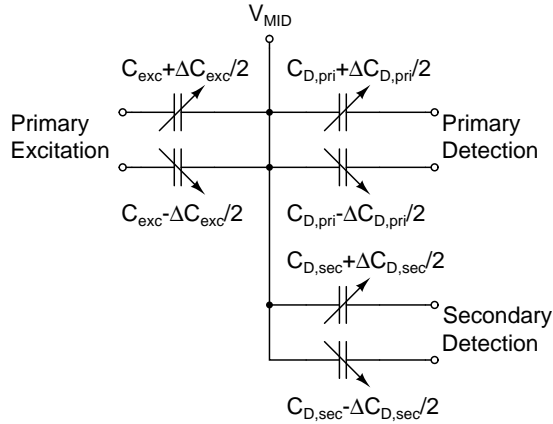
Figure 8.3 A simple electrical model of the sensor element.

Table 8.1 Fundamental parameters of the sensor element.

Primary resonator excitation/detection	
f_{0x}	10 kHz
Static capacitance ($C_{D,pri}$, C_{exc})	0.66 pF
Dynamic capacitance ($\Delta C_{D,pri}$, ΔC_{exc})	0.23 pF (with nominal A_x)
Electrode gap	12 μm
Secondary resonator detection	
f_{0y}	12 kHz
Static capacitance ($C_{D,sec}$)	6.20 pF
Dynamic capacitance ($\Delta C_{D,sec}$)	2.08 aF/$^\circ$/s
Electrode gap	0.75 μm

In Appendix E, a photograph of the sensor element soldered onto a ceramic carrier is shown. This carrier is further soldered onto a PCB, where it is combined with the readout and control electronics.

8.2   System Design

The implemented angular velocity sensor was required to have a digital output, with a full-scale range of $\pm 100°/s$ and a bandwidth of approximately 50 Hz. A continuous-time C/V converter was chosen, as it allows a low noise floor to be achieved. Because of the two-chip implementation, a transimpedance amplifier (CSA) was chosen, as with it the signal gain is insensitive to parasitic capacitances. The sensor element is operated in open loop, because with the moderate resonance gain applied, the element does not limit the system linearity or bandwidth. The A/D conversion of the output signals can be performed either from the resonance frequency or after demodulation. A decision was made to convert the signals from the resonance frequency, because it eliminates the need for analog demodulators without making the ADCs significantly more complicated, and because of the desire to study the use of bandpass $\Sigma\Delta$ ADCs. Various controllers were implemented using DSP, in order to provide flexibility and to study different aspects of the digital implementations, such as the use of $\Sigma\Delta$ modulation in the feedback DACs.

A block diagram of the implemented system is shown in Fig. 8.4. The diagram is divided into three separate parts: the sensor element on the left; the analog part in the middle, and the digital part on the right. The sensor element was introduced in the previous section. The analog part of the system was implemented with a custom ASIC, manufactured using a 0.7-μm high-voltage CMOS technology from AMI Semiconductor Belgium BVBA, Oudenaarde, Belgium. The technology provides analog capacitors and high-ohmic polysilicon resistors, together with high-voltage MOS transistors and diodes. The nominal supply voltage is +5 V. A microphotograph of the implemented ASIC is shown in Appendix F. The manufactured chips were encapsulated into 120-lead CQFP (Ceramic Quad Flat Pack) carriers and combined with the sensor element on a PCB.

The DSP part was implemented with an FPGA (Field Programmable Gate Array) chip (EP1C20F400C7 device from Altera Corporation, San Jose, CA, USA [129]). The chip is mounted on a separate PCB (Altera NIOS Development Board, Cyclone Edition [130]). The two PCBs were connected together with ribbon cables. All the DSP design was done in the VHDL language [131] and synthesized using the software tools provided by the FPGA vendor [132].

In this section, the functionality of the various subsystems will be introduced at the system level. The detailed circuit-level implementations will be presented in Sections 8.3-8.5. The subsystems introduced in this section are the sensor readout and angular velocity detection, the clocking system and synchronous demodulation, the primary resonator excitation, the quadrature compensation, and the system start-up.
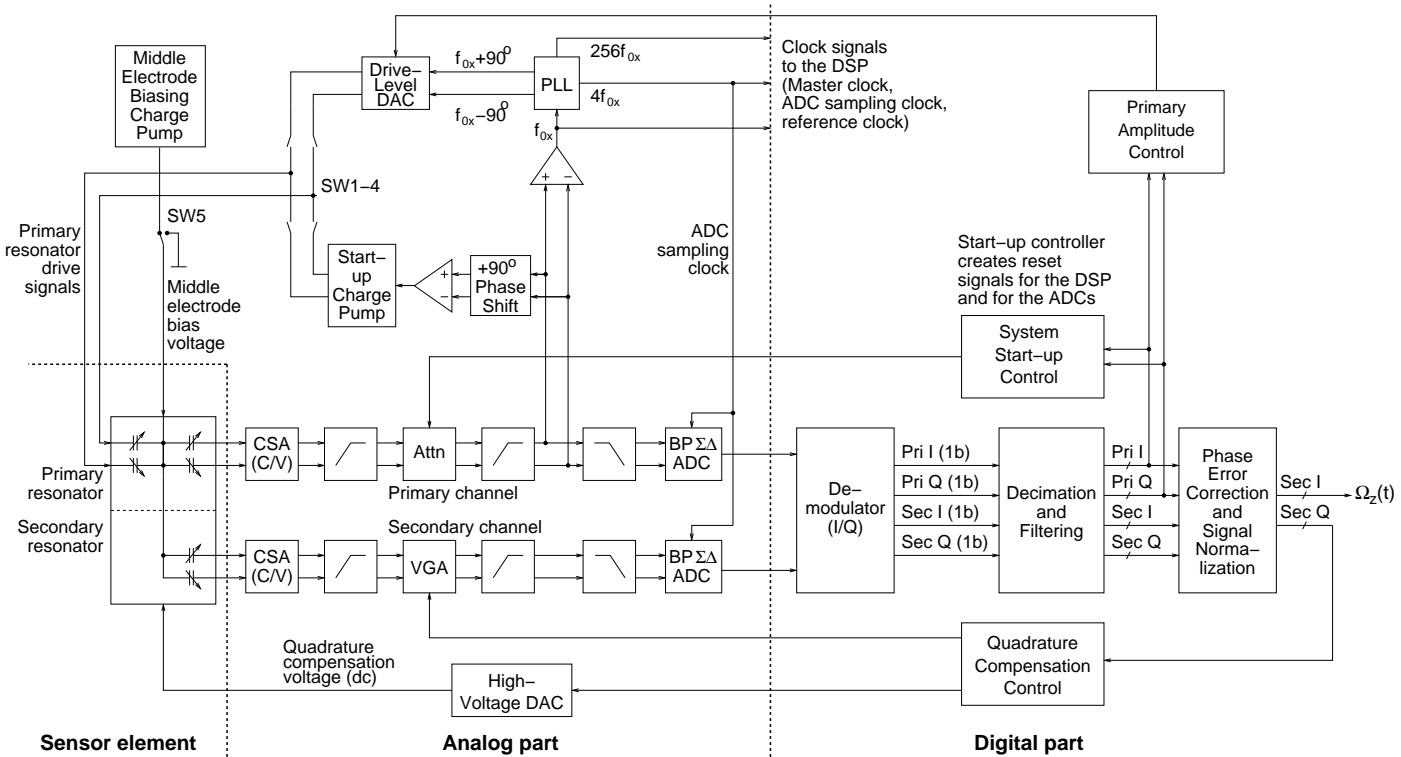
Figure 8.4 A block diagram of the implemented MEMS angular velocity sensor, showing the bulk-micromachined sensor element, the analog part implemented with a custom ASIC, and the digital signal processing part implemented with an FPGA chip.

8.2.1   Sensor Readout and Angular Velocity Detection

The first subsystem, the sensor readout and angular velocity detection, comprises the blocks from the primary and secondary resonator detection electrodes in the sensor element to the angular velocity output in the DSP. The sensor readout is divided into two parallel channels, the primary channel and the secondary channel. They are responsible for the readout of the primary and the secondary resonators, respectively.

In the analog part of this subsystem, the capacitive signals from both the primary and secondary resonators are first converted to voltage with continuous-time CSAs. After C/V conversion, the signals are first high-pass filtered and amplified by $+20\,\mathrm{dB}$ in the first filter. Next, their levels are normalized with a tunable attenuator (Attn) in the primary and a variable-gain amplifier (VGA) in the secondary channel. Then they are high-pass filtered again to remove the dc offset inflicted by the VGA, after which they are low-pass filtered and fed to the A/D converters.

The low-pass filtering is required to prevent the folding noise from causing the SNR to deteriorate in the ADCs. If the filters are required to have any attenuation at the first frequency bands which would fold to the signal band in the sampling process ($3f_{0x}$, $5f_{0x}$ etc.), they are very likely to cause a significant phase delay at f_{0x}. For this reason, the filters can be located only after the primary signal is taken to the PLL. This is because the PLL output is used to close the primary resonator excitation loop, and the phase delay caused by the low-pass filters would reduce the excitation force too much.

Because of the synchronous demodulation used to distinguish between the in-phase and quadrature parts of the output signals, the phase shifts in the primary and secondary channels should be as identical as possible. Additionally, the remaining difference between phase shifts should be as stable over varying operating conditions as possible. By studying Fig. 8.4, it can be seen that the channels are symmetrical, except for the signal level normalization part, which comprises an attenuator in the primary channel and a VGA in the secondary channel. This means that for all the other parts, the absolute phase shift is not so important as long as the phase shifts match[1]. On the other hand, as the attenuator and the VGA have different properties and as the attenuation and the gain are programmable, both of these blocks should exhibit as small an absolute phase shift as possible.

Next, the signals are converted into the digital domain with bandpass $\Sigma\Delta$ ADCs [100, Ch. 5]. An ADC of this type has a narrow signal band centered at $f_s/4$, where f_s is the sampling rate. The topology is suitable for the application, as the gyroscope output is a narrowband signal centered at f_{0x}, with a bandwidth of less than $100\,\mathrm{Hz}$.

---

[1]Again, the phase shift needs to be sufficiently small not to affect the primary resonator excitation force too much. However, this would require a significant phase shift. For example, a phase shift of $8°$ reduces the force by 1%, whereas a phase shift of $18°$ is required to reduce the force by 5%.

By setting $f_s = 4f_{0x}$, the conversion band of the ADCs and the gyroscope output signal band can be made to coincide.

The outputs of both ADCs are next downconverted digitally. Signals are phase-coherently demodulated to in-phase and quadrature components. Then they are filtered and decimated to reduce the oversampling ratio and to achieve their final accuracy. Next, a phase error correction that will be described in detail in Section 8.2.2 is applied to correct the phase error caused by the LPFs and by the clock generation circuitry. The phase error correction also removes any excess noise caused by phase noise in the ADC sampling clock. Finally, the Coriolis signal is revealed by normalizing the in-phase component of the secondary channel output signal. This is performed by dividing the signal by the amplitude of the primary signal. After normalization, the resulting signal is output as the angular velocity $\Omega_z(t)$.

8.2.2   Clocking Scheme and Synchronous Demodulation

The next subsystem that will be discussed is the clocking system. This subsystem forms the frame of the system architecture and operation, as it provides all the clock signals for different purposes. The synchronous demodulation of the signals is also considered here, as it is closely related to the clocking. The clocking system comprises a comparator which converts the sinusoidal primary signal into a square wave and a PLL which is locked to the comparator output. As indicated in Fig. 8.4, the primary signal is taken to the comparator after the second high-pass filter (HPF). The PLL outputs four different clocks: one running at $256f_{0x}$, used to clock the DSP part; two running at f_{0x} with a $\pm 90°$ phase shift compared to the reference clock, used to close the primary resonator excitation loop, as will be described in more detail in Section 8.2.3, and one running at $4f_{0x}$, used as the sampling clock in the $\Sigma\Delta$ ADCs.

By locking the PLL to the primary resonator output signal, it can be ensured that the excitation signals and the ADC sampling clock are always running at a proper frequency and in a correct phase. Because the operating frequency f_{0x} varies from sensor element to sensor element and also as operating conditions change, this eliminates the need for any frequency tuning. The primary resonator also provides a low phase-noise frequency reference, without the need for separate external components.

In the simplest case, the synchronous demodulation of the secondary signal is performed by multiplying it by the primary signal [70]. Then the phase error θ in the synchronous demodulation resulting from the electronics can be defined as the difference between the phase shifts caused by the two channels. If both in-phase and quadrature components of the secondary signal are needed, a PLL is often employed to generate two clock signals from the primary signal, one in phase with it, another 90° phase shifted [57, 86, 90]. Now all the phase delays related to the clock generation,

together with the induced phase noise, are added to θ and thus affect the demodulation accuracy and the final SNR.

In the present implementation, the primary and secondary signals are sampled in the $\Sigma\Delta$ ADCs with a 90° ($\pi/2$) sampling period (sampling frequency of $f_s = 4f_{0x}$). In order to achieve a simple implementation of the subsequent digital demodulator, it is assumed that every second sample represents the amplitude of the in-phase component (alternatively multiplied by -1 and $+1$) and every other sample the amplitude of the quadrature component (similarly multiplied) of the respective signal. In other words, it is assumed that the in-phase and the quadrature components of the ADC input signals are phase-locked with the sampling clock and that the phase difference is 0°. Now, the synchronous demodulation of the secondary signal can be performed in the DSP by multiplying the demodulator input signal by either $\cos(\omega_{0x}t)$ to yield the in-phase component or $\sin(\omega_{0x}t)$ to yield the quadrature component. The components of the primary signal are defined in such a way that the in-phase component is achieved by multiplying by $\sin(\omega_{0x}t)$ and the quadrature component by $\cos(\omega_{0x}t)$. These reduce to sequences of 0, 1, 0, -1,..., leading to a very simple implementation of the digital demodulator.

In Section 3.2, the secondary channel demodulator input signal with a phase shift θ was given in Eq. (3.8). With no limitation of generality, it can be assumed for the following analysis that $\omega_\Omega = 0$ and $\varphi = 0$. Then the demodulator input can be written as

$$V_{in,sec}(t) = I_{in,sec} \cdot \cos(\omega_{0x}t + \theta) + Q_{in,sec} \cdot \sin(\omega_{0x}t + \theta), \qquad (8.1a)$$

where

$$I_{in,sec} = G_{V/\Omega}\Omega_z + V_{error,I} \qquad (8.1b)$$

and

$$Q_{in,sec} = V_{error,Q}. \qquad (8.1c)$$

As discussed in Section 3.2, after the synchronous demodulation, followed by low-pass filtering and a gain of two, the demodulator outputs can be written using matrix representation as

$$\begin{bmatrix} I_{out,sec} \\ Q_{out,sec} \end{bmatrix} = \begin{bmatrix} \cos\theta & \sin\theta \\ -\sin\theta & \cos\theta \end{bmatrix} \begin{bmatrix} I_{in,sec} \\ Q_{in,sec} \end{bmatrix}. \qquad (8.2)$$

Next, on the basis of the assumption regarding the 0° phase difference between the ADC input signals and the sampling clock, and of the definitions shown in Fig. 8.5, the phase error θ can be written as the difference between the phase shifts caused by the path from the secondary resonator to the ADC input and by the path from the primary

resonator to the ADC sampling clock, or

$$\theta = (\theta_{1,sec} + \theta_{LPF,sec}) - (\theta_{1,pri} + \theta_2) = \theta_1 - \theta_2 + \theta_{LPF,pri}, \tag{8.3}$$

where the first term θ_1 denotes the difference between the phase shifts caused by the readout channels from the CSA inputs to the ADC inputs, defined as

$$\theta_1 = (\theta_{1,sec} + \theta_{LPF,sec}) - (\theta_{1,pri} + \theta_{LPF,pri}). \tag{8.4}$$

The second term θ_2 is the phase shift experienced by the signal from the output of the second HPF in the primary channel to the clock input of the secondary channel ADC. This phase shift results from the dc offsets in the output of the second HPF and in the input of the comparator, and from any delay involved with the comparator and the PLL. Finally, the third term $\theta_{LPF,pri}$ is the phase shift caused by the primary channel LPF.
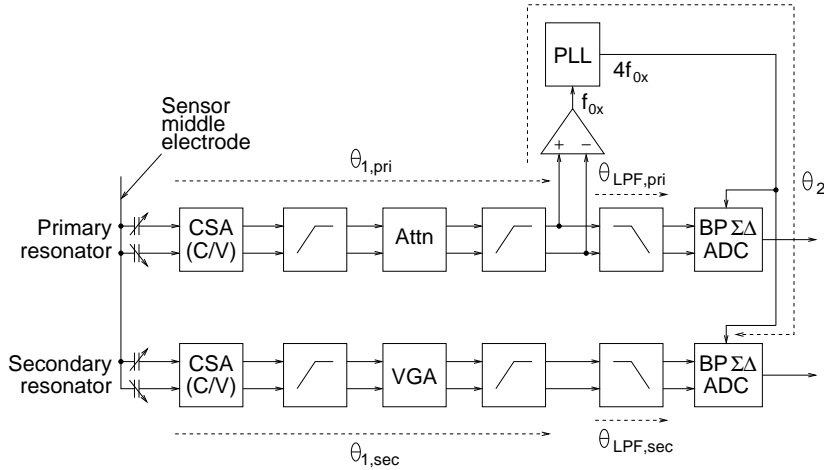
Figure 8.5 Definitions of different phase shift terms in sensor readout.

As discussed in Section 8.2.1, the LPFs cause a significant phase shift at f_{0x} if they are required to have attenuation at the first frequency bands that fold to the actual signal band in the sampling process. Further, the term θ_2 can predominate over the term θ_1 even with small dc offsets at the comparator input. However, both of these terms can be canceled on the basis of the fact that, ideally, there is no quadrature component in the primary signal and hence the primary channel ADC input signal and the sampling clock should be in phase. The only phase difference between these two signals is caused by the phase shifts θ_2 and $\theta_{LPF,pri}$.

One way to perform the cancellation is to drive the quadrature component of the downconverted primary signal to zero in a feedback loop, as described in [18]. This is done by controlling θ_2 by adding offset to the comparator input signal. However, this

approach requires an additional DAC. Its bandwidth is also severely limited because of the delay of the decimation filters, and it affects the dynamics of the primary resonator amplitude control loop.

Another, more efficient method is to correct the phase error in the DSP in feed-forward fashion by employing vector rotation. This is done by first resolving the difference $-\theta_2 + \theta_{LPF,pri}$ from the in-phase and quadrature components of the primary channel demodulator output, and then applying it to cancel the same phase error in the secondary channel demodulation. With a simple matrix inversion of (8.2), the original components $I_{in,sec}$ and $Q_{in,sec}$ of the input signal can be written as

$$\begin{bmatrix} I_{in,sec} \\ Q_{in,sec} \end{bmatrix} = \begin{bmatrix} \cos\theta & -\sin\theta \\ \sin\theta & \cos\theta \end{bmatrix} \begin{bmatrix} I_{out,sec} \\ Q_{out,sec} \end{bmatrix}. \tag{8.5}$$

The primary channel demodulator input signal can be written as

$$\begin{aligned} V_{in,pri}(t) &= I_{in,pri} \cdot \sin(\omega_{0x}t + \theta_{LPF,pri} - \theta_2) \\ &= I_{in,pri} \cdot \sin(\omega_{0x}t + \theta - \theta_1). \end{aligned} \tag{8.6}$$

If it is assumed for a while that $\theta_1 = 0$, the demodulator outputs can be written using matrix representation as

$$\begin{bmatrix} I_{out,pri} \\ Q_{out,pri} \end{bmatrix} = \begin{bmatrix} \cos\theta & -\sin\theta \\ \sin\theta & \cos\theta \end{bmatrix} \begin{bmatrix} I_{in,pri} \\ 0 \end{bmatrix}. \tag{8.7}$$

Based on Eq. (8.7), $\cos\theta$ and $\sin\theta$ can now be written as

$$\cos\theta = \frac{I_{out,pri}}{I_{in,pri}} \tag{8.8a}$$

and

$$\sin\theta = \frac{Q_{out,pri}}{I_{in,pri}}, \tag{8.8b}$$

where

$$I_{in,pri} = \sqrt{I_{out,pri}^2 + Q_{out,pri}^2}. \tag{8.8c}$$

With Eqs. (8.5) and (8.8a)-(8.8c), the original components $I_{in,sec}$ and $Q_{in,sec}$ can now be written as

$$I_{in,sec} = \frac{I_{out,pri}I_{out,sec} - Q_{out,pri}Q_{out,sec}}{\sqrt{I_{out,pri}^2 + Q_{out,pri}^2}} \tag{8.9a}$$

and

$$Q_{in,sec} = \frac{Q_{out,pri}I_{out,sec} + I_{out,pri}Q_{out,sec}}{\sqrt{I_{out,pri}^2 + Q_{out,pri}^2}}. \tag{8.9b}$$

By combining the phase error correction with the normalization of the in-phase and quadrature components of the secondary signal with respect to the primary signal, the final output signals are

$$\widehat{I}_{in,sec} = \frac{I_{in,sec}}{I_{in,pri}} = \frac{I_{out,pri}I_{out,sec} - Q_{out,pri}Q_{out,sec}}{I_{out,pri}^2 + Q_{out,pri}^2} \tag{8.10a}$$

and

$$\widehat{Q}_{in,sec} = \frac{Q_{in,sec}}{I_{in,pri}} = \frac{Q_{out,pri}I_{out,sec} + I_{out,pri}Q_{out,sec}}{I_{out,pri}^2 + Q_{out,pri}^2}. \tag{8.10b}$$

After the term $-\theta_2 + \theta_{LPF,pri}$ has been compensated, the remaining phase error θ is equal to θ_1. This can be verified by substituting $I_{out,sec}$ and $Q_{out,sec}$ from Eq. (8.2) and $I_{out,pri}$ and $Q_{out,pri}$ from Eq. (8.7) into Eqs. (8.9a) and (8.9b) (or (8.10a) and (8.10b)) and simplifying, replacing the phase shift θ in Eq. (8.7) now with the full expression $\theta - \theta_1$. A minor additional phase error is caused by the primary resonator excitation signal, which cross-couples to the primary channel and has a 90° phase shift with respect to the actual primary signal, and by the difference in the sampling instances between the two ADCs. Both of these sources can be considered negligible. Additionally, there is the phase shift ϕ caused by the secondary resonator. Because of the low-pass mode operation, a sufficient quality factor of the resonator will ensure that this error can also be assumed to be negligible compared to θ_1.

Another way of seeing the phase correction is that the secondary signal is effectively demodulated by multiplying it by the 0° and 90° phase shifted versions of the primary signal. The only remaining source of phase error is the difference θ_1 in the phase shifts between the two channels. In principle, this could also have been achieved by first filtering the quantization noise from the $\Sigma\Delta$ ADC output signals with digital band-pass filters, and then multiplying the signals by each other, taking care of the appropriate phase shift (which could have been implemented as a single delay). This implementation, however, would have required very narrow-band digital filters operating at the sampling frequency of $4f_{0x}$, having an adverse effect on both silicon area and power consumption. It is important to realize that it is not possible to simply multiply the ADC output signals by each other, as it would result in the mixing of the quantization noise at and around dc, destroying the performance of the system.

An important property of the phase error correction is that if the phase error θ_2 varies as a result of phase noise, the method introduced also cancels the additional noise inflicted by the phase noise. This means that the effect of the phase noise resulting from the square-wave generation in the comparator described in Section 8.4.1, together with the PLL phase noise, has a reduced effect on the final SNR. This will be verified experimentally in Section 8.6.2. As a result, although the system architecture requires two identical bandpass $\Sigma\Delta$ ADCs, along with their DSP, the requirements for the circuitry

used for clock generation are significantly relaxed, differing from the earlier published works where PLL is used to create clock signals for demodulation [57, 86]. It also makes the design of the LPFs easier, as their phase delays have no effect on the system performance, as long as they match with each other.

Finally, care must be taken to ensure that the noise in the primary signal is lower than the noise in the secondary signal, so that the correction does not degrade the final SNR. As the ratio between the magnitudes of the primary and the Coriolis signals is typically large, this should be trivial. The compensation method also requires the digital decimation filters in all four signal paths (in-phase and quadrature components of both primary and secondary signals) to be identical.

8.2.3   Primary Resonator Excitation

The two clocks from the PLL running at the $\pm 90°$ phase shift are used to close the primary resonator excitation loop during normal operation. Using a properly phased PLL output signal to excite the primary resonator has also been demonstrated in [9, 88–90], for instance. A digital amplitude controller implemented as an integrator (I controller) monitors the error between the actual primary signal and the desired value, as shown in Fig. 8.4. The signal level is controlled by setting the dc level of the excitation signals with a 5-bit drive level DAC. The ac amplitude is kept constant.

As described in Section 4.3, the digital control leads to a discrete number of possible levels for the excitation signal. This, in turn, leads to the oscillation of the primary resonator vibration amplitude between two levels. As the secondary signal is normalized with respect to the primary signal by division, the effect of the time-varying primary amplitude is reduced in the angular velocity output, but it still causes spurious components to the output spectrum, as will be seen in the experimental results. The normalization does not fully remove the effect of the time-varying primary signal, as the secondary signal contains error signals which are not proportional to the primary signal amplitude, as was shown in Chapter 6.

A significant drawback in the time-varying primary signal is that the DSP implementation requires two squaring operations and a divider to perform the normalization described in Eqs. (8.10a) and (8.10b). While this is not a limiting factor in the FPGA implementation, it would increase the silicon area of an integrated DSP significantly. By employing the $\Sigma\Delta$ modulation of the excitation signals described in Section 4.3, the primary signal can be kept constant, leading to a constant denominator of Eqs. (8.10a) and (8.10b). This, in turn, means that the normalization reduces to a division by a constant, which requires significantly less complicated hardware, in the simplest case, only a shifter. Obviously, this comes at the price of the hardware required for the $\Sigma\Delta$ modulation, so it is a trade-off between the complexities of these blocks.

In the present implementation, no $\Sigma\Delta$ modulation of the excitation signals is employed by default. However, the modulation is implemented to show that it can be used to remove the spurious components in the output spectrum. This will be done when the experimental work is presented in Section 8.6.

The PLL is not able to lock to the primary signal until the amplitude has grown sufficiently large. This requires another excitation method for the start-up. While some published implementations use, for example, a frequency sweep of the PLL output to find the operating frequency f_{0x} [88, 89], in the present system, the primary resonator excitation in the system start-up is performed using an analog feedback loop with high-voltage excitation signals. This will be described in more detail in Section 8.2.5.

8.2.4   Quadrature Compensation

The mechanical quadrature signal is compensated with a dc voltage generated by a 7-bit HV DAC. A digital controller implemented as an integrator (I controller) sets the HV DAC output voltage in such a way that the quadrature signal is brought to zero. At the same time, the controller sets the gain of the VGA in such a way that the dynamic range of the secondary channel is maximized. The implementation of the quadrature compensation loop is shown in Fig. 8.4.

To prevent the quadrature signal from oscillating between two levels as a result of the limited resolution of the HV DAC, $\Sigma\Delta$ modulation of the compensation voltage is implemented as described in Section 5.2. The effects of the modulation together with the impact on the system performance are experimentally studied in Section 8.6.

8.2.5   System Start-Up

Before the PLL has locked to the primary signal, the primary resonator is excited using high-voltage signals provided by a charge pump. The $+90°$ phase shift required to drive the resonator at its resonance frequency is implemented with an analog phase shifter realized as a differentiator. Another possibility would have been to realize the phase shifter as an integrator combined with phase inversion. These options will be considered in more detail in Section 8.4.4. The high-voltage excitation ensures the fast start-up of the high-quality factor primary resonator.

During the start-up, the digital system start-up controller shown in Fig. 8.4 monitors the primary signal. Once the signal level is sufficient, the primary resonator excitation is switched to the drive-level DAC with switches SW1-4, and the amplitude controller starts monitoring and controlling the primary signal amplitude. The start-up controller also sets the gain in the primary channel in such a way that at the beginning the gain is sufficient for a reliable start-up, whereas during normal operation the signal level stays within the dynamic range of the readout electronics.

Because of the difficulties of implementing reliable floating HV switches, SW1-4 in the figure are only of a schematic nature. In the actual implementation, HV transistors in cut-off protect the drive-level DAC outputs when the charge pump is providing the excitation signals. When the excitation is switched to the PLL, the charge pump outputs enter a high impedance state, and the HV transistors are turned on, connecting the drive-level DAC outputs to the sensor element.

During start-up, the middle electrode potential is set to ground with SW5 to increase the magnitude of the electrostatic forces. In normal operation, a charge pump sets the bias to 8.25 V. Again, SW5 is only schematic, implemented as a single HV transistor which pulls the middle electrode to ground during start-up, and lets the charge pump set the potential during normal operation.

8.3   Sensor Readout Electronics

This section, together with Section 8.4, will focus on the detailed implementation of the analog circuit blocks. All the blocks described were implemented on the ASIC. In this section, the analog blocks of the sensor readout electronics will be described, from the CSAs to the $\Sigma\Delta$ ADCs. In Section 8.4, other significant blocks (PLL, HV DAC, charge pumps, phase shifter, and drive-level DAC) will be described.

8.3.1   Sensor Front-End

The readout of both the primary and the secondary resonators is performed with continuous-time CSAs; this was introduced in detail in Section 7.2.1. The schematic of the CSA is shown in Fig. 8.6 (a). The transfer function of the CSA from the change in capacitance ΔC_D to differential output voltage $V_{out} = V_{outp} - V_{outn}$ was given in Eq. (7.5). For the sake of convenience, it is rewritten below.

$$H(s) = \frac{V_{out}(s)}{\Delta C_D(s)} = -\frac{s \cdot V_B/C_f}{s + 1/(R_f C_f)}. \tag{8.11}$$

The operational amplifier in the CSA is implemented as a folded-cascode operational amplifier. Its schematic is shown in Fig. 8.6 (b). As already stated in Section 7.2.1, in order to keep the CSA gain stable, the detection bias $V_B = V_{CMIN} - V_{MID}$ has to be held constant. This is ensured by the common-mode feedback (CMFB) circuit that monitors the common-mode level at the input and keeps it constant by controlling the common-mode level at the output. The schematic of the CMFB circuit is shown in Fig. 8.6 (c). The inputs V_{inp} and V_{inn} of the circuit are connected to the equally named inputs of the main amplifier. This CMFB configuration keeps the input bias voltage V_{CMIN} stable at 2.5 V despite any leakage currents that may have to be sup-
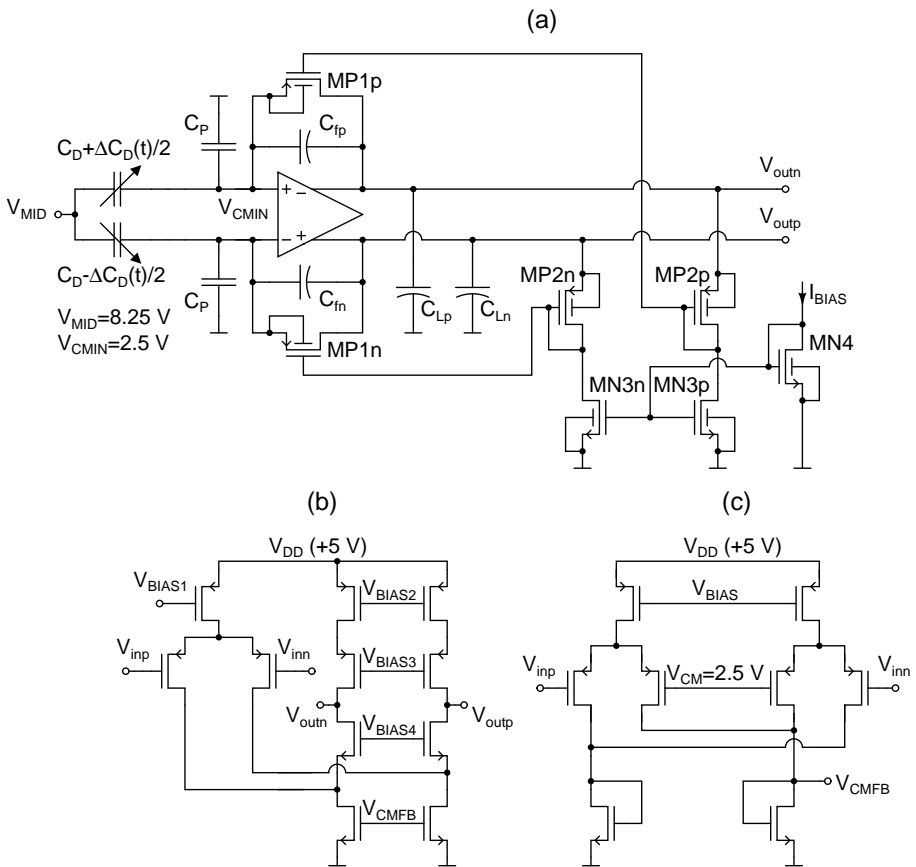
Figure 8.6 (a) The implementation of the CSA, with V_{CMIN} the common-mode voltage at the input. (b) The folded-cascode operational amplifier used in the CSA. (c) The common-mode feedback circuit that keeps the input common-mode level stable.

plied from the CSA input, or any common-mode variation of the input capacitance, ensuring a stable signal gain in the CSA. As the differential voltage between V_{inp} and V_{inn} is practically zero, the CMFB structure shown in the figure is suitable for this application. Large differential input voltages between the inputs V_{inp} and V_{inn} of the CMFB circuit would cause it to go to a nonlinear region and eventually not be able to control the common-mode voltage any more. Another possible configuration for input common-mode level stabilization is presented in [133].

With the middle electrode biasing voltage V_{MID} equal to 8.25 V, a detection bias of $V_B = -5.75$ V is achieved. The feedback capacitors C_{fp} and C_{fn} are both 10 pF. This yields a CSA gain of $575 \cdot 10^9$ V/F in the band of interest.

As described in Section 7.2.1, the size of the feedback resistors in a CSA is determined by both transfer function characteristics and noise properties. It was also found that it is often the noise properties which set the most stringent requirements for the resistor size, rather than the transfer function. There are various alternatives for implementing the large resistors. The most straightforward way is to implement them as polysilicon resistors. This can, however, lead to excessive silicon area consumption, together with possible problems with the parasitic capacitances associated with the resistors. The resistor size can be decreased using the so-called resistor T-network [134], but this leads to increased noise from both the resistors and the operational amplifier and to the amplification of the operational amplifier offset.

Another alternative is to implement the resistors using active devices. This method allows reduction of the silicon area consumption, but care must be taken in order not to increase the noise contribution of the resistors too much. Finally, the resistors can be implemented as external components. In this case, the effects of the parasitics associated with the interconnections to the resistors must be carefully evaluated.

In order to gain sufficient resistance for low-noise operation without excessive silicon area consumption, the feedback resistors in the CSAs are implemented with long-channel P-type MOS (PMOS) transistors MP1p and MP1n. They are biased with a constant drain-gate voltage, as shown in Fig. 8.6 (a) [70]. The N-type MOS (NMOS) current sources MN3p and MN3n connected to the outputs pull a constant 10 nA current from the CSA outputs, biasing the actual feedback devices with $W/L = 1\,\mu\text{m}/250\,\mu\text{m}$. The diode-connected PMOS devices MP2p and MP2n that generate the bias voltages have $W/L = 10\,\mu\text{m}/250\,\mu\text{m}$. This yields a resistance of $R_f = 200\,\text{M}\Omega$ for the feedback resistors under nominal conditions.

With the dimensions described above, the silicon area occupied by the MOS resistors is approximately 0.012 mm^2, if it is assumed that the distance between the individual components and the spacing to the neighboring components are both 5 μm. If the two 200-MΩ resistors were implemented using polysilicon resistors that have a sheet resistance of 2 kΩ and minimum width and spacing of 2 μm, they would occupy

an area roughly equal to $1.6\,\text{mm}^2$. This is well over 100 times the area occupied by the MOS resistors. The technology scaling shrinks the polysilicon resistors but even with a minimum width and spacing of $0.5\,\mu\text{m}$, the area occupied by them would still be equal to $0.1\,\text{mm}^2$. On the contrary, the area of the MOS resistors most probably does not show any significant scaling with technology.

The bulks of the feedback PMOS transistors are connected to the inputs of the operational amplifier, and hence also to the inputs of the CSA. This is to improve the leakage current tolerance, which is necessary because of the two-chip implementation. There are leakage currents associated with both the micromechanical structure and especially with the ESD (Electrostatic Discharge) protection diodes at the CSA input. These diodes are necessary to protect the high-impedance input before and while the two chips are combined.

In general, there are three possible ways to connect the bulks of the feedback devices. They can be connected either to the inputs of the CSA, as in the present case, to the outputs of the CSA, or to the positive supply. Figure 8.7 shows the resulting pn-diodes between the drain and source areas and the n-well in all three cases. In the following paragraphs, the effects of leakage currents in these three cases will be analyzed. In the analysis, it will be assumed that if the bulks of MP1p and MP1n are connected either to the inputs or to the outputs of the CSA, then the bulks of MP2p and MP2n are connected to their sources. If the bulks of MP1p and MP1n are connected to the supply, then the bulks of MP2p and MP2n are also connected to the supply. This is to make the accurate biasing of the devices possible.
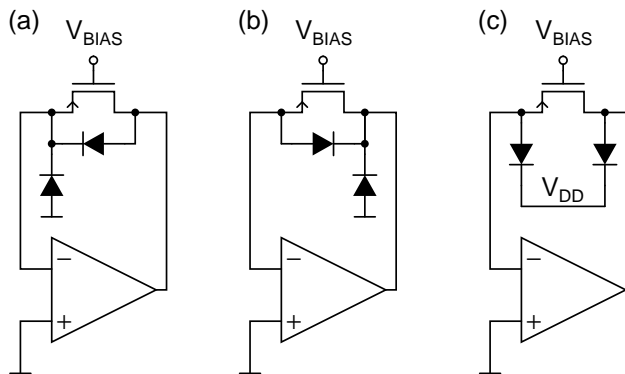
Figure 8.7 Resulting pn-diodes between various terminals as the bulk of the feedback PMOS is connected to: (a) CSA input. (b) CSA output. (c) Supply voltage.

First, the case where current is injected into the CSA inputs will be considered. In this case, the common-mode level at the output drops (the CMFB keeps the input common-mode level constant). The sources of the PMOS transistors MP1p and MP1n stay at the CSA input side of the devices (as the devices are symmetrical, the source

of a PMOS transistor is always the terminal at the higher potential), and the gate-source voltage thus increases. This prevents the feedback PMOS devices from going into saturation, but causes an inevitable decay of the effective resistance. If the bulks of MP1p and MP1n are connected to the CSA inputs, as in the present case, the bulk effect does not affect the resistance as the bulk-source voltages of MP1, MP1n, MP2p, and MP2n all stay at zero.

If the bulks of MP1p and MP1n were connected to the CSA outputs, the threshold voltages of MP1p and MP1n would decrease as the bulk-source voltage increased from zero and the pn-junction started to become forward-biased. This would cause the decay of the effective resistance to be larger than in the case without the bulk effect. Additionally, the bulk-source junction would start conducting, further reducing the effective resistance. Finally, if the bulks were connected to the supply, then the threshold voltages of MP1p and MP1n would not change, whereas the bulk effect would increase the threshold voltages of MP2p and MP2n. Therefore, the decay of the effective resistance would be larger than in the case where the bulks are connected to the CSA inputs, but less than in the case where the bulks are connected to the CSA outputs.

If current is drawn from the CSA inputs, the common-mode level at the output increases and the sources of MP1p and MP1n shift to the CSA output side of the devices. Hence, their gate-source voltages stay constant. If the bulks of the devices MP1p and MP1n were now connected to the CSA outputs, their threshold voltages would not change, as the bulk-source voltages of MP1p, MP1n, MP2p, and MP2n would all be zero. This would cause the devices MP1p and MP1n to saturate, after which they would not be able to conduct the leakage currents any more. If the bulks were connected to the supply, then the threshold voltages of MP1p, MP1n, MP2p, and MP2n would all increase by the same amount, and the devices MP1p and MP1n would again saturate.

On the other hand, if the bulks of the devices MP1p and MP1n are connected to the CSA inputs, as in the present case, the bulk effect causes the threshold voltage of these devices to decrease as the output common-mode level increases and the bulk-source pn-junction starts to become forward-biased. This causes the saturation voltage to increase, helping to keep the devices in the linear region. More importantly, the bulk-source diode in these devices starts conducting, preventing the devices from saturating. The effective resistance becomes smaller, and eventually, when the diode starts conducting fully, negligible.

The behavior is illustrated in Fig. 8.8. It shows the simulated voltage drop over the feedback PMOS devices versus the leakage current I_{leak}, when the bulks are connected to the CSA inputs, to the outputs, or to the supply. Otherwise, the dimensions and the biasing currents are identical and equal to the actual implemented CSA in both cases. The decay in the effective resistance can be seen when current is injected to the inputs

(positive I_{leak}). If the bulks are connected to the outputs, the resistance decays more rapidly than when the bulks are connected to the inputs or to the supply. When current is drawn from the inputs (negative I_{leak}), it can be seen that the voltage drop grows very quickly if the bulks are connected to the outputs or to the supply as the feedback PMOS devices saturate, whereas the CSA stays functional with larger leakage currents when the bulks are connected to the inputs.
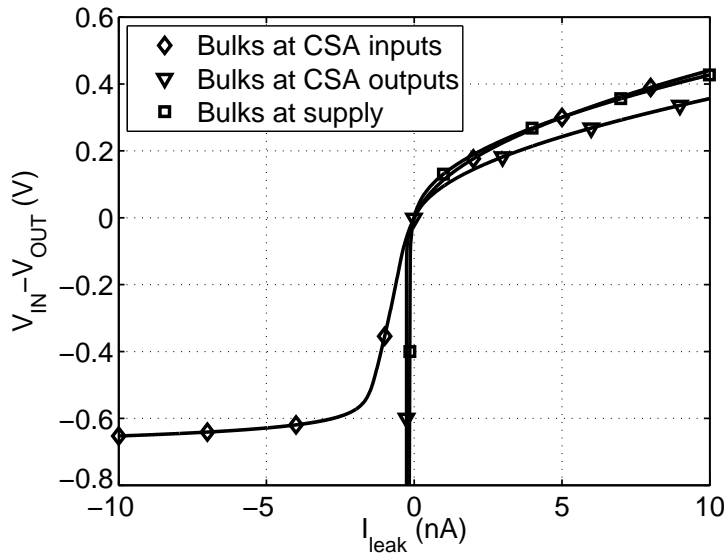
Figure 8.8 Voltage drop over the PMOS resistors ($W/L = 1\,\mu\text{m}/250\,\mu\text{m}$) as a function of the leakage current.

The simulated effective resistance R_{eff} is shown in Fig. 8.9. The graph is achieved by numerically differentiating the voltage drops shown in Fig. 8.8 with respect to the current. The resistance without leakage currents is $200\,\text{M}\Omega$ when the bulks are connected either to the CSA inputs or to the outputs. On the other hand, if the bulks are connected to the supply, the resistance without leakage currents is somewhat higher, about $370\,\text{M}\Omega$. When current is injected into the inputs, the resistance falls in all three cases. As predicted, the decay is fastest when the bulks are connected to the outputs, second fastest when they are connected to the supply, and slowest when the bulks are connected to the inputs. If current is drawn from the inputs, the resistance initially grows very fast. If the bulks are connected to the outputs or to the supply, the growth is more rapid, but as the feedback devices saturate, the CSA becomes non-functional. If the bulks are connected to the inputs, the resistance starts falling after first reaching a peak of approximately $450\,\text{M}\Omega$.

As the operating frequency f_{0x} is $10\,\text{kHz}$ and as the $-3\,\text{dB}$ corner frequency of the CSA should be kept at least one decade below the operating frequency to keep the
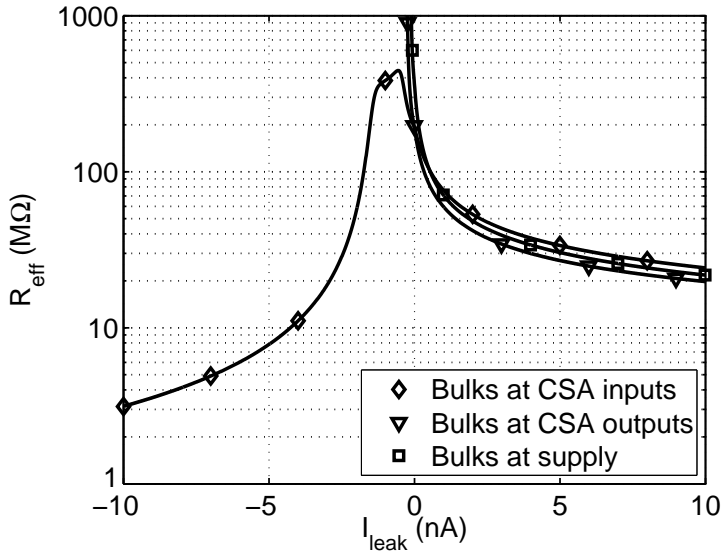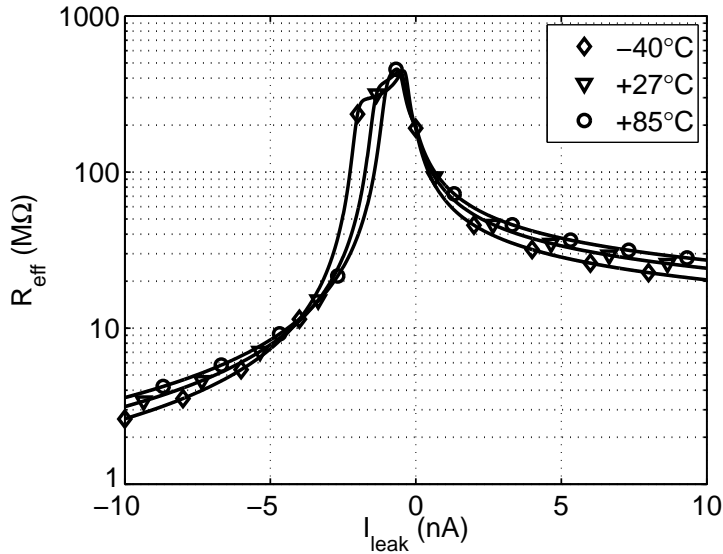
Figure 8.9 Effective resistance of the PMOS resistors ($W/L = 1\,\mu\text{m}/250\,\mu\text{m}$) as a function of the leakage current.

phase shift and signal attenuation under control, then with $C_f = 10\,\text{pF}$, the feedback resistor needs to be at least $R_f = 15\,\text{M}\Omega$. From Fig. 8.9, it can be seen that with the present configuration (feedback PMOS bulks connected to the inputs), this is reached with leakage currents between -3.3 and $> 10\,\text{nA}$. The tolerance of positive leakage currents needs to be larger, as the middle electrode of the sensor element is biased to a positive voltage, and hence all the leakage currents associated with the sensor element are positive. However, although the leakage current range is sufficient for proper operation, the decaying resistance also has an adverse effect on the noise performance, as will be seen later.

From the previous results, it can be concluded that when the leakage current tolerance is considered, the bulks of the feedback PMOS devices should be connected to the CSA inputs as the performance is improved over the other alternatives, irrespective of the leakage current direction or magnitude. However, this adds the well-substrate capacitance of the feedback devices to the parasitic capacitance seen at the CSA input. This increases the noise contribution of the operational amplifier, as will be described shortly.

Because the resistors are implemented with active devices, their sensitivity to process and temperature variations also needs to be considered. Figure 8.10 shows the temperature variation of the effective resistance. The resistance is evaluated in the same way as was done earlier in Fig. 8.9, by numerically differentiating the voltage drop over the resistor with respect to the current. The figure shows that with small

leakage currents, the resistance varies only slightly over the temperature range. The negative leakage current tolerance shows a small improvement at cold temperatures.
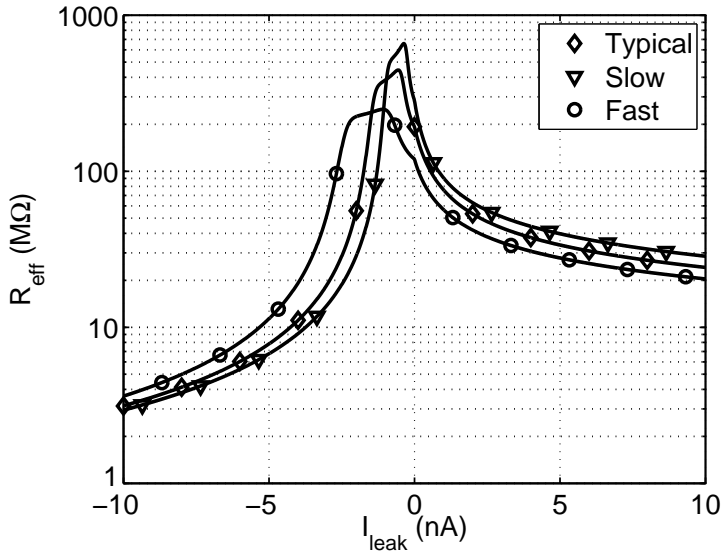

Figure 8.10 Variation of the effective resistance of the PMOS resistors ($W/L = 1\,\mu$m$/250\,\mu$m) over the temperature range.

Figure 8.11 shows the process variation of the resistance at room temperature ($+27°$C). It can be seen that the process variation is much more significant than the temperature variation, with the resistance changing from $100\,$MΩ to $300\,$MΩ between fast and slow process corners. Again, the negative leakage current tolerance improves slightly at the fast process corner.

Finally, the effective resistances and the deviations from the nominal value (typical process, $+27°$C) over temperature and process variations are given in Table 8.2. The table shows that the worst-case variation is $-43.1/+51.5\%$. The table also confirms that the temperature variation of the resistance is largely insignificant when compared to the process variation.

As the first stage that converts the capacitance to voltage, the CSA is the most important block in determining the resolution limit imposed by the readout electronics. As described in Section 7.2.1, the two primary noise sources are the feedback resistors, used to set the input bias voltage, and the operational amplifier. The noise densities, referred to a change in the differential input capacitance, were given in Eqs. (7.6) and (7.8). For convenience, they are rewritten below.

$$C_{n,R}^2 = \frac{8k_BT}{V_B^2 R_f \omega_{0x}^2} \tag{8.12}$$

Figure 8.11 Variation of the effective resistance of the PMOS resistors ($W/L = 1\,\mu\text{m}/250\,\mu\text{m}$) over process variation (at $+27°$C).

Table 8.2 Variation of the effective resistance of the PMOS resistors ($W/L = 1\,\mu\text{m}/250\,\mu\text{m}$) over temperature and process variations ($I_{leak} = 0$.)

Corner	Temperature (°C)	Resistance (MΩ)	Deviation (%)
Typical	−40	191	−0.9
	+27	193	0.0
	+85	200	+3.6
Slow	−40	292	+51.5
	+27	284	+47.3
	+85	288	+49.7
Fast	−40	110	−43.1
	+27	119	−38.2
	+85	128	−33.7

and

$$C_{n,opa}^2 \approx \left(\frac{C_f + C_D + C_P + C_{inW}W}{V_B} \right)^2 \cdot$$
$$\left[\frac{16}{3} k_B T \gamma_n \left(2\mu C_{OX} \frac{W}{L} I_D \right)^{-1/2} + \frac{2K_F}{C_{OX}^2 W L f_{0x}} \right], \tag{8.13a}$$

where

$$C_{inW} = CGDO + CGSO + 0.67 \cdot C_{OX} \cdot L. \tag{8.13b}$$

The input-referred noise of the feedback resistor can be evaluated by substituting $R_f = 200\,M\Omega$, $V_B = -5.75\,V$, and $\omega_{0x} = 2\pi f_{0x} \approx 2\pi \cdot 10\,kHz$ into Eq. (8.12). This yields $C_{n,R} \approx 3.6 \cdot 10^{-20}\,F/\sqrt{Hz}$. Likewise, the input-referred noise of the operational amplifier can be evaluated by substituting the capacitances $C_f = 10\,pF$ and $C_D + C_P \approx 10\,pF$, the dimensions and the biasing current of the operational amplifier input pair $W = 800\,\mu m$, $L = 0.7\,\mu m$, $I_D = 250\,\mu A$, and the various technology-dependent parameters into (8.13a). This yields a noise level of $C_{n,opa} \approx 1.4 \cdot 10^{-20}\,F/\sqrt{Hz}$. The contributions of thermal and flicker noise are roughly equal. The noise performance of the operational amplifier was optimized as described in Section 7.2.1. However, the dimensions were left suboptimal because the optimum would have required impractically wide input devices and as the noise contribution of the feedback resistors is dominant.

The total simulated input-referred noise of the CSA is $C_{n,CSA} \approx 4.2 \cdot 10^{-20}\,F/\sqrt{Hz}$. This corresponds to an output-referred noise voltage of $24\,nV/\sqrt{Hz}$, or to an input-referred noise current of $15\,fA/\sqrt{Hz}$. The contribution of the feedback resistors is $3.1 \cdot 10^{-20}\,F/\sqrt{Hz}$, slightly less than predicted by Eq. (8.12), and the contribution of the operational amplifier is $2.7 \cdot 10^{-20}\,F/\sqrt{Hz}$. The large difference in this figure, compared to the theoretical value, is explained partly by the fact that the simulated transconductance of a single input transistor is over 25% less than the value given by the long-channel formula used to derive Eq. (8.13a), partly because $\gamma_n = 1$ was assumed in the calculations, and partly because of the noise of the other transistors in the operational amplifier.

The well-substrate parasitic of the feedback PMOS devices is calculated to be approximately $0.7\,pF$. This contributes partially to $C_D + C_P \approx 10\,pF$. However, because of the PCB implementation, the value of $C_D + C_P$ used in the calculations is a very rough approximation, and the importance of the well-substrate parasitic to the total capacitance is hard to assess. On the other hand, as the noise $C_{n,R}^2$ contributed by the feedback resistors slightly dominates the overall noise, an accurate estimation of $C_D + C_P$ is not so critical in the present case.

The final point that needs to be made regarding the noise performance is that if the

effective resistance R_f of the feedback devices drops because of leakage currents or because of process and/or temperature variations, the noise performance deteriorates. The amount of excess noise caused by a certain leakage current or by environmental/process variations can be evaluated by substituting the actual resistance to Eq. (8.12) and re-evaluating.

8.3.2 High-Pass Filtering

The next important block regarding the resolution of the readout is the HPF that follows the CSA. It is a single-pole active-RC filter with $+20\,$dB amplification. The schematic of the filter is shown in Fig. 8.12. Because the signal frequency is about $10\,$kHz, the RC time constant required for a sufficiently low $-3\,$dB frequency is large, in the order of $1/(2\pi \cdot 1\,\text{kHz}) = 0.16\,$ms. As the signal is amplified at the same time, the size of the feedback capacitors C_{2P} and C_{2N} is limited, because the input capacitors C_{1P} and C_{1N} must be ten times their size.
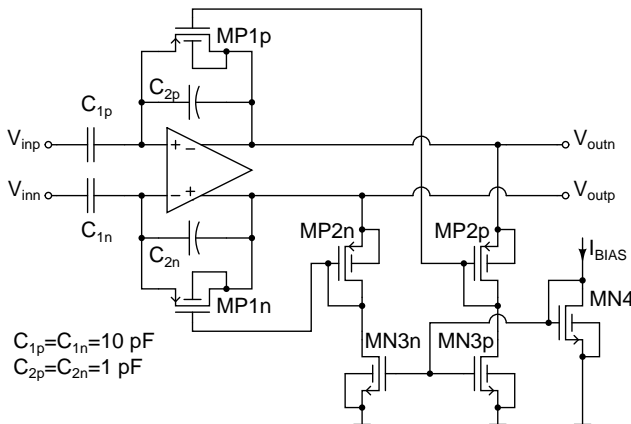
Figure 8.12 The implementation of the first high-pass filter that amplifies the CSA output signal by $+20\,$dB.

To achieve sufficiently large resistance without excessive silicon area, the feedback resistors are implemented in a similar fashion as in the CSAs. However, now the bulks of the feedback PMOS devices are connected to the outputs of the operational amplifier, instead of its input, as in the CSAs. This reduces the leakage current tolerance significantly, as described in Section 8.3.1. In this case, however, this does not limit the performance since there is no need to draw any currents from the input of the operational amplifier in the HPF.

In the HPF, the feedback PMOS devices MP1p and MP1n have $W/L = 1\,\mu\text{m}/5\,\mu\text{m}$. The diode-connected PMOS devices MP2p and MP2n that generate the bias voltages have $W/L = 200\,\mu\text{m}/5\,\mu\text{m}$. With these dimensions, the silicon area occupied by the

MOS resistors is now approximately $0.0054 \, \text{mm}^2$, if it is again assumed that the distance between the individual components and the spacing to the neighboring components are both $5 \, \mu\text{m}$. The minimum feedback resistor size in the HPF is roughly $160 \, \text{M}\Omega$, in order to achieve a pole frequency which is at least one decade below the signal frequency. If two of these resistors were implemented using polysilicon resistors that had a sheet resistance of $2 \, \text{k}\Omega$ and minimum width and spacing of $2 \, \mu\text{m}$, they would occupy an area roughly equal to $1.28 \, \text{mm}^2$. This is now well over 200 times the area occupied by the MOS resistors.

The reason for connecting the bulks to the outputs of the operational amplifier is that it improves the large-signal linearity of the filter significantly. To understand this, the behavior of one half of the differential filter circuit will be considered over a whole cycle of the sinusoidal input signal. In the analysis, to make the accurate biasing of the devices possible, it will again be assumed that if the bulks of MP1p and MP1n are connected either to the inputs or to the outputs of the amplifier, then the bulks of MP2p and MP2n are connected to their sources. If the bulks of MP1p and MP1n are connected to the supply, then the bulks of MP2p and MP2n are also connected to the supply.

When the output signal decreases below the common-mode level, the sources of the PMOS transistors MP1p and MP1n stay at the operational amplifier input side of the devices (as with the CSA, as the devices are symmetrical, the source of a PMOS transistor is always the terminal at the higher potential). Now, the gate-source voltage of the devices increases, preventing them from entering the saturation region. As the bulks of the feedback transistors are connected to the filter output, the bulk-source pn-junction becomes forward-biased (this can be seen from Fig. 8.7 (b)), reducing the threshold voltage and also conducting itself. All this causes the operational amplifier input to start following the output when the signal swing is sufficiently large. If the bulks of the feedback devices were connected to the input side, the bulk effect would not have any effect, and the bulk-source diode would stay reverse-biased. Even then, the amplifier input would still follow the output when the signal swing was sufficient. Likewise, if the bulks were connected to the supply, the bulk effect would increase the threshold voltages of MP2p and MP2n, but the pn-junctions would stay reverse-biased. Again, the amplifier input would follow the output when the signal swing was sufficient.

When the output next increases above the common-mode level, the sources of the feedback PMOS transistors shift to the filter output side of the devices. Now, as the bulks are connected to the amplifier outputs, the gate-source voltages stay constant, as do the bulk-source voltages of MP1p, MP1n, MP2p, and MP2n. The feedback transistor saturates, and only the small saturation current flows through it. At the same time, the pn-junction cannot start conducting. The result of this is that as a large signal

is applied to the filter, the operational amplifier input becomes biased at a voltage which is below the common-mode level, in such a way that the average current over a single cycle of the sinusoidal input signal is zero. This has to be taken into account in the design of the amplifier by ensuring a sufficient ICMR.

If, on the other hand, the bulks of the feedback devices were connected to the inputs of the operational amplifier, then, as the output increased, the device would still saturate but not as early as in the other case, because the bulk effect would reduce the threshold voltage of the feedback device. More importantly, the pn-junction would become forward-biased, forming a low-impedance feedback path and pushing the amplifier input back high again. Because of this signal-dependent feedback path, the filter would distort the output signal badly when the amplitude grew too large.

If the bulks were connected to the supply, the operation would be identical to the case where the bulks are connected to the output. In this case, the bulk effect would reduce the threshold voltages of MP1p, MP1n, MP2p, and MP2n. This, however, would not have any impact on the overall operation.

The simulated distortion is shown in Fig. 8.13. From the figure, it can be seen that if the bulks of the feedback devices are connected to the inputs of the operational amplifier, the distortion starts increasing rapidly after the output signal amplitude exceeds 0.5 V. When the bulks are connected to the outputs or to the supply, the total harmonic distortion (THD) stays below $-58\,\text{dB}$ beyond 1.5 V output amplitude, which is sufficient for the system. It should be noted that the CSA operates with very small output signal amplitudes, and therefore its linearity would not be limited by any of the presented configurations.

From Fig. 8.13 it can be seen that when the bulks are connected to the supply, the simulated THD is slightly better at low signal levels than in the case where the bulks are connected to the outputs. The difference is caused by the fact that the resulting feedback resistance with zero voltage over the device is now larger. At high signal levels, the results are equal to the case where the bulks are connected to the outputs. As the difference is insignificant, the bulks were connected to the outputs in the final implementation.

As already mentioned, the first high-pass filter is critical regarding the total system performance. The simulated input-referred noise voltage of the filter is $v_{n,HPF} \approx 18.8 \cdot 10^{-9}\,\text{V}/\sqrt{\text{Hz}}$ at $f_{0x} = 10\,\text{kHz}$. After this has been reduced by the CSA gain, the resulting noise density is $C_{n,HPF} \approx 3.3 \cdot 10^{-20}\,\text{F}/\sqrt{\text{Hz}}$. The total noise inflicted by the CSA and the HPF is therefore $C_n \approx 5.3 \cdot 10^{-20}\,\text{F}/\sqrt{\text{Hz}}$, corresponding to an input-referred noise current of $19\,\text{fA}/\sqrt{\text{Hz}}$. The noise level could have been reduced further by increasing the gain of the CSA by using smaller feedback capacitors. However, this would have increased the phase shift inflicted by the CSA, unless even larger feedback resistors had been used as well. This, on the other hand, would have limited the leakage
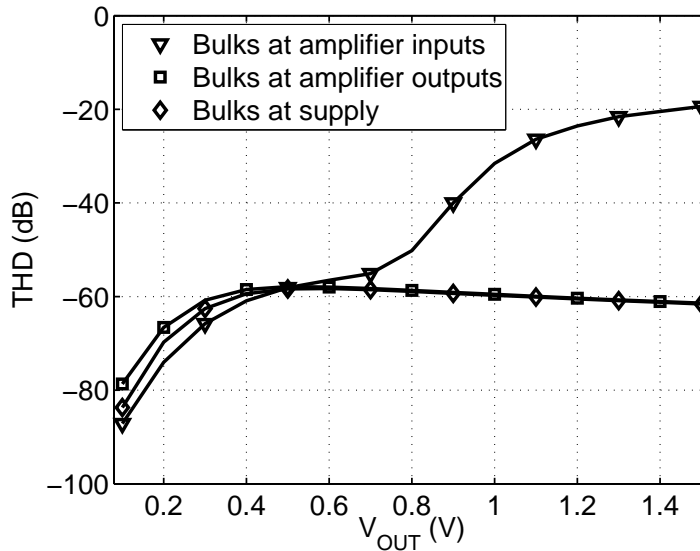
Figure 8.13 Simulated total harmonic distortion of the high-pass filter with three different configurations.

current tolerance too much. Thus, a trade-off was made to gain a smaller phase shift at the expense of an increased noise level.

The second HPFs that follow the tunable attenuator in the primary and the VGA in the secondary channel are realized in the same way as the first filters. Now, however, the secondary signal is sufficiently amplified that the impact on the final noise level is negligible. The schematic is identical to that of the first HPFs shown in Fig. 8.12, but as there is no signal gain in the filters, all the capacitors are equally-sized to 1 pF.

8.3.3 Signal Level Normalization

After the first high-pass filter, the signal levels are normalized with a tunable attenuator in the primary and a VGA in the secondary channel. The normalization is required as the output signal from the primary resonator far exceeds that from the secondary resonator. The difference between the signals in the present system is roughly 60 dB. To provide a suitable signal for the subsequent LPFs and the ADCs, the primary signal needs to be attenuated and the secondary signal amplified.

Figure 8.14 shows two alternative implementations for a VGA. The implementation of Fig. 8.14 (a) is a non-inverting configuration. It does not load the driving stage resistively, but, on the other hand, requires the use of an FDDA [115]. The implementation of Fig. 8.14 (b) is an inverting configuration. It can be realized with a conventional differential operational amplifier, but it always loads the previous stage resistively. Fur-

ther differences are that in the non-inverting configuration, there is no current flowing through the switches used to program the gain, leading to a more accurate gain setup, and that the non-inverting configuration cannot reach gains below one.
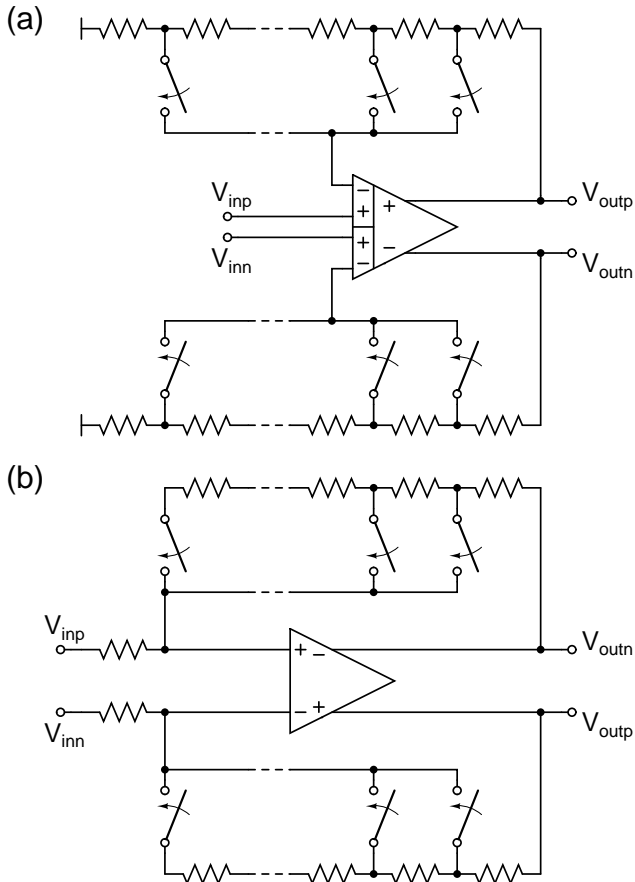
Figure 8.14 Two alternative implementations for a variable-gain amplifier. (a) Non-inverting configuration. (b) Inverting configuration.

In the present system, the VGA was implemented with the non-inverting configuration shown in Fig. 8.14 (a). The gain was further divided into two stages in order to keep the phase shift as small as possible. This is necessary, as the level normalization is the only place where the primary and secondary channels are not identical and hence where the absolute phase shifts matter the most. The VGA has a controllable gain from 1.94 dB to 44.08 dB, with 6.02 dB steps. The attenuator is implemented simply as a resistive divider. Switches are used to control the division ratio, hence the attenuation between 0 dB (which is used only during the system start-up) and 28.52 dB.

8.3.4 Low-Pass Filtering

To sufficiently attenuate the noise of the first frequency bands which would fold to the signal band in the sampling process in the subsequent ADC ($3f_{0x} = 30\,\text{kHz}$, $5f_{0x} = 50\,\text{kHz}$, etc.) a second-order low-pass filter was chosen. The transfer function of such a filter is

$$H(s) = \frac{G\omega_c^2}{s^2 + (\omega_c/Q)\,s + \omega_c^2},\tag{8.14}$$

where G is the gain at $s = 0$ (dc), $\omega_c = 2\pi f_c$ is the cut-off frequency or the critical frequency, and Q is the quality factor. If the critical frequency is placed at the operating frequency f_{0x} and if the quality factor is one, the filter would have an attenuation of 19 dB at $3f_{0x}$. With a white noise floor, the SNR degradation resulting from noise folding would then be less than 0.1 dB.

As in the CSA and the HPFs, the greatest individual design issue when designing the LPF is the need for large time constants. Although the cut-off frequency can be located close to f_{0x}, leading to a time constant a decade smaller than in the CSA or the HPFs, the resulting passive components are still fairly large for integration. For instance, if $f_c = 10\,\text{kHz}$ is required, then with $C = 10\,\text{pF}$, the required resistance is $R = 1.6\,\text{M}\Omega$. Therefore, the possibility of using MOS transistors as resistors should be considered, or, if polysilicon resistors are used, their number should be minimized.

Figure 8.15 shows three possible biquadratic cells which operate as second-order low-pass filters. The first two are so-called single-amplifier biquads, whereas the third is a two-integrator biquad. Table 8.3 presents the design equations for the three filters. Next, their suitability for this application will be investigated.

Table 8.3 Design equations for the low-pass filters in Fig. 8.15.

Filter	G	ω_c	Q
8.15 (a)	$\frac{R_3}{R_1}$	$\frac{1}{\sqrt{R_2 R_3 C_1 C_2}}$	$\sqrt{\frac{C_1}{C_2}} \cdot \frac{R_1\sqrt{R_2 R_3}}{R_1(R_2+R_3)+R_2 R_3}$
8.15 (b)	$1 + \frac{R_3}{R_4}$	$\frac{1}{\sqrt{R_1 R_2 C_1 C_2}}$	$\frac{\sqrt{R_1 R_2 C_1 C_2}}{(R_1+R_2)C_1+(1-G)R_1 C_2}$
8.15 (c)	$\frac{R_2}{R_1}$	$\frac{1}{\sqrt{R_2 R_3 C_1 C_2}}$	$\sqrt{\frac{C_2}{C_1}} \cdot \frac{R_4}{\sqrt{R_2 R_3}}$

First, an observation is made that the Sallen-Key biquad of Fig. 8.15 (b) is more problematic to implement as a differential circuit than the two others, because there are feedbacks to both the positive and negative inputs of the operational amplifier. This implies that an FDDA needs to be used in the implementation. On the other hand,
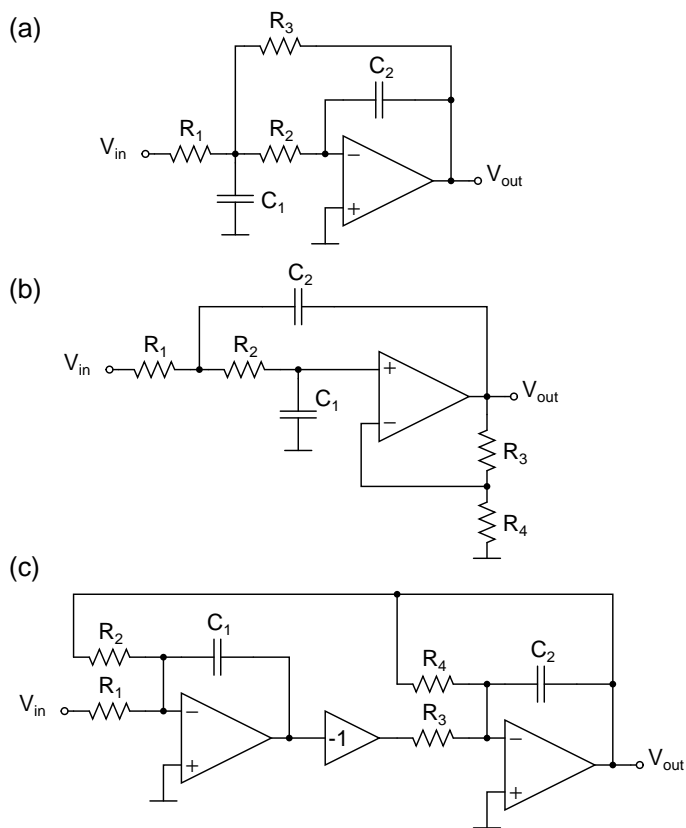
Figure 8.15 Various second-order low-pass filters. (a) Rauch biquad. (b) Sallen-Key biquad. (c) Two-integrator biquad.

the two-integrator biquad in Fig. 8.15 (c) is more easily implemented as a differential circuit than as a single-ended circuit, because the need for an inverting buffer can be eliminated by simply cross-connecting the outputs of the first integrator.

Second, all three implementations need two poles with large time constants, both implemented as a combination of a resistor and a capacitor. To achieve a dc gain and a quality factor close to one, the Rauch biquad in Fig. 8.15 (a) requires one additional large resistor, the Sallen-Key biquad none, and the two-integrator biquad two[2]. When considering the silicon area requirement, it also has to be taken into account that the two-integrator biquad requires two operational amplifiers, whereas the Rauch and the Sallen-Key biquads require only a single amplifier.

If properly biased MOS transistors are used to implement the resistors in the filter, either to achieve a smaller silicon area or to make possible continuous tunability of the critical frequency, then the two-integrator biquad is advantageous for two reasons. First, all the resistors are against the virtual ground of the operational amplifier, improving the linearity, and second, the implementation of the required MOSFET-C (MOSFET stands for Metal-Oxide-Semiconductor Field-Effect Transistor) integrator has been widely studied in the literature. Published implementations include the Banu-Tsividis integrator, dating back to 1983 [135, 136], the Czarnul integrator based on the MOS resistive circuit (MRC) [137–139], and the Moon-Song integrator [140].

For the present implementation, the two-integrator biquad shown in Fig. 8.15 (c) was chosen. This was to enable the feedback resistors to be implemented as MOS transistors, in order to save the silicon area. Another reason was to enable the continuous tuning of the critical frequency to be implemented, although this feature was not used in the system measurements. The integrators in the biquad are realized using the MRC. The schematic of the filter is shown in Fig. 8.16. The size of the integration capacitors is $4\,pF$ each, and the dimensions of the MOS transistors are $W/L = 2\,\mu m/100\,\mu m$. Equally-sized capacitors and resistors lead to a quality factor $Q = 1$. The difference between the voltages V_{C1} and V_{C2} is used to tune the critical frequency of the filter, as described in [138].

As long as the phase shifts in the LPFs in the primary and secondary channels match and the attenuation is sufficient under all operating conditions, no tuning of the critical frequency is required. However, a tuning circuit can be implemented to improve the performance, primarily the attenuation of the first folding signal bands. The tuning can be performed, for example, by monitoring the phase delay of the LPF in the primary channel and tuning it in such a way that it equals $90°$. This is possible, as there is a signal with a known frequency and amplitude in the primary channel.

---

[2]It is assumed for the sake of simplicity that both time constants are implemented with two equally-sized resistors and two equally-sized capacitors. This is not necessarily the best method to minimize the total silicon area occupied by the components.
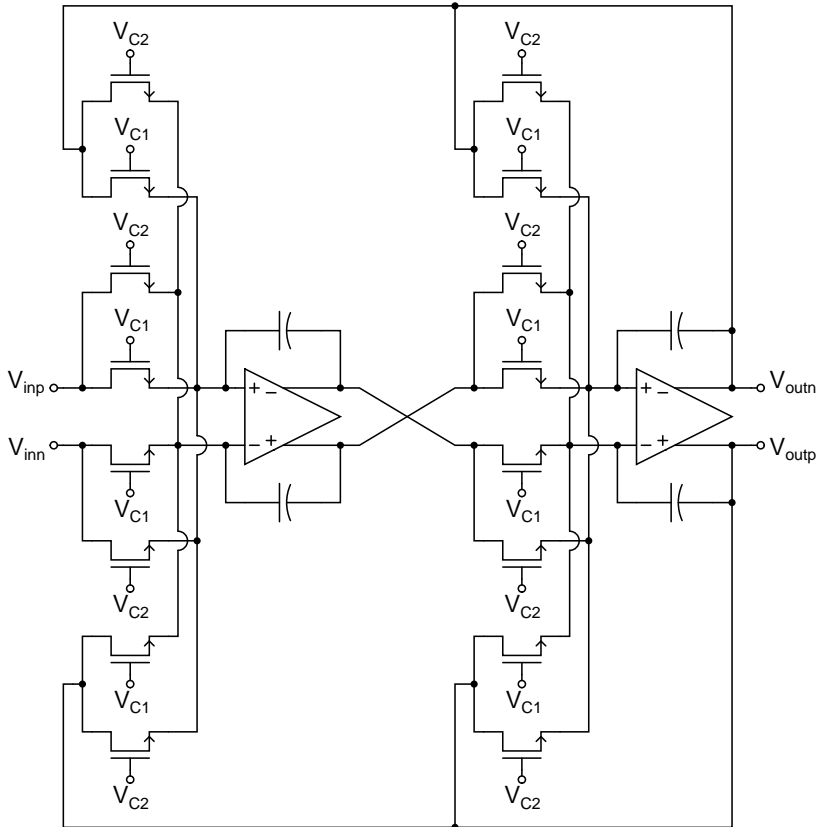
Figure 8.16 Schematic of the implemented low-pass filter.

8.3.5   Bandpass ΣΔ ADCs

A bandpass ΣΔ ADC is a quantization noise-shaping A/D converter that has a rela-
tively narrow signal band centered at a certain carrier frequency [100, Ch. 5]. This
is advantageous in the readout of a vibratory gyroscope, as a large oversampling ratio
(OSR) can be achieved with a much smaller sampling frequency when compared to the
low-pass counterpart.

In the present implementation, the required signal bandwidth is 125 Hz. Therefore,
an OSR of 320 is achieved with a sampling frequency of 40 kHz. The sampling fre-
quency is determined by the chosen implementation, as setting it to four times the cen-
ter frequency leads to a simple SC realization of the resonators, together with straight-
forward synchronous demodulation later in the DSP. The theoretical maximum signal-
to-quantization noise ratio (SQNR) of a 4th-order (two-resonator) converter is [141,
Ch. 14]

$$SQNR = 6.02N_{bits} + 1.76 - 12.9 + 50\log(OSR), \tag{8.15}$$

where N_{bits} is the number of output bits. The OSR of 320 with a single-bit output
yields a maximum theoretical SQNR of 120 dB, which is more than sufficient from the
system point of view. Therefore, there is no need to increase the modulator order[3].

To achieve the same (although unnecessarily large) OSR with a low-pass ΣΔ ADC
(with all zeroes of the noise transfer function at the origin), a sampling frequency
of 6.4 MHz would be required with the operating frequency of $f_{0x} = 10$ kHz. Even
with a more realistic OSR of 64 (yielding a theoretical maximum SQNR of 85 dB),
the required sampling frequency for a low-pass ΣΔ ADC would still be 1.28 MHz.
This means that a bandpass ΣΔ ADC has a clear advantage over a low-pass ΣΔ ADC
when the sampling frequency is considered. On the other hand, the lower sampling
frequency also means that the specifications for the analog anti-aliasing filter preceding
the converter are tighter in the case of a bandpass ΣΔ ADC than when a low-pass ΣΔ
ADC is used.

A block diagram of the implemented 4th-order bandpass ΣΔ ADC before multiplier
scaling is shown in Fig. 8.17 (a). The converter uses single-bit quantization, resulting
in a simple implementation of the quantizer and the feedback DAC. A simulated output
spectrum with a sampling frequency of $f_s = 40$ kHz is illustrated in Fig. 8.18. As can
be seen, the signal band is located at one quarter of the sampling frequency.

As the sampling frequency is low, it is most straightforward and efficient in terms
of silicon area to implement the ADC as an SC circuit. The resonators were designed
using the double-delay topology. A block diagram of a single resonator is shown in

---

[3]In principle, a 2nd-order (single-resonator) modulator would still yield a sufficient theoretical SQNR.
However, to avoid issues such as limit cycles or signal-dependent quantization noise, a 4th-order modulator
was chosen.
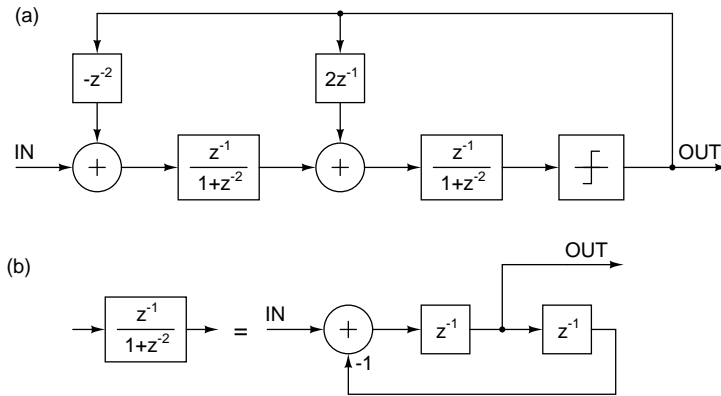
Figure 8.17 (a) Block diagram of the implemented bandpass ΣΔ ADCs. (b) Block diagram of a double-delay resonator.
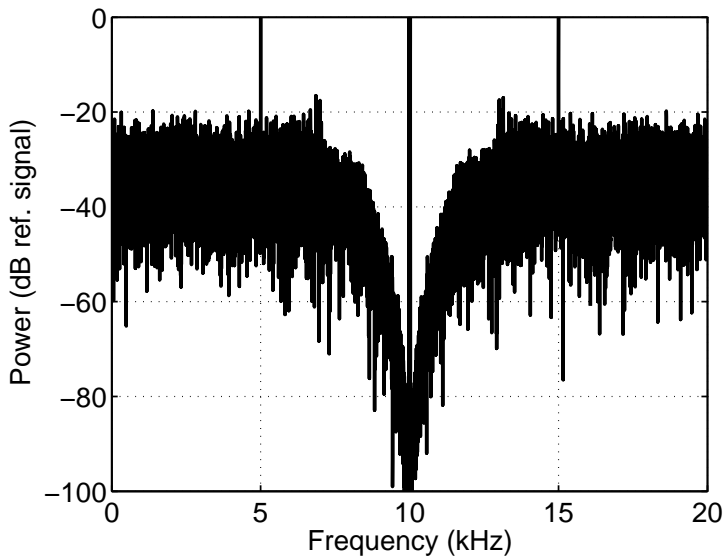
Figure 8.18 Output spectrum of the bandpass ΣΔ ADCs, simulated with a Matlab Simulink model. (40 000-point FFT, Kaiser window with β = 13, sampling frequency 40 kHz, −3 dB full-scale input)

Fig. 8.17 (b). By a simple calculation, it can be seen that it realizes the desired transfer function ($z^{-1}/(1+z^{-2})$). This simple implementation fixes the center frequency at $f_s/4$, irrespective of capacitor mismatch, without the need for tuning. Various other implementations of SC resonators have been studied in [142, Ch. 4].

A double-delay resonator is realized using a single operational amplifier [143]. The quantizer is implemented as a latched comparator. A full schematic of the ADCs is shown in Fig. 8.19.

8.4 Other Analog Circuit Blocks

In this section, the detailed implementation of other analog circuit blocks apart from the sensor readout electronics will be presented. These blocks include the PLL, the HV DAC, the charge pumps, the phase shifter required during start-up, and the drive-level DAC.

8.4.1 Phase-Locked Loop and Reference Clock Generation

The block diagram of the implemented charge-pump PLL [21] is shown in Fig. 8.20. An asynchronous phase-frequency detector (PFD) controls the charge pump, which feeds a continuous-time loop filter. The loop filter output voltage is buffered and fed to a voltage-controlled oscillator (VCO). A frequency divider (DIV) creates the required clock signals from the VCO output. The division factors used are indicated in the figure.

The PFD [141, Ch. 16] requires both the reference clock and the divided VCO output to be square wave signals. Whereas the divided VCO output is already a square wave, the reference clock needs to be converted into a square wave from the sinusoidal primary signal. This is performed with the comparator shown in the block diagram in Fig. 8.4. The comparator is implemented as a straightforward two-stage comparator, with a differential first stage and common-source second stage.

The loop filter is implemented within optimal chip area as a single-ended, on-chip, passive-RC filter. The time constant is determined by the reference signal frequency f_{0x}. The component values of the filter are $R_1 = 7.1\,\mathrm{M\Omega}$ and $C_1 = 50\,\mathrm{pF}$. The resistor is realized as a polysilicon resistor, whereas the capacitor is an MOS capacitor. Advantage is taken of the large parasitic capacitance of R_1 towards ground by utilizing it to realize the capacitor C_2. The total silicon area of the loop filter is approximately $0.067\,\mathrm{mm}^2$. The charge pump current is $150\,\mathrm{nA}$.

The VCO is shown in detail in Fig. 8.21. It is implemented as a differential relaxation oscillator, consisting of a current-controlled oscillator (CCO) and a transconductance amplifier which converts the control voltage V_{CTRL} into a current I_{CTRL}, with
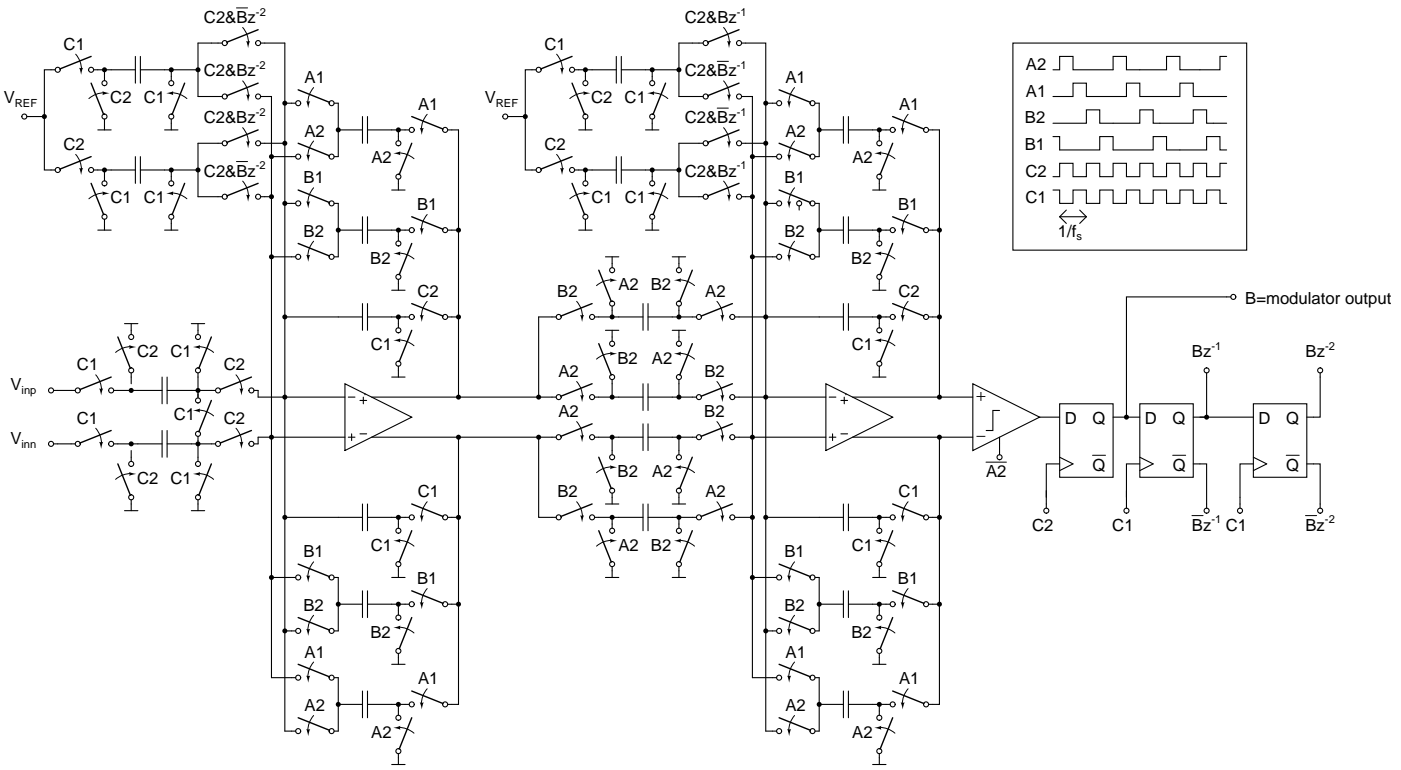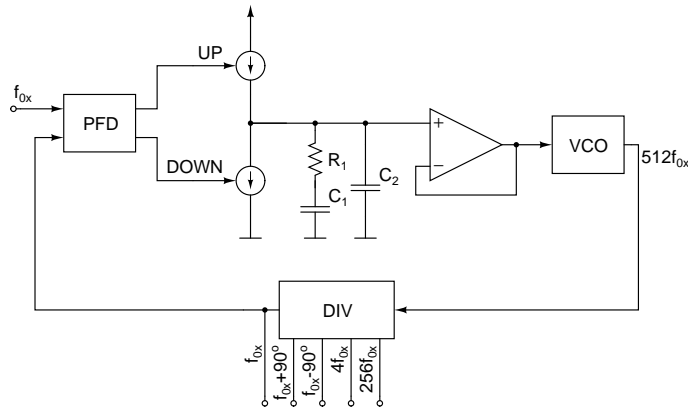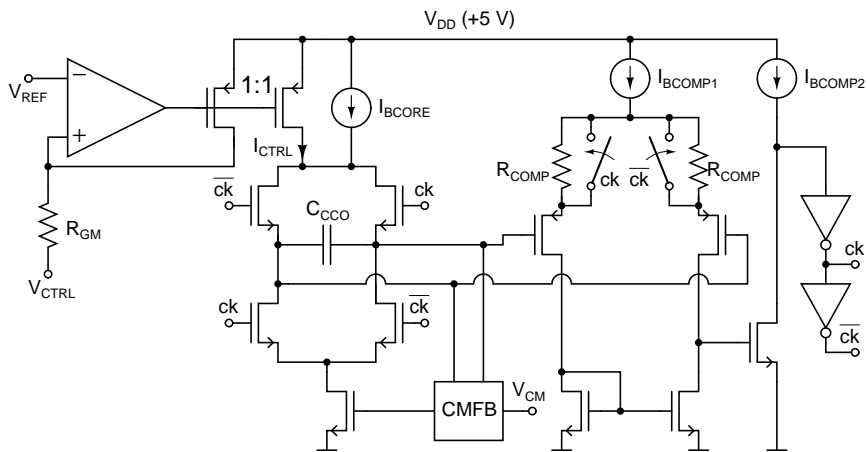
Figure 8.19 Schematic of the implemented bandpass ΣΔ ADCs.

Figure 8.20 A block diagram of the PLL.

$g_m = 1/R_{GM} = 10\,\mu A/V$. The CCO itself comprises a comparator with internal hysteresis, together with a floating capacitor $C_{CCO} = 1.33\,\mathrm{pF}$ between two current sources. The static current source $I_{BCORE} = 5\,\mu A$ provides additional biasing current to set the free-running frequency and the tuning range to the desired value.

Figure 8.21 Schematic of the VCO used in the PLL.

Because the flicker (1/f) noise is substantially higher in NMOS devices than in PMOS devices, PMOS current sources are preferred to NMOS current sources. In the implemented VCO, the differential switching configuration charging and discharging C_{CCO} has a CMFB circuit, which forces the current of the NMOS transistor to follow $I_{BCORE} + I_{CTRL}$, which are both provided by a PMOS current source. This removes the effect of the high flicker noise of the NMOS current source.

The biasing currents used in the comparator are $I_{BCOMP1} = 100\,\mu A$ and $I_{BCOMP2} = 50\,\mu A$. The resistors R_{COMP} that, together with the clocked switches, provide the hys-

teresis are equal to $15\,k\Omega$. The output frequency of the VCO as a function of the control voltage is

$$f_{VCO} = \frac{1}{2 \cdot R_{COMP} \cdot I_{BCOMP1} \cdot C_{CCO}} \cdot \left(\frac{V_{REF} - V_{CTRL}}{R_{GM}} + I_{BCORE} \right). \qquad (8.16)$$

By substituting the given parameters, a free-running frequency (with $V_{CTRL} = V_{REF}$) of $1.25\,MHz$ and a VCO gain of $2.5\,MHz/V$ are achieved.

The three most important sources of phase noise in the clocking system are the VCO and the large resistor in the passive-RC loop filter, together with the phase noise coming from the comparator that generates the reference clock. The first two sources can be considered as being internal to the actual PLL, whereas the third is independent of the PLL.

With a low reference frequency f_{0x} determined by the micromechanical resonator, the bandwidth of the PLL is forced to be narrow, leading to poor rejection of the phase noise caused by flicker noise. This has been taken into account in the VCO design by minimizing the effect of flicker noise sources, as described earlier.

Wideband noise at the input of the comparator can also increase the phase noise content of the reference clock and thus of the PLL output [23]. This noise folds to the reference frequency at the moment the comparator output changes its state, and thereby becomes converted to phase noise. The comparator bandwidth determines the band from which noise folding occurs. In the worst case, with a sufficiently fast comparator and a sufficient noise level, the output can change its state more than once during the zero crossing of the input. This will cause the PLL to lose its lock and to create false output, which destroys the system functionality. While other noise effects can be removed with the phase correction described in Section 8.2.2, this type of behavior causes irreversible degradation of the output signal. False switching can be prevented by adding some hysteresis to the comparator. The phase correction compensates for the resulting delay.

8.4.2 High-Voltage DAC

The HV DAC [22] is implemented with a low-voltage (LV) resistor-string DAC and an HV operational amplifier. A resistor-string DAC was chosen because of its guaranteed monotonicity, which is important in order to ensure the stability of the control loop. The amplifier is powered by a charge pump, which provides a regulated and filtered supply voltage of $+28\,V$. The implementation of the charge pump will be described in more detail in the following section.

The schematic of the amplifier is shown in Fig. 8.22. To minimize the silicon area and the loading of the charge pump, only the second stage is operated with the high-

voltage output. The HV cascode transistors MN11, MP14, and MN15 make it possible to implement the current sources with LV transistors, with improved matching properties compared to HV devices. The diode cascade formed by MN17-MN20 prevents the voltage at the drain of MN16 from floating above the maximum tolerated voltage when V_{out} is slewing up.
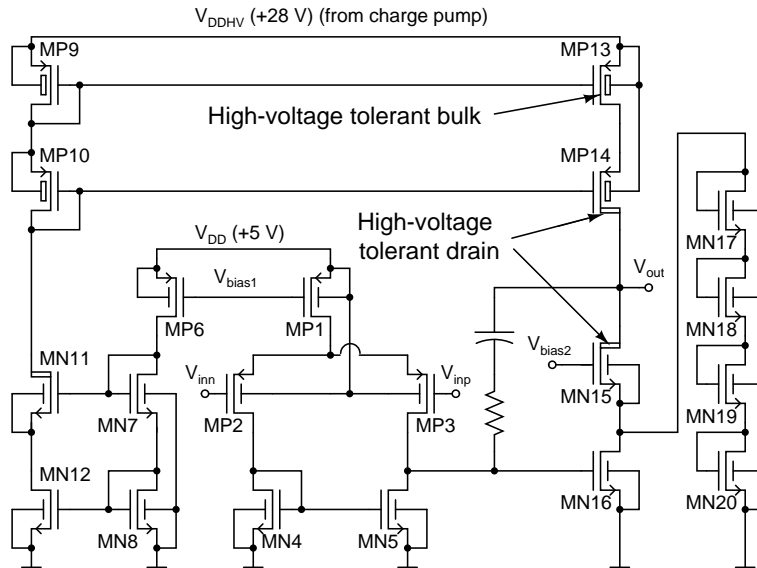
Figure 8.22 A schematic of the high-voltage operational amplifier used in the high-voltage DAC to amplify the low-voltage DAC output.

With the HV amplifier connected in non-inverting configuration using resistive feedback, it will amplify the LV DAC full-scale output of 2.5 V to 27.5 V with a maximum output current of $10\,\mu$A. The LSB size of the amplified compensation voltage is approximately 30 mV, yielding a tuning range of ±1.92 V with the 7-bit control. A 4-bit coarse tuning of the DAC is used to set the output around a desired level, with an LSB size of 1.7 V.

The measured maximum INL/DNL (Integral/Differential Nonlinearity) of the 4-bit coarse tuning part are $0.00445/0.00143$ LSBs, respectively. The maximum INL/DNL of the 7-bit control are $0.227/0.140$ LSBs, respectively. [22]

8.4.3 Charge Pumps

The high supply voltages for the HV amplifier in the HV DAC and for the primary resonator excitation in the start-up phase (described in Section 8.2.5) are generated from the nominal $+5$ V supply by using charge pumps. The pumps are fully integrated, with their designs being based on the traditional Dickson charge pump [144]. The implementation and the optimization of the pumps are described in detail in [20, 22].

From the silicon area point of view, the most effective way to generate voltages higher than the supply is voltage doublers. However, because voltages close to $+30\,\text{V}$ are required, the switching transistors cannot tolerate full-swing gate-source voltages. This would lead to complicated clock-generating circuits and possible start-up problems if doublers were used.

To avoid these problems, Dickson charge pumps with diodes can be used instead. The high-voltage output of a Dickson charge pump, without taking the effect of parasitic capacitances or resistive loading into consideration, is

$$V_{HV} = (N_{stages} + 1)(V_{DD} - V_d),\qquad(8.17)$$

where N_{stages} is the number of charge pump stages and V_d is the forward voltage drop of a diode. This can lead to a large number of stages and hence high silicon area consumption if high output voltages are required.

In the present implementation, the silicon area of a traditional Dickson charge pump is reduced by dividing the pump into two stages. The clock signals for the second stage are generated using the output voltage of the first stage. Thus, a smaller chip area can be attained at the expense of somewhat increased power consumption [145]. A basic schematic of the charge pump is shown in Fig. 8.23. The first stage is presented in Fig. 8.23 (a), the medium-voltage (MV) clock generator in Fig. 8.23 (b), and the second stage in Fig. 8.23 (c). The clock signal CLK and its inversion are generated with a dedicated oscillator that is not shown in the schematic.
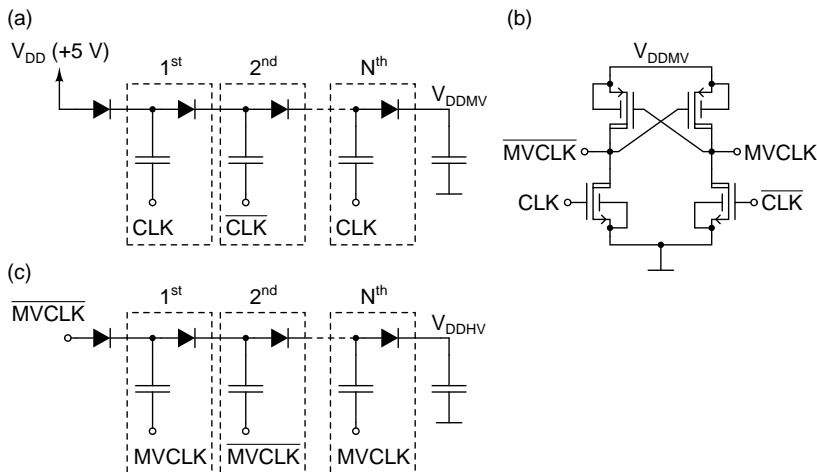
Figure 8.23 (a) First stage of the overall charge pump. (b) Medium-voltage clock generator. (c) Second stage of the overall charge pump.

In the charge pump generating the high-voltage supply for the amplifier in the HV DAC, a limiter implemented as a controllable resistive load regulates the output voltage

V_{DDHV} to the desired level. The load is controlled in a closed-loop configuration. This charge pump also provides another regulated output, which serves as the $+8.25\,$V bias voltage for the sensor middle electrode during normal operation.

In the charge pump used to excite the primary resonator during the start-up, output voltage regulation is not necessary. The only condition that needs to be fulfilled is that the pump provides a high enough voltage to ensure a reliable start-up in a given time. A typical single-ended excitation voltage is $20\,$V peak-to-peak [20].

In this charge pump, the second stage is doubled. In this way, differential excitation can be performed by turning off one of the two outputs at a time (setting it to a high-impedance state) and by pulling the output to ground with an HV NMOS device, while the other output biases the opposite excitation electrode to high voltage. With this kind of implementation, the use of floating series switches, which are again complicated to implement, is avoided. When the primary resonator excitation is switched to the PLL, both outputs are turned off, together with the first stage and the oscillator generating the clock.
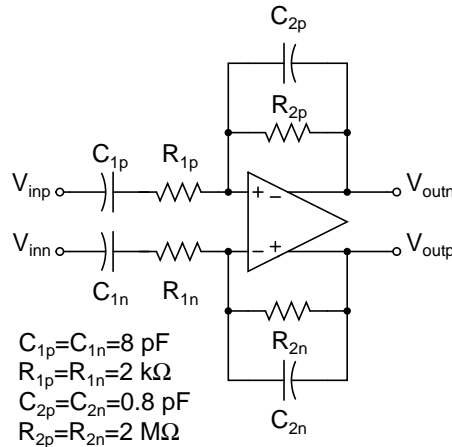
8.4.4   Phase Shifter

The analog phase shifter which provides a $90°$ phase lead during start-up is implemented as a differentiator. A generic schematic of the circuit is shown in Fig. 8.24. If the operational amplifier is assumed to be ideal, the transfer function can be written as

$$H\left(s\right) = \frac{sC_1R_2}{\left(1+sR_1C_1\right)\left(1+sR_2C_2\right)}, \tag{8.18}$$

where $C_1 = C_{1p} = C_{1n}$, $C_2 = C_{2p} = C_{2n}$, $R_1 = R_{1p} = R_{1n}$, and $R_2 = R_{2p} = R_{2n}$. The components are typically dimensioned in such a way that both poles of the circuit are at least one decade higher than the operating frequency, in this case $f_{0x} = 10\,$kHz. At the operating frequency, the capacitors C_{1p} and C_{1n} dominate the input impedance and the resistors R_{2p} and R_{2n} the feedback impedance. This provides a $90°$ phase lead. A slight error in the phase lead is not significant, as it only reduces the resulting excitation force proportionally to the cosine of the error.

In the present implementation, the first pole is determined by the resistors R_{2p} and R_{2n}, together with the capacitors C_{2p} and C_{2n}, and is located at $100\,$kHz. The second pole that limits the bandwidth of the phase shifter is provided by the operational amplifier and is located between 100 and $200\,$kHz. The pole determined by the resistors R_{1p} and R_{1n} together with the capacitors C_{1p} and C_{1n} is located at a higher frequency, in order to provide additional filtering at frequencies beyond the amplifier bandwidth.

When designing the phase shifter as a differentiator, it is necessary to ensure that the functionality of this or any subsequent circuit blocks is not compromised by the

Figure 8.24 Schematic of the implemented phase shifter.

high-frequency noise of the circuit [23]. This is why the bandwidth of the implemented differentiator is limited with the poles. Another significant factor in the excitation of a micromechanical resonator is to ensure that the magnitude-phase properties of the whole feedback loop do not enable any parasitic vibration modes to start oscillating and prevent reliable start-up.

When both of these issues are considered, a phase shifter implemented as an integrator combined with phase inversion would perhaps be a better choice. The schematic of such a circuit is identical to that shown in Fig. 8.24, but in an integrator, the operating frequency f_{0x} is beyond both poles, and at the operating frequency the resistors R_{1p} and R_{1n} dominate the input impedance and the capacitors C_{2p} and C_{2n} the feedback impedance. In this way, a phase lag of $90°$ is achieved. The gain rolls off by 20 dB per decade after f_{0x}, instead of increasing up to the frequency of the first pole, as in the differentiator. This provides attenuation for both high-frequency noise and for the loop gain at any parasitic vibration modes beyond f_{0x}. The most significant disadvantage of the integrator is that the time constants are at least two orders of magnitude higher than in the differentiator, resulting in a significant penalty in terms of silicon area consumption. The silicon area can be reduced by removing the capacitors C_{1p} and C_{1n} altogether, but then the input-referred offset voltage of the operational amplifier is amplified by $1 + R_2/R_1$, leading to possible problems, especially if the phase shifter is followed by a comparator.

8.4.5 Drive-Level DAC

The drive-level DAC is implemented as a resistor string DAC, with 32 possible output levels between the supply rails of $+5$ and 0 volts (including the rails). Using the DAC,

both the high and low levels of the two excitation signals can be set, with an LSB size of approximately $161\,\text{mV}$. In this way, both the dc and the ac components of the excitation signals can be set to a desired value.

8.5   Digital Signal Processing

After the $\Sigma\Delta$ ADCs, the rest of the signal processing is performed in the digital domain. This includes the downconversion and the decimation of the output data and the phase error correction described in Section 8.2.2, also including the normalization of the secondary signals with respect to the primary signal.

Additionally, the controllers required by the system are implemented using DSP. They are the primary resonator amplitude controller and the quadrature signal compensation controller. Finally, there is a start-up controller, which controls the start-up sequence of the DSP and sets various parameters in the ASIC to make a reliable start-up possible.

8.5.1   Downconversion, Decimation, and Phase Correction

The oversampled output data from a $\Sigma\Delta$ ADC need to be filtered and decimated in order to reach the final desired accuracy and sampling rate [100]. Additionally, in the case of a bandpass $\Sigma\Delta$ ADC, the data need to be demodulated before filtering.

As stated at the beginning of Section 8.2.2, the $\Sigma\Delta$ ADCs have a sampling period of $90°$ ($\pi/2$). It is assumed that every second sample represents the amplitude of the in-phase component (alternatively multiplied by -1 and $+1$) and every other sample the amplitude of the quadrature component (similarly multiplied) of the respective signal. Therefore, the demodulation can be performed by multiplying the output data stream from the A/D converter by a sequence $\{1,\, 0,\, -1,\, 0,\dots\}$, representing a digital cosine wave with a frequency $f_s/4$ or one quarter of the sampling frequency. The $90°$ phase-delayed version of this is a digital sine wave. Similarly to the cosine wave, it reduces to a sequence $\{0,\, 1,\, 0,\, -1,\dots\}$. Proper phasing of the signals is ensured by monitoring the output signal from the comparator that generates the reference clock for the PLL.

After the demodulation, the results can immediately be decimated by two by removing the zeroes from the sequences. This operation reduces the sample rates to $f_s/2$, which results in the folding of the spectra to the frequency range $[0\dots f_s/4[$. The outcome is that the decimated outputs are implicitly multiplied by two.

The output data stream from the ADC is a single-bit sequence of 0s and 1s. If 0 is taken to represent -1, the demodulation consists of the multiplication operations $-1 \cdot (-1) = 1$, $-1 \cdot 1 = -1$, $1 \cdot (-1) = -1$, and $1 \cdot 1 = 1$. This can be implemented

as an XOR operation, resulting in a single-bit output sequence from the demodulator, consisting only of 1s and -1s (which is again representable as 0s and 1s).

After demodulation and the initial decimation by two, the data are filtered to remove the out-of-band quantization noise and decimated to reduce the sampling rate. The implementation of decimation filters has been studied, for example, in [146–148]. The so-called CIC (Cascaded Integrator-Comb) structure, also known as the Hogenauer structure [149], leads to a very simple hardware implementation. However, it might not provide sufficient passband ripple properties and/or attenuation of folding spectral components. An alternative is to use a digital low-pass filter, followed by a decimation. This gives the designer freedom to choose the pass-band properties and stop-band attenuation to yield the desired performance, but it increases the hardware complexity. Typically, the decimation is performed in multiple stages, in such a way that the sampling rate is not reduced to the final value in a single decimation but in smaller consecutive steps. This reduces the overall complexity of the decimation filters.

In the present implementation, the decimation is performed in three stages, with decimation factors of 10, 8, and 2. With the initial decimation by two performed in the demodulator, this leads to a total decimation factor of 320. With a typical sampling rate of 40 kHz, the final output sampling frequency is 125 Hz. The last decimation filter limits the output bandwidth in such a way that the -3 dB corner frequency is at 40 Hz when the final $f_s = 125$ Hz. The decimation filters are implemented as FIR (Finite Impulse Response) digital filters. Because of the FPGA implementation, the hardware complexity of the individual filters was not optimized. However, a single set of hardware was used in a time-multiplexed fashion to perform the decimation for all four outputs of the demodulators (in-phase and quadrature components of both primary and secondary signals).

The phase correction and the signal normalization described by Eqs. (8.10a) and (8.10b) were implemented with the basic arithmetic blocks offered by the design environment. No hardware optimization was performed for them either.

8.5.2   Controllers

The primary resonator amplitude controller is implemented as an I controller. The amplitude control is performed by monitoring the value $I_{out,pri}^2 + Q_{out,pri}^2$, which is readily available from the phase correction described in Section 8.2.2, and driving it to a desired level. In this way, the effect of the phase shift $\theta_{LPF,pri}$ is eliminated and the true primary resonator vibration amplitude can be accessed. On the other hand, the controller now monitors the square of the amplitude, which has to be taken into account while designing the dynamics of the control loop.

The controller output directly controls the amplitude of the electrostatic force used for excitation, as shown in Fig. 4.5. The control is performed by setting the dc component of the excitation voltage. The resolution of the drive-level DAC M is 5 bits.

A $\Sigma\Delta$ modulation of the primary resonator excitation signal is also implemented to show that it can be used to remove the spurious components resulting from the time-varying primary resonator vibration amplitude from the output spectrum. The implementation of the modulator was shown in Fig. 4.6. The dc component of the excitation voltage is modulated.

When $\Sigma\Delta$ modulation is applied, the resolution of the controller output was chosen to be $K = 18$ bits and the frequency of the interpolated signal 10 kHz. This gives an interpolation factor of $m_{IF} = 80$. The value of K was chosen experimentally by first measuring the change of the primary resonator output signal caused by a change of a single LSB at the drive-level DAC output, and then evaluating how many more bits of resolution are required to suppress the change below 0.5 LSB. The frequency of the interpolated signal was chosen in such a way that the dc component of the excitation voltage changes once during every period, giving a frequency equal to the 10-kHz operating frequency. In this way, the dc-level changes can be made to coincide with the rising edges of the excitation signal, minimizing the possible cross-coupling issues but, at the same time, maximizing the interpolated frequency. The interpolation is performed with a zero-order hold. The resolution of the excitation DAC is 5 bits, yielding $M = 5$. The simulated output signal was shown in Fig. 4.7 (a) and the resulting spectra in Figs. 4.8 (a) and 4.9.

The quadrature compensation controller is implemented as an I controller. The integrator output is brought to a $\Sigma\Delta$ modulator, the output of which is then used to control the HV DAC. The implementation of the modulator was shown in Fig. 5.6. The resolution of the controller output was chosen to be $K = 15$ bits and the frequency of the interpolated signal 500 Hz. This gives an interpolation factor of $m_{IF} = 4$. The interpolation is performed with a zero-order hold. Again, K was chosen experimentally using the same methodology as with the $\Sigma\Delta$ DAC used to create the primary resonator excitation signals. The frequency of the interpolated signal was chosen by simulating the system using Matlab Simulink and finding a value that gives a sufficiently low level of the quantization noise. The resolution of the HV DAC is 7 bits, yielding $M = 7$. The simulated output signal was shown in Fig. 5.7 and the resulting spectrum in Fig. 5.8.

The quadrature compensation controller also sets the gain of the VGA in such a way that the dynamic range of the secondary channel is maximized. This means that the quadrature component of the demodulator output is monitored, and it is kept at certain limits by controlling the gain. As the quadrature compensation drives the component towards zero, the gain is increased.

The start-up controller is implemented as a state machine. The state changes are

triggered by the primary resonator vibration amplitude. First, the sensor middle electrode is biased to ground and the charge pump is used to excite the primary resonator. As the amplitude grows, the attenuation in the primary channel is increased. After the PLL has locked to the primary signal and the amplitude is sufficient, it takes over the excitation, and amplitude control is enabled. At the same time, other blocks such as the quadrature compensation control are enabled.

8.6   Experimental Results

In this section, the experimental results achieved with the implemented system will be presented. First, the measured results for the sensor readout electronics from the CSA to the $\Sigma\Delta$ ADC input will be shown. Next, the phase correction described in Section 8.2.2 will be studied. Then, different implementations of the quadrature compensation loop will be presented, first without and then with $\Sigma\Delta$ techniques to improve the resolution. Next, the ZRO properties of the system will be presented. At the same time, techniques for performing the ZRO measurements will be given. Finally, the performance of the whole system will be characterized.

Because of the very limited number of sensor element samples available, an element with a lower-than-expected primary resonator quality factor had to be used during the measurement. For this reason, the dc level of the excitation voltage was increased using additional components on the PCB. Apart from compensating for the low quality factor, this also affects the ZRO component caused by the direct excitation of the secondary resonator. This will be taken into account when the measured ZRO results are discussed.

8.6.1   Sensor Readout

The measured noise spectrum at the bandpass $\Sigma\Delta$ ADC input in the secondary channel is shown in Fig. 8.25. The spectrum has been scaled by dividing by the gain of the channel at $f_{0x} = 10\,\mathrm{kHz}$, equal to $5.75 \cdot 10^{13}\,\mathrm{V/F}$. From the figure, it can be seen that the noise level at the operating frequency is approximately $0.07\,\mathrm{aF}/\sqrt{\mathrm{Hz}}$ at $10\,\mathrm{kHz}$. The first folding component at $30\,\mathrm{kHz}$ is approximately $0.025\,\mathrm{aF}/\sqrt{\mathrm{Hz}}$, increasing the resulting noise level after sampling by $0.5\,\mathrm{dB}$.

The measured noise level at $10\,\mathrm{kHz}$ corresponds to an output-referred noise voltage density of $4\,\mu\mathrm{V}/\sqrt{\mathrm{Hz}}$, or an input-referred noise current density of $25\,\mathrm{fA}/\sqrt{\mathrm{Hz}}$. As discussed in Section 8.3, the noise results primarily from the CSA and the first highpass filter. The measured noise level is $2.4\,\mathrm{dB}$ larger than the simulated one. This can be accounted for either by process variation of the feedback resistances or additional parasitic capacitance connected to the CSA inputs.
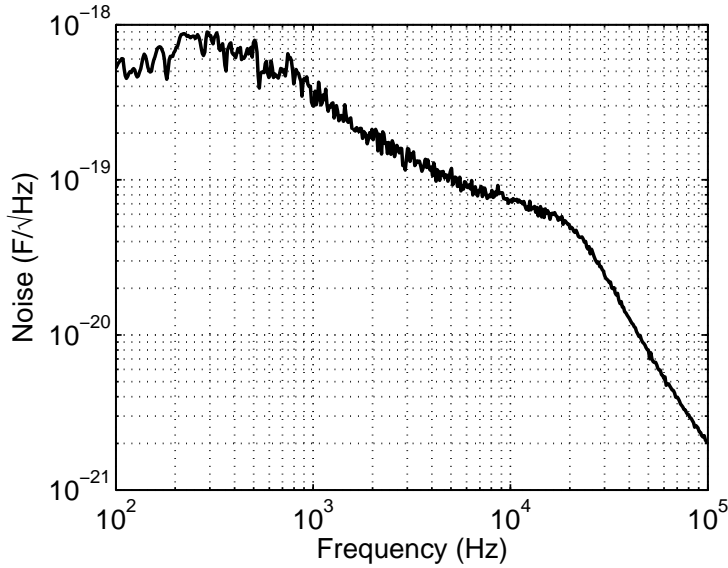
Figure 8.25 Measured output noise spectrum of the secondary channel, scaled with its gain at 10 kHz.

The measured difference between the phase shifts caused by the primary and the secondary channel θ_1 is shown in Fig. 8.26. The temperature coefficient from -40 to $+85°C$ is $8.7 \cdot 10^{-3}\,°/°C$ or $0.15\,\text{mrad}/°C$.

8.6.2 Phase Error Correction

The effectiveness of the phase error correction and noise cancellation described in Section 8.2.2 was studied experimentally by feeding sinusoidal test signals to the primary and secondary channels and externally controlling the phase shift θ_2 by adding offset to the signal just before feeding it to the comparator shown in Fig. 8.4. For ease of implementation, the test signals were fed to the outputs of the first HPFs instead of the high-impedance CSA inputs. Therefore, the noise level coming from the readout electronics differs from the nominal case. The values of θ_1 also lack the effect of the CSAs and the first HPFs. A full-scale signal was kept at the ADC inputs. The down-conversion and decimation of the $\Sigma\Delta$ ADC outputs, together with the subsequent phase correction, was performed with Matlab. The algorithms applied were identical to those of the FPGA implementation.

First, the effectiveness of the phase correction with a static error was studied. Figure 8.27 shows θ after the phase correction (corrected θ) as a function of θ before the phase correction (uncorrected θ), while θ_2 is varied. The contribution of the term $\theta_{LPF,pri}$ to the uncorrected θ (defined in Eq. (8.3)) is approximately $-30°$. The mea-
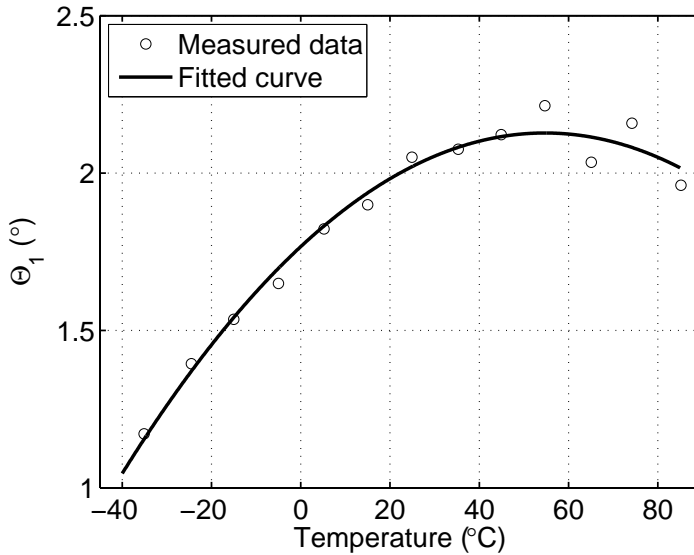
Figure 8.26 Measured difference between phase shifts θ_1 over temperature.

surement was performed for two cases. In the first case, plotted in Fig. 8.27 (a), the signal fed to the secondary channel has a $90°$ phase lag compared to the signal fed to the primary channel, i.e. it is in phase with the Coriolis signal. In the second case, plotted in Fig. 8.27 (b), the signals fed to the primary and the secondary channels are in phase. Now, the signal in the secondary channel is in phase with the mechanical quadrature signal.

From the results, it can be seen that while the secondary signal is in phase with the mechanical quadrature signal (Fig. 8.27 (b)), the phase correction is practically perfect. The remaining variation is random and is due to measurement uncertainty. On the other hand, when the secondary signal is in phase with the Coriolis signal (Fig. 8.27 (a)), the error is not completely removed, but is attenuated by $38\,$dB. This can perhaps be accounted for by cross-coupling from the comparator output to the secondary channel that slightly turns the phase of the secondary signal.

Next, the phase noise attenuation was studied. Excess noise was added to θ_2 and output noise levels were measured. Figure 8.28 shows the r.m.s. noise levels of the in-phase and quadrature components of the downconverted secondary signal before and after the phase correction was performed. The noise levels are plotted as a function of the phase shift of the signal fed into the secondary channel compared to the signal fed into the primary channel.

The figure shows two cases. In the first case, noise was added in such a way that when the secondary signal phase is $0°$ (in phase with the primary signal), the
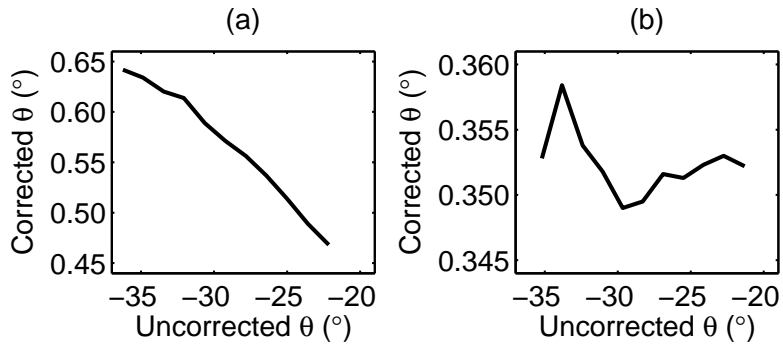
Figure 8.27 The effect of phase correction with static error. (a) Secondary data in phase with the Coriolis signal. (b) Secondary data in quadrature.

r.m.s. noise level rose by approximately 20 dB. In the second case, the noise level was increased by a further 10 dB.

In both figures, a noise minimum at a phase shift of approximately $-60°$ can be observed in the in-phase component of the demodulator output before correction. At the same time, the uncorrected quadrature component exhibits a noise maximum. This can be understood as follows: the $60°$ phase lag of the secondary channel input signal with respect to the primary channel input signal is combined with the $30°$ phase lag caused by the LPF. Because it is assumed in the demodulation that every second sample of the ADC output signal carries the amplitude of the in-phase component and every other sample the amplitude of the quadrature component, then as a result of the total phase lag of $90°$, the in-phase component is sampled when the sinusoidal secondary signal is either at its minimum or maximum and its first derivative is thus zero, whereas the quadrature component is sampled when the secondary signal is crossing the zero level and the first derivative is now at its extremum. Therefore, the jitter caused by the phase noise has very little effect on the sampled value of the in-phase component, leading to the noise minimum. The minimum is very narrow, as the second derivative is now at its extremum. At the same time, the quadrature component is sampled when the first derivative is at its extremum, leading to maximum sensitivity to jitter and hence to the noise maximum. The maximum is broad, as now the second derivative is at its minimum.

If the phase lag were increased further, a noise minimum could be observed in the quadrature component and a maximum in the in-phase component of the output signal when the lag reaches $150°$. This can be explained in the same way as above, but now the quadrature component is sampled when the derivative is equal to zero and the in-phase component when the derivative is at its extremum.

From the measured results, it can be seen that the phase correction cancels the effect of phase noise. The effectiveness of cancellation varies slightly, but the resulting
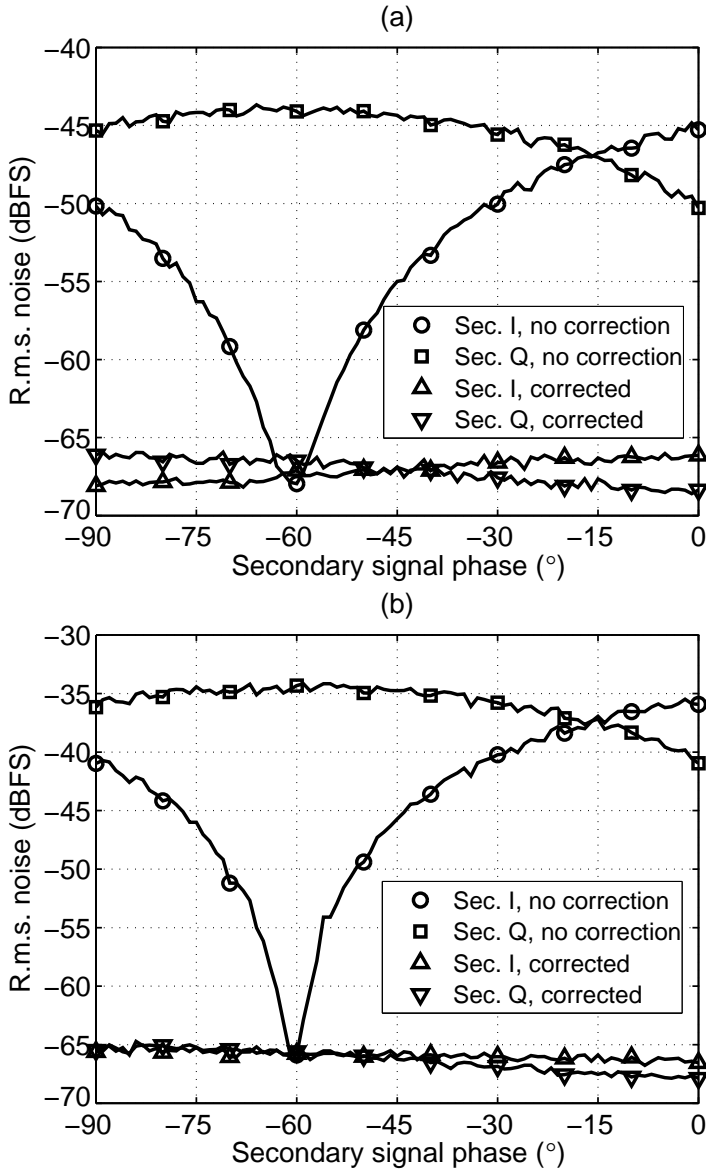
Figure 8.28 Measured r.m.s. noise levels in in-phase and quadrature components of the down-converted secondary signal before and after phase correction as a function of the secondary signal phase. (a) Phase noise added to increase the noise level of uncorrected quadrature component by 20 dB when the phase is 0°. (b) Phase noise increased by further 10 dB.

r.m.s. noise after correction stays between -65.5 and $-68\,$dBFS in both cases. The measured r.m.s. noise without phase noise effects is $-68\,$dBFS. Figure 8.29 shows the measured output spectra of the in-phase and quadrature components of the secondary data before and after correction while the phase is equal to $0°$.
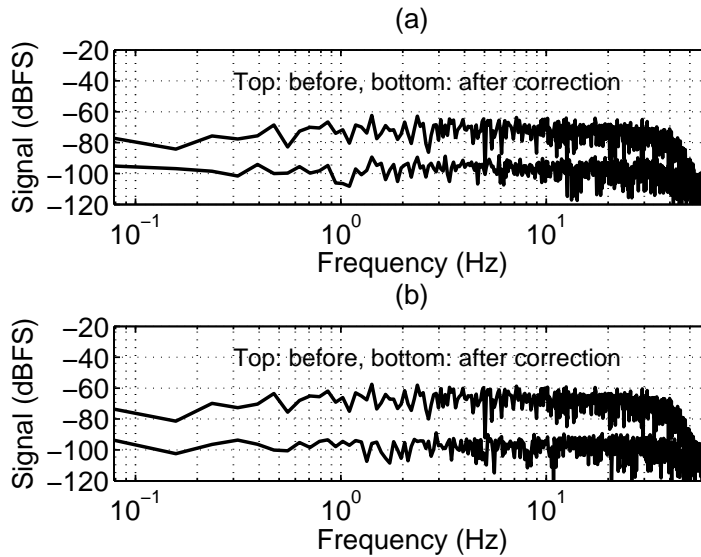

Figure 8.29 Measured noise spectra of (a) in-phase and (b) quadrature parts of the downconverted secondary signal before and after correction when the phase is equal to $0°$. (1590-point FFT, no windowing, sampling frequency $125\,$Hz)

8.6.3   Quadrature Signal Compensation

Next, the quadrature signal compensation schemes presented in Section 5.2 were studied experimentally. The uncompensated mechanical quadrature signal of the sensor element was measured as being 20 times the full-scale Coriolis signal, so the need for compensation was evident. In the first implementation, the quadrature compensation was performed as shown in Fig. 5.5. The controller was implemented as an I controller. The DAC is the 7-bit HV DAC presented in Section 8.4.2.

The measured quadrature signal is shown in Fig. 8.30. As can be seen, the signal exhibits oscillation between two levels, with a difference of about 130 LSBs. The average of the quadrature signal is zero. The spectrum of the corresponding Coriolis signal can be seen in Fig. 8.31. The spectral components indicated by the triangles are caused by the time-varying quadrature signal and the phase error in synchronous demodulation, together with the differences of the transfer functions of the two sidebands of the force through the secondary resonator.
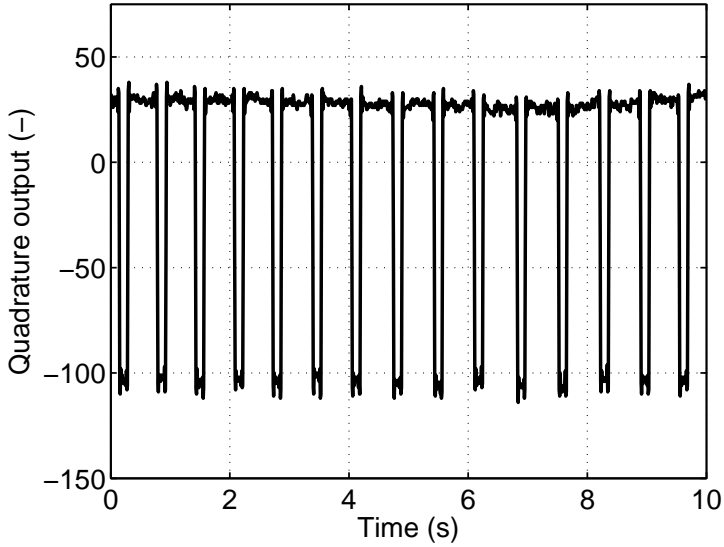
Figure 8.30 Quadrature signal when the compensation is performed with a 7-bit DAC, illustrating the oscillation between two levels as a result of the limited DAC resolution.
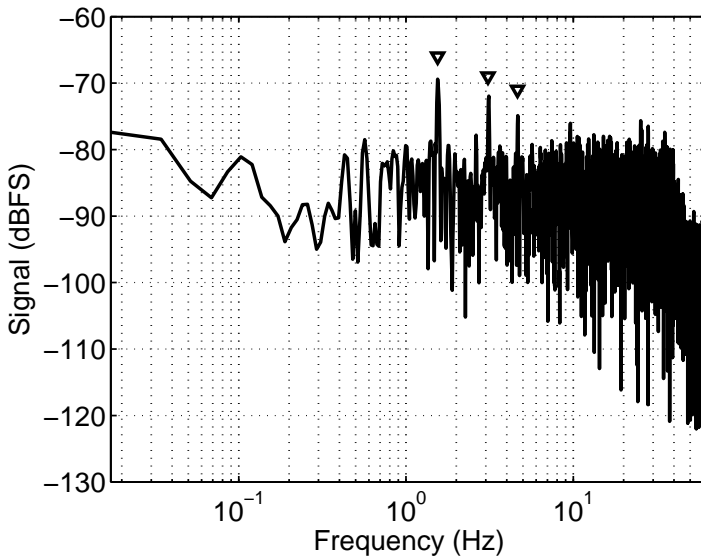
Figure 8.31 Spectrum of the resulting Coriolis output when the quadrature signal varies between two levels as a result of limited compensation resolution. (7281-point FFT, Kaiser window with $\beta = 13$, sampling frequency $125\,\mathrm{Hz}$, FS $= 100°/\mathrm{s}$)

The result indicates that the DAC resolution needs to be increased by at least 8 bits in order to remove the spurious components. This was done by next implementing the quadrature compensation with a second-order $\Sigma\Delta$ DAC (Fig. 5.6). The controller was still implemented as an I controller. The parameters of the modulator were given in Section 8.5.2, when the DSP implementation was described.

The simulated output spectrum of the DAC was shown in Fig. 5.8. It can be seen that there is a notch at 10 kHz, corresponding to the operating frequency. This means that the effect of the cross-coupling on the final SNR is minimized. Figure 8.32 shows the measured quadrature signal. Now, the oscillation observed in Fig. 8.30 has been removed. Figure 8.33 shows a measured output spectrum of the Coriolis signal. For comparison, a spectrum with the quadrature compensation performed with an external dc voltage source is shown in Fig. 8.34. The spectral components at approximately 0.3 Hz are caused by the time-varying primary signal. By comparing Figs. 8.33 and 8.34, it can be seen that the compensation has no effect on the final SNR. This will be verified in Section 8.6.5.
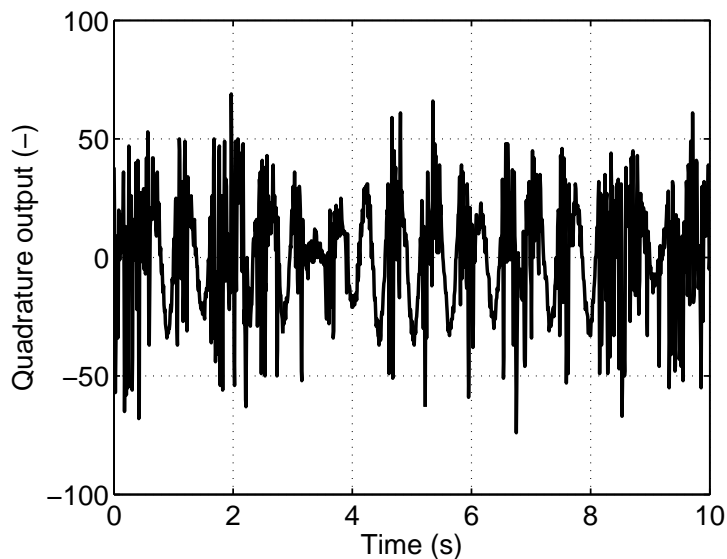
Figure 8.32 Quadrature signal when the compensation is performed with a $\Sigma\Delta$ DAC.

8.6.4 Zero-Rate Output

Next, the various ZRO sources were experimentally studied. During the ZRO measurements, both the phase error correction and the compensation of the mechanical quadrature signal with the $\Sigma\Delta$ DAC were used. A challenge is to find suitable measurement methods which can distinguish between the various sources. By examining
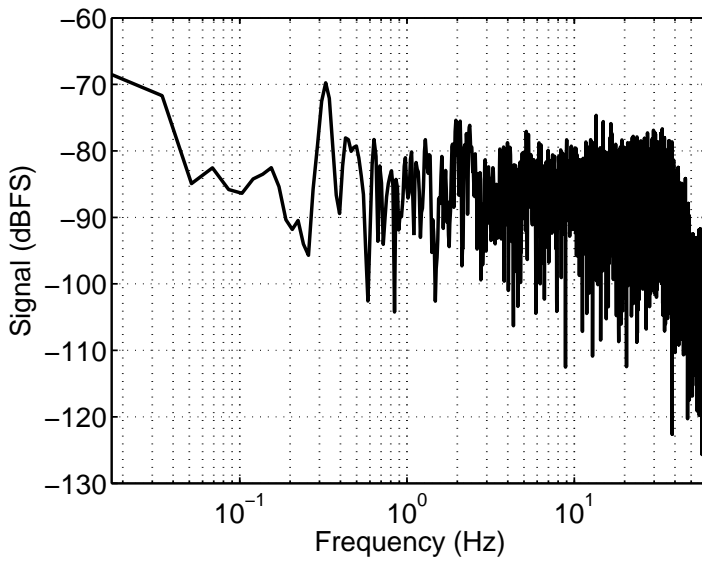
Figure 8.33 Spectrum of the resulting Coriolis output when a ΣΔ DAC is used for compensation. (7281-point FFT, Kaiser window with β = 13, sampling frequency 125 Hz, FS = 100°/s)
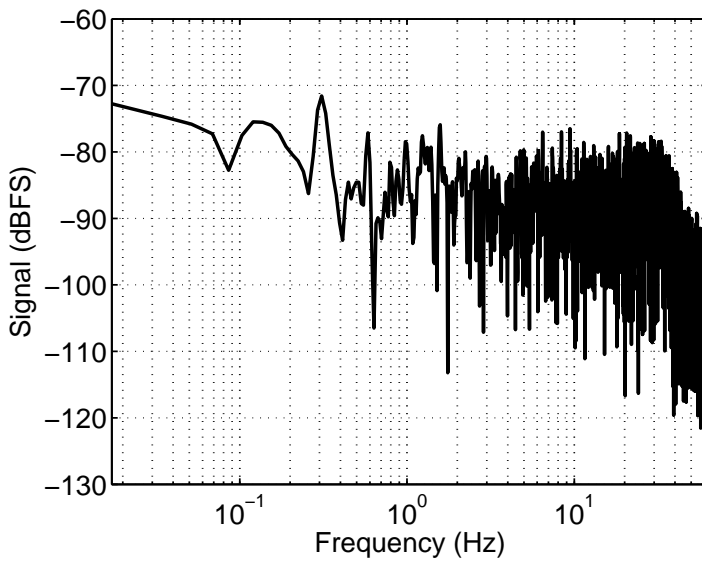
Figure 8.34 Spectrum of the resulting Coriolis output when the quadrature signal is compensated with a dc voltage. (7281-point FFT, Kaiser window with β = 13, sampling frequency 125 Hz, FS = 100°/s)

Eq. (6.16), it can be recognized that the electrical cross-coupling $\gamma V_{AC} \cdot \cos(\theta)$ and the direct excitation of the secondary resonator $\delta V_{DC} V_{AC} G_{y/F} G_{V/y} \cdot \cos(\theta)$ can be found by varying the dc and ac components V_{DC} and V_{AC} of the primary resonator excitation signal, if it can be ensured at the same time that the primary resonator vibration amplitude A_x is not altered. The term $\gamma \cdot \cos(\theta)$ can easily be found by changing V_{AC} and letting the primary resonator amplitude control loop keep A_x and, at the same time, the product $V_{DC} V_{AC}$ constant.

The measurement of the term $\delta G_{y/F} G_{V/y} \cdot \cos(\theta)$ is not as straightforward, as varying the product $V_{DC} V_{AC}$ also affects the primary resonator vibration amplitude and hence the other ZRO sources. However, the measurement can be performed by modulating the dc voltage with a low frequency ω_e [150], so that the exciting voltage in Eq. (6.2) becomes

$$V_{exc}(t) = V_{DC} + \Delta V_{DC} \cdot \sin(\omega_e t + \upsilon) + V_{AC} \cdot \cos(\omega_{0x} t). \qquad (8.19)$$

In the equation, ΔV_{DC} represents the amplitude and υ the phase of the modulating signal. The frequency ω_e can be freely chosen, as long as it lies within the final output bandwidth of the angular velocity sensing system and the phase shift of the system at that frequency is known. From Eq. (8.19), it can be seen that there are no electrically cross-coupling components apart from the signal at ω_{0x}, whereas, because the electrostatic force is proportional to the square of the exciting voltage, there are force components at $\omega_{0x} - \omega_e$ and $\omega_{0x} + \omega_e$. Because of the high quality factor of the primary resonator, the primary movement excited by these components is negligible, whereas the secondary movement can be measured and the parameter $\delta G_{y/F} G_{V/y} \cdot \cos(\theta)$ found.

In the preceding description, the possibility that ζ_I is also dependent on V_{AC} has been ignored. However, if the middle electrode biasing impedance Z_B is resistive, the ac excitation causes the potential to vary in phase with the Coriolis signal because of cross-coupling through C_{exc} in Fig. 6.1. This effect can be mitigated by ensuring a sufficiently low biasing impedance while $\gamma \cdot \cos(\theta)$ is being measured. If this is not possible, then the measurement error has to be accepted.

Then the terms $\beta A_x \omega_{0x} G_{y/F} G_{V/y} \cdot \cos(\theta)$, $\zeta_I \cdot \cos(\theta)$, $\eta_I \cdot \cos(\theta)$, and $\iota_I A_x \cdot \cos(\theta)$ are still left. The sum of the last two terms can be found by disconnecting the inputs of the secondary resonator detection circuit from the sensor element, after which only the signals cross-coupled in the electronics appear at the output. The term $\iota_I A_x \cdot \cos(\theta)$ can be distinguished from clock signals by letting A_x vary with time with a known frequency and measuring the cross-coupling of the time-dependent component. Then, $\eta_I \cdot \cos(\theta)$ can be solved by a simple subtraction operation.

The term $\zeta_I \cdot \cos(\theta)$ can be found by temporarily providing a low biasing impedance for the middle electrode. This can be done, for example, by a sufficiently large capac-

itor towards ground from the middle electrode. Now, by observing the change in the ZRO, $\zeta_I \cdot \cos(\theta)$ can be resolved. Finally, the last remaining term $\beta A_x \omega_{0x} G_{y/F} G_{V/y} \cdot \cos(\theta)$ can be evaluated by subtracting all the other components from the total ZRO.

The measured ZRO components are shown in Table 8.4. All values are calculated from five repeated measurements, except the electrical cross-coupling $\gamma V_{AC} \cdot \cos(\theta)$, which is evaluated on the basis of line fitting. The ZRO inflicted by varying middle electrode potential was made negligible by the large capacitor C_B, which was made possible by the PCB implementation.

Table 8.4 Measured ZRO components, reduced to input Ω_z.

Term	Magnitude (°/s)	Standard deviation (°/s)
$\beta A_x \omega_{0x} G_{y/F} G_{V/y} \cdot \cos(\theta)$ (Non-proportional damping)[1]	$-3.2/$ $+4.5$ [2]	0.43
$\gamma V_{AC} \cdot \cos(\theta)$ (Electrical cross-coupling in the sensor element)	$+10.8$	0.41 [3]
$\delta V_{DC} V_{AC} G_{y/F} G_{V/y} \cdot \cos(\theta)$ (Direct excitation of the secondary resonator)	± 3.9 [4]	0.10
$\zeta_I \cdot \cos(\theta)$ (Varying middle electrode bias)	$-$ [5]	$-$
Total cross-coupling in electronics	$+62.1$	0.036
$\eta_I \cdot \cos(\theta)$ (Cross-coupling of the clock signals)[6]	$+42.0$	1.32
$\iota_I A_x \cdot \cos(\theta)$ (Cross-coupling of the primary resonator output signal)	$+20.0$	1.32
Total ZRO	$+73.5$	0.024

[1] Evaluated by subtracting all the other components from the total ZRO
[2] Depending on the sign of the direct excitation component
[3] Norm of residuals
[4] Sign could not be resolved
[5] Ensured by large C_B in PCB implementation
[6] Evaluated by subtracting the following component from the preceding component

First, the signal cross-coupled in the electronics was measured to be 62.1 °/s, accounting for 84.5% of the total ZRO[4]. The parameter ι_Q was measured as being $16\,\mathrm{dB}$ higher than the parameter ι_I. This is an expected result, as described in Section 6.1.6.

Next, the electrical cross-coupling of the primary resonator excitation signal was measured. Because the sensor element and the interface IC were combined on a PCB,

---

[4] All the percentages are calculated as ratios between the absolute value of each component and the total ZRO. Hence, they do not add up to 100%.

this component of the ZRO proved to be extremely sensitive to any disturbances. However, by keeping the configuration completely intact during the measurement, the electrical cross-coupling could be reliably resolved, although it would change immediately if the measurement setup were altered.

The measured ZRO as a function of the peak-to-peak amplitude $V_{sq,pp}$ of the square-wave primary resonator excitation signal is shown in Fig. 8.35. The figure also shows a fitted line, together with the correlation coefficient R_{corr} and the norm of the residuals σ. The ZRO caused by the electrical cross-coupling is then evaluated on the basis of the line and the nominal $V_{sq,pp}$. The result is $10.8\,^\circ/\mathrm{s}$, accounting for 14.7% of the total ZRO.
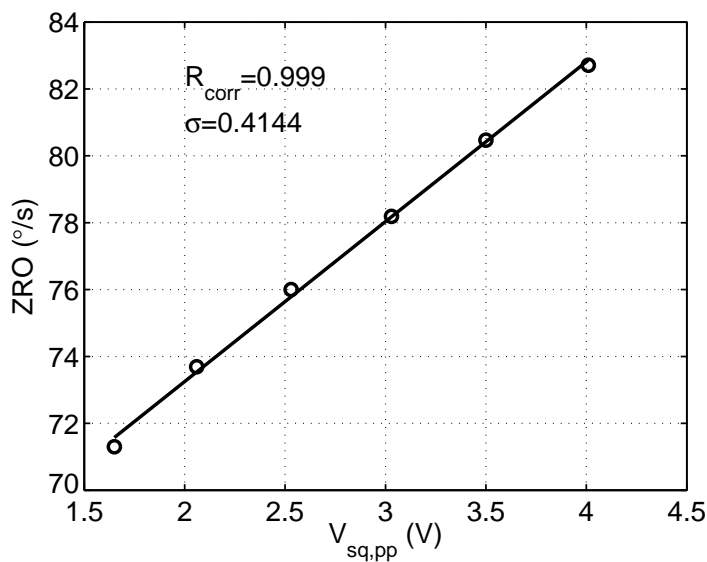
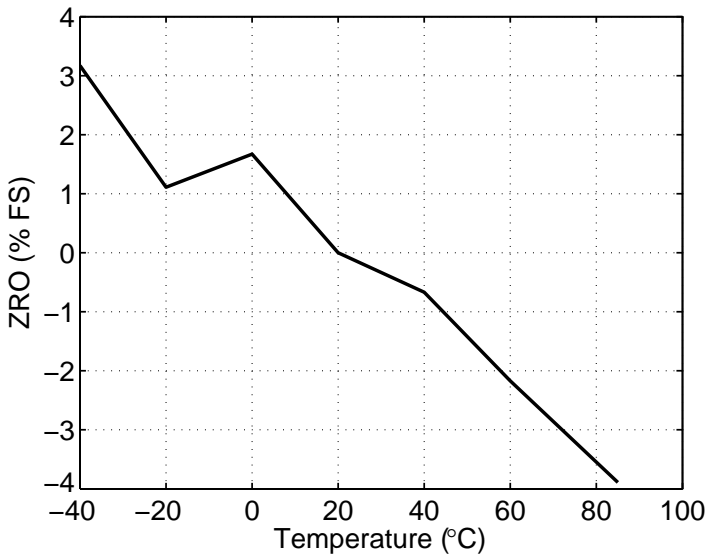**Figure 8.35** Measured ZRO as a function of the peak-to-peak amplitude $V_{sq,pp}$ of the square-wave primary resonator excitation signal.

The total ZRO was measured in conjunction with the previous measurement. Then, the ZRO caused by the direct excitation of the secondary resonator $\delta V_{DC} V_{AC} G_{y/F} G_{V/y} \cdot \cos(\theta)$ was measured. As it was not possible to reliably control the phase υ of the varying dc component ΔV_{DC}, only the absolute value of this component could be resolved, but not its sign. The absolute value is $3.9\,^\circ/\mathrm{s}$, accounting for 5.3% of the total ZRO. This term is increased by the fact that the dc component V_{DC} of the excitation voltage was increased because of the lower-than-expected quality factor of the primary resonator. Finally, the ZRO caused by non-proportional damping was evaluated by subtracting all the other components from the total ZRO. The result is either $-3.2\,^\circ/\mathrm{s}$ or $+4.5\,^\circ/\mathrm{s}$, depending on the sign of the component caused by direct excitation. This accounts for either 4.4% or 6.1% of the total ZRO.

Finally, the measured change of the zero-rate output from the ZRO at $+20\,^\circ\mathrm{C}$ as a function of temperature is shown in Fig. 8.36. This measurement has been performed with another proto-assembly (ASIC, sensor element, and the PCB) compared to the other measurements. As described above, the ZRO is very sensitive to even minor disturbances in the measurement setup. Therefore, although this measurement shows a certain performance, it is very difficult to repeat it even with the same proto-assembly.

Figure 8.36 Measured change of the zero-rate output from the ZRO at $+20\,^\circ\mathrm{C}$ as a function of temperature.

8.6.5   System Performance

To measure the performance of the complete MEMS angular velocity sensor, the system was first attached to a rate table and excited with angular velocities ranging from -100 to $+100\,^\circ/\mathrm{s}$. Again, the phase error correction and the compensation of the mechanical quadrature signal with the $\Sigma\Delta$ DAC were used. The measured output signal, together with a fitted line, is shown in Fig. 8.37. The maximum deviation between the measured data and the line (defined as dc nonlinearity) is $\pm 2\,^\circ/\mathrm{s}$.

Next, an Allan variance analysis [151] was performed to find out the white noise floor and the long-term bias stability of the system. Approximately 90 minutes of output data was recorded with a logic analyzer (limited by the memory depth of the analyzer), and it was analyzed using Matlab. Figure 8.38 shows the resulting root Allan variance plot. The white noise floor can be read from the point where the slope at short averaging times meets the averaging time of one [152], resulting in $0.042\,^\circ/\mathrm{s}/\sqrt{\mathrm{Hz}}$.
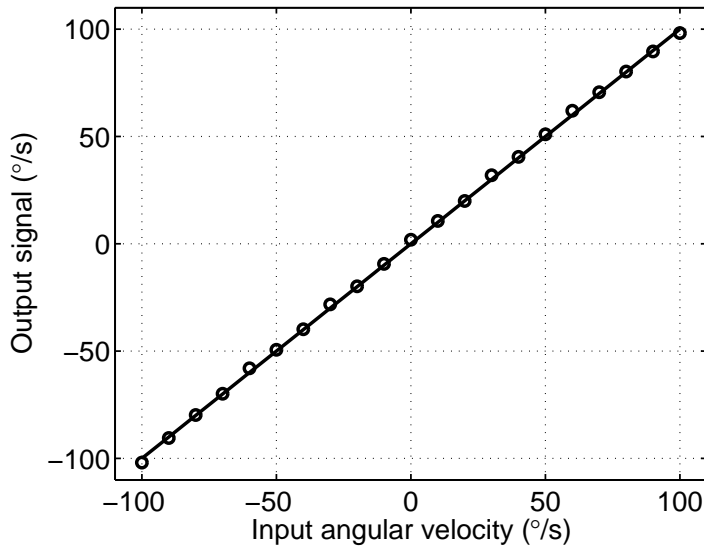
Figure 8.37 Measured output signal, with angular velocity inputs from -100 to $+100\,°/\text{s}$.

This noise is caused purely by the noise of the front-end circuit. The decrease in the root Allan variance at the shortest averaging time (corresponding to the original sampling interval) is due to the bandwidth limitation of the system. The long-term bias stability can be read from the low limit of the plot [152], giving approximately $0.05\,°/\text{s}$. However, the root Allan variance starts increasing again with averaging times of approximately $30\,\text{s}$, perhaps limiting the reliability of the bias stability readout. The slope indicates that the increasing root Allan variance is due to rate random walk [152], corresponding to an $1/f^2$ component at the low frequencies of the output spectrum. After averaging times of over 300 seconds, the limited number of data points starts causing significant measurement uncertainty.

The rise of the root Allan variance between averaging times of 0.1 and 4 s is caused by the time-varying primary signal, which is still left in the angular velocity data after normalization. Such a rise is caused by a sinusoidal interferer [152]. The interferer can also be seen in the spectrum in Fig. 8.33.

In order to remove the interferer, the $\Sigma\Delta$ modulation of the primary resonator excitation signal was enabled. The resulting root Allan variance is shown in Fig. 8.39. The figure also shows the root Allan variance plot without $\Sigma\Delta$ modulation for comparison. It can be seen that the rise between averaging times of 0.1 and 4 s is removed, without the white noise floor being affected. On the other hand, the rate random walk increases for an unknown reason. Because of the increase, the long-term bias stability cannot be reliably read any more.
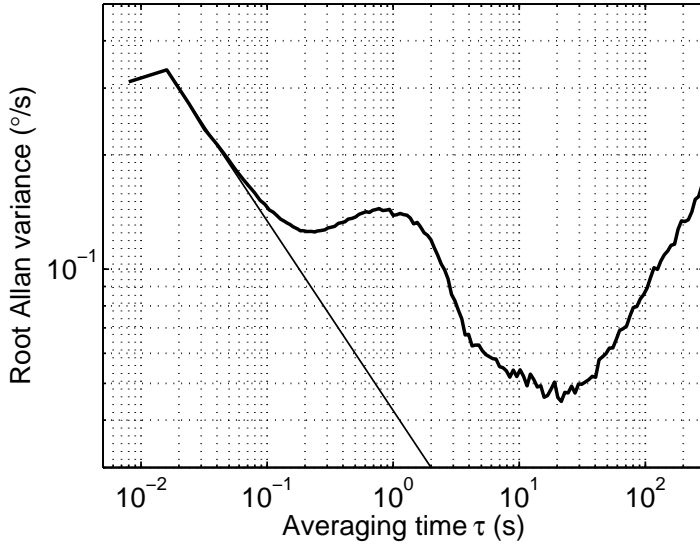
Figure 8.38 Measured root Allan variance.
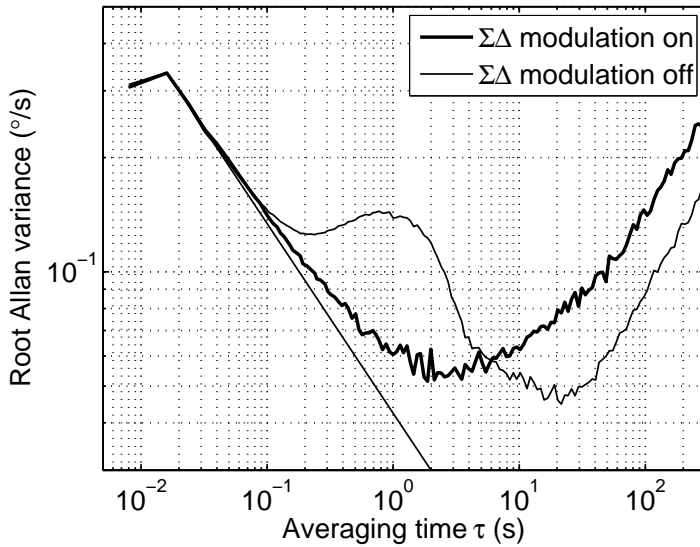
Figure 8.39 Measured root Allan variance, showing the effect of the $\Sigma\Delta$ modulation of the primary resonator excitation signal.

Allan variance analysis was also used to study the effect of the ΣΔ modulation of
the quadrature compensation voltage on the overall system performance. The resulting
root Allan variance when the quadrature compensation is performed with an external dc
voltage source is shown in Fig. 8.40. The root Allan variance plot with ΣΔ modulated
voltage is also shown for comparison. From the figure, it can be seen that the impact
of the ΣΔ modulation on the white noise floor is insignificant, an observation identical
to that made in Section 8.6.3. As in the case of the ΣΔ modulated primary resonator
excitation voltage, the modulation causes the rate random walk to increase. Again, the
reason for this is unclear.
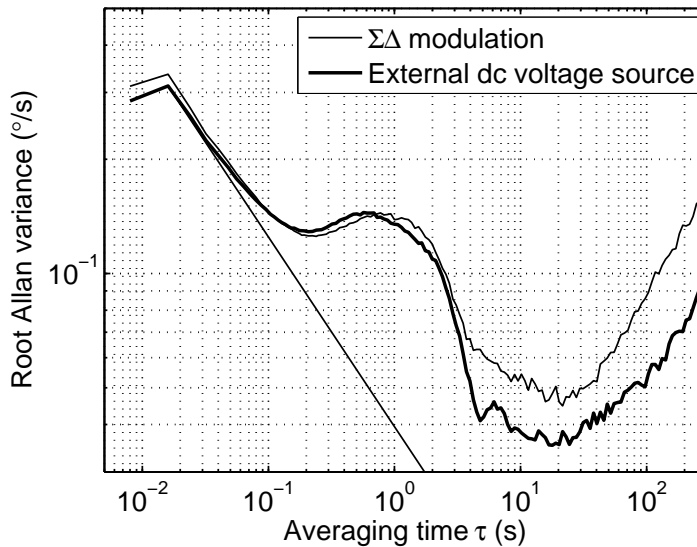
Figure 8.40 Measured root Allan variance, showing the effect of the ΣΔ modulation of the
quadrature compensation voltage.

When integrated over the signal band of 40 Hz, the measured white noise floor of
$0.042 °/s/\sqrt{Hz}$ yields an SNR of 51.6 dB, when compared to a dc angular velocity
signal of $100 °/s$. This corresponds to a resolution of 8.6 bits. It should be noticed that
this is not the maximum reachable SNR, as the input angular velocity is not limited to
$100 °/s$ by any physical factor, but is instead a specified value.

A summary of the measured performance is given in Table 8.5.

Table 8.5 Summary of the measured system performance.

Technology	0.7-μm double-metal, double-polysilicon CMOS with HV MOS transistors and diodes
Operating voltage	+5 V
Total silicon area	26.57 mm^2
Effective silicon area	8.0 mm^2 (ex. pads)
Current consumption	6.1 mA (ex. references and DSP)
Full-scale angular velocity [1]	$\pm 100\,^\circ/s$
Spot noise	$0.042\,^\circ/s/\sqrt{Hz}$
Bandwidth	40 Hz
SNR with FS dc input	51.6 dB (8.6 bits)
Max. dc nonlinearity	$\pm 2\,^\circ/s$
Long-term bias stability	$0.05\,^\circ/s$
Zero-rate output drift (from -40 to $+85^\circ$C)	$\pm 4\%$ of full-scale [2]

[1] Specified, not physically limited

[2] Measured with another proto assembly

Chapter 9

Conclusions and Future Work

In this thesis, the design of a MEMS angular velocity sensor has been studied. The basic properties of a vibratory microgyroscope were presented in the first part of the work. The second part concentrated on the system-level design. The following aspects were considered: synchronous demodulation of the secondary resonator output signal; primary resonator excitation; compensation of the mechanical quadrature signal, and zero-rate output. Synchronous demodulation and the zero-rate output were analyzed in detail, providing the effects of various non-idealities and deriving detailed formulae. Primary resonator excitation and quadrature compensation were analyzed on a less detailed level, but still the most significant properties were provided and important aspects regarding the design were listed. The use of digital techniques in primary resonator excitation and in quadrature compensation, in particular $\Sigma\Delta$ modulation, was described.

The third part of the work concentrated on the electronics design and the implemented system. Several ways to perform the readout of a capacitive sensor were thoroughly studied. Their limitations and non-idealities were analyzed, concentrating especially on their noise performance. Finally, the implemented MEMS angular velocity sensor was presented, with a detailed description of the system-level design and the analog circuit blocks related to the sensor readout. Other analog blocks and the DSP were introduced on a more general level. Detailed experimental results achieved with the system were presented.

The implemented system demonstrated the effect of $\Sigma\Delta$ modulation on both the primary resonator excitation and the quadrature compensation. It was shown that certain interferers resulting from a time-varying primary signal and a mechanical quadrature signal could be eliminated without compromising the noise performance. However, the long-term stability of the system was reduced for an unknown reason.

The system also demonstrated the effect of a phase error compensation performed

using DSP. In this way, the effect of several phase delays in the analog circuitry could be eliminated, and the additional noise caused by clock jitter could be considerably reduced. If properly designed, the compensation does not require significant amounts of additional hardware.

The measured noise level (in $°/s/\sqrt{\text{Hz}}$) of the system is better than the median of the published microgyroscopes. However, it does not reach the present state of the art. While this was not even targeted during the design, it is helpful to consider the limiting factors. In the electronics, the noise is limited by the CSA used as a capacitance-to-voltage converter and by the following high-pass filter. The noise contribution of the filter could be reduced by increasing the gain of the CSA, with the adverse effects described in the text. The filter itself could also be further optimized for noise, although this is not expected to lead to any dramatic improvement. The noise of the CSA is limited by the feedback resistors, where the maximum size is determined by leakage current considerations and by implementation-dependent limitations. According to the simulations, the replacement of the active PMOS-transistor implementation of the resistors with passive polysilicon resistors would not reduce their noise contribution. Finally, if the mechanical sensitivity (from the angular velocity to change in capacitance) of the sensor element were larger, the noise level would naturally be proportionally lowered.

As the experimental results show, the largest contributor to the ZRO signal of the implemented gyroscope is the cross-coupling in the electronics. This source accounts for 84.5 % of the total ZRO. The large magnitude of the cross-coupling is probably caused by the fact that the two read-out channels, the primary and the secondary channels, were located as close to each other as possible during the layout design, in order to achieve as good a matching as possible between the phase shifts of the two channels. However, the cross-coupling was not considered at this stage. In particular, the feedback components of the two CSAs are located in the same well regions. The same applies to the two HPFs following the CSAs, to the second HPFs, and to the two LPFs. To reduce the cross-coupled signal, the placement of various components should be reconsidered, perhaps at the cost of a slight impact on the matching of the phase shifts.

The design issues related to a MEMS gyroscope are always heavily dependent on the chosen implementation and the system architecture. However, while appreciating these limitations, an attempt was made in this thesis to provide as general-purpose an analysis as possible, especially in the part of the work that concentrated on system-level design.

As possible future work, neither a detailed analysis of the primary resonator excitation loop and its dynamics in various realizations nor one of the various quadrature compensation loops can yet be found in the literature. The analysis of the various feedback loops could also include an analysis of the total system start-up time, from

power-up to the point where the sensor output has stabilized and is valid. Additionally, the use of $\Sigma\Delta$ modulation, which was studied mostly with experimental methods in this thesis, deserves a more detailed theoretical analysis. In particular, the reason for the reduced long-term stability needs to be found. Another area where detailed theoretical analysis should be performed is the behavior of phase noise in the digital phase error correction. In the circuit implementation part, the various C/V converter implementations could be further compared regarding their suitability to the primary or secondary resonator readout. Finally, as possible experimental work in the future, the stability of the sensitivity of the system and the stability of various ZRO components over tempererature variations, together with the start-up time, could be characterized.

Bibliography

[1] H. C. Nathanson and R. A. Wickstrom, "A resonant-gate silicon surface transistor with high-Q band-pass properties," *Appl. Phys. Lett.*, vol. 7, no. 4, pp. 84–86, Aug. 1965.

[2] H. C. Nathanson, W. E. Newell, R. A. Wickstrom, and J. R. Davis, JR, "The resonant gate transistor," *IEEE Trans. Electron Devices*, vol. ED-14, no. 3, pp. 117–133, Mar. 1967.

[3] National Semiconductor history 1970. National Semiconductor. Santa Clara, CA, USA. [Online]. Available: http://www.national.com/company/pressroom/history70.html, cited September 18, 2007

[4] VTI history. VTI Technologies. Vantaa, Finland. [Online]. Available: http://www.vti.fi/en/company/history/, cited November 7, 2007

[5] A. P. Pisano, "Foreword," in *An introduction to microelectromechanical systems engineering*, 2nd ed. Norwood, MA, USA: Artech House, Inc., 2004, pp. xiii–xiv, book authored by N. Maluf.

[6] P. Salomon, "Micro sensors – world wide markets and economic impact," keynote presentation at Eurosensors 2006, Göteborg, Sweden, Sep. 2006, presentation slides available online at http://www.enablingmnt.com/Micro_sensors_-_world_wide_markets_and_economic_impact_-Eurosensors_Sept2006_Patric_Salomon.pdf (cited September 17, 2007).

[7] N. Yazdi, F. Ayazi, and K. Najafi, "Micromachined inertial sensors," *Proc. IEEE*, vol. 86, no. 8, pp. 1640–1659, Aug. 1998.

[8] A. M. Madni, L. E. Costlow, and S. J. Knowles, "Common design techniques for BEI GyroChip quartz rate sensors for both automotive and aerospace/defence markets," *IEEE Sensors J.*, vol. 3, no. 5, pp. 569–578, Oct. 2003.

[9] R. Neul, U.-M. Gómez, K. Kehr, W. Bauer, J. Classen, C. Döring, E. Esch, S. Götz, J. Hauer, B. Kuhlmann, C. Lang, M. Veith, and R. Willig, "Micromachined angular rate sensors for automotive applications," *IEEE Sensors J.*, vol. 7, no. 2, pp. 302–309, Feb. 2007.

[10] J. Söderkvist, "Micromachined gyroscopes," *Sens. Actuators A*, vol. 43, pp. 65–71, May 1994.

[11] P. Greiff, B. Boxenhorn, T. King, and L. Niles, "Silicon monolithic micromechanical gyroscope," in *Tech. Dig. Int. Conf. Solid-State Sensors and Actuators*, San Francisco, CA, USA, Jun. 1991, pp. 966–968.

[12] Company web pages. VTI Technologies. Vantaa, Finland. [Online]. Available: http://www.vti.fi/

[13] M. Saukoski, L. Aaltonen, T. Salo, and K. Halonen, "Interface and control electronics for a bulk micromachined capacitive gyroscope," Sens. Actuators A, 2008, accepted for publication.

[14] M. Saukoski, L. Aaltonen, and K. Halonen, "Effects of synchronous demodulation in vibratory MEMS gyroscopes: a theoretical study," IEEE Sensors J., 2008, accepted for publication.

[15] ——, "Zero-rate output and quadrature compensation in vibratory MEMS gyroscopes," *IEEE Sensors J.*, vol. 7, no. 12, pp. 1639–1652, Dec. 2007.

[16] M. Saukoski, L. Aaltonen, T. Salo, and K. Halonen, "Readout electronics with bandpass delta-sigma A/D converter for a bulk micromachined capacitive gyroscope," in *Proc. IEEE Instrumentation and Measurement Technology Conf.*, Ottawa, ON, Canada, May 2005, pp. 769–774.

[17] ——, "Fully integrated charge sensitive amplifier for readout of micromechanical capacitive sensors," in *Proc. IEEE Int. Symp. Circuits Syst.*, Kobe, Japan, May 2005, pp. 5377–5380.

[18] ——, "Readout and control electronics for a microelectromechanical gyroscope," in *Proc. IEEE Instrumentation and Measurement Technology Conf.*, Sorrento, Italy, Apr. 2006, pp. 1741–1746.

[19] ——, "Integrated readout and control electronics for a microelectromechanical angular velocity sensor," in *Proc. Eur. Solid-State Circuits Conf.*, Montreux, Switzerland, Sep. 2006, pp. 243–246.

[20] L. Aaltonen, M. Saukoski, and K. Halonen, "Fully integrated charge pump for high voltage excitation of a bulk micromachined gyroscope," in *Proc. IEEE Int. Symp. Circuits Syst.*, Kobe, Japan, May 2005, pp. 5381–5384.

[21] ——, "Design of clock generating fully integrated PLL using low frequency reference signal," in *Proc. Eur. Conf. Circuit Theory and Design*, Cork, Ireland, Aug. 2005, pp. 161–164.

[22] ——, "On-chip digitally tunable high voltage generator for electrostatic control of micromechanical devices," in *Proc. IEEE Custom Integrated Circuits Conf.*, San Jose, CA, USA, Sep. 2006, pp. 583–586.

[23] L. Aaltonen, M. Saukoski, I. Teikari, and K. Halonen, "Noise analysis of comparator performed sine-to-square conversion," in *Proc. Baltic Electronics Conf.*, Tallinn, Estonia, Sep. 2006, pp. 103–106.

[24] M. Paavola, M. Kämäräinen, J. A. M. Järvinen, M. Saukoski, M. Laiho, and K. Halonen, "A micropower interface ASIC for a capacitive 3-axis micro-accelerometer," *IEEE J. Solid-State Circuits*, vol. 42, no. 12, pp. 2651–2665, Dec. 2007.

[25] ——, "A 62μA interface ASIC for a capacitive 3-axis micro-accelerometer," in *IEEE Int. Solid-State Circuits Conf. Dig. Tech. Papers*, San Francisco, CA, USA, Feb. 2007, pp. 318–319.

[26] M. Kämäräinen, M. Saukoski, and K. Halonen, "A micropower front-end for capacitive microaccelerometers," in *Proc. IEEE Norchip Conf.*, Linköping, Sweden, Nov. 2006, pp. 261–266.

[27] M. Kämäräinen, M. Saukoski, M. Paavola, and K. Halonen, "A 20μA front-end for three-axis capacitive microaccelerometers," in *Proc. IEEE Instrumentation and Measurement Technology Conf.*, Warzaw, Poland, May 2007.

[28] M. Kämäräinen, M. Paavola, M. Saukoski, E. Laulainen, L. Koskinen, M. Kosunen, and K. Halonen, "A 1.5μA 1V 2$^{\text{nd}}$-order $\Sigma\Delta$ sensor front-end with signal boosting and offset compensation for a capacitive 3-axis micro-accelerometer," in *IEEE Int. Solid-State Circuits Conf. Dig. Tech. Papers*, San Francisco, CA, USA, Feb. 2008, pp. 578–579.

[29] D. Kleppner and R. J. Kolenkow, *An introduction to mechanics*. Singapore: McGraw-Hill Book Co., 1984.

[30] H. Goldstein, C. Poole, and J. Safko, *Classical mechanics*, 3rd ed. Upper Saddle River, NJ, USA: Pearson Education International, 2002.

[31] L. Meirovitch, *Elements of vibration analysis*, 2nd ed.   New York, NY, USA: McGraw-Hill Book Co., 1986.

[32] S. Franssila, *Introduction to microfabrication*.   Chichester, England: John Wiley & Sons, Ltd., 2004.

[33] J. W. Gardner, V. K. Varadan, and O. O. Awadelkarim, *Microsensors, MEMS, and smart devices*.   Chichester, England: John Wiley & Sons, Ltd., 2001.

[34] *VHDL Analog and Mixed-Signal Extensions*, IEEE Std. 1076.1, 1999.

[35] A. S. Phani, A. A. Seshia, M. Palaniapan, R. T. Howe, and J. A. Yasaitis, "Modal coupling in micromechanical vibratory rate gyroscopes," *IEEE Sensors J.*, vol. 6, no. 5, pp. 1144–1152, Oct. 2006.

[36] R. L. Kubena, D. J. Vickers-Kirby, R. J. Joyce, and F. P. Stratton, "A new tunneling-based sensor for inertial rotation rate measurements," *J. Microelectromech. Syst.*, vol. 8, no. 4, pp. 439–447, Dec. 1999.

[37] C. Acar and A. M. Shkel, "Nonresonant micromachined gyroscopes with structural mode-decoupling," *IEEE Sensors J.*, vol. 3, no. 4, pp. 497–506, Aug. 2003.

[38] ——, "An approach for increasing drive-mode bandwidth of MEMS vibratory gyroscopes," *J. Microelectromech. Syst.*, vol. 14, no. 3, pp. 520–528, Jun. 2005.

[39] ——, "Inherently robust micromachined gyroscopes with 2-DOF sense-mode oscillator," *J. Microelectromech. Syst.*, vol. 15, no. 2, pp. 380–387, Apr. 2006.

[40] T. B. Gabrielson, "Mechanical-thermal noise in micromachined acoustic and vibration sensors," *IEEE Trans. Electron Devices*, vol. 40, no. 5, pp. 903–909, May 1993.

[41] R. P. Leland, "Mechanical-thermal noise in vibrational gyroscopes," in *Proc. Amer. Control Conf.*, Arlington, VA, USA, Jun. 2001, pp. 3256–3261.

[42] S. Beeby, *MEMS mechanical sensors*.   Norwood, MA, USA: Artech House, Inc., 2004.

[43] T. W. Kenny, S. B. Waltman, J. K. Reynolds, and W. J. Kaiser, "Micromachined silicon tunnel sensor for motion detection," *Appl. Phys. Lett.*, vol. 58, no. 1, pp. 100–102, Jan. 1991.

[44] G. T. A. Kovacs, N. I. Maluf, and K. E. Petersen, "Bulk micromachining of silicon," *Proc. IEEE*, vol. 86, no. 8, pp. 1536–1551, Aug. 1998.

[45] J. M. Bustillo, R. T. Howe, and R. S. Muller, "Surface micromachining for microelectromechanical systems," *Proc. IEEE*, vol. 86, no. 8, pp. 1552–1574, Aug. 1998.

[46] J. Kiihamäki, "Fabrication of SOI micromechanical devices," doctoral dissertation, Helsinki Univ. Technology, 2005, available at http://lib.tkk.fi/Diss/2005/isbn9513864367/.

[47] H. Xie and G. K. Fedder, "Integrated microelectromechanical gyroscopes," *J. Aerosp. Eng.*, vol. 16, no. 2, pp. 65–75, Apr. 2003.

[48] Chip-on-MEMS- Heterogeneous integration of MEMS and circuits. VTI Technologies. Vantaa, Finland. [Online]. Available: http://www.vti.fi/en/products-solutions/technology/com/, cited November 8, 2007

[49] H. Luo, G. Fedder, and L. R. Carley, "Integrated multiple-device IMU system with continuous-time sensing circuitry," in *IEEE Int. Solid-State Circuits Conf. Dig. Tech. Papers*, San Francisco, CA, USA, Feb. 2003, pp. 204–205.

[50] A. Witvrouw, A. Mehta, A. Verbist, B. D. Bois, S. V. Aerde, J. Ramos-Martos, J. Ceballos, A. Ragel, J. Mora, M. Lagos, A. Arias, J. Hinojosa, J. Spengler, C. Leinenbach, T. Fuchs, and S. Kronmüller, "Processing of MEMS gyroscopes on top of CMOS ICs," in *IEEE Int. Solid-State Circuits Conf. Dig. Tech. Papers*, San Francisco, CA, USA, Feb. 2005, pp. 88–89.

[51] S. Lewis, S. Alie, T. Brosnihan, C. Core, T. Core, R. Howe, J. Geen, D. Hollocher, M. Judy, J. Memishian, K. Nunan, R. Paine, S. Sherman, B. Tsang, and B. Wachtmann, "Integrated sensor and electronics processing for >10ˆ8 "iMEMS" inertial measurement unit components," in *Tech. Dig. IEEE Int. Electron Devices Meeting*, Washington, DC, USA, Dec. 2003, pp. 39.1.1–39.1.4.

[52] W. Yun, R. T. Howe, and P. R. Gray, "Surface micromachined, digitally force-balanced accelerometer with integrated CMOS detection circuitry," in *Tech. Dig. Solid-State Sensor and Actuator Workshop*, Hilton Head Island, SC, USA, Jun. 1992, pp. 126–131.

[53] C. Lu, M. Lemkin, and B. E. Boser, "A monolithic surface micromachined accelerometer with digital output," in *IEEE Int. Solid-State Circuits Conf. Dig. Tech. Papers*, San Francisco, CA, USA, Feb. 1995, pp. 160–161.

[54] B. E. Boser and R. T. Howe, "Surface micromachined accelerometers," *IEEE J. Solid-State Circuits*, vol. 31, no. 3, pp. 366–375, Mar. 1996.

[55] M. Lemkin and B. E. Boser, "A three-axis micromachined accelerometer with a CMOS position-sense interface and digital offset-trim electronics," *IEEE J. Solid-State Circuits*, vol. 34, no. 4, pp. 456–468, Apr. 1999.

[56] X. Jiang, "Capacitive position-sensing interface for micromachined inertial sensors," doctoral dissertation, Univ. California, Berkeley, 2003.

[57] W. A. Clark, R. T. Howe, and R. Horowitz, "Surface micromachined Z-axis vibratory rate gyroscope," in *Tech. Dig. Solid-State Sensor and Actuator Workshop*, Hilton Head Island, SC, USA, Jun. 1996, pp. 283–287.

[58] T. Juneau and A. P. Pisano, "Micromachined dual input axis angular rate sensor," in *Tech. Dig. Solid-State Sensor and Actuator Workshop*, Hilton Head Island, SC, USA, Jun. 1996, pp. 299–302.

[59] W. A. Clark, "Micromachined vibratory rate gyroscopes," doctoral dissertation, Univ. California, Berkeley, 1997.

[60] T. N. Juneau, "Micromachined dual input axis rate gyroscope," doctoral dissertation, Univ. California, Berkeley, 1997.

[61] A. A. Seshia, "Integrated micromechanical resonant sensors for inertial measurement systems," doctoral dissertation, Univ. California, Berkeley, 2002.

[62] X. Jiang, J. I. Seeger, M. Kraft, and B. E. Boser, "A monolithic surface micromachined Z-axis gyroscope with digital output," in *Symp. VLSI Circuits Dig. Tech. Papers*, Honolulu, HI, USA, Jun. 2000, pp. 16–19.

[63] X. Jiang, S. A. Bhave, J. I. Seeger, R. T. Howe, B. E. Boser, and J. Yasaitis, "$\Sigma\Delta$ capacitive interface for a vertically-driven X&Y-axis rate gyroscope," in *Proc. Eur. Solid-State Circuits Conf.*, Florence, Italy, Sep. 2002, pp. 639–642.

[64] V. P. Petkov and B. E. Boser, "A fourth-order $\Sigma\Delta$ interface for micromachined inertial sensors," in *IEEE Int. Solid-State Circuits Conf. Dig. Tech. Papers*, San Francisco, CA, USA, Feb. 2004, pp. 320–321.

[65] ——, "A fourth-order $\Sigma\Delta$ interface for micromachined inertial sensors," *IEEE J. Solid-State Circuits*, vol. 40, no. 8, pp. 1602–1609, Aug. 2005.

[66] V. P. Petkov, "High-order $\Sigma\Delta$ interface for micromachined inertial sensors," doctoral dissertation, Univ. California, Berkeley, 2004.

[67] K. Funk, H. Emmerich, A. Schilp, M. Offenberg, R. Neul, and F. Lärmer, "A surface micromachined silicon gyroscope using a thick polysilicon layer," in *Proc. IEEE Conf. MEMS*, Orlando, FL, USA, Jan. 1999, pp. 57–60.

[68] B. V. Amini, R. Abdolvand, and F. Ayazi, "A 4.5mW closed-loop ΔΣ micro-gravity CMOS-SOI accelerometer," in *IEEE Int. Solid-State Circuits Conf. Dig. Tech. Papers*, San Francisco, CA, USA, Feb. 2006, pp. 288–289.

[69] J. A. Geen, S. J. Sherman, J. F. Chang, and S. R. Lewis, "Single-chip surface-micromachined integrated gyroscope with $50°/h$ Allan variance," in *IEEE Int. Solid-State Circuits Conf. Dig. Tech. Papers*, San Francisco, CA, USA, Feb. 2002, pp. 426–427.

[70] ——, "Single-chip surface micromachined integrated gyroscope with $50°/h$ Allan deviation," *IEEE J. Solid-State Circuits*, vol. 37, no. 12, pp. 1860–1866, Dec. 2002.

[71] W. Geiger, B. Folkmer, U. Sobe, H. Sandmaier, and W. Lang, "New designs of micromachined vibrating rate gyroscopes with decoupled oscillation modes," in *Proc. Int. Conf. Solid-State Sensors and Actuators*, Chicago, IL, USA, Jun. 1997, pp. 1129–1132.

[72] W. Geiger, B. Folkmer, J. Merz, H. Sandmaier, and W. Lang, "A new silicon rate gyroscope," *Sens. Actuators A*, vol. 73, pp. 45–51, Mar. 1999.

[73] W. Geiger, J. Merz, T. Fischer, B. Folkmer, H. Sandmaier, and W. Lang, "The silicon angular rate sensor system DAVED®," *Sens. Actuators A*, vol. 84, pp. 280–284, Sep. 2000.

[74] W. Geiger, W. U. Butt, A. Gaißer, J. Frech, M. Braxmaier, T. Link, A. Kohne, P. Nommensen, H. Sandmaier, W. Lang, and H. Sandmaier, "Decoupled micro-gyros and the design principle DAVED," *Sens. Actuators A*, vol. 95, pp. 239–249, Jan. 2002.

[75] A. Gaißer, W. Geiger, T. Link, J. Merz, S. Steigmajer, A. Hauser, H. Sandmaier, W. Lang, and N. Niklasch, "New digital readout electronics for capacitive sensors by the example of micro-machined gyroscopes," *Sens. Actuators A*, vol. 97-98, pp. 557–562, Apr. 2002.

[76] W. Geiger, H. Sandmaier, and W. Lang, "A mechanically controlled oscillator," *Sens. Actuators A*, vol. 82, pp. 74–78, May 2000.

[77] M. Lutz, W. Golderer, J. Gerstenmeier, J. Marek, B. Maihöfer, S. Mahler, H. Münzel, and U. Bischof, "A precision yaw rate sensor in silicon microma-chining," in *Proc. Int. Conf. Solid-State Sensors and Actuators*, Chicago, IL, USA, Jun. 1997, pp. 847–850.

[78] A. Thomae, R. Schellin, M. Lang, W. Bauer, J. Mohaupt, G. Bischopink, L. Tanten, H. Baumann, H. Emmerich, S. Pintér, K. Funk, G. Lorenz, R. Neul, and J. Marek, "A low cost angular rate sensor in Si-surface micromachining technology for automotive application," presented at the SAE 1999 World Congr., Detroit, MI, USA, Mar. 1999, Tech. Paper 1999-01-0931.

[79] U.-M. Gómez, B. Kuhlmann, J. Classen, W. Bauer, C. Lang, M. Veith, E. Esch, J. Frey, F. Grabmaier, K. Offterdinger, T. Raab, H.-J. Faisst, R. Willig, and R. Neul, "New surface micromachined angular rate sensor for vehicle stabilizing systems in automotive applications," in *Proc. Int. Conf. Solid-State Sensors, Actuators and Microsystems*, Seoul, Korea, Jun. 2005, pp. 184–187.

[80] M. S. Kranz and G. K. Fedder, "Micromechanical vibratory rate gyroscopes fabricated in conventional CMOS," in *Proc. Symp. Gyro Technology*, Stuttgart, Germany, Sep. 1997, pp. 3.0–3.8.

[81] H. Luo, G. K. Fedder, and L. R. Carley, "An elastically gimbaled z-axis CMOS-MEMS gyroscope," in *Proc. Int. Symp. Smart Structures Microsystems*, Hong Kong, China, Oct. 2000, pp. B1–2.

[82] H. Luo, X. Zhu, H. Lakdawala, L. R. Carley, and G. K. Fedder, "A copper CMOS-MEMS z-axis gyroscope," in *Proc. IEEE Conf. MEMS*, Las Vegas, NV, USA, Jan. 2002, pp. 631–634.

[83] H. Xie and G. K. Fedder, "A CMOS-MEMS lateral-axis gyroscope," in *Proc. IEEE Conf. MEMS*, Interlaken, Switzerland, Jan. 2001, pp. 162–165.

[84] M. F. Zaman, A. Sharma, and F. Ayazi, "High performance matched-mode tuning fork gyroscope," in *Proc. IEEE Conf. MEMS*, Istanbul, Turkey, Jan. 2006, pp. 66–69.

[85] A. Sharma, M. F. Zaman, and F. Ayazi, "A 104 dB SNDR transimpedance-based CMOS ASIC for tuning fork microgyroscopes," in *Proc. IEEE Custom Integrated Circuits Conf.*, San Jose, CA, USA, Sep. 2006, pp. 655–658.

[86] ——, "A 104-dB dynamic range transimpedance-based CMOS ASIC for tuning fork microgyroscopes," *IEEE J. Solid-State Circuits*, vol. 42, no. 8, pp. 1790–1802, Aug. 2007.

[87] ——, "A $0.2°/$hr micro-gyroscope with automatic CMOS mode matching," in *IEEE Int. Solid-State Circuits Conf. Dig. Tech. Papers*, San Francisco, CA, USA, Feb. 2007, pp. 386–387.

[88] S. R. Zarabadi, P. E. Castello-Borelly, and J. D. Johnson, "An angular rate sensor interface IC," in *Proc. IEEE Custom Integrated Circuits Conf.*, San Diego, CA, USA, May 1996, pp. 311–314.

[89] S. Chang, M. Chia, P. Castillo-Borelley, W. Higdon, Q. Jiang, J. Johnson, L. Obedier, M. Putty, Q. Shi, D. Sparks, and S. Zarabadi, "An electroformed CMOS integrated angular rate sensor," *Sens. Actuators A*, vol. 66, pp. 138–143, Apr. 1998.

[90] F. Ayazi and K. Najafi, "A HARPSS polysilicon vibrating ring gyroscope," *J. Microelectromech. Syst.*, vol. 10, no. 2, pp. 169–179, Jun. 2001.

[91] ——, "High aspect-ratio combined poly and single-crystal silicon (HARPSS) MEMS technology," *J. Microelectromech. Syst.*, vol. 9, no. 3, pp. 288–294, Sep. 2000.

[92] S. Sels and E. Axten, "MEMS sensors – The success factor for innovative vehicle stabilization systems," presented at the Vehicle Dynamics Expo 2005, Stuttgart, Germany, May 2005, available online at http://www.vehicledynamics-expo.com/05vdx_conf/pres/day2/sels_axten.pdf (cited July 6, 2007).

[93] Z. C. Feng and K. Gore, "Dynamic characteristics of vibratory gyroscopes," *IEEE Sensors J.*, vol. 4, no. 1, pp. 80–84, Feb. 2004.

[94] S. D. Senturia, *Microsystem design*. Dordrecht, The Netherlands: Kluwer Academic Publishers, 2001, second printing.

[95] W. C. Tang, T.-C. H. Nguyen, and R. T. Howe, "Laterally driven polysilicon resonant microstructures," *Sens. Actuators*, vol. 20, pp. 25–32, Nov. 1989.

[96] ——, "Laterally driven polysilicon resonant microstructures," in *Proc. IEEE Conf. MEMS*, Salt Lake City, UT, USA, Feb. 1989, pp. 53–59.

[97] W. C. Tang, M. G. Lim, and R. T. Howe, "Electrostatic comb drive levitation and control method," *J. Microelectromech. Syst.*, vol. 1, no. 4, pp. 170–178, Dec. 1992.

[98] J. I. Seeger and B. E. Boser, "Parallel-plate driven oscillations and resonant pull-in," in *Tech. Dig. Solid-State Sensor and Actuator Workshop*, Hilton Head Island, SC, USA, Jun. 2002, pp. 313–316.

[99] G. N. Nielson and G. Barbastathis, "Dynamic pull-in of parallel-plate and torsional electrostatic MEMS actuators," *J. Microelectromech. Syst.*, vol. 15, no. 4, pp. 811–821, Aug. 2006.

[100] R. Schreier and G. C. Temes, *Understanding delta-sigma data converters*. Hoboken, NJ, USA: John Wiley & Sons, Inc., 2005.

[101] J. F. Kaiser, "Nonrecursive digital filter design using the I_0-sinh window function," in *Proc. IEEE Int. Symp. Circuits Syst.*, San Francisco, CA, USA, Apr. 1974, pp. 20–23.

[102] J. A. Geen, "A path to low cost gyroscopy," in *Tech. Dig. Solid-State Sensor and Actuator Workshop*, Hilton Head Island, SC, USA, Jun. 1998, pp. 51–54.

[103] J. A. Geen and D. W. Carow, "Micromachined gyros," U.S. Patent 6,505,511, Jan. 14, 2003.

[104] P. Ward, "Electronics for coriolis force and other sensors," U.S. Patent 5,672,949, Sep. 30, 1997.

[105] M. S. Weinberg and A. Kourepenis, "Error sources in in-plane silicon tuning fork MEMS gyroscopes," *J. Microelectromech. Syst.*, vol. 15, no. 3, pp. 479–491, Jun. 2006.

[106] H. Xie and G. K. Fedder, "Fabrication, characterization, and analysis of a DRIE CMOS-MEMS gyroscope," *IEEE Sensors J.*, vol. 3, no. 5, pp. 622–631, Oct. 2003.

[107] L. Aaltonen, M. Saukoski, and K. Halonen, "Upconverting capacitance-to-voltage converter for readout of a micromechanical gyroscope," in *Proc. IEEE Norchip Conf.*, Linköping, Sweden, Nov. 2006, pp. 267–270.

[108] S. Günthner, M. Egretzberger, A. Kugi, K. Kapser, B. Hartmann, U. Schmid, and H. Seidel, "Compensation of parasitic effects for a silicon tuning fork gyroscope," *IEEE Sensors J.*, vol. 6, no. 3, pp. 596–604, Jun. 2006.

[109] N. Yazdi, H. Kulah, and K. Najafi, "Precision readout circuits for capacitive microaccelerometers," in *Proc. IEEE Conf. Sensors*, Vienna, Austria, Oct. 2004, pp. 28–31.

[110] H. Leuthold and F. Rudolf, "An ASIC for high-resolution capacitive microaccelerometers," *Sens. Actuators A*, vol. 21, pp. 278–281, Feb. 1990.

[111] Y. Nemirovsky and O. Bochobza-Degani, "A methodology and model for the pull-in parameters of electrostatic actuators," *J. Microelectromech. Syst.*, vol. 10, no. 4, pp. 601–615, Dec. 2001.

[112] W. M. Sansen and Z. Y. Chang, "Limits of low noise performance of detector readout front ends in CMOS technology," *IEEE Trans. Circuits Syst.*, vol. 37, no. 11, pp. 1375–1382, Nov. 1990.

[113] Z. Y. Chang and W. M. C. Sansen, *Low-noise wide-band amplifiers in bipolar and CMOS technologies*.   Dordrecht, The Netherlands: Kluwer Academic Publishers, 1991.

[114] S. E. Alper and T. Akin, "A single-crystal silicon symmetrical and decoupled MEMS gyroscope on an insulating substrate," *J. Microelectromech. Syst.*, vol. 14, no. 4, pp. 707–717, Aug. 2005.

[115] H. Alzaher and M. Ismail, "A CMOS fully balanced differential difference amplifier and its applications," *IEEE Trans. Circuits Syst. II*, vol. 48, no. 6, pp. 614–620, Jun. 2001.

[116] R. Schreier, J. Silva, J. Steensgaard, and G. C. Temes, "Design-oriented estimation of thermal noise in switched-capacitor circuits," *IEEE Trans. Circuits Syst. I*, vol. 52, no. 11, pp. 2358–2368, Nov. 2005.

[117] C. C. Enz and G. C. Temes, "Circuit techniques for reducing the effects of op-amp imperfections: Autozeroing, correlated double sampling, and chopper stabilization," *Proc. IEEE*, vol. 84, no. 11, pp. 1584–1614, Nov. 1996.

[118] R. Poujois and J. Borel, "A low drift fully integrated MOSFET operational amplifier," *IEEE J. Solid-State Circuits*, vol. SC-13, no. 4, pp. 499–503, Aug. 1978.

[119] N. Wongkomet and B. E. Boser, "Correlated double sampling in capacitive position sensing circuits for micromachined applications," in *Proc. IEEE Asia-Pacific Conf. Circuits Syst.*, Chiangmai, Thailand, Nov. 1998, pp. 723–726.

[120] J. Wu, G. K. Fedder, and L. R. Carley, "A low-noise low-offset capacitive sensing amplifier for a 50-μg$/\sqrt{\text{Hz}}$ monolithic CMOS MEMS accelerometer," *IEEE J. Solid-State Circuits*, vol. 39, no. 5, pp. 722–730, May 2004.

[121] W. Henrion, L. DiSanza, M. Ip, S. Terry, and H. Jerman, "Wide dynamic range direct digital accelerometer," in *Tech. Dig. Solid-State Sensor and Actuator Workshop*, Hilton Head Island, SC, USA, Jun. 1990, pp. 153–157.

[122] T. Smith, O. Nys, M. Chevroulet, Y. DeCoulon, and M. Degrauwe, "A 15b electromechanical sigma-delta converter for acceleration measurements," in *IEEE Int. Solid-State Circuits Conf. Dig. Tech. Papers*, San Francisco, CA, USA, Feb. 1994, pp. 160–161.

[123] C. Condemine, N. Delorme, J. Soen, J. Durupt, J.-P. Blanc, M. Belleville, and A. Besançon-Voda, "A 0.8mA 50Hz 15b SNDR $\Delta\Sigma$ closed-loop 10g accelerometer using an 8th-order digital compensator," in *IEEE Int. Solid-State Circuits Conf. Dig. Tech. Papers*, San Francisco, CA, USA, Feb. 2005, pp. 248–249.

[124] C. Hierold, B. Clasbrummel, D. Behrend, T. Scheiter, M. Steger, K. Oppermann, H. Kapels, E. Landgraf, D. Wenzel, and D. Etzrodt, "Low power integrated pressure sensor system for medical applications," *Sens. Actuators A*, vol. 73, pp. 58–67, Mar. 1999.

[125] Y. Cao and G. C. Temes, "High-accuracy circuits for on-chip capacitance ratio testing or sensor readout," *IEEE Trans. Circuits Syst. II*, vol. 41, no. 9, pp. 637–639, Sep. 1994.

[126] B. Wang, T. Kajita, T. Sun, and G. C. Temes, "High-accuracy circuits for on-chip capacitance ratio testing or sensor readout," *IEEE Trans. Instrum. Meas.*, vol. 47, no. 1, pp. 16–20, Feb. 1998.

[127] H. Kuisma, T. Ryhänen, J. Lahdenperä, E. Punkka, S. Ruotsalainen, T. Sillanpää, and H. Seppä, "A bulk micromachined silicon angular rate sensor," in *Proc. Int. Conf. Solid-State Sensors and Actuators*, Chicago, IL, USA, Jun. 1997, pp. 875–878.

[128] P. Klemetti, "Temperature dependence and noise of angular rate sensor element," Master's thesis, Helsinki Univ. Technology, 2004, in Finnish.

[129] *Cyclone Device Handbook*, Altera Corporation, 2007.

[130] *Nios Development Board, Reference Manual, Cyclone Edition*, Altera Corporation, 2004.

[131] *VHDL Language Reference Manual*, IEEE Std. 1076, 2002.

[132] *Quartus II Version 7.1 Handbook*, Altera Corporation, 2007.

[133] K. Bult and G. J. G. M. Geelen, "A fast-settling CMOS op amp for SC circuits with 90-dB DC gain," *IEEE J. Solid-State Circuits*, vol. 25, no. 6, pp. 1379–1384, Dec. 1990.

[134] J. Graeme, *Photodiode Amplifiers: Op Amp Solutions*. New York, NY, USA: McGraw-Hill, 1996.

[135] M. Banu and Y. Tsividis, "Fully integrated active RC filters in MOS technology," *IEEE J. Solid-State Circuits*, vol. SC-18, no. 6, pp. 644–651, Dec. 1983.

[136] Y. Tsividis, M. Banu, and J. Khoury, "Continuous-time MOSFET-C filters in VLSI," *IEEE J. Solid-State Circuits*, vol. SC-21, no. 1, pp. 15–30, Feb. 1986.

[137] Z. Czarnul, "Modification of Banu-Tsividis continuous-time integrator structure," *IEEE Trans. Circuits Syst.*, vol. CAS-33, no. 7, pp. 714–716, Jul. 1986.

[138] ——, "Novel MOS resistive circuit for synthesis of fully integrated continuous-time filters," *IEEE Trans. Circuits Syst.*, vol. CAS-33, no. 7, pp. 728–721, Jul. 1986.

[139] J. I. Osa and A. Carlosena, "Limitations of the MOS resistive circuit in MOSFET-C implementation: Bandwidth, noise, offset and non-linearity," *Analog Integrated Circuits Signal Processing*, vol. 28, no. 3, pp. 239–252, Sep. 2001.

[140] U.-K. Moon and B.-S. Song, "Design of a low-distortion 22-kHz fifth-order Bessel filter," *IEEE J. Solid-State Circuits*, vol. 28, no. 12, pp. 1254–1264, Dec. 1993.

[141] D. A. Johns and K. Martin, *Analog integrated circuit design*. New York, NY, USA: John Wiley & Sons, Inc., 1997.

[142] T. Salo, "Bandpass delta-sigma modulators for radio receivers," doctoral dissertation, Helsinki Univ. Technology, 2003, available at http://lib.tkk.fi/Diss/2003/isbn9512264110/.

[143] A. Hairapetian, "An 81-MHz IF receiver in CMOS," *IEEE J. Solid-State Circuits*, vol. 31, no. 12, pp. 1981–1986, Dec. 1996.

[144] J. F. Dickson, "On-chip high-voltage generation in NMOS integrated circuits using an improved voltage multiplier technique," *IEEE J. Solid-State Circuits*, vol. SC-11, no. 3, pp. 374–378, Jun. 1976.

[145] M. Zhang and N. Llaser, "Optimization design of the Dickson charge pump circuit with a resistive load," in *Proc. IEEE Int. Symp. Circuits Syst.*, vol. V, Vancouver, BC, Canada, May 2004, pp. 840–843.

[146] R. E. Crochiere and L. R. Rabiner, "Optimum FIR digital filter implementations for decimation, interpolation, and narrow-band filtering," *IEEE Trans. Acoust., Speech, Signal Process.*, vol. ASSP-23, no. 5, pp. 444–456, Oct. 1975.

[147] L. R. Rabiner and R. E. Crochiere, "A novel implementation for narrow-band FIR digital filters," *IEEE Trans. Acoust., Speech, Signal Process.*, vol. ASSP-23, no. 5, pp. 457–464, Oct. 1975.

[148] R. E. Crochiere and L. R. Rabiner, "Further considerations in the design of decimators and interpolators," *IEEE Trans. Acoust., Speech, Signal Process.*, vol. ASSP-24, no. 4, pp. 296–311, Aug. 1976.

[149] E. B. Hogenauer, "An economical class of digital filters for decimation and interpolation," *IEEE Trans. Acoust., Speech, Signal Process.*, vol. ASSP-29, no. 2, pp. 155–162, Apr. 1981.

[150] L. Aaltonen, P. Rahikkala, M. Saukoski, and K. Halonen, "Continuous time interface for $\pm 1.5\,\mathrm{g}$ closed-loop accelerometer," in *Proc. IEEE Int. Conf. IC Design and Technology*, Austin, TX, USA, May 2007, pp. 187–190.

[151] *Recommended Practice for Inertial Sensor Test Equipment, Instrumentation, Data Acquisition and Analysis*, IEEE Std. 1554, 2005.

[152] *Specification Format Guide and Test Procedure for Single-Axis Interferometric Fiber Optic Gyros*, IEEE Std. 952, 1997, Annex C.

Appendix A

Effect of Nonlinearities

The signal given in Eq. (3.13) is fed through a nonlinear system. Rewritten here for convenience, the signal is

$$
\begin{aligned}
V_{in,sec}(t) = & \frac{G_{V/y}G_{y/\Omega,LSB}\Omega_z}{2} \cdot \cos\left((\omega_{0x} - \omega_\Omega)t - \varphi + \phi_{LSB} + \theta + T_d\omega_\Omega\right) + \\
& \frac{G_{V/y}G_{y/\Omega,USB}\Omega_z}{2} \cdot \cos\left((\omega_{0x} + \omega_\Omega)t + \varphi + \phi_{USB} + \theta - T_d\omega_\Omega\right) + \\
& V_{error,I} \cdot \cos\left(\omega_{0x}t + \theta\right) + V_{error,Q} \cdot \sin\left(\omega_{0x}t + \theta\right).
\end{aligned}
\tag{A.1}
$$

To improve the readability of the expressions, the following substitutions are used[1]:

$$
A = \frac{G_{V/y}G_{y/\Omega,LSB}\Omega_z}{2},
\tag{A.2a}
$$

$$
B = \frac{G_{V/y}G_{y/\Omega,USB}\Omega_z}{2},
\tag{A.2b}
$$

$$
C = V_{error,I},
\tag{A.2c}
$$

and

$$
D = V_{error,Q}.
\tag{A.2d}
$$

Now, (A.1) can be written as

$$
\begin{aligned}
V_{in,sec}(t) = & A \cdot \cos\left((\omega_{0x} - \omega_\Omega)t - \varphi + \phi_{LSB} + \theta + T_d\omega_\Omega\right) + \\
& B \cdot \cos\left((\omega_{0x} + \omega_\Omega)t + \varphi + \phi_{USB} + \theta - T_d\omega_\Omega\right) + \\
& C \cdot \cos\left(\omega_{0x}t + \theta\right) + D \cdot \sin\left(\omega_{0x}t + \theta\right).
\end{aligned}
\tag{A.3}
$$

---

[1]The symbols A, C, and D are used with other meanings elsewhere in this thesis. The use of the definitions given here is limited to this appendix and Section 3.4.

First, the effect of a second-order nonlinearity is considered. In that case, the output is

$$
\begin{aligned}
[V_{in,sec}(t)]^2 = {}& \frac{A^2}{2} + \frac{B^2}{2} + \frac{C^2}{2} + \frac{D^2}{2} \\
& + AC \cdot \cos(\omega_\Omega t - T_d \omega_\Omega + \varphi - \phi_{LSB}) \\
& + AD \cdot \sin(\omega_\Omega t - T_d \omega_\Omega + \varphi - \phi_{LSB}) \\
& + BC \cdot \cos(\omega_\Omega t - T_d \omega_\Omega + \varphi + \phi_{USB}) \\
& - BD \cdot \sin(\omega_\Omega t - T_d \omega_\Omega + \varphi + \phi_{USB}) \\
& + AB \cdot \cos(2\omega_\Omega t - 2T_d \omega_\Omega + 2\varphi - \phi_{LSB} + \phi_{USB}) \\
& + \frac{A^2}{2} \cdot \cos((2\omega_{0x} - 2\omega_\Omega)t + 2T_d \omega_\Omega - 2\varphi + 2\phi_{LSB} + 2\theta) \\
& + AC \cdot \cos((2\omega_{0x} - \omega_\Omega)t + T_d \omega_\Omega - \varphi + \phi_{LSB} + 2\theta) \\
& + AD \cdot \sin((2\omega_{0x} - \omega_\Omega)t + T_d \omega_\Omega - \varphi + \phi_{LSB} + 2\theta) \\
& + AB \cdot \cos(2\omega_{0x}t + \phi_{LSB} + \phi_{USB} + 2\theta) \\
& + \frac{C^2}{2} \cdot \cos(2\omega_{0x}t + 2\theta) \\
& + CD \cdot \sin(2\omega_{0x}t + 2\theta) \\
& - \frac{D^2}{2} \cdot \cos(2\omega_{0x}t + 2\theta) \\
& + BC \cdot \cos((2\omega_{0x} + \omega_\Omega)t - T_d \omega_\Omega + \varphi + \phi_{USB} + 2\theta) \\
& + BD \cdot \sin((2\omega_{0x} + \omega_\Omega)t - T_d \omega_\Omega + \varphi + \phi_{USB} + 2\theta) \\
& + \frac{B^2}{2} \cdot \cos((2\omega_{0x} + 2\omega_\Omega)t - 2T_d \omega_\Omega + 2\varphi + 2\phi_{USB} + 2\theta).
\end{aligned}
\tag{A.4}
$$

From (A.4), it can be seen that there are frequency components at dc, ω_Ω, $2\omega_\Omega$, $2\omega_{0x} - 2\omega_\Omega$, $2\omega_{0x} - \omega_\Omega$, $2\omega_{0x}$, $2\omega_{0x} + \omega_\Omega$, and $2\omega_{0x} + 2\omega_\Omega$. No components are residing at or around the operating frequency ω_{0x}. If this signal is synchronously demodulated by multiplying by either $\cos(\omega_{0x}t)$ or $\sin(\omega_{0x}t)$, amplified by two and low-pass filtered to remove all the frequency components in the vicinity of ω_{0x} and above, the result will be zero.

In the case of a third-order nonlinearity, the output is

$$
\begin{aligned}
[V_{in,sec}(t)]^3 = {}& \frac{3A^2B}{4} \cdot \cos((\omega_{0x} - 3\omega_\Omega)t + 3T_d \omega_\Omega - 3\varphi + 2\phi_{LSB} - \phi_{USB} + \theta) \\
& + \frac{3A^2C}{4} \cdot \cos((\omega_{0x} - 2\omega_\Omega)t + 2T_d \omega_\Omega - 2\varphi + 2\phi_{LSB} + \theta) \\
& - \frac{3A^2D}{4} \cdot \sin((\omega_{0x} - 2\omega_\Omega)t + 2T_d \omega_\Omega - 2\varphi + 2\phi_{LSB} + \theta) \\
& + \frac{3ABC}{2} \cdot \cos((\omega_{0x} - 2\omega_\Omega)t + 2T_d \omega_\Omega - 2\varphi + \phi_{LSB} - \phi_{USB} + \theta)
\end{aligned}
\tag{A.5}
$$

$$+ \frac{3ABD}{2} \cdot \sin((\omega_{0x} - 2\omega_\Omega)t + 2T_d\omega_\Omega - 2\varphi + \phi_{LSB} - \phi_{USB} + \theta)$$

$$+ \frac{3A^3}{4} \cdot \cos((\omega_{0x} - \omega_\Omega)t + T_d\omega_\Omega - \varphi + \phi_{LSB} + \theta)$$

$$+ \frac{3AB^2}{2} \cdot \cos((\omega_{0x} - \omega_\Omega)t + T_d\omega_\Omega - \varphi + \phi_{LSB} + \theta)$$

$$+ \frac{3AC^2}{2} \cdot \cos((\omega_{0x} - \omega_\Omega)t + T_d\omega_\Omega - \varphi + \phi_{LSB} + \theta)$$

$$+ \frac{3AD^2}{2} \cdot \cos((\omega_{0x} - \omega_\Omega)t + T_d\omega_\Omega - \varphi + \phi_{LSB} + \theta)$$

$$+ \frac{3BC^2}{4} \cdot \cos((\omega_{0x} - \omega_\Omega)t + T_d\omega_\Omega - \varphi - \phi_{USB} + \theta)$$

$$+ \frac{3BCD}{2} \cdot \sin((\omega_{0x} - \omega_\Omega)t + T_d\omega_\Omega - \varphi - \phi_{USB} + \theta)$$

$$- \frac{3BD^2}{4} \cdot \cos((\omega_{0x} - \omega_\Omega)t + T_d\omega_\Omega - \varphi - \phi_{USB} + \theta)$$

$$+ \frac{3A^2C}{2} \cdot \cos(\omega_{0x}t + \theta)$$

$$+ \frac{3A^2D}{2} \cdot \sin(\omega_{0x}t + \theta)$$

$$+ \frac{3ABC}{2} \cdot \cos(\omega_{0x}t + \phi_{LSB} + \phi_{USB} + \theta)$$

$$- \frac{3ABD}{2} \cdot \sin(\omega_{0x}t + \phi_{LSB} + \phi_{USB} + \theta)$$

$$+ \frac{3B^2C}{2} \cdot \cos(\omega_{0x}t + \theta)$$

$$+ \frac{3B^2D}{2} \cdot \sin(\omega_{0x}t + \theta)$$

$$+ \frac{3C^3}{4} \cdot \cos(\omega_{0x}t + \theta)$$

$$+ \frac{3C^2D}{4} \cdot \sin(\omega_{0x}t + \theta)$$

$$+ \frac{3CD^2}{4} \cdot \cos(\omega_{0x}t + \theta)$$

$$+ \frac{3D^3}{4} \cdot \sin(\omega_{0x}t + \theta)$$

$$+ \frac{3A^2B}{2} \cdot \cos((\omega_{0x} + \omega_\Omega)t - T_d\omega_\Omega + \varphi + \phi_{USB} + \theta)$$

$$+ \frac{3AC^2}{4} \cdot \cos((\omega_{0x} + \omega_\Omega)t - T_d\omega_\Omega + \varphi - \phi_{LSB} + \theta)$$

$$+ \frac{3ACD}{2} \cdot \sin((\omega_{0x} + \omega_\Omega)t - T_d\omega_\Omega + \varphi - \phi_{LSB} + \theta)$$

$$- \frac{3AD^2}{4} \cdot \cos((\omega_{0x} + \omega_\Omega)t - T_d\omega_\Omega + \varphi - \phi_{LSB} + \theta)$$

$$+ \frac{3B^3}{4} \cdot \cos((\omega_{0x} + \omega_\Omega)t - T_d\omega_\Omega + \varphi + \phi_{USB} + \theta)$$

$$+ \frac{3BC^2}{2} \cdot \cos((\omega_{0x} + \omega_\Omega)t - T_d\omega_\Omega + \varphi + \phi_{USB} + \theta)$$

$$+ \frac{3BD^2}{2} \cdot \cos((\omega_{0x} + \omega_\Omega)t - T_d\omega_\Omega + \varphi + \phi_{USB} + \theta)$$

$$+ \frac{3ABC}{2} \cdot \cos((\omega_{0x} + 2\omega_\Omega)t - 2T_d\omega_\Omega + 2\varphi - \phi_{LSB} + \phi_{USB} + \theta)$$

$$+ \frac{3ABD}{2} \cdot \sin((\omega_{0x} + 2\omega_\Omega)t - 2T_d\omega_\Omega + 2\varphi - \phi_{LSB} + \phi_{USB} + \theta)$$

$$+ \frac{3B^2C}{4} \cdot \cos((\omega_{0x} + 2\omega_\Omega)t - 2T_d\omega_\Omega + 2\varphi + 2\phi_{USB} + \theta)$$

$$- \frac{3B^2D}{4} \cdot \sin((\omega_{0x} + 2\omega_\Omega)t - 2T_d\omega_\Omega + 2\varphi + 2\phi_{USB} + \theta)$$

$$+ \frac{3AB^2}{4} \cdot \cos((\omega_{0x} + 3\omega_\Omega)t - 3T_d\omega_\Omega + 3\varphi - \phi_{LSB} + 2\phi_{USB} + \theta)$$

$$+ \frac{A^3}{4} \cdot \cos((3\omega_{0x} - 3\omega_\Omega)t + 3T_d\omega_\Omega - 3\varphi + 3\phi_{LSB} + 3\theta)$$

$$+ \frac{3A^2C}{4} \cdot \cos((3\omega_{0x} - 2\omega_\Omega)t + 2T_d\omega_\Omega - 2\varphi + 2\phi_{LSB} + 3\theta)$$

$$+ \frac{3A^2D}{4} \cdot \sin((3\omega_{0x} - 2\omega_\Omega)t + 2T_d\omega_\Omega - 2\varphi + 2\phi_{LSB} + 3\theta)$$

$$+ \frac{3A^2B}{4} \cdot \cos((3\omega_{0x} - \omega_\Omega)t + T_d\omega_\Omega - \varphi + 2\phi_{LSB} + \phi_{USB} + 3\theta)$$

$$+ \frac{3AC^2}{4} \cdot \cos((3\omega_{0x} - \omega_\Omega)t + T_d\omega_\Omega - \varphi + \phi_{LSB} + 3\theta)$$

$$+ \frac{3ACD}{2} \cdot \sin((3\omega_{0x} - \omega_\Omega)t + T_d\omega_\Omega - \varphi + \phi_{LSB} + 3\theta)$$

$$- \frac{3AD^2}{4} \cdot \cos((3\omega_{0x} - \omega_\Omega)t + T_d\omega_\Omega - \varphi + \phi_{LSB} + 3\theta)$$

$$+ \frac{3ABC}{2} \cdot \cos(3\omega_{0x}t + \phi_{LSB} + \phi_{USB} + 3\theta)$$

$$+ \frac{3ABD}{2} \cdot \sin(3\omega_{0x}t + \phi_{LSB} + \phi_{USB} + 3\theta)$$

$$+ \frac{C^3}{4} \cdot \cos(3\omega_{0x}t + 3\theta)$$

$$+ \frac{3C^2D}{4} \cdot \sin(3\omega_{0x}t + 3\theta)$$

$$- \frac{3CD^2}{4} \cdot \cos(3\omega_{0x}t + 3\theta)$$

$$- \frac{D^3}{4} \cdot \sin(3\omega_{0x}t + 3\theta)$$

$$+ \frac{3AB^2}{4} \cdot \cos((3\omega_{0x} + \omega_\Omega)t - T_d\omega_\Omega + \varphi + \phi_{LSB} + 2\phi_{USB} + 3\theta)$$

$$+ \frac{3BC^2}{4} \cdot \cos((3\omega_{0x} + \omega_\Omega)t - T_d\omega_\Omega + \varphi + \phi_{USB} + 3\theta)$$

$$+ \frac{3BCD}{2} \cdot \sin((3\omega_{0x} + \omega_\Omega)t - T_d\omega_\Omega + \varphi + \phi_{USB} + 3\theta)$$

$$- \frac{3BD^2}{4} \cdot \cos((3\omega_{0x} + \omega_\Omega)t - T_d\omega_\Omega + \varphi + \phi_{USB} + 3\theta)$$

$$+ \frac{3B^2C}{4} \cdot \cos((3\omega_{0x} + 2\omega_\Omega)t - 2T_d\omega_\Omega + 2\varphi + 2\phi_{USB} + 3\theta)$$

$$+ \frac{3B^2D}{4} \cdot \sin((3\omega_{0x} + 2\omega_\Omega)t - 2T_d\omega_\Omega + 2\varphi + 2\phi_{USB} + 3\theta)$$

$$+ \frac{B^3}{4} \cdot \cos((3\omega_{0x} + 3\omega_\Omega)t - 3T_d\omega_\Omega + 3\varphi + 3\phi_{USB} + 3\theta).$$

From (A.5), it can be seen that there are frequency components at $\omega_{0x} - 3\omega_\Omega$, $\omega_{0x} - 2\omega_\Omega$, $\omega_{0x} - \omega_\Omega$, ω_{0x}, $\omega_{0x} + \omega_\Omega$, $\omega_{0x} + 2\omega_\Omega$, $\omega_{0x} + 3\omega_\Omega$, $3\omega_{0x} - 3\omega_\Omega$, $3\omega_{0x} - 2\omega_\Omega$, $3\omega_{0x} - \omega_\Omega$, $3\omega_{0x}$, $3\omega_{0x} + \omega_\Omega$, $3\omega_{0x} + 2\omega_\Omega$, and $3\omega_{0x} + 3\omega_\Omega$.

The in-phase component of the final output is next evaluated by multiplying (A.5) by $\cos(\omega_{0x}t)$, amplifying it by two and filtering with an ideal low-pass filter which removes the frequency components at ω_{0x} and above. The output signal has frequency components at dc, ω_Ω, $2\omega_\Omega$, and $3\omega_\Omega$. They are

$$I_{out,sec,dc}(t) =$$
$$\left(\frac{3A^2C}{2} + \frac{3B^2C}{2} + \frac{3C^3}{4} + \frac{3CD^2}{4} \right) \cdot \cos\theta +$$
$$\left(\frac{3A^2D}{2} + \frac{3B^2D}{2} + \frac{3C^2D}{4} + \frac{3D^3}{4} \right) \cdot \sin\theta + \qquad \text{(A.6a)}$$
$$\frac{3ABC}{2} \cdot \cos(\phi_{LSB} + \phi_{USB} + \theta) -$$
$$\frac{3ABD}{2} \cdot \sin(\phi_{LSB} + \phi_{USB} + \theta),$$

$$I_{out,sec,\omega_\Omega}(t) =$$
$$\left(\frac{3A^3}{4} + \frac{3AB^2}{2} + \frac{3AC^2}{2} + \frac{3AD^2}{2} \right) \cdot \cos(\omega_\Omega(t - T_d) + \varphi - \phi_{LSB} - \theta) +$$
$$\left(\frac{3A^2B}{2} + \frac{3B^3}{4} + \frac{3BC^2}{2} + \frac{3BD^2}{2} \right) \cdot \cos(\omega_\Omega(t - T_d) + \varphi + \phi_{USB} + \theta) +$$
$$\left(\frac{3AC^2}{4} - \frac{3AD^2}{4} \right) \cdot \cos(\omega_\Omega(t - T_d) + \varphi - \phi_{LSB} + \theta) +$$
$$\left(\frac{3BC^2}{4} - \frac{3BD^2}{4} \right) \cdot \cos(\omega_\Omega(t - T_d) + \varphi + \phi_{USB} - \theta) +$$

$$\text{(A.6b)}$$

$$\frac{3ACD}{2} \cdot \sin\left(\omega_\Omega(t - T_d) + \varphi - \phi_{LSB} + \theta\right) -$$

$$\frac{3BCD}{2} \cdot \sin\left(\omega_\Omega(t - T_d) + \varphi + \phi_{USB} - \theta\right),$$

$$I_{out,sec,2\omega_\Omega}(t) =$$

$$\frac{3A^2C}{4} \cdot \cos\left(2\omega_\Omega(t - T_d) + 2\varphi - 2\phi_{LSB} - \theta\right) +$$

$$\frac{3B^2C}{4} \cdot \cos\left(2\omega_\Omega(t - T_d) + 2\varphi + 2\phi_{USB} + \theta\right) +$$

$$\frac{3A^2D}{4} \cdot \sin\left(2\omega_\Omega(t - T_d) + 2\varphi - 2\phi_{LSB} - \theta\right) -$$

$$\frac{3B^2D}{4} \cdot \sin\left(2\omega_\Omega(t - T_d) + 2\varphi + 2\phi_{USB} + \theta\right) + \qquad \text{(A.6c)}$$

$$\frac{3ABC}{2} \cdot \cos\left(2\omega_\Omega(t - T_d) + 2\varphi - \phi_{LSB} + \phi_{USB} - \theta\right) +$$

$$\frac{3ABC}{2} \cdot \cos\left(2\omega_\Omega(t - T_d) + 2\varphi - \phi_{LSB} + \phi_{USB} + \theta\right) -$$

$$\frac{3ABD}{2} \cdot \sin\left(2\omega_\Omega(t - T_d) + 2\varphi - \phi_{LSB} + \phi_{USB} - \theta\right) +$$

$$\frac{3ABD}{2} \cdot \sin\left(2\omega_\Omega(t - T_d) + 2\varphi - \phi_{LSB} + \phi_{USB} + \theta\right),$$

and

$$I_{out,sec,3\omega_\Omega}(t) =$$

$$\frac{3A^2B}{4} \cdot \cos\left(3\omega_\Omega(t - T_d) + 3\varphi - 2\phi_{LSB} + \phi_{USB} - \theta\right) + \qquad \text{(A.6d)}$$

$$\frac{3AB^2}{4} \cdot \cos\left(3\omega_\Omega(t - T_d) + 3\varphi - \phi_{LSB} + 2\phi_{USB} + \theta\right),$$

respectively.

Appendix B

Effect of Mechanical-Thermal Noise

The power spectral density of the mechanical-thermal noise force acting on the y-directional resonator is

$$F_n^2 = 4k_B T D_{yy}. \tag{B.1}$$

Two infinitesimally narrow noise bands, centered around $\omega_{0x} - \omega$ and $\omega_{0x} + \omega$ and with a bandwidth of $d\omega$, are considered. The noise power in each band is then $4k_B T D_{yy} d\omega$, and the noise signals can be modeled with two sinusoids in such a way that

$$
\begin{aligned}
F_n(t) = {} & \sqrt{8k_B T D_{yy} d\omega} \cdot \sin\left((\omega_{0x} - \omega)t + \phi_-\right) + \\
& \sqrt{8k_B T D_{yy} d\omega} \cdot \sin\left((\omega_{0x} + \omega)t + \phi_+\right),
\end{aligned} \tag{B.2}
$$

where ϕ_- and ϕ_+ are random phase shifts of the two signals. The powers of both sinusoids are equal to the noise power concentrated into the band.

Next, these signals traverse through force-to-displacement and displacement-to-voltage conversion. For the sake of brevity, the total gains are now denoted as G_- and G_+ for the lower and the upper sidebands, respectively. At the end of this appendix, the gains will be defined in more detail, with the symbols used elsewhere in this thesis. The phase shifts occurring in the conversions can be disregarded, as the initial phase shifts ϕ_- and ϕ_+ are random.

After synchronous demodulation performed by multiplying by $\cos(\omega_{0x}t)$ and the subsequent gain of two and the low-pass filtering, the contribution of the noise signals

to the in-phase component of the output signal is

$$
\begin{aligned}
I_{out,sec,n}(t) = & G_- \sqrt{8k_B T D_{yy} d\omega} \cdot \sin(-\omega t + \phi_-) + \\
& G_+ \sqrt{8k_B T D_{yy} d\omega} \cdot \sin(\omega t + \phi_+).
\end{aligned}
\tag{B.3}
$$

By using the substitutions[1]

$$
\overline{G} = \frac{G_+ + G_-}{2},
\tag{B.4a}
$$

$$
\Delta G = \frac{G_+ - G_-}{2},
\tag{B.4b}
$$

$$
\overline{\phi} = \frac{\phi_+ + \phi_-}{2},
\tag{B.4c}
$$

and

$$
\Delta\phi = \frac{\phi_+ \phi_-}{2},
\tag{B.4d}
$$

the result can be written as

$$
\begin{aligned}
I_{out,sec,n}(t) = & -\overline{G}\sqrt{8k_B T D_{yy} d\omega} \cdot \left[\sin(\omega t - \overline{\phi} + \Delta\phi) - \sin(\omega t + \overline{\phi} + \Delta\phi)\right] + \\
& \Delta G\sqrt{8k_B T D_{yy} d\omega} \cdot \left[\sin(\omega t - \overline{\phi} + \Delta\phi) + \sin(\omega t + \overline{\phi} + \Delta\phi)\right].
\end{aligned}
\tag{B.5}
$$

By applying the trigonometric function product formulae, the form

$$
\begin{aligned}
I_{out,sec,n}(t) = & \overline{G}\sqrt{8k_B T D_{yy} d\omega} \cdot 2 \cdot \cos(\omega t + \Delta\phi) \cdot \sin(\overline{\phi}) + \\
& \Delta G\sqrt{8k_B T D_{yy} d\omega} \cdot 2 \cdot \sin(\omega t + \Delta\phi) \cdot \cos(\overline{\phi})
\end{aligned}
\tag{B.6}
$$

results.

The mean-square noise power at ω, as a function of $\overline{\phi}$, can now be written as

$$
I^2_{out,sec,n,rms}(\overline{\phi}) = 16k_B T D_{yy} d\omega \cdot \left[\overline{G}^2 \sin^2(\overline{\phi}) + \Delta G^2 \cos^2(\overline{\phi})\right].
\tag{B.7}
$$

The mean-square noise power can be solved by averaging over the random phase shift $\overline{\phi}$, resulting in

$$
I^2_{out,sec,n,rms} = \frac{1}{2\pi}\int_0^{2\pi} I^2_{out,sec,n,rms}(\overline{\phi})d\overline{\phi} = 8k_B T D_{yy} d\omega \cdot \left(\overline{G}^2 + \Delta G^2\right).
\tag{B.8}
$$

Finally, the power spectral density is resolved by dividing by the bandwidth $d\omega$. The result is

$$
I^2_{out,sec,n} = 8k_B T D_{yy} \cdot \left(\overline{G}^2 + \Delta G^2\right).
\tag{B.9}
$$

By performing synchronous demodulation by multiplying by $\sin(\omega_{0x}t)$ and fol-

---

[1]The symbols $\overline{\phi}$ and $\Delta\phi$ are used with other meanings elsewhere in this thesis. The use of the definitions given here is limited to this appendix.

lowing an identical path, the power spectral density in the quadrature component of the output signal can be shown to be equal to that in the in-phase component, that is,

$$Q^2_{out,sec,n} = 8k_B T D_{yy} \cdot \left(\overline{G}^2 + \Delta G^2\right). \tag{B.10}$$

If it is now defined that $\omega = \omega_\Omega$, the gains G_- and G_+ can be written as

$$G_- = \frac{G_{V/y} G_{y/\Omega,LSB}}{2A_x \omega_{0x} m_x} \tag{B.11a}$$

and

$$G_+ = \frac{G_{V/y} G_{y/\Omega,USB}}{2A_x \omega_{0x} m_x}, \tag{B.11b}$$

where it has been assumed that the gain $G_{V/y}$ of the displacement-to-voltage conversion is frequency-independent. By now substituting (B.11a) and (B.11b) into (B.4a) and (B.4b), and then the result into (B.9) and (B.10), the noise densities can be written as

$$\begin{aligned} I^2_{out,sec,n} = Q^2_{out,sec,n} &= \frac{G_{V/y} \cdot 8k_B T D_{yy} \cdot \left(\overline{G_{y/\Omega}}^2 + \Delta G^2_{y/\Omega}\right)}{(2A_x \omega_{0x} m_x)^2} \\ &= \frac{4G_{V/y} \cdot 2k_B T D_{yy} \cdot \left(\overline{G_{y/\Omega}}^2 + \Delta G^2_{y/\Omega}\right)}{(2A_x \omega_{0x} m_x)^2}, \end{aligned} \tag{B.12}$$

where the definitions of Eqs. (3.12a) and (3.12b) have been applied.

Appendix C

Parallel-Plate Actuator with Voltage Biasing

The parallel-plate electrostatic actuator biased with a constant voltage source can be modeled with the circuit shown in Fig. C.1. If the unloaded terminal voltage of the capacitor C_{BAT} is V, the charge stored in the system is $Q_{BAT} = C_{BAT}V$. When the limit $C_{BAT} \rightarrow \infty$ is taken, C_{BAT} turns into an ideal voltage source, with terminal voltage V.

$$C = \frac{A\varepsilon_0\varepsilon_r}{x_0+x} \qquad Q_{BAT}=C_{BAT}V \qquad C_{BAT} \longrightarrow \infty$$
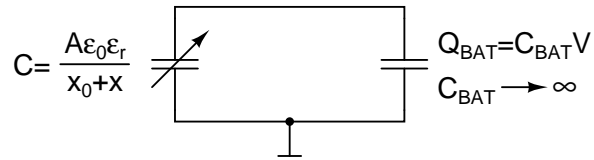
Figure C.1 Circuit used to model the parallel-plate electrostatic actuator biased with a constant voltage.

After connecting the capacitive load C into the system, the total energy stored in the system is

$$
\begin{aligned}
E_{tot} &= \frac{Q_{BAT}^2}{2\left(C+C_{BAT}\right)} = \frac{\left(C_{BAT}V\right)^2}{2\left(C+C_{BAT}\right)} \\
&= \frac{C_{BAT}V^2}{2} \cdot \left(\frac{1}{1+C/C_{BAT}}\right) \\
&= \frac{C_{BAT}V^2}{2} \cdot \left(1+\frac{C}{C_{BAT}}\right)^{-1}.
\end{aligned}
\tag{C.1}
$$

As defined in Eq. (4.1), the electrostatic force can now be evaluated as

$$F_{es} = -\frac{\mathrm{d}E_{tot}}{\mathrm{d}x} = -\frac{\mathrm{d}E_{tot}}{\mathrm{d}C} \cdot \frac{\mathrm{d}C}{\mathrm{d}x}. \tag{C.2}$$

By differentiating,

$$F_{es} = -\left[-\frac{V^2}{2} \cdot \left(1 + \frac{C}{C_{BAT}}\right)^{-2}\right] \cdot \left[-\frac{A\varepsilon_0\varepsilon_r}{(x_0 + x)^2}\right]$$

$$= -\frac{A\varepsilon_0\varepsilon_r V^2}{2(x_0 + x)^{-2}} \cdot \left(1 + \frac{C}{C_{BAT}}\right)^{-2}. \tag{C.3}$$

Now, when $C_{BAT} \to \infty$,

$$F_{es} \to -\frac{A\varepsilon_0\varepsilon_r V^2}{2(x_0 + x)^2}. \tag{C.4}$$

Appendix D

# Noise Properties of SC Readout Circuits with CDS

The noise sources of the CDS voltage amplifier of Fig. 7.8 (a) in both clock phases are shown in Fig. D.1. The noise performance will first be analyzed for a single-stage OTA. Assuming that $1/g_m \gg R_{1\ldots6}$, where g_m is the transconductance of the operational amplifier, and that $C_1 > C_2$, the mean-square switch noise power referred to change in input capacitance is

$$C_{n,sw,rms}^2 \approx \frac{k_B T \cdot g_m R_1 C_1^2}{(C_1 + C_2) \cdot V_{REF}^2} + \frac{k_B T \cdot g_m R_5 C_2^2}{(C_1 + C_2) \cdot V_{REF}^2} + \frac{k_B T \cdot g_m R_2}{\left(\frac{1}{C_1} + \frac{C_L}{C_1 C_2} + \frac{C_L}{C_1^2}\right) \cdot V_{REF}^2} + \frac{k_B T}{\left(\frac{C_L^2}{C_1 C_2} + \frac{C_L^2}{C_2^3} + \frac{C_L}{C_2}\right) \cdot V_{REF}^2}.$$ (D.1a)

The first two terms are caused by the noise of SW1 and SW5 sampled into C_1 and C_2, respectively, at the end of clock phase ϕ_1, and the last two terms are caused by the noise of SW2, SW4, and SW6 sampled into C_L at the end of clock phase ϕ_2. If $C_2 > C_1$, then the last two terms are not correct, and the noise contributions of SW2, SW4, and SW6 in clock phase ϕ_2 need to be calculated by integrating the transfer functions from the noise sources to the output.

The mean-square noise power of the operational amplifier referred to change in input capacitance is

$$C_{n,opa,rms}^2 = \frac{4\gamma_n k_B T}{3} \cdot \left[\frac{C_1 + C_2}{V_{REF}^2} + \frac{(C_1 + C_2)^2}{\left(C_1 + C_L + \frac{C_1 C_L}{C_2}\right) \cdot V_{REF}^2} \right].$$ (D.1b)
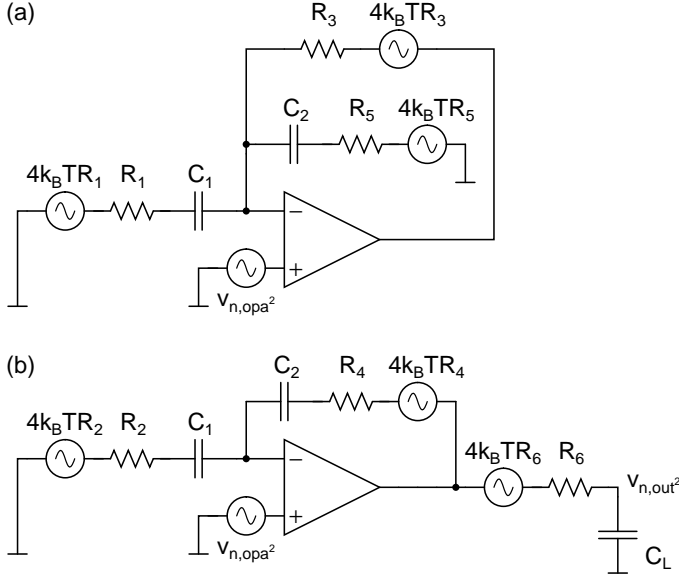
Figure D.1 Noise sources of the CDS SC voltage amplifier shown in Fig. 7.8 (a). (a) Clock phase ϕ_1. (b) Clock phase ϕ_2.

Here, the first term is caused by the noise of the amplifier sampled into C_1 and C_2 at the end of clock phase ϕ_1 and the second term by the noise sampled into C_L at the end of clock phase ϕ_2.

If the operational amplifier is a multi-stage frequency compensated amplifier instead of a single-stage OTA, the mean-square noise power induced by the switches is

$$C_{n,sw,rms}^2 \approx \frac{k_B T \cdot g_m R_1 C_1^2}{C_C \cdot V_{REF}^2} + \frac{k_B T \cdot g_m R_5 C_2^2}{C_C \cdot V_{REF}^2} + \frac{k_B T \cdot g_m R_2 C_1^2}{C_C \cdot V_{REF}^2} + \frac{k_B T}{\left(\frac{C_L^2}{C_1 C_2^2} + \frac{C_L^2}{C_2^3} + \frac{C_L}{C_2^2} \right) \cdot V_{REF}^2},$$

(D.2a)

and the mean-square noise power of the operational amplifier is

$$C_{n,opa,rms}^2 = \frac{4\gamma_n k_B T}{3} \cdot \left[2 \cdot \frac{(C_1 + C_2)^2}{C_C \cdot V_{REF}^2} \right].$$

(D.2b)

In Eqs. (D.2a) and (D.2b), the terms caused by different noise sources are at the same locations as in Eqs. (D.1a) and (D.1b). That is, the cause of the first term in Eq. (D.2a) is the same as that of the first term in Eq. (D.1a), etc. This convention will be followed throughout the rest of this appendix.

The noise sources of the CDS voltage amplifier of Fig. 7.8 (b) in both clock phases

are shown in Fig. D.2. With the same assumptions as above and with a single-stage OTA, the mean-square switch noise power referred to change in input capacitance is

$$C_{n,sw,rms}^2 \approx \frac{k_B T \cdot C_1}{V_{REF}^2} + \frac{k_B T \cdot g_m R_4 C_2^2}{C_{CDS} \cdot V_{REF}^2} + \frac{k_B T \cdot C_2}{V_{REF}^2} +$$
$$\frac{k_B T \cdot g_m R_2}{\left(\frac{1}{C_1} + \frac{C_L}{C_1 C_2} + \frac{C_L}{C_1^2} \right) \cdot V_{REF}^2} + \frac{k_B T}{\left(\frac{C_L^2}{C_1 C_2} + \frac{C_L^2}{C_2^3} + \frac{C_L}{C_2^2} \right) \cdot V_{REF}^2}.$$

(D.3a)

Now, the first three terms are caused by the noise of SW1 and SW4 sampled into C_1, the noise of SW4 sampled into C_{CDS}, and the noise of SW6 sampled into C_2, all at the end of clock phase ϕ_1, and the two last terms by the noise of SW2, SW3, and SW7 sampled into C_L at the end of clock phase ϕ_2. As above, if $C_2 > C_1$, then the last two terms are not correct.
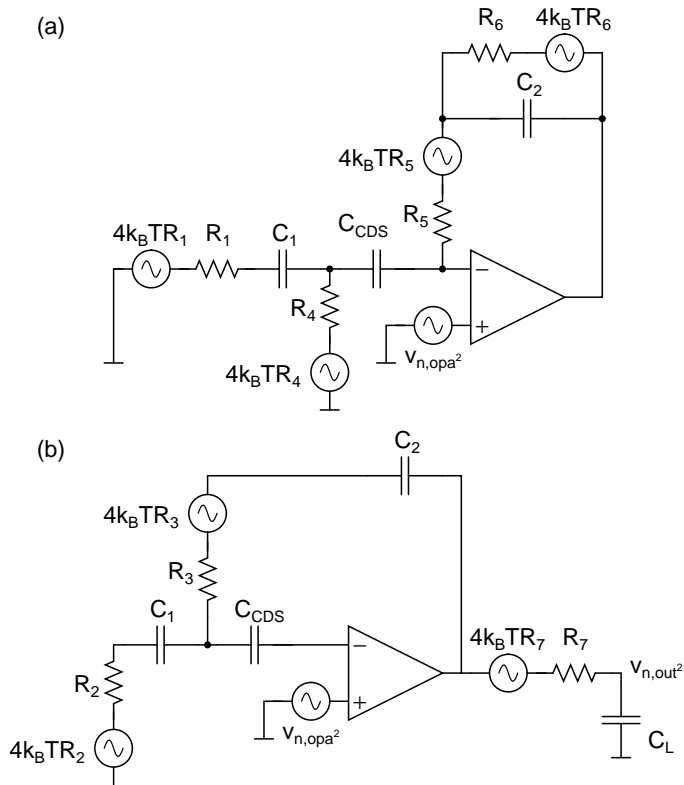
Figure D.2 Noise sources of the CDS SC voltage amplifier shown in Fig. 7.8 (b). (a) Clock phase ϕ_1. (b) Clock phase ϕ_2.

The mean-square noise power of the operational amplifier referred to change in

input capacitance is

$$C_{n,opa,rms}^2 = \frac{4\gamma_n k_B T}{3} \cdot \left[\frac{C_2^2}{C_{CDS} \cdot V_{REF}^2} + \frac{(C_1 + C_2)^2}{\left(C_1 + C_L + \frac{C_1 C_L}{C_2}\right) \cdot V_{REF}^2} \right]. \qquad \text{(D.3b)}$$

Here, the first term is caused by the noise of the amplifier sampled into C_{CDS} at the end of clock phase ϕ_1 and the second term by the noise sampled into C_L at the end of clock phase ϕ_2.

For the multi-stage amplifier, the mean-square noise power induced by the switches is

$$\begin{aligned} C_{n,sw,rms}^2 \approx & \frac{k_B T \cdot C_1}{V_{REF}^2} + \frac{k_B T \cdot g_m R_4 C_2^2}{C_C \cdot V_{REF}^2} + \frac{k_B T \cdot C_2}{V_{REF}^2} + \\ & \frac{k_B T \cdot g_m R_2 C_1^2}{C_C \cdot V_{REF}^2} + \frac{k_B T}{\left(\frac{C_L^2}{C_1 C_2^2} + \frac{C_L^2}{C_2^3} + \frac{C_L}{C_2^2}\right) \cdot V_{REF}^2}, \end{aligned} \qquad \text{(D.4a)}$$

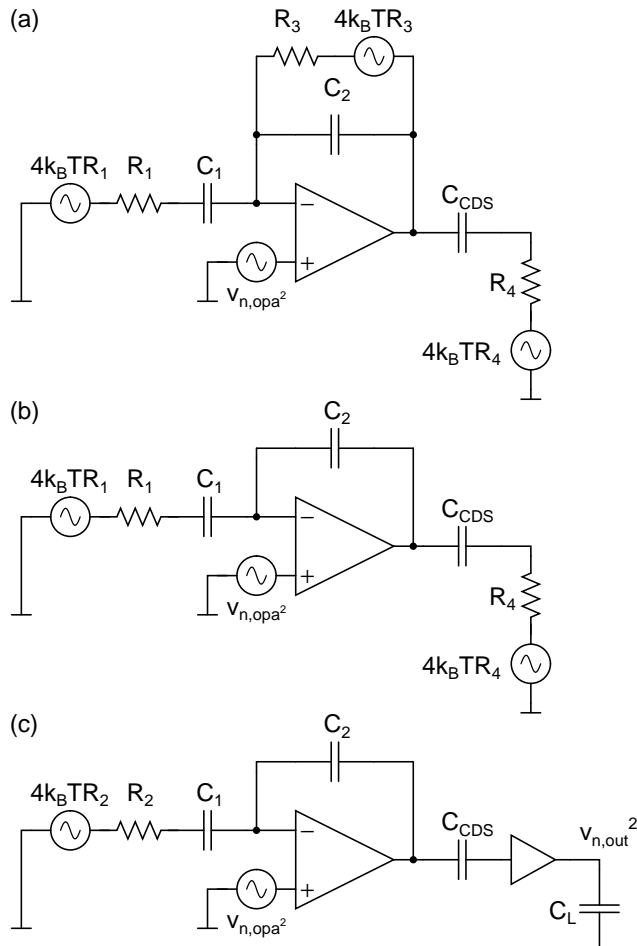and the mean-square noise power of the operational amplifier is

$$C_{n,opa,rms}^2 = \frac{4\gamma_n k_B T}{3} \cdot \left[\frac{C_2^2}{C_C \cdot V_{REF}^2} + \frac{(C_1 + C_2)^2}{C_C \cdot V_{REF}^2} \right]. \qquad \text{(D.4b)}$$

The noise sources of the CDS voltage amplifier shown in Fig. 7.8 (c) in all three clock phases are shown in Fig. D.3. In the last clock phase, the output at the right-hand-side plate of C_{CDS} is driving a high-impedance node, in this case an ideal buffer, which then drives the load capacitance C_L. The output could also drive a virtual ground, in which case the noise equations need to be rederived. With the same assumptions as above and with a single-stage OTA, the mean-square switch noise power referred to change in input capacitance is

$$\begin{aligned} C_{n,sw,rms}^2 \approx & \frac{k_B T \cdot g_m R_1}{\left(\frac{1}{C_1} + \frac{C_{CDS}}{C_1 C_2} + \frac{C_{CDS}}{C_1^2}\right) \cdot V_{REF}^2} + \frac{k_B T \cdot g_m R_4}{\left(\frac{C_1}{C_2^2} + \frac{C_{CDS}}{C_2^2} + \frac{C_1 C_{CDS}}{C_2^3}\right) \cdot V_{REF}^2} + \\ & \frac{k_B T}{\left(\frac{C_{CDS}^2}{C_1 C_2^2} + \frac{C_{CDS}^2}{C_2^3} + \frac{C_{CDS}}{C_2^2}\right) \cdot V_{REF}^2} + \frac{k_B T \cdot g_m R_2}{\left(\frac{1}{C_1} + \frac{C_{CDS}}{C_1 C_2} + \frac{C_{CDS}}{C_1^2}\right) \cdot V_{REF}^2}. \end{aligned} \qquad \text{(D.5a)}$$

Now, the first three terms are caused by the noise of SW1 and SW4 sampled into C_{CDS} at the end of clock phase $\phi_1 \& \overline{\phi_1'}$ and the fourth term by the low-frequency (within the operational amplifier's bandwidth) noise of SW2 sampled into C_L at the end of clock phase ϕ_2. It should be observed that the high-frequency noise of SW2 (beyond the amplifier's bandwidth) is not bandwidth-limited. Thus, its mean-square value can not be evaluated until some element is used to limit its bandwidth. As above, if $C_2 > C_1$,

then the last two terms are not correct.

Figure D.3 Noise sources of the CDS SC voltage amplifier shown in Fig. 7.8 (c). (a) Clock phase $\phi_1 \& \phi_1'$. (b) Clock phase $\phi_1 \& \overline{\phi_1'}$. (c) Clock phase ϕ_2.

The mean-square noise power of the operational amplifier referred to change in input capacitance is

$$C_{n,opa,rms}^2 = \frac{4\gamma_n k_B T}{3} \cdot \left[\frac{(C_1 + C_2)^2}{\left(C_1 + C_{CDS} + \frac{C_1 C_{CDS}}{C_2}\right) \cdot V_{REF}^2} + \frac{(C_1 + C_2)^2}{C_1 \cdot V_{REF}^2} \right]. \qquad \text{(D.5b)}$$

The first term is caused by the noise of the amplifier sampled into C_{CDS} at the end of clock phase $\phi_1 \& \overline{\phi_1'}$ and the second term by the noise sampled into C_L at the end of clock phase ϕ_2.

For the multi-stage amplifier, the mean-square noise power induced by the switches

is

$$C_{n,sw,rms}^2 \approx \frac{k_B T \cdot g_m R_1 C_1^2}{C_C \cdot V_{REF}^2} + \frac{k_B T \cdot g_m R_4 C_2^2}{C_C \cdot V_{REF}^2} +$$
$$\frac{k_B T}{\left(\frac{C_{CDS}^2}{C_1 C_2^2} + \frac{C_{CDS}^2}{C_2^3} + \frac{C_{CDS}}{C_2^2}\right) \cdot V_{REF}^2} + \frac{k_B T \cdot g_m R_2 C_1^2}{C_C \cdot V_{REF}^2}. \tag{D.6a}$$

and the mean-square noise power of the operational amplifier is

$$C_{n,opa,rms}^2 = \frac{4\gamma_n k_B T}{3} \cdot \left[2 \cdot \frac{(C_1 + C_2)^2}{C_C \cdot V_{REF}^2}\right]. \tag{D.6b}$$

Tables D.1 and D.2 show the resulting noise levels for the different circuit configurations evaluated with the example values $C_1 = 4\,\text{pF}$, $C_2 = 1\,\text{pF}$, $C_{CDS} = 1\,\text{pF}$, $C_L = 1\,\text{pF}$, $f_s = 50\,\text{kHz}$, $V_{REF} = 2.5\,\text{V}$, $R_{1...n} = 1\,\text{k}\Omega$, and $\gamma_n = 1$. In Table D.1, a single-stage OTA with $g_m = 40\,\mu\text{A/V}$ has been assumed, whereas in Table D.2, a multi-stage operational amplifier with C_C large enough to render the noise of the amplifier negligible has been assumed. The performance of the circuit without CDS is included for reference.

Table D.1 Input-referred noise levels of various SC voltage amplifiers assuming a single-stage OTA.

Circuit	$C_{n,sw,rms}$	$C_{n,opa,rms}$	$C_{n,rms}$	Spectral density of C_n
Fig. 7.7	33.3 aF	77.4 aF	84.2 aF	$0.53\,\text{aF}/\sqrt{Hz}$
Fig. 7.8 (a)	20.8 aF	82.9 aF	85.4 aF	$0.54\,\text{aF}/\sqrt{Hz}$
Fig. 7.8 (b)	60.7 aF	57.8 aF	83.8 aF	$0.53\,\text{aF}/\sqrt{Hz}$
Fig. 7.8 (c)	19.8 aF	89.3 aF	91.5 aF	$0.58\,\text{aF}/\sqrt{Hz}$

Table D.2 Input-referred noise levels of various SC voltage amplifiers assuming a multi-stage amplifier with $C_C \to \infty$ such that $g_m/C_C = 2\pi \cdot 700\,\text{kHz}$.

Circuit	$C_{n,sw,rms}$	$C_{n,opa,rms}$	$C_{n,rms}$	Spectral density of C_n
Fig. 7.7	32.4 aF	–	32.4 aF	$0.20\,\text{aF}/\sqrt{Hz}$
Fig. 7.8 (a)	19.8 aF	–	19.8 aF	$0.13\,\text{aF}/\sqrt{Hz}$
Fig. 7.8 (b)	60.5 aF	–	60.5 aF	$0.38\,\text{aF}/\sqrt{Hz}$
Fig. 7.8 (c)	19.8 aF	–	19.8 aF	$0.13\,\text{aF}/\sqrt{Hz}$

Appendix E

Photograph of the Sensor Element
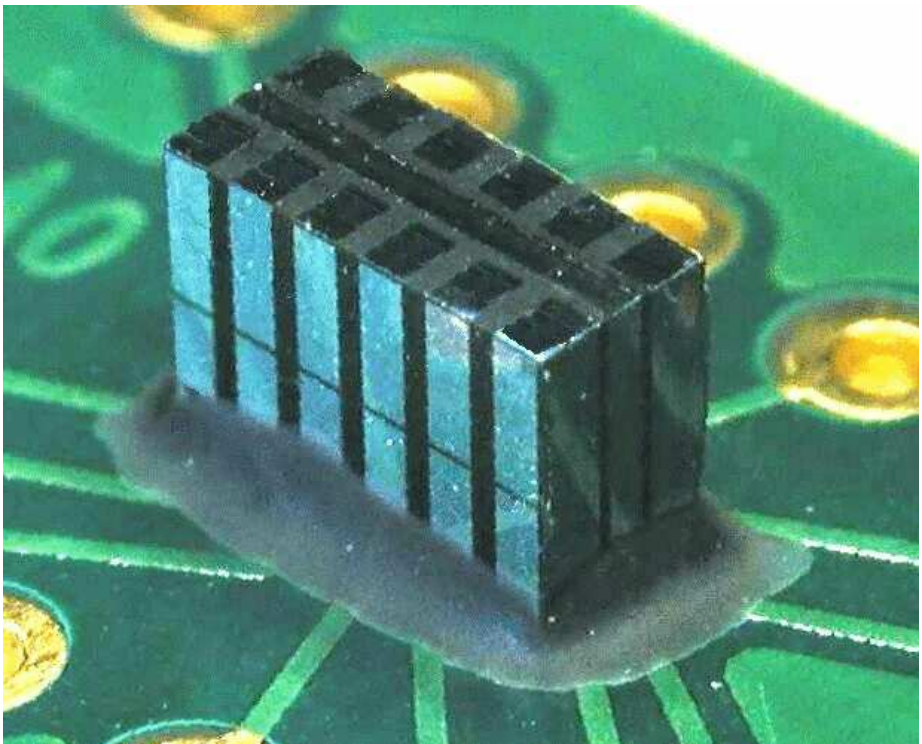
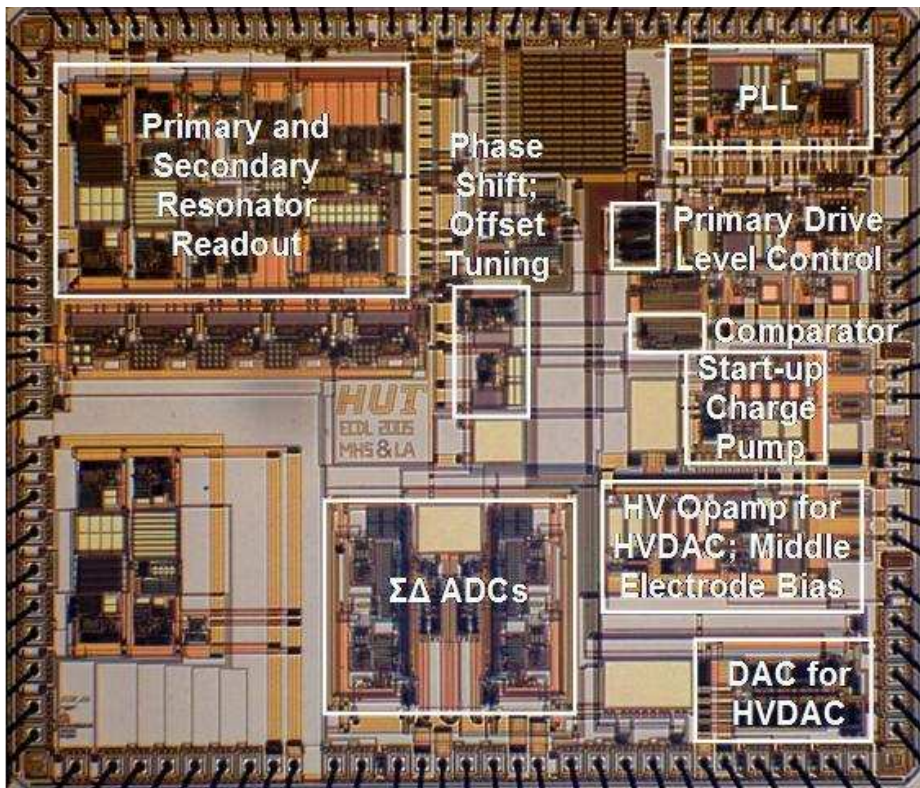**Figure E.1** The sensor element, soldered onto a ceramic carrier. (Courtesy of VTI Technologies, Vantaa, Finland)
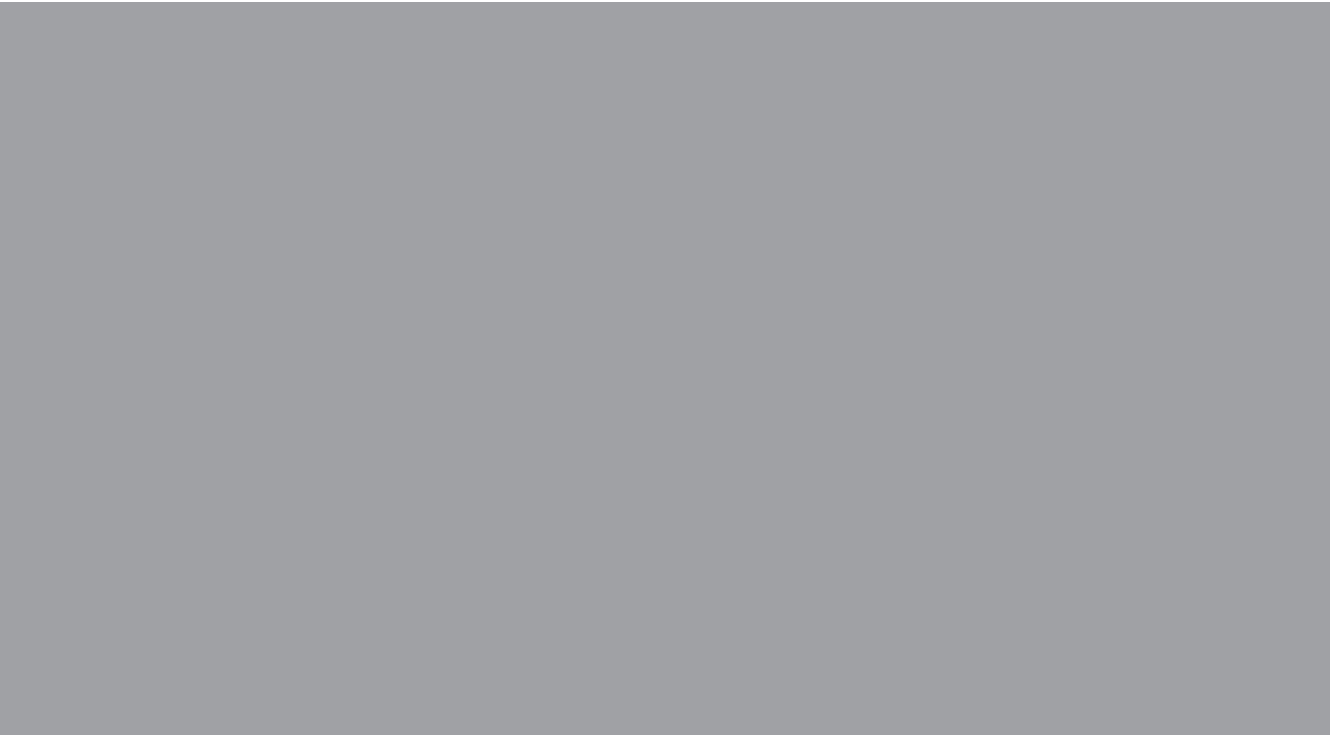
Appendix F

Microphotograph of the Implemented ASIC

Figure F.1 A microphotograph of the implemented ASIC.